Towards the Glass Transition in Vibrated Granular Matter

THÈSE N° 5336 (2012)

PRÉSENTÉE LE 23 MARS 2012
À LA FACULTÉ DES SCIENCES DE BASE
LABORATOIRE DE PHYSIQUE DE LA MATIÈRE COMPLEXE
PROGRAMME DOCTORAL EN PHYSIQUE

ÉCOLE POLYTECHNIQUE FÉDÉRALE DE LAUSANNE

POUR L'OBTENTION DU GRADE DE DOCTEUR ÈS SCIENCES

PAR

Alessandro Luigi SELLERIO

EPFL

ÉCOLE POLYTECHNIQUE
FÉDÉRALE DE LAUSANNE

Suisse
2012

To my dearest ones.

Abstract

Granular materials are large sets of macroscopic particles that interact solely via contact forces. The static behavior depends on the contact network and on the surface friction forces between grains; when they are set in motion (typically by vibrations) their dynamics is dominated by inelastic collisions. For these reasons granular media show an extremely rich phenomenology, ranging from fluid-like properties (if strongly vibrated), to "jamming", glassy, behavior (if weakly vibrated), to aging and hysteretical phenomena observed when they become trapped in frozen, amorphous states.

The objective of this work is to study these states and transitions, and to characterize the analogies found between the dynamic behavior of vibrated granular media and the glass transition observed in thermal glass-formers. These analogies justify the interest in granular materials, because granular media can be seen as simplified model systems useful in the study of out of equilibrium thermodynamics, and, in general, to the larger framework known as "complexity".

The granular materials considered here are composed of spheric, polished glass spheres. Since the surface state plays an important role in the grain-grain interaction, some measurements were also performed with acid etched beads, having different surface roughness. The samples are vertically vibrated to achieve vibrofluidization. Different kinds of vibration are used, to highlight different properties of the system.

We first consider the transition between the fluid and the subcooled glassy phase, using different experimental techniques. The most important one is a torsion oscillator, that interacts with the granular media via immersed probes. The torsion oscillator can be used in forced mode. A torque is applied on the probe, and we measure the mechanical response function (complex susceptibility). In general, a relaxation is found and it is interpreted as the signature of the irreversible energy loss (damping) in granular collisions. This relaxation has an intrinsic time scale, and systematic analysis of it shows that a clear parallel can be traced to the behavior of "strong" glasses. In particular, it is found that (*i*) the relaxation time is a function of a unified control parameter, proportional to the square root of the average vibration, and phenomenologically equivalent to an effective temperature; (*ii*) the functional form with which the relaxation times approach the final "frozen" state has an Arrhenius, or Vögel-Fulcher-Tamman (VFT) behavior.

The same torsion oscillator is employed in free mode. In this case, no external torque is

Abstract

applied, and the probe moves adapting its position under the effect of the continuous rear-rangements in the sample. The system is studied by computing the power spectral density of the (angular position) time series. The resulting spectra represent a "configurational noise" as the system randomly hops from one configuration to the following. This allows to define, using a completely different approach, the same intrinsic time scale observed in forced mode measurements. The comparison of the two techniques allows to obtain a more complete and detailed picture of the dynamics in the jamming region. From this comparison, it was inferred that the system is also influenced by an effective vibration frequency, and that the relaxation time has indeed a non-Arrhenius behavior as a function of a control parameter defined as $a_s = \sqrt{\Gamma}/\omega_s$.

A model was developed combining rheological observations to a statistic approach describing extremal phenomena. This model justifies the appearance of both the control parameter and the VFT evolution of the relaxation. Furthermore, the model is predictive and exposes the effect of a few other rheologic properties of granular system. The effect of surface roughness are considered, showing that the static and dynamic surface friction coefficients are well described by the model.

A second relevant part of this work is devoted to an explicit verification that macroscopic probes act as brownian objects. This fact is often used to interpret experimental data (also in the present work) and to propose theoretical model. However, no explicit evidence has ever been discussed. This is hard to do, using a constrained system such as the torsion oscillator, because the restoring coefficient influences the dynamics of diffusion. To overcome the problem we built a different apparatus, called "brownian motor", where the probes are mounted on ball bearings, so that they are free to turn without constraint. The properties of the time series of the position of the free turning probe and of the torsionally constrained oscillator can finally be analyzed and compared with simple simulations. The data show an overall diffusion-like behavior, that is influenced by the presence of constraints. Using fractal analysis we estimate the diffusion, or Hurst exponent. This allows to verify that a "macroscopic" object (the probe) immersed in the "microscopic" granular medium indeed behaves as a Brownian object, and that its dynamics can be studied in detail, showing that it undergoes anomalous diffusion.

This work is concluded with a discussion on a few possible developments. The most promising idea is a novel approach to the study of the geometrical properties of the contact network of granular assemblies, that is responsible for many of the properties of the granular sample. By using Magnetic Resonance Imaging, the static 3-D structure of granular media can be reconstructed with unprecedented accuracy, resolution and ease of reproducibility. From the spatial information we can extract all the properties of static granular media: the compaction factor, the grain-grain correlation function, the free volume and other observables. Systematic studies could allow experimental confirmations of the many theoretical models that have been proposed in the last years and that still lack a thorough comparison with experiments.

This idea does not conclude the perspectives of this work, that are vast and intriguing. A few promising subjects are reviewed more into detail in the corresponding Perspective section. To

name a few we cite: measurements of induced aging in non-vibrated samples, the brownian motor, stick and slip phenomena and their comparison with earthquakes.

Résumé

Les matériaux granulaires sont des assemblages de nombreuses particules macroscopiques qui n'interagissent que par des forces de contact. Leur comportement statique dépend du réseau des contacts et des forces de frottement de surface entre les grains. Lorsqu'ils sont mis en mouvement, par exemple par des vibrations, leur dynamique est dominée par des collisions inélastiques. Pour ces différentes raisons, les milieux granulaires présentent une phénoménologie extrèmement riche, qui va de propriétés similaires à celles de fluides lorsqu'ils sont très fortement vibrés à des comportements de solidification ("jamming") similaires aux transitions vitreuses lorsqu'ils sont faiblement vibrés. Des phénomènes de vieillissement et des phénomènes hystérétiques sont aussi observés lorsqu'ils sont "gelés" dans un état amorphe. L'objectif de ce travail est d'étudier les états et les transitions de milieux ganulaires vibrés, et de caractériser les analogies trouvées entre leur comportement dynamique et la transition vitreuse observée en fonction de la température dans les verres usuels. Ces analogies justifient l'intérêt porté aux milieux granulaires, car ceux-ci peuvent être considérés comme des systèmes modèles simples pour l'étude de la thermodynamique hors-équilibre, et plus généralement pour l'étude du domaine plus vaste de la "complexité".

Les milieux granulaires utilisés dans ce travail sont composés de sphères de verre polies. Comme l'état de surface joue un rôle très important dans l'interaction entre grains, certaines mesures ont été faites avec des billes présentant une surface plus rugueuse grâce à une attaque de leur surface par un acide. Pour obtenir une fluidisation, les échantillons sont vibrés verticalement par plusieurs types de vibrations afin de mettre en évidence les différentes propriétés du système.

Nous considérons en premier lieu la transition entre le fluide et la phase vitreuse en utilisant différentes techniques expérimentales. La plus importante est l'oscillateur de torsion, qui interagit avec le milieu granulaire grâce à une sonde immergée. L'oscillateur de torsion peut être utilisé dans un mode forcé, en appliquant un couple à la sonde et en mesurant sa réponse mécanique (susceptibilité complexe). En général, on observe une relaxation qui peut être interprétée comme la signature des phénomènes de dissipations irréversibles par frottement entre les grains. Cette relaxation possède une échelle de temps propre, dont l'analyse systématique permet de déduire une analogie très claire avec les verres dits "durs". En particulier, il est trouvé que (*i*) le temps de relaxation est fonction d'un paramètre unique proportionnel à la racine carrée de l'amplitude moyenne de vibration, et qui est phénoménologiquement

l'analogue d'une température effective, que (*ii*) la fonction avec laquelle les temps de re-laxation approchent l'état final "gelé" présente un comportement de type Arrhenius, ou un comportement de type Vögel-Fulcher-Tamman.

Le même oscillateur de torsion peut aussi être utilisé en mode libre. En ce cas, aucun couple extérieur n'est exercé, et la sonde tourne sous l'effet des réarrangements continus intervenant au sein du milieu granulaire vibré. Le système est alors étudié en analysant la densité spectrale de puissance contenue dans le signal de position angulaire de la sonde. Les spectres ainsi obtenus représentent le "bruit de configuration" lié aux sauts aléatoires du système d'une configuration à la suivante. Ceci permet de définir, en utilisant une approche complètement différente, la même échelle de temps propre que celle observée en mode forcé. La comparaison des résultats des deux techniques permet d'obtenir une image plus complète et plus détaillée de la dynamique du milieu dans le domaine du "jamming". Elle permet aussi de conclure que le temps de relaxation du système granulaire présente effectivement un comportement qui n'est pas de type Arrhenius en fonction du paramètre de contrôle défini comme $a_s = \sqrt{\Gamma}/\omega_s$.

Ce comportement expérimental est modélisé en combinant des observations rhéologiques avec une approche statistique décrivant les phénomènes extrêmes. Ce modèle justifie à la fois l'apparence du paramètre de contrôle et l'évolution de la relaxation de type Vögel-Fulcher-Tamman. De plus, le modèle est prédictif et permet de rendre compte d'autres propriétés rhéologiques du système granulaire. Par exemple, les effets de rugosité de surface des billes ont été considérés, ce qui a permis de montrer que les coefficients statiques et dynamiques de frottement sont bien décrits par le modèle.

Une deuxième partie importante de ce travail consiste à vérifier expérimentalement que la sonde macroscopique agit bien comme un objet brownien. Ce fait est souvent utilisé pour interpréter des données expérimentales (aussi dans ce travail), et pour proposer des modèles théoriques, alors qu'une preuve de ce fait n'a jamais été explicitement mise en évidence. Ceci n'est d'ailleurs pas facile à faire en utilisant un système contraint comme un oscillateur de torsion, car le coefficient de rappel influence la dynamique de la diffusion. Pour surmonter ce problème, nous avons construit un appareil différent, appelé "moteur brownien", dans lequel les sondes sont montées sur roulements à billes, de sorte qu'elles sont libres de tourner sans contrainte. Les propriétés des séries temporelles de position d'une sonde libre et d'une sonde contrainte peuvent alors être analysées, et comparées avec des simulations numériques simples. Les données présentent un comportement général similaire à de la diffusion, influencé par la présence des contraintes. En utilisant des techniques d'analyse fractale, nous avons estimé l'exposant de Hurst de la diffusion. Ceci nous a permis de vérifier qu'un objet "macroscopique" tel que la sonde, immergé dans un milieu "microscopique" tel que les billes, se comporte effectivement comme un objet brownien, et que sa dynamique peut être étudiée en détail et présente des phénomènes de diffusion anormale.

Le travail se termine sur une discussion de ses développements possibles. L'idée la plus prometteuse est une approche nouvelle pour étudier les propriétés géométriques du réseau de contacts d'un assemblage granulaire, qui est responsable de nombreuses propriétés du milieu granulaire. En utilisant l'Imagerie par Résonance Magnétique, la structure tridimen-

sionnelle du milieu granulaire peut être reconstruite avec une précision, une résolution et une reproductibilité inégalées. De ces informations spatiales, on peut extraire toutes les propriétés statiques du milieu granulaire: le facteur de compactage, la fonction de corrélation entre grains, le volume libre, et encore d'autres observables. Des études systématiques pourraient ainsi permettre de vérifier expérimentalement de nombreux modèles théoriques qui ont été proposés ces dernières années et qui souffrent toujours d'un manque de confirmations expérimentales. Mais cette idée ne conclue pas les perspectives de ce travail, qui sont en fait très vastes. Quelques sujets prometteurs sont passés en revue dans le chapitre des perspectives, parmi lesquels la mesure du vieillissement induit dans des échantillons non vibrés, les propriétés quantitatives des moteurs browniens, les phénomènes de "stick and slip" et leur comparaison avec les tremblements de terre, etc.

Contents

Contents

List of Figures

Reading Guide

In order to guide the reader through the five chapters of this work and to anticipate the main results, a short summary of each chapter can be found in this Reading Guide.

Chapter 1

The first chapter, the Introduction, fulfills two main purposes. The sections composing the first part are devoted to a general introduction on the physics of granular materials. They present a brief overview of the main features of granular media. Whenever possible, references to a few key texts are given, with the hope that the text maintain a balance between being informative but not excessively detailed. The importance of the physics of granular media, with respect to other fields of research, is recalled with a few examples.

Once the main topic has been introduced, the sections that compose the second part present a short but detailed review of all the already known facts, methods and techniques that will be used in the following Chapters. The main goal was to discuss all of the state of the art knowledge, while distinguishing it as clearly as possible, from the original work which is instead discussed in the subsequent chapters.

Chapter 2

The second chapter focuses on the two main experimental installations used in this thesis. The first one is a torsion pendulum, that had already been employed to perform measurements on strongly vibrated granular media. This work focuses more on the weakly vibrated states, and this required a thorough revision and improvement of the existing setup, which is discussed in the first part.

The second instrument is an implementation of a *brownian motor*. The idea is to construct a measurement system where a probe is suspended in a granular medium, while being able to rotate without constraints. The realization of a similar setup, with the sensitivity conditions required for our goals, proved to be a non trivial task, and required a significant effort in both design and testing. The installation that resulted from these efforts is described in detail.

Chapter 3

Chapter three contains the main experimental results of this work. It is conceptually divided into three parts.

The first section discusses in detail the concept of mechanical response function and its application to the study of granular media. The technique used to measure it, its limits of applicability and the key results are presented. The measurements indicate that weakly vibrated granular systems are characterized by a relaxation time, which is a function of the vibration intensity. This allows to draw an analogy to thermal system, suggesting that the relaxation times evolve in a non-Arrhenius behavior.

The second section presents a slightly different approach, that is instead based on free mode measurements and Fourier analysis. Comparison between free and forced mode experiments indicate that the system can be described by an unified control parameter, and that the characteristic time scale shows a Vögel-Fulcher-Tamman behavior.

The third section proposes a model that justifies both the observed control parameter and the dependence of the characteristic time on it. The model find its roots, on one side, in simple rheologic observations, and on the other hand, in extremal event statistics. The validity of the model is tested with experiments performed with a different granular medium. This model suggest that the analogy between the relaxation time of granular system and thermal ones is due to the extremal nature of the dynamics of the network of chain of forces.

Chapter 4

The fourth chapter focuses on the relationships between free movement of a probe in vibrated granular media and brownian motion. The free mode analysis used in this thesis and many other references in the literature either suggest or that probes immersed in granular media behave as brownian particles. However, in general, only indirect evidence is given to support this conclusion.

This chapter describes a fractal analysis of the problem that can be used to directly estimate the diffusion exponent for the probe-granular interaction. The validity of the method is assured with both numerical simulations and a comparison with the forced mode measurements of Chapter 3.

Chapter 5

The fifth and final Chapter is dedicated to the possible perspective work and can be divided into three parts.

The first, and more important, one presents a new NMR technique that can be used to fully reconstruct, with an unprecedented accuracy, the three dimensional structure of a non vibrated granular system. This result allows to extract a number of interesting physical properties, such as the two-body correlation function, the number of nearest neighbors and of mechanical contacts, or the particle free volume.

The second perspective comes back to the measurement of the mechanical response function of a non vibrated granular sample. In this case the mere presence of the probe induces aging in the sample (at least around the probe), which can be measured by the variation of the stiffness and damping capacity of the sample.

The third section departs from weakly vibrated media and focuses to the evolution of the mechanical response function, when the system is driven towards strongly vibrated conditions. The observations permit to extract interesting properties of the system around the fluidization transitions. A good agreement is observed with results obtained with different techniques and found in literature. Furthermore the data permit to position the different regimes of vibrated granular media in a coherent, intelligible phase diagram.

The fourth part sketches other interesting possibilities of research that could be easily approached, using existing installations and starting from the current knowledge of the field.

Appendixes

There are five appendixes to this work, that discuss problems or results that are relevant to the thesis but that are not its main focus.

The first appendix focuses on the concept of fractals and fractal analysis, with the goal of studying experimental position time series and compare them with simulated data.

The second one is connected with the first and reviews the key concepts associated with brownian motion: the Wiener process, normal and anomalous diffusion, and the diffusion or Hurst exponent. Once again the goal is not to give a detailed review of the field, but to give the main tools needed to understand the rest of the work.

The third appendix presents some experimental remarks about the physics of vibrated granular media. Although they do not appear to be directly related to the main topic, they show specific effects that had to be taken into account during the rest of the work.

The fourth one is devoted to a real glass transition in a thermal polymer (1-Hexadecanol) that had been studied with the same torsion pendulum used to investigate the granular samples.

Finally, the fifth and last appendix briefly reviews the definition and practical usefullness of the Voronoi space decomposition and of Steinhardt order parameters, that are extensively discussed in the analysis of Magnetic Resonance Imaging.

Chapter 1

Introduction

Granular media have fascinated philosophers, physicists and curious people since the early days of civilization. In this introductory chapter, we review the key features characterizing granular materials. Our goal is to give a brief overview on the vast phenomenology that can be observed in this puzzling, vast subject [1].

However, due to broad nature of the field, our attention will focus on the phenomena that are more relevant to our experiments. Whenever possible review articles will be highlighted to provide a deeper background to the different subjects.

This chapter starts with a general introduction to the properties which are specific to granular system. We present and consider the similarities and differences between them and amorphous solids and liquids. This leads us to a more general approach to the idea of "jamming", and to relevant concepts of the physics of glasses and of the glass transition. Finally, in order to be able to draw parallels with "fluids", we briefly review the concepts and key features of Brownian motion.

1.1 Granular materials

A true definition of granular material is a complex task on its own. This is quite surprising, given the vast abundance of granular systems, and their importance to man throughout history. In the last twenty years, however, granular materials have attracted an increasing interest from the scientific community. We will try to summarize the few key reasons in this chapter, hopefully also presenting a comprehensive bibliography.

Traditionally, physics discriminates the most prominent forms of appearance of material by classifying them into phases: plasma, gas, liquid and solid. In this picture, a phase is defined as a region of space (a thermodynamic system), throughout which all physical properties of a material are essentially uniform [2].

This is true for many common situations, and similar descriptions can be found in philosophic works dating thousands of years. However, there are systems that cannot be put strictly under one of these categories, because they show different properties that can be related to two or more "regular" states of matter.

This is the case of granular media [3]. In general, a granular material is a conglomeration of

large number of interacting macroscopic solid particles. The particles, or grains, interact solely (or mainly) via contact forces. They may also be subject to external forces: gravity, induced vibrations, and contact interaction with containing walls and external objects (for example, mechanic probes).

Granular materials are generally composed of macroscopic particles, meaning that they are large enough not to be subject to quantum mechanics or thermal effects. This means that each grain should be ideally distinguishable with the naked eye. Powders represents a limit case of granular materials, and they show slightly different behaviors: for example, they are extremely sensitive to humidity and electrostatic interaction. Colloids are yet another system that looks similar to a granular material, and that show nonetheless different behaviors.

Finally, the constituting grains retain their form, in spite of the affecting forces. The incidentally arising constraint forces between them are substantially smaller than the inner cohesion of the individual granules.

These properties make granular systems a very challenging field of research. Their study has broad application field, and we will try to review them in the following.

1.1.1 Industry

Granular materials represent, in volume, the second largest handled kind of medium, after water. It has been observed that current granular materials manipulation and storage techniques are very inefficient.

For example, we know that forces are distributed non uniformly within the material, and therefore the walls of its container silo. If the force becomes too strong in some area, this can lead to structural failure. For this reason, oversize solution are often considered, leading to a reduced efficiency and to high handling costs [4].

Efficiency improvements in handling of granular materials is a commercially important goal, in fields as diverse as polymer industry, constructions, pharmaceutics, agriculture, and energy production [5, 6].

If we consider a broader view, granular materials are also involved in many different fields in civil and chemical engineering. Materials of geological origin are encountered as foundation and fill materials in geotechnical engineering. Efficient design of such materials requires understanding of the physical processes which control the behavior and interaction of their constituent particles. Efficient design of applications requires understanding of the ways in which they flow, the ways in which groups of particles form, different sizes segregate and individual particles fracture. Engineering soil mechanics is required to make predictions of the performance of geotechnical structures under static or dynamic loading using numerical models of soil behavior. Many of the models that have been produced are empirically based. The sophistication of this modeling is not necessarily matched by confidence in the underlying physical principles [7].

The importance of research into granular materials is thus directly applicable and dates back at least to Charles-Augustin de Coulomb. His first experiments were focused on the resistance of masonries and the behavior of supporting walls, and led him to formulate his phenomenologic law of friction.

1.1.2 Science

Granular materials are also a very important field for fundamental research, and have been subject of increasing interest in the last twenty years. Granular materials form what are called "collective" systems, because the evolution is determined by the particles contact interactions. In a sandpile, for instance, each particle touches only a few others, but these "short range" interactions determine what happens to the whole pile. In this sense, a sandpile could be a model for the behavior of, for example, cells in a colony or workers in an economy.

Also, Granular materials exhibit a rich variety of dynamical behavior, much of which is poorly understood. Fractal-like stress chains, convection, a variety of wave dynamics, including waves which resemble capillary waves, 1/f noise, and fractional Brownian motion provide examples. Although granular materials consist of collections of interacting particles, there are important differences between the dynamics of a collection of grains and the dynamics of a collection of molecules. In particular, the ergodic hypothesis is generally invalid for granular materials, so that ordinary statistical physics does not apply. Fluctuations on laboratory scales in such quantities as the stress can be very large, as much as an order of magnitude greater than the mean [8].

Interesting and unexpected observation abound. For example, the dynamics of planetary rings [9]: the collective motion of the rock and ice shards, that forms and stabilizes the orbits of the rings depend on the strong damping of out-of-phase elements as they oscillate away from their dynamic equilibrium positions.

Finally, achieving better understanding on the behavior of granular system would profit enormously to the applied sciences of soil mechanics and the related fields in engineering. The interest in better understanding these fields motivated the first studies on the statics of granular materials, pioneered by Da Vinci (circa 1500), Coulomb (1785) and Reynolds (1866) [10, 11, 12].

1.1.3 Static properties

Density

The density, or *packing fraction* is one of the most important properties of granular assemblies. In such systems, it is defined as the ratio of the total volume of a set of objects packed into a region of space, to the volume of that region. In fact, density can be directly related to models of liquid or gases.

Furthermore, the packing fraction, is also intimately related to the "kissing number", that is, the number of contacts between the elements of the granular. This is also an interesting parameter, because the dry friction dynamics of granular system depend on the distribution of inter-particle contact networks.

Kissing number

The number of contacts between elements is also called Newton number, coordination number, or ligancy. Determining the number of surface contacts between spheres is a basic geometric problem that got its name from billiards: Two balls "kiss" if they touch. The kissing number problem asks how many balls can touch one given ball at the same time, if all the balls
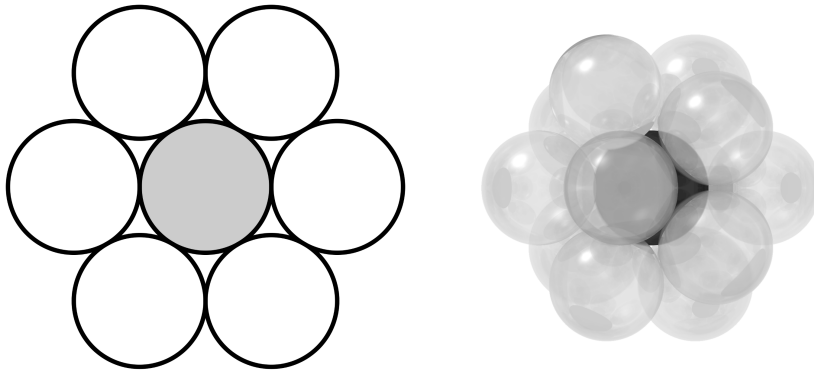
Figure 1.1: Example showing regular packing of identical spheres and corresponding coordination numbers. The image on the left represents the 2D case, where a central circle is in contact with exactly 6 neighbors. The image on the right represents the 3D case where a central sphere (solid black) is surrounded by 12 nearest neighbors.

have the same size. If you arrange the balls on a pool table, it is easy to see that the answer is exactly six: Six balls just perfectly surround a given ball.

In three dimension the situation is different, and dates back to Newton, who conjectured that the highest possible value was 12 (though there is much space left over, suggesting that one 13th sphere could be arranged in [13]). The proof that the solution is actually 12 was only given in 1953 [14]. In general, the field itself is very interesting and we refer to the work of Conway for a more general review [15], Fig. 1.1 shows the regular configuration in the 2D and 3D case.

Regular ordering of spheres

The sphere packing problem is the general problem to determine the maximal density of a packing of identical spheres in a Euclidean n-space. One class of packings to consider are lattice packings, which are invariant under any translation that takes one ball of the packing to the other.

For example, it is a simple to prove, for dimension two, that the "obvious" hexagonal packing of equal-sized disks (two-dimensional balls) in the plane (as shown in Fig. 1.1) is the optimal lattice packing (though, is not easy to prove that the hexagonal packing is indeed *the* optimal sphere packing for dimension two; for more detail we refer to the works of Hales [16]).

In the case of identical spheres in 3D space, the situation is more complex. It can be shown that there are three distinct, stable periodic packings: body-centered cubic lattice (BCC), face-centered cubic lattice (FCC), and hexagonal lattice (HC).

It was hypothesized by Kepler in 1611 that the two close packing lattices (FCC or HC, which have equivalent packing densities) are the densest possible, and this assertion is known as the *Kepler conjecture*. The problem of finding the densest packing of spheres (not necessarily periodic) is therefore known as the Kepler problem, where

$$\eta_{\text{Kepler}} = \eta_{\text{FCC}} = \eta_{\text{HC}} = \frac{\pi}{3\sqrt{2}} \approx 74.048\%$$

Packing	Analytical	Observed
loosest possible	–	0.0555
tetrahedral lattice	$(\pi\sqrt{3})/(16)$	0.3401
cubic lattice	$\pi/6$	0.5236
simple hexagonal lattice	$\pi/(3\sqrt{3})$	0.6046
body centered packing (BCC)	$\pi\sqrt{3}/8$	0.6807
cubic close packing (FCC)	$\pi/(3\sqrt{2})$	0.7405
hexagonal close packing (HC)	$\pi/(3\sqrt{2})$	0.7405
random loose	–	≈ 0.56
random close	–	≈ 0.64

Table 1.1: Packing fraction for different 3D assemblies of identical spheres. The values were obtained from different sources, as indicated in the main text. For regular lattices, these can be obtained by computing the volume fraction in the primitive unit cell. The random values are only indicative, as they were obtained by extrapolation [26, 28].

In the case of regular lattices this result was considered correct since before Kepler himself, but, curiously, it was only proved very recently [16, 17].

Other possible (regular) packing produce different densities. These are shown in Table 1.1 where we report a few examples. Note that some of these example, though possible for 3D spheres, are not dynamically stable in the case of purely contact forces. Therefore it is highly improbable to actually observe them in a granular system. They can be found, however, in atomic structures where the forces have a very different nature. More information on these structure can be found in works from different authors [18, 19, 20, 21, 22, 23, 24, 25, 26, 27].

Irregular ordering spheres

The case of irregular ordering is quite different from the regular one. As we will discuss later, it is directly related to jamming and the glass transition.

The first studies on the packing fraction of randomly ordered spherical particles were performed in the Fifties by Bernal [29]. The main idea was that random assemblies of spheres could be used to model liquids. While this approach proved unsuccessful, further development by Scott [26] started to pose the first questions on the meaning of density of nonperiodic structures.

In fact, Scott and Bernal were the first to experimentally study statistical properties of random spheres. They computed the radial distribution function and the kissing number and established two empirical density valued now known as *random loose packing* and *random close packing*, to indicate an asymptotic "ideal" case where the system is respectively in condition of minimal and maximal density, without having any kind of long range order. The found values were 60.0% and 63.7%, respectively [26, 28]. Several other measurements and numerical studies [30] have been since carried out, and the random close packing limit is usually agreed to have the value $63.5 \pm 0.5\%$ [31, 32]. The random loose packing limit, on the other hand, strongly depends on the packing method and on whether gravitational and friction forces

are taken into account: it is easier to obtain a mechanically stable loose packing when no gravitation is present, and for a "strong" value of friction. For example, by matching the density (in the limit where $g \rightarrow 0$), the random loose packing fraction is found to be $55.5 \pm 0.5\%$ [33]. It is interesting to notice that these results are still largely debated [34]. This is due to the delicate nature of the required measurement, as it will be discussed in Sec. 5.3.3.

Pressure in granular systems

In the case of granular materials only a fraction of the total weight is felt at the bottom of the container, while the rest is sustained by the lateral walls, because of friction.

The measurements of Janssen[35] showed that the pressure P at the bottom of a container depends on the filling height h according to the law

$$P(h) = pgd(1 - e^{-h/d}) \tag{1.1}$$

where p is the specific mass of the grains, and d is a characteristic length, proportional to the width of the container. This law can be obtained by a simple model involving the force balance between pressure, gravity and friction with the walls. Since Janssen, large efforts were made to understand this behavior [36, 37, 38].

It is interesting to observe that at small depths (for $h \ll d$), the usual hydrostatic law $P \propto pgh$ applies. The maximum pressure $P_{\max} = pgd$ which is reached is thus also proportional to the container lateral width and does not depend on the height to which the granular column is filled: after a certain height h, all the additional weight is supported by the walls. This fact is of great importance for the efficient design of silos.

Arching and chains of forces

The peculiar behavior of the pressure, discussed in the previous section, depends on the formation of arches in the granular system. These arches can sustain, partially or completely, the granular medium. Formation of arches is the principal reason of interruptions in granular flows [39].

From a physicist's perspective, arching can be described as a transfer of forces between a yielding fraction of the granular system, and its neighboring regions. Stresses redistribute in the bulk, so that the shearing resistance increase in the yielding block. This is accompanied by a corresponding increase of the pressure in the block, and a decrease outside [40].

The formation of arches distributes the applied stress in a very inhomogeneous, nonlocal way. The distribution of the resulting stresses in the granular system is dependent on the local arrangement (history) and in general on the compaction level. Because of the random nature of the packing, the chains of force are transmitted in the granular along paths that follow the contact networks [41] (this was also observed in simulations [42]).

Experiments have provided a qualitative description of the force chain distribution for the 2D case [43, 44], and studied the probability distribution of contact forces in that case. An example is shown in Figure 1.2.
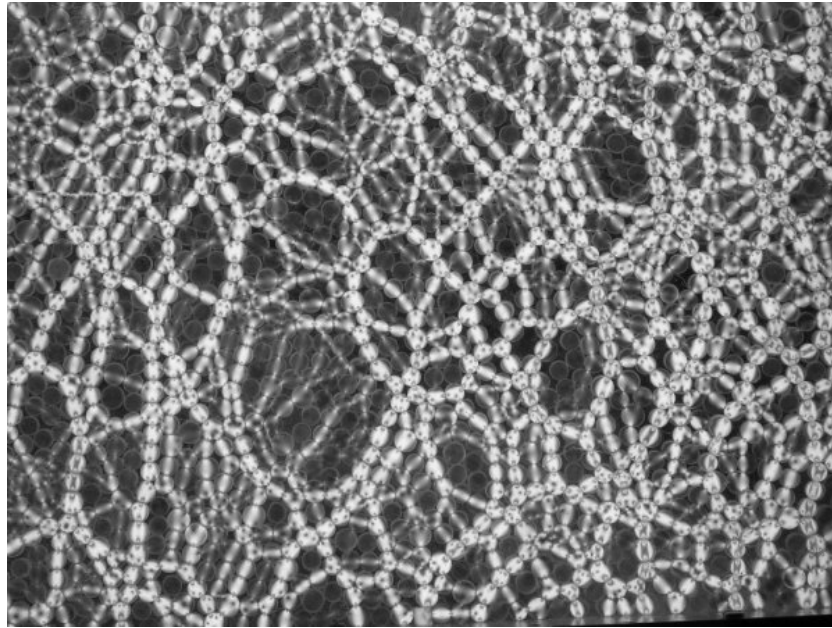
Figure 1.2: Image of a force chain network in a granular medium as viewed between two crossed circular polarizers. The particles, 3-mm Pyrex spheres, are placed in a box and a force is exerted on a piston that covers the top surface. The beads carrying most of the load can be seen as bright spots (the brightness is due to their stress-induced birefringence). The image shows a 305 by 305 mm region. (Image from [43]).

More quantitatively, it was shown (in two-dimensional [45] and three dimensional [46, 47] systems) that, for forces larger than the mean force, the probability distribution (to find a normal force of given magnitude against a container wall) decays exponentially. At small forces, on the other hand, the shape of the force distribution is found to be almost uniform [47, 48]. Finally, in some situations (namely, in "jammed" systems), the force distribution exhibits a peak, for low forces [49, 50]. The current interpretation is that the presence of the peak can be related to the *Angell fragility* of the system, and this fact is seen as a possible link between granular jamming phenomena and the glass transition [51, 52]. However, a complete picture of all the relationships between the structure of the chains of forces, the packing fraction (and other observables) is still lacking.

Radial distribution function

One possible way to highlight some of the key properties of granular system can be borrowed from chemistry.

The radial distribution function (also known as RDF, or the pair correlation function), is a measure to determine the correlation between particles within a system. Specifically, it is a measure of, on average, the probability of finding a particle at a distance of r away from a given reference particle[53].

The radial distribution function can be determined by calculating the distance between all particle pairs and grouping them into a histogram (aside from a normalization factor). This is
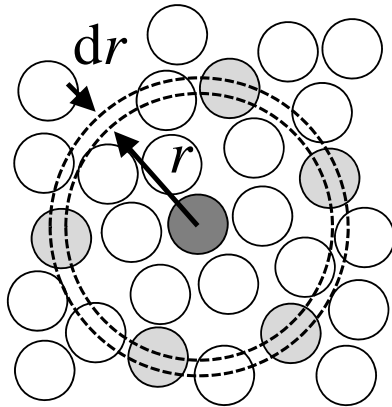
Figure 1.3: Sketch showing the algorithm to compute the radial (or two-body) correlation function. Starting from a given sphere, the space is divided into spherical shells, of fixed thickness and of growing size. The number of sphere centers falling in these shells is counted and normalized. An exact algorithm will be discussed in Ch. 5.

done by counting how many particles are found within a distance of r and $r + dr$ away from a particle. The idea is shown in Fig 1.3.

What is interesting with this observable, in the case of granular systems, is that it contains a great amount of information in a compact form [29, 26]. The values of this function in region around 1 diameter allows to estimate the kissing number, and also the polydispersity of the sample. At intermediate range, the function is extremely sensitive to the microstructure of the medium, and to the presence or absence of local regular structures versus amorphous behavior. Finally, at long distance, it allows to calculate the spatial correlation length and the average density.

1.1.4 Dynamic properties

Granular media obey a dissipative dynamics, dominated by inelastic collisions and loss of energy due to grain-grain dry friction effects. Their dynamics is, a priori, very different from "traditional" Hamiltonian evolution. This, in turns, leads to a very rich phenomenology.

Probably the most common example of granular media is given by the hourglass. In a hourglass, grains flow along an inclined surface, following the effect of gravity. The properties of the granular material employed, together with the geometry of the container were cleverly exploited in the Middle Ages to produce a reliable and accurate clock.

To this day, on the other hand, in most industrial applications and scientific studies, granular systems are typically set into motion by an applied vibration. This applied vibration introduces kinetic energy in the system, which, without the external drive is rapidly lost. Depending on the nature of the granular media, typical figures show that the average kinetic energy required to lift a grain is between 10^9 and 10^{14} times larger than the average thermal energy available to each grain at room temperature. For this reasons, granular media are referred to as *non-thermal systems*. Despite this, many observation have suggested that deep similarities could be drawn with the behavior of thermal glasses [54].

Given that granular media consist of a large number of similar object, there is a strong motivation to derive a statistical mechanics approach to a "thermodynamical" description [55]. We will briefly review these ideas later in this chapter.

In this section we will review the dynamic effects that we observed in our work. For this reason we will focus on vibrated systems.

Compaction

Granular compaction is the first evidence of a "glassy" behavior in granular systems [54]. Depending on the history of the system, each different granular sample is characterized (as we have discussed) by a specific density, or packing fraction. *Compaction* means that, under external vibration, granular system show very slow relaxation towards a "more" stable stationary state of "high" density.

In order to observe compaction due to rearrangements, it is first necessary to start from an initially looser packing. This can be obtained by carefully preparing the sample [26]. In our case, however, we do not use any kind of density matching techniques [33, 56] that are now considered the best method to correctly define "random close packing". As we will discuss in Ch. 2, our dynamic experiments are done with a two-phases medium consisting of glass spheres under a non-controlled atmosphere (air).

In order to induce rearrangements in the granular piles, an external perturbation is applied by vibrating the container. Experiments [57] and simulations [58], supported by theoretical arguments [59], reveal that the granular density ρ increases.

The dynamic of the density increase has been studied extensively (see Ref. [60]). Starting with a loose packing of the grains, the granular system was perturbed by a series of taps of varying intensities. The tapping routine initially removes the unstable loose voids, reducing quickly (and irreversibly) the density. As the measurement progresses, the density of the resulting configuration is dependent on the tapping amplitude and the number of taps. The mechanism of the compaction process leading to a steady-state density is extremely slow; in fact, it is logarithmic in the number of taps. This part of the dynamics is represented by the irreversible branch of the curve of Fig. 1.4

Once the memory effects of the pile construction details have been removed, the dependence of the density of grains on the external perturbation of the system is known as the reversible branch of the "compaction curve" [61]. In this region, the larger is the amplitude of vibration, the lower is the density. Collisions push the grains farther away from each other, allowing to reach less packed configurations. This is shown in the reversible branches of the curves in Fig 1.4.

There have been several further experiments confirming these results for different system geometries, particle elasticities and compaction techniques. For example, the system can be mechanically tapped or oscillated, vibrated using a loudspeaker, slowly sheared in a couette geometry, or even allowed to relax under large pressures over long periods of time, all to the same effect [61, 63, 64, 65, 62].

It is worth noting that the empiric informations that one can obtain from the experiments are not conclusive. The experiments performed with a very thin and tall tube may involve
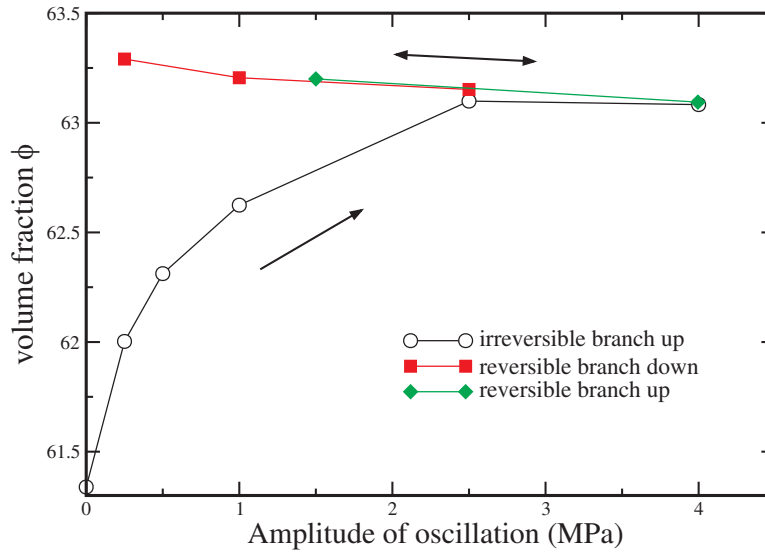
Figure 1.4: Compaction curve for a packing of glass beads under an oscillating pressure. Increasing the amplitude of oscillation initially increases the density by filling the loose voids, after which a reversible regime is achieved (image from [62]).

significant boundary effects, but prevent convection to occur. On the other hand, the more recent experiments using wider containers [66, 66] encounter the opposite situation: the boundary effects are less important, but convection is observed. Comparison between the experiments, show that a steady state can indeed be obtained. However, in the case of tall and narrow cylinders the final density is higher for weaker vibrations, while for large cylinders the final density reached is lower for stronger vibrations.

The packing fraction (in the static sense) and the compaction (in the dynamic sense) appear to be strongly dependent on the geometry of the system and of the particles. Interestingly, vibrating an assembly of elongated grains (cylinders) reveals that the system tends to reach a very ordered state, where the rods are aligned vertically, and the volume fraction exhibits a steep rise as the ordering process takes place [67]. Recent reviews of these issues may be found in [54, 55].

Convection

For conventional materials, *convection* is a large scale movement of molecules within liquids and gases, and is one of the major modes of heat and mass transfer. It cannot take place in solids, since neither bulk current flows nor significant diffusion can take place in solids.

Convection is also pertinent to granular materials: dry granular material confined to a cylindrical vessel convects when subjected to either continuous or discrete vertical oscillations. The geometry has a great influence on the presence and the amplitude of the convection phenomena, one example of which is shown in Fig. 1.5.

If the container is narrow (with respect to the grain size), no or very little convection is observed. On the other hand, granular media in larger containers show this kind of instability.
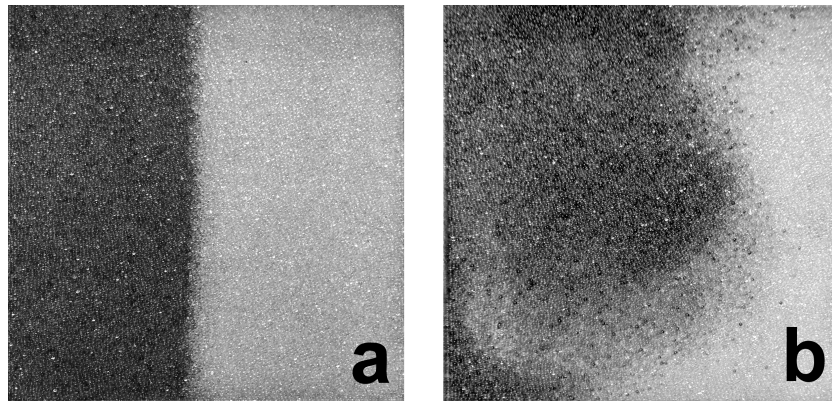
Figure 1.5: Convection in granular materials. In this case we show one example of horizontal convection on a 25 mm thick layer of 1 mm diameter, smooth glass beads, placed into a square container. The beads on the left were colored with Methylene Blue ink, those on the right were rinsed and dried clean. Image **a** shows the system as prepared. The beads were vibrated with a vertical acceleration of $0.8g$ at 113 Hz for approximately 80 minutes. The curls on the surface seen in image **b** clearly show the effects of convection.

In a cylindrical container, the granular components typically rise in the center in a wide swath and sink back along the container walls in narrow bands. This can also lead to a slightly deformed granular surface, lens shaped, with the center part slightly higher than the sides in contact with the contained cylinder.

Experiments carried out in right cylindrical containers whose walls are covered with a layer of beads reveal that the upward flow velocity along the container axis is highest at the surface, and decreases exponentially with the depth [68]. In containers whose walls are tilted outward, the opposite phenomenon may take place, with the particles moving down along the axis and up along the walls. Convection rolls rising from the center appear to happen for vertical walls, and up to a certain tilt angle, beyond which the "reverse" convection takes place [69]. The normal rolls seem to be favored in general when the container walls are rougher, revealing the importance of friction.

Pattern formation

The surface of vibrated granular systems is a particularly interesting region. The upper layers of the granular medium are not constrained by the weight of other layer, as happens in the bulk, and may exhibit all kinds of complex patterns.

This phenomenon, observed in numerous experimental studies, reveals that the patterns formed can have various shapes, like squares, stripes or hexagons depending on the shaking amplitude, the frequency, and the filling height. Remarkable effects are found in the literature [70, 71, 72, 73, 74]. We observed a few of them, with the help of a high speed camera, as shown in Fig. 1.6.

The pattern formation mechanisms are described in several models that can reproduce, at least qualitatively, some experimental observations [75, 76, 77, 78].
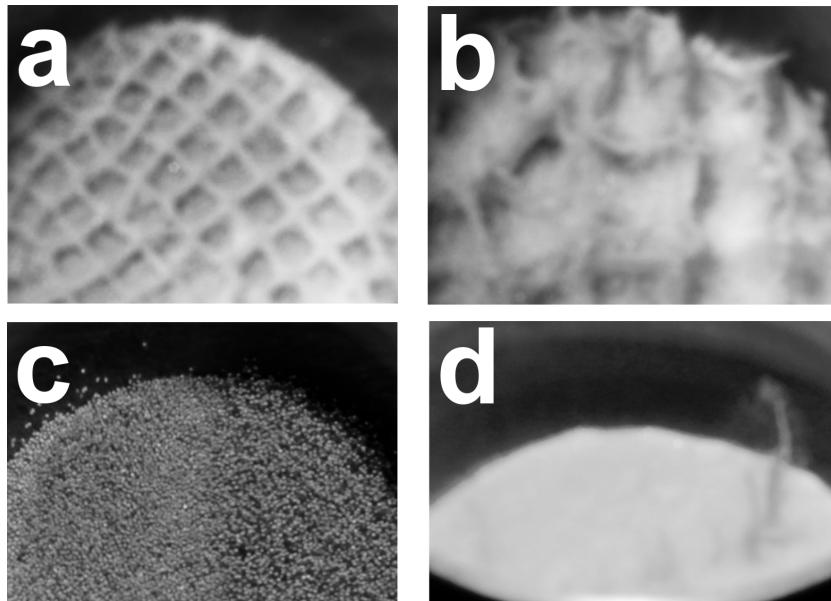
Figure 1.6: Pattern formation in vibrated granular media. Part **a** shows square structures oscillating at the first subharmonic ($f/2$) of the vertical vibration. However, if the frequency is varied enough the patterns become chaotic, as shown in Part **b**. Part **c** shows the formation of waves in the surface of larger and heavier bronze beads. Finally, the image in Part **d** captures an *oscillon* that form in slightly thicker layers. All the images were taken with a high speed camera (Casio EXILIM Pro EX-F1).

Angle of repose and avalanches

When granular media are piled up, they tend to roll and end up forming, as a first approximation, a mound of conical shape. The grains can be piled up until some instability threshold is reached. At that moment a collective motion (avalanche) occurs [79, 80, 81].

In the static case, the conical structure is characterized by the angle between the sandpile sides and the horizontal: the angle of repose θ_r. When the sandpile is formed by continuous addition of grains at a certain point, observations show that the value of the angle is not unique.

The addition of sand may simply create steeper slopes, therefore increasing the angle, up to a certain value θ_m (maximal angle of stability), where a critical point is reached and an avalanche is triggered. Once the avalanche has stopped, the angle has dropped to a value lower than the limit. For all intermediate angles, the pile may be either at rest or flowing, depending on the history [82, 83, 84].

The angle of repose θ_r depends strongly on the nature of the granular medium, and of other possible factors influencing the cohesion: humidity, electrostatics, etc. Typically, it ranges from about 22° for dry spherical grains to over 60° for very irregular grains.

When the slope of a sand pile exceeds the critical threshold corresponding to the maximal angle of stability θ_m, an avalanche is produced. Between θ_m and θ_r, a localized perturbation can provoke an avalanche, which may even propagate uphill (involve grains situated above
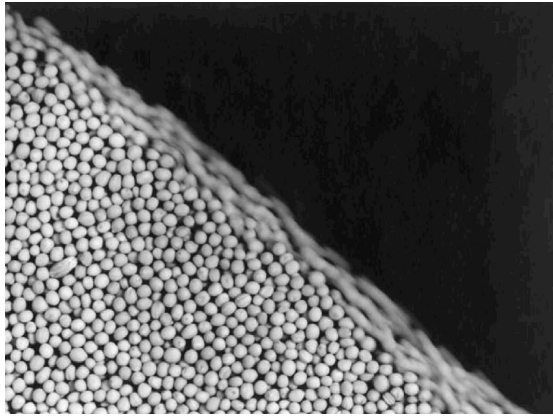
Figure 1.7: Photograph showing an avalanche in a pile of mustard seeds. Only the top layers are moving: they appear blurred. The grains a few layers below the surface do not move at all, or only very little. Image from [85].

the perturbation location) if the initial angle is close enough to θ_m [83].

Interestingly, when sand is continuously added at a constant rate to a sand pile, avalanches occur at approximately always the same time interval [85, 86]. This might be related to the constant flow rates observed in gravity induced flows, such as in hourglasses.

It is also worth noting that the flow of an avalanche usually consists of the motion of a thin surface layer, while the bulk of the material remains almost static (see Fig. 1.7).

Some theoretical models are based on this observation, and aim at describing superficial flows [87, 88] or are refined in order to deal with thicker avalanches [89]. These general theoretical studies, using both continuum approaches (similar to hydrodynamics) and discrete approaches (in order to account for grains interactions) [90, 91], have helped the development of tools to simulate real avalanches and landslides [92, 5]. As a final remark it is worth noting that the shape of the flowing grains have been observed to influence drastically the avalanche type, with irregular grains and polydisperse media being usually involved in faster and bigger flows than spherical, monodisperse grains [93, 94].

1.2 Fundamentals of jamming and glass transition

In this section we will review the concept of *jamming* in granular materials and the basic properties of the glass transition in usual materials. We begin presenting an overview of the key features of equilibrium and non-equilibrium systems, from a thermodynamical perspective. This review does not cover extensively the subject, and we refer to a few key texts for a much more detailed discussion [53, 95, 96, 97] Afterwards we introduce the concept of jamming and we review jamming as the arrest of the dynamics in glassy systems. Finally, we draw the key parallels between glass and granular materials.

1.2.1 Equilibrium and non-equilibrium

From an industrial point of view, thermodynamics is probably one of the most important scientific frameworks ever invented by man. During the 17th century, chemistry was becoming a field accessible to scientific studies. Scientists become interested in the dynamics of chemical processes, and the exchange of energy and heat. Growing knowledge of chemistry led to even more important technological breakthroughs: in the early 18th century, steam operated machines started address industrial problems that previously required large human and animal efforts. The first steam machine were used to pump water away from mines, producing cloths, empowering the first railroads and ships.

Thermodynamics developed to understand and improve the efficiency of those machines, while scientists and engineers had countless systems to study. The foundations of the field are set by von Guericke and Boyle (1650-60) [98]. while the formulation of modern thermodynamics is historically attributed to Carnot (1824) [99], During the course of more than three centuries, thermodynamics grew to a detailed, rigorous theory that describes the mechanisms of heat and mass exchange, to extremely good levels of predictability.

However, we now know that thermodynamics has its limit. The thermodynamic transformations must be quasistatic, so that in principle one can only exactly describe those transformations that happen infinitely slowly. While this framework is sufficient for many applications, some systems cannot be well described with this approach. For example, one could consider a thermal system placed between two thermal baths at different temperatures [100]; in fluid dynamics one could consider the Couette flow, where a fluid is enclosed between two walls moving in opposite directions [101]; in atomic physics, lasers work because a large part part of the atom population is kept to an higher "temperature" than the rest of the crystal (population inversion).

Today, using contemporary terminology we distinguish between equilibrium and out-of-equilibrium systems. We can illustrate the two definitions in the following way. Take a system of interest, and isolate it from all contact with the remainder of the universe. Once this is done we can begin study the model system by making observations. These must be delicate enough not to themselves significantly perturb the system. We perform these non-perturbing measurement at long intervals, and we wait until we cannot measure any changes on the observed quantities. Some quantities that we might measure might fluctuate in time: then we would demand that they do not evolve in a statistical sense. Eventually the system reaches what we will call *thermodynamic equilibrium.*

We now consider how long did it take to reach equilibrium. Typically we might expect transient effects to die out quite rapidly. For example, a prepared, non-Maxwellian, distribution of velocities in a gas may return close to the equilibrium Maxwellian distribution in a time comparable to the collision time between molecules (around 10^{-9} s, at room temperature and pressure). On the other hand we might encounter much longer relaxation times. For example if we take a large box of gas but now prepare it in a state where one half of the box is at higher density than the other half, there will be an oscillatory motion of the gas that we call sound, that decays on much longer time scales, perhaps seconds or longer. Usually we will not have any doubt when we have waited long enough, although there are some counter examples
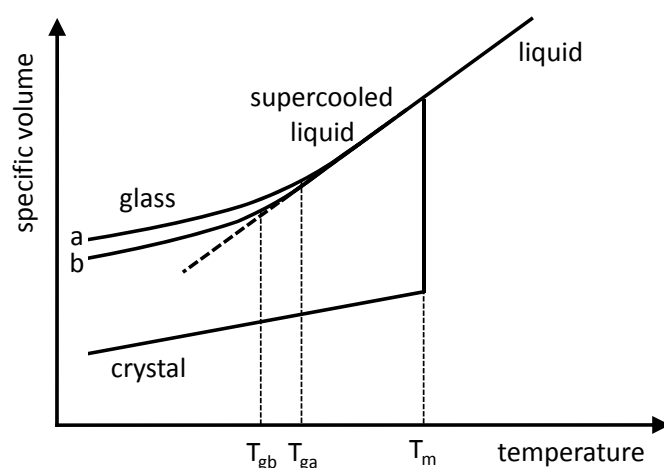
Figure 1.8: Subcooling and the glass transition. The graph shows a sketch of the behavior of the specific volume of a hypothetic substance as a function of the temperature. For temperatures higher than T_m, the system is simply in a liquid phase. If the temperature is reduced, the liquid (right-hand side) may crystallize at T_m, or it may undergo supercooling. If in this state the temperature is reduced enough, it may form a glass. The glass transition temperature may be identified as the one where the slope start to deviate from the equilibrium (liquid and supercooled) region. The exact value of T_g is not necessarily unique, and can depend on the cooling rate. In this graph, glass (b) was obtained with a faster cooling rate than glass (a): glass (a) had more time to rearrange before the temperature was further reduced and could therefore remain at equilibrium for slightly lower temperatures, resulting in a denser arrangement.

to this, where the characterization as equilibrium or nonequilibrium may not be clear. An example is familiar window glass, and other similar very slowly relaxing systems that are now called "glassy". In the following we will focus on these systems and their features.

1.2.2 Subcooling and the glass transition

When the temperature of a liquid is reduced below its standard freezing temperature T_m, it may crystallize: in this case we say it has undergone a first-order phase transition. Normally, this is associated to an abrupt reduction of the specific volume. The formation of a solid, regular structure is mainly a growth phenomenon, that is strongly favored by the presence of starting nucleation points. Depending on the conditions, impurities in the liquid, the walls of the container, and spontaneous crystal nucleation can provide such nuclei.

However, if nucleation can be avoided, the liquid state can be maintained, while the temperature is lowered below T_m. In this case the system is said to be a "supercooled" liquid [102, 103, 104]. This supercooled state is unstable, and crystallization may be defavored in the case of rapid cooling rates or for particularly pure liquids. In these conditions, the specific volume does not exhibit rapid changes, and continues to evolve regularly as it did at temperatures above T_m. This is shown in Fig. 1.8. Other thermodynamic properties also do not seem to reveal any striking feature at this temperature.
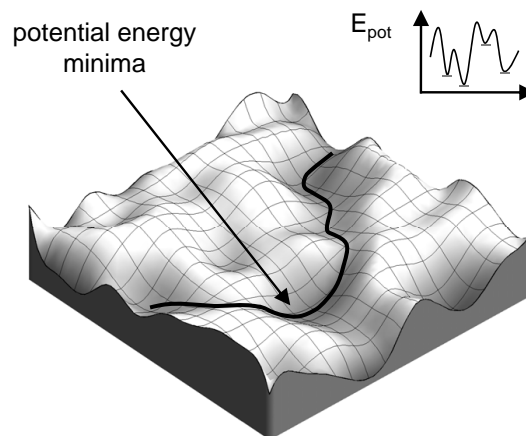
Figure 1.9: Graphical 2-D representation of a multidimensional energy landscape of a glassy system. As the temperature is decreased, Brownian dynamics slow down. Below that, the system can no longer equilibrate (loses its ergodicity) and becomes sensitive to a strongly irregular energy landscape. The shape of the landscape dominates the dynamics in the glassy region, as the system explores the "inherent structures" defined as the potential energy minima [107, 108]. A trajectory through the landscape is shown and the analogy between these inherent structures.

As the temperature is further reduced, the viscosity of the fluid increases, and the dynamics become slower and slower. This increase can be as much as 17 orders of magnitude [105, 106]. The relaxation times associated with the structural rearrangements in the system increase drastically. Eventually, the system evolves so slowly that no significant changes can be observed in the time scale of any reasonable observation, therefore manifesting solid-like mechanical properties. At the lowest scale lengths, the molecules may not have time to rearrange before the temperature is further lowered, and the system falls out of equilibrium. A glass is obtained

In this perspective, therefore, transition from a liquid to a glass is in contrast to the freezing or crystallization transition, which is a first-order phase transition in the Ehrenfest classification and involves discontinuities in thermodynamic and dynamic properties such as volume, energy, and viscosity. The onset of the glass transition is established, by convention, at the temperature T_g for which the relaxation time exceeds about 100 seconds, or the viscosity exceeds the value of 10^{13} poise (by comparison, the viscosity of water at room temperature is only 0.01 poise). The glass transition temperature T_g, as defined in terms of the corresponding relaxation time, also depends on the cooling rate: for slow cooling, the system may have more time to rearrange and may therefore remain at equilibrium for slightly lower temperatures. However, this dependence is rather weak: a difference of an order of magnitude in cooling rate results in a change of only about 3 to 5 Kelvin in T_g. For example, cooling rates applied in experiments can be of a few kelvins per minute (considered rather slow) up to around 100 K/min for faster cooling.

1.2.3 Glass phenomenology

As they approach their glass transition temperature, supercooled liquids can undergo viscosity (or corresponding relaxation time τ) variation of 15-17 orders of magnitude while the temperature decreases by a factor two [103].

Arrhenius behavior

An useful way to represent this variation is to plot $\log(\eta)$ as a function of the inverse temperature l/T (Arrhenius plot). If the evolution were a straight line in such a graph, it would reveal a so-called Arrhenius behavior:

$$\eta(T) = \eta_0 \exp(B/T) \tag{1.2}$$

where η_0 and B are constants that may depend on the material, for example. However, as shown in Fig. 1.10, many supercooled liquids do not exhibit this behavior as they approach their glass transition. While some may follow quite well the Arrhenius law 1.2, like GeO_2 or SiO_2, most curves clearly follow a very different trend. Following Angell's now widely used classification, glass-forming liquids are therefore commonly divided between "strong" systems (those that follow the simple Arrhenius law) or "fragile" ones (those that rather exhibit a "non-Arrhenius", or "super-Arrhenius", behavior) [109, 110, 104, 111]. Experimentally, the viscosity and the relaxation time can be related as follows. The (shear) viscosity measures the response to shear stress, and is related to the corresponding relaxation time τ of the system by $\eta = G_\infty \tau$, where G_∞ is the shear modulus at high frequency. With typical values of $G_\infty = 1 - 10$ GPa, it means that a viscosity at the glass transition of approximately 10^{12} Pa s corresponds to typical "long" relaxation times ($100 - 1000$ s).

Vögel-Fulcher-Tamman and other non-Arrhenius behavior

For a large number of those glass-formers that do not follow an Arrhenius behavior, the evolution of the viscosity can be well described by the empirical Vögel-Fulcher-Tammann (VFT) law

$$\eta(T) = \eta_0 \exp\left(D\frac{T_0}{T - T_0}\right) \tag{1.3}$$

where η_0, D and T_0 are constants [112, 113, 114, 115]. In the limit $T_0 \to 0$, provided that DT_0 does not vanish, the simple Arrhenius behavior of Eq. 1.2 can be recovered. This formula is interesting because it introduces a divergence at $T_0 \neq 0$, describing the phenomenology of the glass transition. Experimentally, the VFT temperature T_0 is found by fitting data as in Fig. 1.10 to Eq. 1.3. More details on the VFT law can be found in [115, 116, 117].

It should be noted that the VFT law is not the only one that was proposed to fit and interpret the experimental data. Furthermore, it can prove hard to distinguish which one provides the best fit. This is due to the fact that the relaxation times grow exponentially large as we approach the glass transition. For this reason, it takes longer and longer times to obtain data.
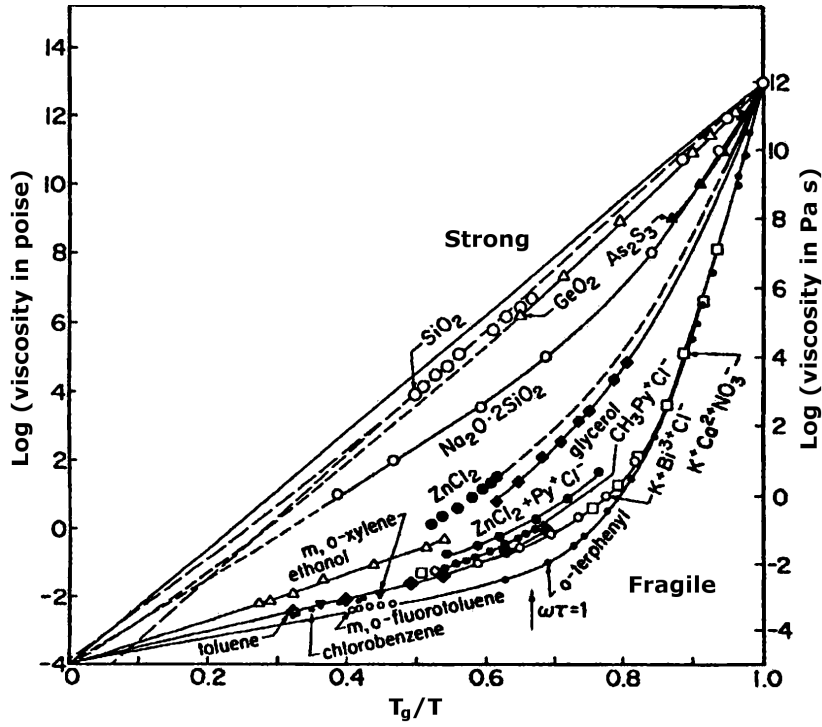
Figure 1.10: Evolution of the viscosity for different glass formers as a function of the temperature. The horizontal axis shows the reduced temperature T_g/T, where T_g indicates the glass transition temperature of each liquid. With this scaling, the temperatures are colder in the right hand side of the graph and the glass transition occurs on the right margin of the graph for all liquids. This representation, called "Angell plot", classifies glass formers into "strong" and "fragile" varieties. Image from [109].

For example, let us consider the VFT law for the relaxation times, Eq. 1.4.

$$\tau = \tau_0 \exp\left(D\frac{T_0}{T - T_0}\right) \tag{1.4}$$

Given a reasonable high temperature relaxation time $\tau_0 = 10^{-13}$ s, a fragility parameter $D \approx 10$ (an intermediate value) and experimental times of the order of 10 days, the coldest temperature that can be tested is approximately $T_{\text{low}} \approx 1.2 T_0$, which is still far away from the divergence (this is discussed in detail in [118]).

Depending on the range of the data available and the proposed explanation mechanisms, different empirical relations have been proposed [109]. One of these, which will prove useful in the context of granular media, is a generalization of the VFT in the form:

$$\eta(T) = A \exp\left[D\left(\frac{T_0{}^p}{T^p - T_0{}^p}\right)\right] \tag{1.5}$$

where p is an empirical exponent to be determined experimentally.

1.2.4 Glass transition and the concept of *jamming*

The exponential increase of the viscosity of supercooled liquids as the temperature is reduced, as discussed above, has been indicated as an example of a more general phenomenon, called "jamming". In general, a glass transition occurs when the liquid state is cooled, resulting in an increase in viscosity, even if no crystalline structure are formed. In a similar way, the jamming transition happens when density is increased: the resulting crowding prevents the particles from exploring the phase space, making the aggregate material behave as a solid. In fact, during the last two decades, a number of physical systems have been observed to exhibit similar behaviors.

Spin glasses

Spin glass systems are magnetic alloys in which magnetic impurities are replaced in a magnetically inert host. The impurities occupy practically static random positions: during experimental time scales they do not change position. The interactions between the impurities depend on the distance between them, and since the latter are random, the interactions themselves take random values that can vary very quickly.

In these systems it is fairly straightforward to measure the relaxation times and the response function to external fields as a function of other parameters, such as temperature or an external imposed stress. As in other systems, spin glasses clearly fall out of equilibrium at a transition temperature T_g, which again depends on the cooling rate and procedures used. Prototypical systems of quenched disorder, spin glasses have attracted the attention of experimentalists and theoreticians, and we refer to other works [119, 120, 118] for a more detailed overview.

Granular materials

Granular systems are known to exhibit jamming: if properly excited by vibrations (as we will discuss throughly in this work) or shearing [121] they can flow with fluid-like properties, only to abruptly stop if these conditions are changed. Avalanches are an examples of unjamming due to shearing; the clogging and unclogging of salt in a salt shaker is another jamming effect experienced daily.

Jamming: a common framework

There are many other systems that show strong analogies with glasses. In many physical systems, it is possible to observe a divergence of a relaxation time as a function of a experimental parameter. For example, we can cite systems showing domain growth, colloidal dispersions (eg. laponite), so called "vortex glasses" in type II superconductors [122], motion of dislocations in solids [123, 124], or aging effects.

In all these situations, there are certainly big differences in the microscopic models that influence the relaxation times and response function, be it the dislocation-point defect interactions when the applied force is too weak to allow depinning, or the way a colloidal suspension becomes highly viscous due to increasing volume fraction, or again when the temperature in a spin glass system drops to a level at which the nearest-neighbor interaction term starts to
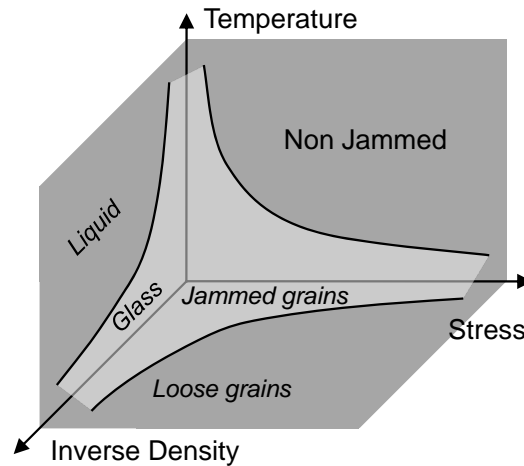
Figure 1.11: Sketch of the generalized Jamming phenomenon. As discussed in the text, a large number of physical systems present a recognizable slowdown pattern (jamming) with respect to an external parameter. Depending on the exact situation, the latter can be an externally applied stress, the variation of density or the evolution of the temperature. This led to a speculative diagram, suggesting an unified picture of all these phenomena, and proposed by Liu and Nagel in [51]. The region closer to the axes and the origin contains the jammed states, and the boundary defines the onset of the *jamming transition.*

substantially influence the Hamiltonian operator. However, the same key observables show striking similarities (the VFT law usually used for the glass transition is also applicable in many other of these examples). Since so many different things tend to get jammed in ways that may after all not be so different, one can wonder whether there exists some common conceptual framework that might address all the observed phenomena. Liu and Nagel [51, 125] have proposed a phase diagram that summarizes the various jamming possibilities with an ideal "phase diagram" that we show in Fig. 1.11.

The key idea is that this diagram (which is not a real phase diagram in thermodynamical sense, since it also represents out of equilibrium situations) links the behavior of glasses (thermal systems) and bubbles, grains, droplets (athermal systems) by the dynamics of their approach to jamming [126, 3].

It should be noted that, for any given system, not all axes of the jamming diagram need to be equally relevant. For example, the case of granular media can be considered when the particles are so large that they do not really feel the thermal fluctuations. In this case, the (thermodynamic) temperature axis plays no role. However, there are other non-equilibrium ways to insert energy such systems, as we will show in the following chapter, using vibrations to drive the particles. The resulting behavior can sometimes be described in terms of effective temperatures, or via "control parameters".

Under this conceptual framework, the goal of this work is twofold. We observed the jamming route in granular media, and we propose a description with an effective temperature. However, more in general, we can even hope that the observation we make in granular system could lead to a better understanding of jamming in general [127].

The case of granular system is especially interesting, because the jamming transition is, at least in principle, well-defined (understanding a conceptually simple system can help understanding a more complicated system that displays similar behavior). In fact, the grains do not interact when they do not touch, so that the number of contacts in the system is, in principle, well-defined. When they touch, the interaction is repulsive. Therefore, the jamming transition at zero temperature and zero applied stress becomes sharply defined [55]. Consider a collection of frictionless spheres in a box. If the density is below a critical value ρ_c, the particles fit in the box without touching each other, so that they do not interact, and the system is not jammed. Above ρ_c, the grains cannot avoid touching, and start repelling one another. A pressure builds up and the system is jammed. Exactly at ρ_c, the spheres just start to touch, but are not pressed into each other yet. For large systems, ρ_c converges to a well-defined value that does not depend on the initial conditions of the packing procedure, making the jamming transition on the density axis sharply defined. For a more detailed overview of the relationships between the glass transition in thermal system and the jamming transition in granular system we refer to the detailed review of Makse et al. [55] and the recent paper by Berthier et al. [128].

1.3 Fundamentals of brownian motion

The nature of the granular media suggest that, during flowing or as an effect of imposed vibrations, the particles can start mixing in a chaotic way. However, as soon as one tries to perform careful observations, a number of seemingly unrelated phenomena can be observed. It seems therefore reasonable to apply already-known approaches, and the random-like movements of the grains suggest to look to Brownian motion, and to try and propose parallels. For this reason, we will review in a general perspective the main characteristics of Brownian motion, from the early models to the more recent mathematical generalization. This short review will focus on those concepts, problem and physical observables which are relevant for granular materials.

1.3.1 History and key concepts

Brownian motion was, and still is, one of the most important and discussed phenomena of physics. Starting from ancient times, to the observations of R. Brown, to Einstein's work and up to the more recent studies on fractal geometry, Brownian motion represent a link between Newtonian dynamics, thermodynamics, statistical mechanics, geometry and probability theory.

For these reasons, Brownian motion has been studied in detail, and books and reviews on the subject abound. We refer to a few of this works for a much more detailed overview [129, 130, 131, 132, 129, 133, 134, 135].

Before Brown

The first observation of Brownian motion actually date back to ancient times. The Roman philosopher Lucretius's scientific poem "de Rerum Natura" ("On the Nature of Things"), written

around 60 BC has a remarkable description of Brownian motion of dust particles. With limited technical possibilities, the philosopher uses this as a proof of the existence of atoms:

Contemplator enim, cum solis lumina cumque
inserti fundunt radii per opaca domorum:
multa minuta modis multis per inane videbis
corpora misceri radiorum lumine in ipso
5   et vel ut aeterno certamine proelia pugnas
edere turmatim certantia nec dare pausam,
conciliis et discidiis exercita crebris;
conicere ut possis ex hoc, primordia rerum
quale sit in magno iactari semper inani.
10   Dum taxat, rerum magnarum parva potest res
exemplare dare et vestigia notitiai.
Hoc etiam magis haec animum te advertere par est
corpora quae in solis radiis turbare videntur,
quod tales turbae motus quoque materiai
15   significant clandestinos caecosque subesse.
Multa videbis enim plagis ibi percita caecis
commutare viam retroque repulsa reverti
nunc huc nunc illuc in cunctas undique partis.
Scilicet hic a principiis est omnibus error.
20   Prima moventur enim per se primordia rerum,
inde ea quae parvo sunt corpora conciliatu
et quasi proxima sunt ad viris principiorum,
ictibus illorum caecis inpulsa cientur,
ipsaque pro porro paulo maiora lacessunt.
25   Sic a principiis ascendit motus et exit
paulatim nostros ad sensus, ut moveantur
illa quoque, in solis quae lumine cernere quimus
nec quibus id faciant plagis apparet aperte.

The English translation reads: "Observe what happens when sunbeams are admitted into a building and shed light on its shadowy places. You will see a multitude of tiny particles mingling in a multitude of ways. Their dancing is an actual indication of underlying movements of matter that are hidden from our sight. It originates with the atoms which move of themselves. Then those small compound bodies that are least removed from the impetus of the atoms are set in motion by the impact of their invisible blows and in turn thrust themselves against slightly larger bodies. So the movement mounts up from the atoms and gradually emerges to the level of our senses, so that those bodies are in motion that we see in sunbeams, moved by blows that remain invisible."

This atomistic view of the world however, was only based on logical speculation. It did not develop further, and was abandoned until the 18th century. In fact, seemingly chaotic movement of small particles comes back to the attention of researchers when in 1785, the
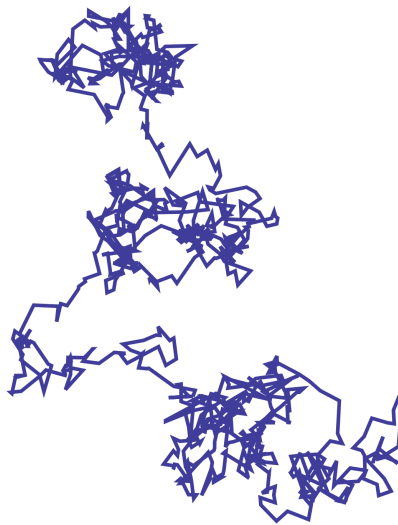
Figure 1.12: A simulated example of 1000 steps of an approximation to a Brownian motion. This graph shows a Lévy flight in two dimensions [140]. From the origin of the motion, the angular direction is uniformly distributed and the step size is distributed according to a Normal distribution. This is a special case of a Lévy distribution with $\alpha = 2$ and $\beta = 0$.

Dutch scientist Jan Ingenhousz describes the irregular movement of coal dust on the surface of alcohol [136]. However, he did not pursue research on the field.

From Brown to the 20th century

The first to realize that the random motion of suspended particles was actually an important physical phenomenon was Robert Brown. In his first paper (dated the 30th of July 1828, and republished several times elsewhere [137, 138, 139]), Brown reported on the random movement of different particles that are small enough to be in suspension in water. It is an extremely erratic motion, apparently without end. A (simulated) example is shown in Fig. 1.12. Though at first Brown wrote about "active molecules", opening to the possibility that motion was due to life, Brown's biggest scientific merit was in gradually emancipating himself from the misconception evidencing that the movements were due to the particles being living beings. He also made a systematic study of the ubiquity of "active molecules", and checked the presence of this movement with grains of pollen, dust and soot, pulverized rock, and even a fragment of stone from the Great Sphinx. His efforts eventually eliminated the "vital force" hypothesis.

Furthermore, even if Brown could not explain the origin of this motion, he was able to rule out easy explanations, like convection currents or evaporation. After a period of relative interest from the scientific community, the work of Brown lost attractiveness, and between 1831 and 1857 no other references to Brown's observations can be found. It was only starting from the 1860's that his work began to draw large interest, also in intellectual circles [141].

It became clear that Brownian motion increases when the size of the suspended particles

decreases (one essentially ceases to observe it when the radius is above several microns), when the viscosity of the fluid decreases, or when the temperature increases. In the 1860's, the idea emerged that the cause of the Brownian motion has to be found in the internal motion of the fluid, namely that the zigzag motion of suspended particles is due to collisions with the molecules of the fluid.

However, many scientist remained unconvinced of this interpretation, mainly because at the end of the 19th century the controversy was raging between those who accepted the "atomic" theory, and those who believed in a continuous description of nature.

Between the people who did believe in the atomic explanation of the phenomena, those worth citing are C. Wiener and L.-G. Gouy. The first reaffirmed in 1863 that the cause must be found in the liquid itself, implicating a theory of motion of molecules. The second confirmed in 1888 that the hypothesis of molecular agitation gave an admissible explanation of the Brownian movement, but that no other cause of the movement could be imagined, which especially increased the significance of the atomic hypothesis [142].

At the turn of the century, a few key features were indisputable [134, 143, 144]. Tiny particles suspended in a fluid undergo a random motion with the following properties: (*i*) the motion is extremely irregular, and the trajectory seems not to have a tangent. (*ii*) two Brownian particles, even close, have independent motion from one another. (*iii*) the smaller the particles, the wider their motion. (*iv*) the nature and the density of the particles have no influence. (*v*) the motion is most active in less viscous liquids. (*vi*) the motion is most active at higher temperatures. (*vii*) the motion never stops.

1.3.2 Theories of Brownian motion

Between 1905 and 1908 a theory explaining Brownian motion was independently developed by Einstein [145, 146, 147, 148, 149], Langevin [150], and Smoluchowski [151].

Einstein

Einstein, in 1905, obtained the expression of the diffusion constant of a suspended particle in a fluid [145]. In a slightly more modern form, we consider a particle in a fluid, undergoing a viscous friction force $-\eta v$, proportional to v (where η is the viscous friction coefficient). For simplicity we follow the first of Einstein's arguments. If we restrict to a 1D case of a spherical particle of radius r we obtain:

$$D \propto \frac{k_B T}{6\pi \eta r} \tag{1.6}$$

where D represent the coefficient of diffusion[1]. In the following works Einstein completes these results by means of mathematical and probabilistic considerations. After rederiving Fick's law [152] he obtains the evolution of the probability density, as we show here. Let

---

[1]The derivation follows the limit case of a particle of radius r moving at a terminal velocity v limited by the viscous friction η. Using the Langevin formalism we will show that that Eq. 1.6 can be generalized to include the transient inertial effects; in this case the particle mass m appears at the denominator [134, 95].

$P(x, y, z; t)$ be the probability density of finding a Brownian particle at a point (x, y, z) at the time t. This density satisfies the diffusion equation:

$$\frac{\partial P}{\partial t} = D \Delta P \tag{1.7}$$

Omitting the calculations, if the Brownian particle is located at the origin $(0, 0, 0)$ at the instant $t = 0$ then the solution of equation (1.7) is Gaussian and written as:

$$P(x, y, z; t) = \frac{1}{(4\pi D t)^{3/2}} \exp\left(-\frac{x^2 + y^2 + z^2}{4Dt}\right) \tag{1.8}$$

One can find the density $P(x, t)$ by integrating over the variables y and z. From these results one can evaluate the integral of the average quadratic displacement along, say, the x axis. One obtains:

$$\begin{aligned}
\langle x^2 \rangle_t &= \int_{-\infty}^{+\infty} x^2 P(x; t) \, \mathrm{d}x \\
&= \frac{1}{(4\pi D t)^{1/2}} \int_{-\infty}^{+\infty} x^2 \exp\left(-\frac{x^2}{4Dt}\right) \mathrm{d}x \\
&= 2Dt
\end{aligned} \tag{1.9}$$

It is interesting to note that the solution in Eq. 1.9 is identical to the one that can be computed for the the average quadratic variation produced by the thermal agitation [134]. This fact reflects the scale invariance of Brownian motion, a concept that could not yet be appreciated in 1905 (An extensive discussion of scale invariance can be found in [153]).

Smoluchowski

In 1906, Smoluchowski obtained similar results with an approach based on probability theory. He thought (like Gibbs and Boltzmann) that probability theory, which was at looked down by many scientists, could be useful for physics. Without knowing it, Smoluchowski opened a new sub- field of statistical physics, that nowadays bears the name of Stochastic Processes. One of his important results that we would like to highlight is the generalized diffusion equation for particles interacting with a force field $F(x)$ [151]:

$$\frac{\partial}{\partial t} P = D \Delta P - \frac{1}{\eta m} \frac{\partial}{\partial x} (F(x) P) \tag{1.10}$$

A particular situation that will be of interest in the following is the case of a harmonically bound particle, with $F(x) = -Kx$. The solution $P(x, t)$ of Eq. 1.10 for this force permits to calculate all statistical properties [154, 155] which, under certain conditions, are the same as those obtained in the more general approach obtained by Langevin [150].

Perrin and experimental confirmation

The final experimental validation of the molecular theory of Brownian motion of Einstein, Smoluchowski and Langevin is mostly due to Perrin's careful measurements. After his first contribution in 1908, Perrin, a faithful atomist, produces a series of papers (reviewed in [156]) presenting experimental data that attempt to obtain the weigh of atoms, estimate the size of molecules, and provide a determination of the Avogadro number, based on the Einstein relation Eq. 1.6.

Langevin

The third approach we discuss here is the one due to Langevin, and first published in 1908. His work is scientifically very important because it contains the first mathematical example of a stochastic equation, from which we can directly extract some relevant informations.
Langevin's argument [150] can be summarized as follows [134]. The starting point is the Maxwell equipartition theorem of kinetic energy. It states that the energy of a particle in suspension inside a fluid in thermal equilibrium has an average kinetic energy equal to that of any gas molecule, in a given direction, at the same temperature.
A particle which is large compared to the molecules of a fluid, moving at speed v with respect to it, experiences a viscous resistance force equal to $-6\pi\eta r v$, according to Stokes' formula. In reality this is only an average effect, and because of the irregular shocks of the surrounding molecules, the action of the fluid on the particle fluctuates around the average value. Then, the equation of motion along (for example) the direction x, given by Newtonian dynamics, is

$$m\frac{\mathrm{d}v}{\mathrm{d}t} = m\frac{\mathrm{d}^2 x}{\mathrm{d}t^2} = -6\pi\eta r v + X \tag{1.11}$$

The key idea here is to introduce the complementary random force X. Since it is random, we know little about it. We only require that it is likely to be positive or negative with the same probability, and that its magnitude is such that it maintains the particle's agitation: without this force the particle would stop because of the viscous resistance. In other words, we suppose that the influence of the external fluid on the particle can be described by two distinct contributions ("Langevin hypothesis"):

- a slowly varying contribution, consisting of a viscous friction force proportional to the velocity of the Brownian particle v.

- a rapidly varying contribution, consisting of random fluctuating forces, about which we only need to make simple assumptions.

It can be shown that if one supposes that the particle was observed at the origin $x = 0$ at time $t = 0$, Langevin's method indeed reproduces Einstein's result (see Doob in [133]). In his paper Langevin introduced, without knowing it, the first element (the random force X) of what was to become stochastic calculus.

The properties of the random force X influence the behavior of the solutions. The simplest choice, as done by Langevin, consists in choosing a white, non correlated noise[2].

A more modern formulation proceeds from the time-correlation functions of the stochastic force X in canonical form. Since the noise X describes the collisions in a homogeneous and isotropic medium, it should be zero on average:

$$\langle X(t) \rangle = 0 \tag{1.12}$$

In this definition the average $\langle \ldots \rangle$ indicates the ensemble average of all the possible realizations of a collection of signals. A more detailed overview on the mathematical tools used to analyze non-deterministic signal can be found in the literature (see for example [158, 159]).

The second observation is to assume that the random forces $X(t_1)$ and $X(t_2)$ acting at different times $t_1 \neq t_2$ are uncorrelated:

$$\langle X(t)X(t') \rangle = q\delta_{t,t'} \tag{1.13}$$

where q is a coefficient representing the amplitude of the correlations, and $\delta(t - t')$ is the Dirac distribution.

This choice is physically meaningful as long as the number of collision is large enough that the characteristic correlation times between two collision are much smaller than the time considered between two experimental measurements.

The equations 1.12 and 1.13 represent therefore the simplest requirements needed to correctly describe Brownian motion in the Langevin formalism. A signal X satisfying Eq. 1.12 and 1.13 is called a "white noise". The name stems from its frequency-domain representation, which is flat: it contains the same amount of energy at all the frequencies, and therefore it is "white".

Power spectral density

The Langevin equation is specially interesting, because in this framework different physical observables can be computed. A first useful quantity is the power spectral density, which represents the density of energy available at each frequency. The power spectral density is related to the Fourier transform of the signal:

$$S(\omega) = \lim_{T \to \infty} \frac{2}{T} \langle \left| \hat{x}_T(\omega)^2 \right| \rangle \tag{1.14}$$

Assuming that the system is ergodic, and using the Wiener-Khintchine theorem [160], the power spectral density can be calculated. Finally, if we integrate it we obtain

$$\int_0^\infty S(\omega) \, \mathrm{d}\omega = \langle x^2 \rangle \tag{1.15}$$

This expression is interesting because it allows to evaluate the spectral power density by measuring the position of the Brownian particle.

---

[2] The derivations presented in this section can also be obtained with different noise choices (using so called "colored" noise), though the results are slightly more complicated [157].

Response function

A very different situation can be studied if one consider the temporal evolution of the system submitted to a (macroscopic) external force, and neglecting the effects of the noise. In this case, Eq. 1.11 allows to compute the response function, or *susceptibility*, of the system, for different external stimuli.

Due to the form of Eq. 1.11 the overall behavior is that of an harmonic oscillator [161, 162]. The response can be in the underdamped, critical and overdamped regime as a function of the viscosity η and the forcing pulsation ω.

If we consider a sinusoidal external force $f_{ext} = f \sin(\omega t)$, in Fourier representation the susceptibility χ becomes:

$$\chi(\omega) = \frac{1}{m(\omega_0^2 - \omega^2 + i\eta\omega)} \tag{1.16}$$

where ω_0 is the harmonic oscillator eigenfrequency. Often the susceptibily χ is split in its real and imaginary part, $\chi = \chi' - i\chi''$. It can be noted that $\chi'(\omega)$ is an even function and $\chi''(\omega)$ is an odd function of ω. This is a general property of the complex response function, and comes from the fact that χ is the Fourier transform of a Real function [160]. This will prove useful in the next paragraph.

The imaginary part χ'' of the complex susceptibility χ is related to the energy dissipated in the system when the external force f_{ext} is applied. This is completely equivalent to what happens in electrodynamics, and the algebra is essentially the same (see, for example [163]).

This can be shown in a very simple way if we consider the effect of a single external impulse $f_{ext}(t) = A\delta$. The total energy dissipated can be written as:

$$
\begin{aligned}
E_{diss} &= \int_{-\infty}^{+\infty} f_{ext}(t)\langle \dot{x}(t)\rangle \, \mathrm{d}t \\
&= A\langle \dot{x}(0)\rangle \\
&= A^2 \langle \dot{\chi}(0)\rangle \\
&= \frac{A^2}{2\pi} \int_{-\infty}^{+\infty} i\omega\chi(\omega) \, \mathrm{d}\omega \\
&= \frac{A^2}{2\pi} \int_{-\infty}^{+\infty} \omega\chi''(\omega) \, \mathrm{d}\omega
\end{aligned}
$$

In this case the equivalence between step 2 and 3 can be proved by considering that the position x must be given by the integral over time of the response function multiplied by the susceptibility ($\dot{x}$ can also be obtained by taking the time derivative):

$$\langle x(t)\rangle = \int \chi(t - t') f_{ext}(t') \, \mathrm{d}t' = A\chi(t) \tag{1.17}$$

Einstein relation

The equations 1.6 and 1.8 are also know as "Einstein relation", because they relate the diffusion coefficient of a particle in a fluid to the temperature and the friction coefficient. Neglecting

the effect of the restoring force, the Langevin equation becomes:

$$m\ddot{x}(t) + m\eta\dot{x}(t) = X \tag{1.18}$$

the Einstein relation can then be derived in the following way. Let us assume that the same properties discussed above hold for the random force term X, namely that:

$$\langle X(t) \rangle = 0 \quad \text{and} \quad \langle X(t)X(t') \rangle = q\delta_{t,t'} \tag{1.19}$$

Using the equipartition of energy principle we relate the spring energy K to the temperature T of the thermal bath in which the Brownian particle lies:

$$\frac{1}{2}K\langle X(t)^2 \rangle = \frac{1}{2}k_B T \tag{1.20}$$

Finally, the amplitude q of the random force X can be related to the restoring coefficient K by evaluating the limit $t \to \infty$ of the two-times correlation function $\langle x(t)x(t') \rangle$, and obtain $q = 2m\eta k_B T$. Eventually one can calculate:

$$\langle X(t)^2 \rangle \overset{t\to\infty}{\propto} 2Dt \quad \text{with} \quad D = \frac{k_B T}{m\eta} \tag{1.21}$$

Rotational Brownian motion

We conclude this section with a brief review of the slightly different geometric configuration. The motion studied by Brown consists mostly of the irregular displacements of pollen grams, considered as points. Gerlach and Lehrer, in 1926, observed a rotational Brownian motion. They registered by means of reflected light the irregular deviations of a small mirror suspended on a very fine wire [164], an experiment that was later studied theoretically by Uhlenback and Goudsmit [165].

It is important that the adoption of a rotational geometry does not substantially change the properties of Brownian motion. In fact, the experimental installation discussed in this work is built in the same rotational configuration. In this work the surrounding gas (equilibrium medium) used by Gerlach and Lehrer is replaced by a vibrated granular system (nonequilibrium system).

1.3.3 Brownian motion and diffusion

The term *diffusion* describes the spread of particles from an initial, concentrated region, to regions of lower concentration, through random motion. The time dependence of the statistical distribution in space is given by the diffusion equation:

$$\frac{\partial \phi(\mathbf{r}, t)}{\partial t} = \nabla \cdot \left[D(\phi, \mathbf{r}) \nabla \phi(\mathbf{r}, t) \right] \tag{1.22}$$

which is also the same equation governing the flux of heat[3]. In this case, the diffusion is modeled as a continuous phenomenon.

As discussed before, the mechanism of diffusion can also be modeled, and explained as an average effect of a large number of small impacts. With the proper choice of the random noise X one can recover the same results obtained by solving the diffusion equation.

In reality, this kind of diffusion is difficult to observe because of the interactions between particles. In general, gases represent the ideal case, while in liquids and solids often these equations do not correctly compute the diffusion (even in the absence of other relevant mass transfer mechanisms, such as convection).

As shown in Eq. 1.21, in a typical diffusion process the mean squared displacement is a linear function of time. The relation between the mean square displacement and time can be generalized to an arbitrary power law [166], $\sigma_x^2 \propto Dt^\alpha$. In this case, whenever $\alpha \neq 1$, the diffusion process is non regular, and the effect is called *anomalous* diffusion. A similar behavior is typically observed in disordered media [167] or in complex systems [166].

The mathematical tools used to describe these phenomena stem from the pioneering works of Norbert Wiener. About 15 years after the works of Smoluchowski, Wiener [168] proposed a rigorous mathematical model that defined a stochastic process exhibiting a behavior similar to what was observed in Brownian motion. In modern terms, the Wiener process is a continuous-time stochastic process, and is also a special case of what are now known as L'evy processes. The Wiener process has applications throughout the sciences. Apart from Brownian motion and the problem of diffusion, it was the starting point for the development of the Fokker-Planck equations. It also forms the basis for the rigorous path integral formulation of quantum mechanics (by the Feynman-Kac formula [169]), and the study of inflation in cosmology [170]. It is also prominent in the mathematical theory of finance [171] (more details can be found in [172]).

This historical overview of brownian motion and its ramifications in both theory and experiments is concluded here. The goal of this review was to present the subject in order to conceptually support the analysis that will be described in the following Chapters number 3 and 4. In this perspective, the discussion would proceed to the relationships between brownian motion, the Wiener process and the fractal nature of brownian trails. However, since these arguments will require a more technical discussion, they are presented separately in Appendix A and B.

---

[3]In fact the equation of diffusion was introduced by analogy with the equation governing heat. These were well known since the 18th century and were much more easily to compare with experiments.

Chapter 2

Experimental Setup

In the previous chapter, the varied phenomenology of effects that can be observed in granular systems has been reviewed. The goal of this chapter is to present, in a systematic way, all the experimental setups we designed, built and employed to study vibrated granular media as they are driven through the jamming transition.

The chapter consists of three principal sections. The first one is devoted to the characterization of the granular media used in the experiments; all the relevant physical properties will be reviewed here. The second section contains the main experimental setup consisting of a torsion oscillator, immersed in a bath of vibrated beads. The third part shows a slightly different system, called "brownian motor", in which the immersed probe is no more torsionally constrained. In this case, on the contrary, a rotating probe immersed in the granular system is left free to move, suspended by ball bearings.

2.1 The granular system

2.1.1 Borosilicate glass beads

The experiments were performed with one model granular medium composed of millimeter size glass beads, and a sample is shown in Fig. 2.1. Borosilicate glass beads represent an ideal model for granular materials, because of their high durability and mechanical resistance, especially to surface wear[1]. Beads are commonly used as fillers for distillation towers and other chemical processes. Most of the experiment presented in this work were performed using 1 mm diameter beads from the glass manufacturer *Assistent - Glaswarenfabrik Karl Hecht GmbH*. The main specifications are as follows.

- **Diameter.** The average diameter of the spheres lies between 1 and 1.2 mm, averaging around $D = 1.1$ mm, with an approximate 80% of the beads falling in that size window.

- **Dispersion.** The corresponding error was evaluated by measuring the diameter of 100 beads along different direction, and taking the average, giving an estimate of $\sigma_D \approx 8\%$.

---

[1] The roughness of the contact surface in granular media is one of the most influent parameter in granular dynamics. It is therefore very important to consider any variation of the surface state during the experiments. Highly durable materials greatly reduce the need for repeated checks and substitutions.
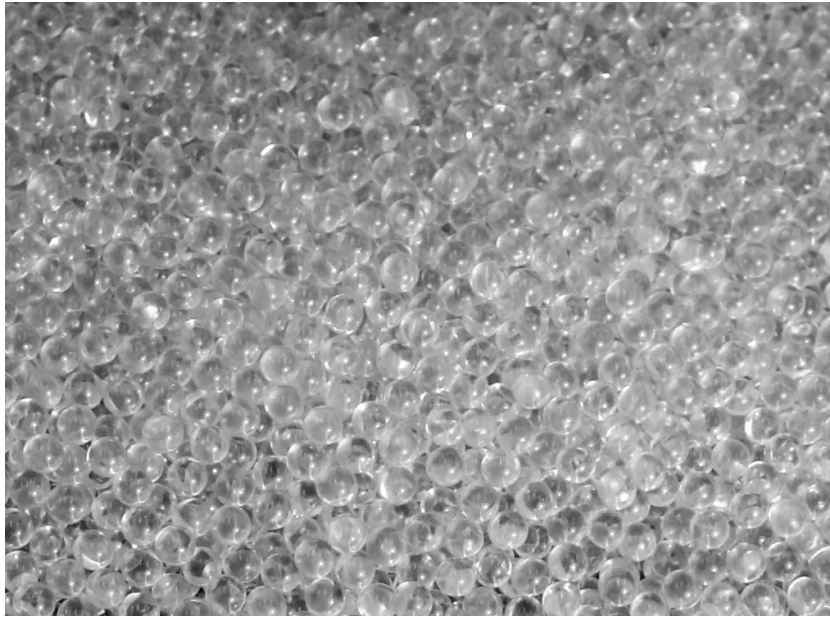
Figure 2.1: Closeup view of a sample of borosilicate glass beads used in the experiments.

However, the distribution of the diameters does not appear to be Gaussian, and is much flatter instead.

- **Density.** The density of borosilicate glass can vary substantially, as it is a function of the exact chemical composition. The glass used in these beads has a density $\rho \approx 2700 \pm 200 \mathrm{kg/m^3}$.

- **Mass.** The mass of the beads was measured considering 100 beads simultaneously, and using a precision balance, obtaining an average value of $m = 1.8 \pm 0.1$ mg. These figures are in good agreement with the measurement of the diameter, via the density.

- **Bulk modulus.** The tabulate value is approximately 13 GPa.

- **Speed of Sound.** In borosilicate glasses, the speed of sound is approximately 5200 m/s.

Besides the 1 mm diameter spheres, larger diameters (2 and 3 mm), glass and plastics beads were employed to perform NMR measurements (discussed in Ch. 5). In this case, the geometrical properties of the spheres (precise spherical shape, little size dispersion in the sample, compatibility with NMR requirements) are more important. Both borosilicate glass spheres (*Sigma-Aldritch*), and plastics (Polyoxymethylene) spheres (*R.P.G. International*) were considered. Since these specific media are specific to the NMR measurement, their properties will be discussed more in detail in Ch. 5.

2.1.2 The granular sample

The glass spheres that form the granular medium are contained in metallic buckets, unless otherwise noted. The standard containers have an internal diameter of 95 mm and are either

60 or 94 mm tall.

The choice of a metallic structure helps to keep under control unwanted electrostatic effects and perturbations due to dielectric nature of the beads (electric repulsion due to friction induced electrostatic polarization). However, one transparent plastic container (made of PMMA, diameter 95 mm, height 55 mm) was also successfully employed. This allowed a more detailed observation of the movements of the grains in contact with the container walls. This specific container is shown in Fig. 2.2.

Moisture-induced aging effects [173, 174], and interstitial gas effects [175], are not observed due to the relatively large bead size. For this reason, all the experiments were performed in a non controlled atmosphere (air).

A volume of 1 liter is occupied by about 1.6 kg of glass beads, if one considers an average compaction of 60%. Therefore, to fill the container described above to a level $D = 10$ mm, about 0.11 kg of granular matter are needed. This corresponds to approximately 60,000 beads. In general, the container is almost completely filled to insure that there is a large number of grain layers between the bottom of the container and the immersed probe. Considering a value $D = 50$ mm, the granular medium is composed of approximately $300,000$ beads.

It should be noted that these figures are only indicative, and that these values also depend on the compaction state of the system. Variation in height can attain levels of approximately 5 to 7%. This level of precision is enough for the case of vibrated system, concerning the following Ch. 3 and 4. A much more detailed study will be performed in the case of static granular system, as it will be discussed in Ch. 5.

2.1.3 The vibrations

The container is fastened to the moving element of a vibration motor, which in turn, is held in place by a trunnion[2] placed on a stable support. The vibration motor can impose vibrations in a large frequency range (from DC to many kHz), with amplitudes of several millimeters.

In the experiments, the vibration motor is driven either with a given fixed-frequency vibration intensity, at frequency $f_s = \omega_s/2\pi$, or with an broadband signal. In the latter case, the spectral representation of the signal is a filtered white noise cut off below 70 Hz and above approximately 1 kHz. In both cases, a vibration intensity parameter Γ is defined and measured with an accelerometer placed on the base plate of the vibrating element. The accelerometer can be seen in the foreground of Fig. 2.2.

Sinusoidal vibrations

If one considers a sinusoidal vibration of frequency ω_s and amplitude a_s, and feeds it to the vibration motor, the vertical position z of the vibrating element varies as Eq. 2.1:

$$z(t) = a_s \sin(\omega_s t) \tag{2.1}$$

---

[2]A trunnion is a heavy, U-shaped anchor element; it is the orange basis with yellow feet seen in Fig. 2.5

Figure 2.2: Granular sample composed of 1 mm glass beads, in the transparent plastics (PMMA) container. In this case the system is composed of approximately 0.5 kg of glass spheres. The bottom vibrating plate is also visible, with an accelerometer fastened to it.

and the corresponding acceleration of the container is given by the second derivative with respect to the time:

$$\ddot{z}(t) = -a_s \omega_s^2 \sin(\omega_s t) \tag{2.2}$$

The acceleration reaches its maximum value $\ddot{z}_{\text{max}}$ at the extremal position of the cycle. The vibration intensity parameter Γ is defined as the ratio of the peak acceleration to the acceleration of gravity g, as shown in Eq. 2.3:

$$\Gamma = \frac{\ddot{z}_{\text{max}}}{g} = \frac{a_s \omega_s^2}{g} \tag{2.3}$$

From this definition, the value $\Gamma = 1$ corresponds to the conditions where the peak acceleration becomes equal to gravity. This point is called the fluidization limit. This threshold separates the lower vibration regimes, where the elements of the granular medium are always in contact, from the high vibration regime, where at least some of the grains (typically the upper part) can

fly above the others and undergo free fall for a short time at each cycle.

In both regions, the dynamic of the granular medium shows strong dependence on the chosen frequency. If the frequency is chose to correspond to one of the eigenfrequencies of the container, some parts of the surface are visibly well agitated, while others not at all. Depending on the strength of the vibration, the specific eigenmode, and the height of the granular bed, several types of zones may be more strongly or weakly vibrated, and formation of patterns may be observed (as discussed in Section 1.1.4 and shown in Fig. 1.6). The phenomena of convection is also often observed (see Section 1.1.4 and Fig. 1.5), and it may be accentuated or inhibited accordingly to the characteristics of the imposed signal.

White noise vibrations

Spurious phenomena often appear in granular systems due to unwanted resonances that are excited by sinusoidal vibrations (either directly or from harmonics). In order to reduce the problem, it is often a good idea to employ broadband signals. In this case, energy is inserted in the system at different frequencies, reducing the chance that one resonance can fully dominate the dynamics of the system.

The simplest choice for a signal that inputs energy homogeneously on a wide range of frequency is given by choosing a filtered[3] white noise. In this case, the lower limit for the signal should be set high enough to prevent the appearance of effects on the time scales of the experiments. Furthermore, it is also a good idea to avoid those frequencies that could excite the lowest eigenmodes of the physical installation.

On the other hand, the high frequency boundary should be set high enough to allow for an excitation in a frequency window as broad as possible, but avoiding the resonant frequency of the vibration motor oscillating element. The resonance frequency of the vibration motor is rated to approximately 12 kHz (factory value). However, the increase in mass due to the metallic container and the granular medium, has the effect to decrease this value. In the typical experimental condition used to obtain the data presented in this work, this resonance is moved down to approximately 1 kHz; a variation of a few tens of Hertz is possible, depending on the exact weight of the granular medium considered.

In case of broadband excitations, the vibration intensity parameter Γ can be defined in the following way. As in the case of sinusoidal vibrations, the vertical accelerations $\ddot{z}(t)$ of the system are measured with the accelerometer. Using Parseval's theorem of Fourier analysis [160, 176] the power spectral density (PSD) of the acceleration can be computed:

$$A(f) = \lim_{\tau \to \infty} \frac{2}{\tau} \left| \frac{1}{g} \int_{-\tau/2}^{\tau/2} \ddot{z}(t) \exp(-2\pi i f t) \, \mathrm{d}t \right|^2 \tag{2.4}$$

---

[3]The white noise is "filtered" because it is not possible to inject the same amount of energy, in unit time, at all frequencies: this would mean injecting an infinite power. This "filtering", therefore, refers to a restricted frequency window.

The parameter Γ can then be defined as:

$$\Gamma = \sqrt{\int_{-\infty}^{\infty} A(f)\, \mathrm{d}f} \tag{2.5}$$

Fig. 2.3 shows an example of the power spectral density of a filtered white noise imposed on the vibration motor. The data on the left graph represent one measurement taken at the output of the current amplifier that drives the motor[4].

This definition is coherent with the one given in the previous paragraph, for sinusoidal vibrations. In this case, one can consider a sinusoidal vibration of amplitude a_s and frequency $f_s = \omega_s/2\pi$. We can treat it as a narrowband signal, by perform its Fourier transform as it was done in Eq. 2.4 it can be quickly proven that one obtains (as one would expect) a PSD of the form:

$$S(f) = \frac{a_s^2 \omega_s^4}{g^2} \left(\frac{1}{2}\delta_{f,f_s} + \frac{1}{2}\delta_{f,-f_s}\right) \tag{2.6}$$

Finally, after integration (as in Eq. 2.5) one obtains $\Gamma = a_s \omega_s^2/g$. This demonstrates that the two approaches define the same parameter. An example measurement performed by vibrating a granular sample is shown in Fig. 2.3. The graph on the left shows the spectrum of the filtered white noise signal that is used to drive the vibration motor. The graph on the right shows the resulting vertical acceleration measured with an accelerometer. As it can be seen the response of the system is non linear. This is mainly due to the effect of the granular material, and partly to the vibration motor.

As a final remark, it should be noted that the different frequencies composing the broadband noise have different effects on the granular sample. In general, lower frequencies contribute more to the overall granular mixing and jumping, while higher frequencies contribute more to a viscous-like flowing aging of the system. For this reason, while the average vibration intensity parameter Γ is chosen as a control parameter, possibly important information is discarded when using broadband spectrum signals (white noise vibrations). This fact will be relevant for the experiments of Ch. 3, and a more detailed review will be given in Appendix C. In short, the different spectral components of the noise interact in different ways with the probe, depending on its geometry.

2.2   Torsion oscillator

The main experimental apparatus used in this work consists of a vertical torsion oscillator. The rotation around its axis is used to study the rearrangements of the granular medium. Part of the work of this thesis consisted in the improvement of the existing installation. A similar apparatus had been used to study granular materials in the fluidized, high Γ, regimes. As the

---

[4]In this case the data represent the power spectral density in radical units, or in other words it represents the square root of (the complex modulus of) the power spectral density. This representation is common in signal processing; the corresponding Fourier–Perceval's representation can be computed simply by squaring.
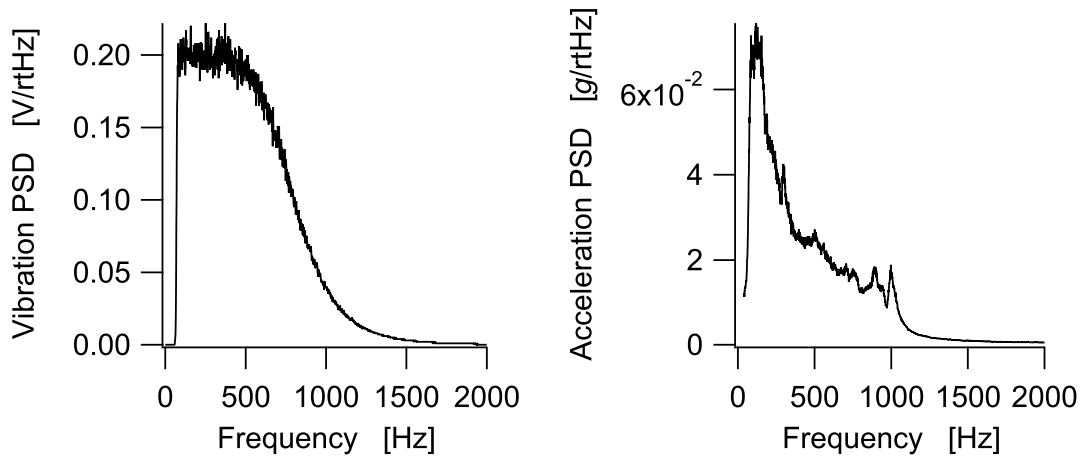
Figure 2.3: Filtered white noise vibrations. **Left**: Power spectral density $S(f)$ (in this case expressed in radical units) of the vibration signal fed to the vibration motor. This signal has a spectral representation of a filtered white noise. The cutoffs are set at 70 Hz (96 dBm) and 800 Hz (12 dBm). **Right**: resulting acceleration power spectral density measured by the accelerometer placed on the base plate. In this case the vibration intensity parameter Γ, equal to the square root of the integral of the power spectral density, is approximately 1.

jamming transition is reached, an higher sensitivity is required, and therefore effort was put into an improved design.

The main improvements made to the system pertain to the suspension system, the angular position detection and the electronic. The torsion oscillator suspension was tested, and different materials were considered for the spring element, depending on the damping capacity and the spring stiffness. The angular position detection was redesigned, resulting in a longer optical arm (10×) and a new photo cell, larger and more sensitive. Finally, the electronic chain of measurement was carefully tested, and checked for possible source of noise. Where needed, the system was adapted to enhance sensitivity to the smaller movement expected in the jamming region. The general properties of the system will be now reviewed.

The geometry of the torsion oscillator is sketched in Fig. 2.4; Fig. 2.5 shows a view of the important details. The torsion oscillator is composed of a thin metallic rod. A laser diode (**a**) is focused on a mirror (**b**) coaxial to the rod, and the laser beam is reflected to an analog photocell (**c**) that is used as a position sensor.

The torsion rod is held into position by the means of a pair of suspension wires. The wires are fastened by means of two pairs of clamps, two mounted on a fixed frame (**d**) (that houses the whole structure) and two on the rod (**e**). The suspension wires are made of spring steel and provide a restoring coefficient with a relatively low damping factor.

On the lower end of the rod, differently shaped probes (e.g., a two-finger-shaped probe **f**, or a cylindrically shaped probe **g**) can be mounted, and immersed by a given length (**L**) in a granular bath (**h**) of a given depth (**D**).

The fixed frame to which the oscillator is secured is suspended on a anti-vibration support and is mechanically decoupled from the vibration motor assembly (parts **h** and **i**) and from
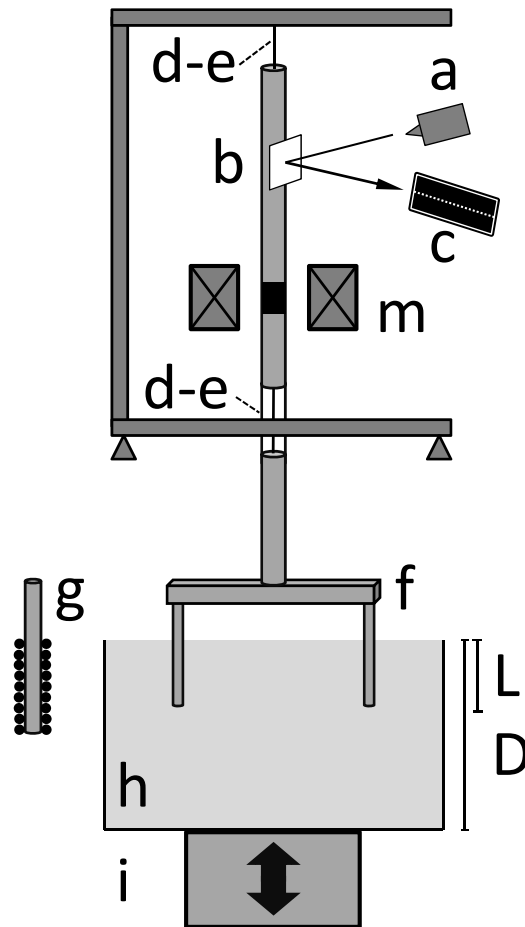
Figure 2.4: Sketch of the forced torsion oscillator. The two-finger-shaped probe f is immersed at a depth L into a granular bath of height D. The granular media is composed of glass spheres, as discussed in the text. A second probe is sketched aside g. It consists of a cylinder of radius 2 mm, the surface of which is covered with a single layer of glued glass beads. The container, filled with the granular material, is vertically shaken by a vibration motor. An accelerometer (not shown) measures the intensity of vibration, Γ. The scheme of the oscillator includes: a = laser diode; b = mirror; c = photocell; d = fixed suspension clamp; e = rod suspension clamp; m = electromagnetic coils and permanent magnet; f = finger probe; g = cylindrical probe; h = granular medium; i = vibrator motor.

the ground. Of the whole setup, only the rod can move, and its only allowed degree of freedom is the rotation around its axis. (the probe cannot move in the vertical direction).

The system can move either in a free mode, either in a forced mode. In the latter case, a pair of electromagnetic coils can be electrically driven to impart a torque on the axis, via a permanent magnet that is fixed coaxially on the rod (**m**).

Figure 2.5: Complete view of the torsion oscillator experimental setup. The labels correspond to the ones used in the sketch of Fig. 2.4. This image does not show the electronic chain of measurement that is located in a rack besides the oscillator.

2.2.1 Resonant frequency and moment of inertia

Due to the complex geometry of the rod, of the suspension parts, and of the different probes used, it would be very difficult to directly compute its moment of inertia from its geometry and mass distribution.

It is possible, however, to measure it indirectly, by the means of additional inertial masses. If the oscillator is left free to move, its intrinsic mechanical loss, due to the damping of the suspension wires, is very low (around 5×10^3). The oscillator eigenfrequency is given by Eq. 2.7:

$$f_0 = \frac{1}{2\pi}\sqrt{\frac{G}{I}} \tag{2.7}$$

The frequency of the normal mode can be accurately measured measuring a few free oscillations and computing the corresponding Fourier transform.

Afterwards, we fastened coaxially an additional metallic disk of known moment of inertia I_a. This would offset the eigenfrequency of the pendulum to the new value:

$$f_a = \frac{1}{2\pi}\sqrt{\frac{G}{I + I_a}} \tag{2.8}$$

Where the only two unknown values are again the restoring coefficient G and the original moment of inertia I. These values can be found by substituting one of them in either Eq. 2.7 or Eq. 2.8. In our case, the eigenfrequency corresponding to the main rod only is approximately 14 Hz, and we obtain:

$$I = 2.24 \pm 0.02 \times 10^6 \text{ kg m}^2 \tag{2.9}$$

Also, the spring restoring coefficient can also be estimated to a value of:

$$G = 17.8 \pm 0.1 \times 10^{-3} \text{ N m/rad} \tag{2.10}$$

The torsional elastic constant can also be measured directly by using a dynamometer and measuring the angular displacement as a known force is applied at a known distance (lever arm) from the rotation axis.

These measurements are slightly more accurate than the indirect measurement obtained with the inertial disks; nonetheless they show complete agreement. The measured value is $G = 17.4 \pm 0.7 \times 10^{-3}$ N m/rad.

2.2.2 Detection of angular position

The displacement of the oscillator is detected optically. A laser beam is reflected by a mirror on the oscillator axis onto an analog photo cell. An electronic amplifier powers the cell and gives an output voltage signal, proportional to the position of the laser spot on the cell.

In order to reduce possible perturbations and noise due to other light sources, the whole system is encased in a black cover that prevents stray light from reaching the photo cell. The
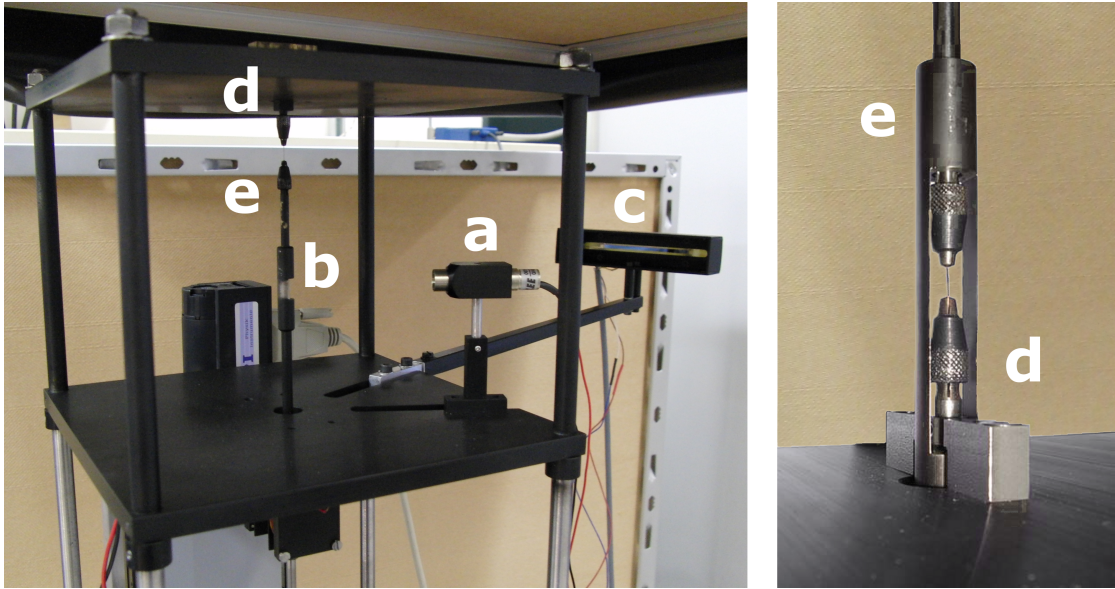
Figure 2.6: Detailed view of the torsion oscillator. **Left image**: view of the optical measurement of the oscillator angular position (top part). The laser diode **a** is aligned towards a mirror **b** coaxially fastened to the oscillator rod, and shines its spot on it. The laser beam is reflected back to the photocell **c**, which measures the position of the spot. The photocell itself rests on a metal bar and is placed farther away from the axis to increase the instrument's optical arm. The upper (fixed) suspension clamp **d** and the upper rod clamp **e** are also visible; a low damping metal wire keeps the torsion oscillator suspended in place. **Right image**: detail of the bottom suspension point. The oscillator axis with its bottom clamp **e** and the corresponding lower (fixed) suspension clamp **d** are shown. A second metallic wire ensures that the system has only one degree of freedom (rotation on its axis). The electromagnetic coils (not shown) are located below the horizontal support, as can be seen in Fig. 2.5.

cover is not mechanically in contact with the oscillator, and is suspended from the ceiling. This can be clearly seen in Fig. 2.5 and Fig. 2.6, where one side is opened to take the picture. The output of the cell is linear with respect to the torsion angle, $V = A\theta$, where θ represents the angular displacement, and A is a coefficient. The system can be calibrated to obtain a value of:

$$A = 100.74 \pm 2.54 \times 10^{-3} \text{ rad/V} \tag{2.11}$$

2.2.3 Applied torque

The system can also be exploited in forced mode to measure the response function. In this case, an external torque is applied on the probe by the means of a pair of electromagnetic coils placed besides a permanent magnet that is placed on the rod. The (complex) response function can then be calculated by concurrently measuring the applied torque (which is proportional to the current induced in the coils) and the corresponding displacement.

The relationship between the circulating current and the resulting torque can be assumed linear $T = B'I$. If we consider slow enough excitation frequencies, we can neglect the inductive behavior of the coil circuit, so that the current circulating is directly proportional to the imposed tension V, so to read $T = BV$. Knowing the restoring coefficient G, the coefficient B can be computed: $B = 0.174 \pm 0.002$ N m/V.

2.2.4 Electronic instrumentation

The main experimental informations that need to be measured in the system are two: the photocell output, containing the information on the movement of the probe, and the accelerometer output, used to compute the average vibration intensity parameter Γ.

In most experiments, Γ is measured by feeding the accelerometer signal to a digitizing, low noise, AC, true RMS voltmeter (e.g., Agilent Technologies model 34410A), and afterwards recorded on a computer. Considering a vibration frequency limited to frequencies higher than 50 Hz, this means that a sampling time of 1 s is more than enough to compute the mean value. However, since generally each experiment involves keeping vibration conditions constant for a long time (up to hours), Γ is measured as an average computed on many, 1 s long, samples.

The analog voltage signal from the photocell, on the other hand, has been measured in different ways. To obtain the response function during forced mode experiments, we used a Schlumberger mod. Solartronic 1250 Frequency Response Analyzer. This instrument can be used to generate the signal needed to drive the electromagnetic coils. The signal generator allows a choice of different waveforms (sine, square, triangular wave) of given frequency and amplitude. The signal is sent to a power supply for amplification, and used to drive the electromagnetic coils. The response function can then computed, from the fundamental tone to the 16th harmonic, by simultaneously measuring the torque T applied on the probe and its position θ: $G \propto T/\theta$.

On the other hand, if no external torque is applied, one can measure the spontaneous rearrangements of the probe. In this case an H.P. mod. 89410A Digital Voltage Analyzer was used to perform Fourier analysis of the signal, and to compute the Power Spectral Density of the position time series. These two techniques will be discussed in Ch. 3.

Finally, in order to study fractal characteristics of the trail of the probe, we recorded the time series of the photocell signal. Angular position time series of length of up to 1800 s and with sampling frequencies up to 20 kHz were recorded on a PC by the means of a National Instruments NiDAQ 6009 voltmeter. The recorded data were analyzed afterwards with specific signal analysis routines. This part will be discussed in detail in Ch. 4.

2.3 Brownian motor

A slightly different installation used in this work is the so-called *brownian motor* setup. In some experimental situations, the torsion constraint discussed in Section 2.2 introduces a preferential orientation of the probe. This fact complicates the analysis of the data, and it would be interesting to be able to perform measurement without this constraint.

Furthermore, numerous experiments have shown the appearance of directed motion in driven granular media [177, 178, 179, 180]. As we discuss in the next subsection, these observations are related to the out of equilibrium nature of vibrated granular media. We will now introduce the key feature of "ratchet systems" and "brownian motors" from a general perspective. This will help clarify the properties of the "brownian motor setup" that we will describe afterwards.

2.3.1 Ratchets and rectification of thermal noise

The history of this kind of devices dates back to the beginning of the 20th century and the Smoluchowsky-Feynman ratchet [181, 182] (sketched in Fig. 2.7). The device consists of a ratchet that rotates freely in one direction but is prevented from rotating in the opposite direction by a pawl. The ratchet is connected by an axle to a paddle wheel that is immersed in a fluid of molecules at temperature T_1. The molecules constitute a heat bath and they undergo Brownian motion with a mean kinetic energy that is determined by the temperature. The device is imagined as being small enough so that the impulse from a single molecular collision can turn the paddles. Although such collisions would tend to turn the rod in either direction with equal probability, the pawl allows the ratchet to rotate in one direction only. The net effect of many such random collisions should be for the ratchet to rotate continuously in that direction. One could imagine that the energy necessary to perform work would come from the heat bath, without any heat gradient. However, this behavior would violate the second law of thermodynamics, and the device is now a well know example of a perpetual motion machine of the second kind [182].

What is interesting in this device is the observation that it cannot work as intended if the paddles are kept in an equilibrium system, but the second principle of thermodynamics does not apply to out of equilibrium systems.

The modern concept of "Brownian motors", was introduced in 1995 by Hänngi [183, 184, 185], to describe devices by which some kind of thermal processes, inherently dominated by chaotic motion, can be used to generate directed motion and do mechanical or electrical work.

These device work by exploiting an asymmetry in some out of equilibrium medium. A sketch to exemplify this setup is shown in Fig. 2.8; the gray semitransparent cylinder represents a granular medium. In this case, a bed of grains is vibrated, and a probe, free to turn in either direction is immersed into it. A symmetric probe will move according to a brownian motion. However, a given asymmetry will increase the probability of moment transfer between the granular system and the probe in a given direction. This will result in a net rotation of the probe around its axis [180].

2.3.2 Brownian motor setup

Part of the work of this thesis (as for the improvement of the torsion oscillator) consisted in the design, construction and test of an experimental apparatus that could capture the general idea of a Smoluchowsky-Feynman ratchet, with the granular material playing the role of the thermal fluid.

The key features of this setup require a free rotating probe, interacting with the granular medium, and a way to record the movements of the probe. This is obtained by mounting the
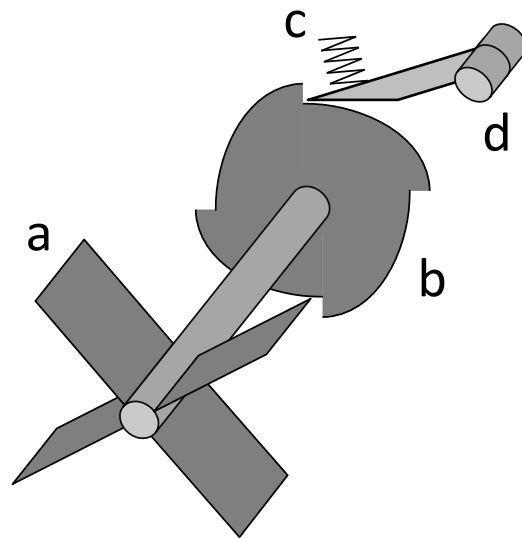
Figure 2.7: Sketch of a Smoluchowsky-Feynman ratchet. The paddle system a is immersed in a region of space occupied by moving particles and is subject to the collisions with the medium; The paddles are connected to a ratchet b with a solid axle. A spring c keeps a pawl d pressed against the ratchet. A superficial analysis could suggest that such a device could be used to rectify thermal noise. However, Feynman [182] very clearly illustrates that this would be a perpetual motion machine of the second kind.
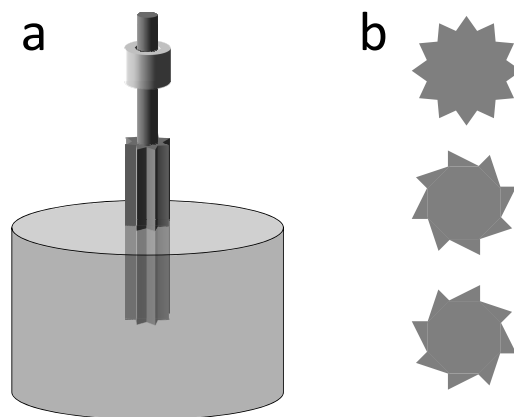
Figure 2.8: Sketch representing a probe immersed in a granular system (a). If probes of symmetric section are used (b, top section) no net rotation is observed. If asymmetric probes are considered (b, bottom), the geometry induces a net rotation.

axis of the probe in two coaxial ball bearings. These allow free rotation around the axis, while keeping the probe in place.

This configuration has the following experimental requirements: (**i**) the required torque to start the rotation is as little as possible, together with sliding friction; and (**ii**) the position of the probe is recorded with the highest possible accuracy. The main complication arising from point (**ii**) is that the probe does not oscillate around an equilibrium position, but is free to perform multiple full turns. Therefore the optical position detector must be designed in a way that allows it to continuously track the probe.

During both the design and construction stages, care was taken so that the system adheres as much as possible to the requirements, and that it is properly dimensioned, so that it can allow measurements of good quality. A sketch of the device is shown in Fig. 2.9; a general overview of the installation can be seen in the photo of Fig. 2.10, while more detailed photos, showing the key parts of the instrument are shown in Fig. 2.11.

The probe (p) is sustained by the ball bearings (e). We measured the starting torque required to start the rotation of a free probe. This was done by fastening a plastic rod perpendicular to the probe axis. A load was then applied with a high precision, low force, dynamometer. Knowing the length of the lever arm and the size of the axis we obtain a starting torque of approximately 5×10^{-5} N m. This value should be only considered as an estimate, since the measurements indicate a considerable scatter. This is expected, on the other hand, due to the low value of the measured constraint. Finally, it is important to note that, since the instrument is meant to operate at very slow speed, we neglected to consider the speed-proportional dissipation phenomena typical of ball bearings, and which are influenced largely by the choice of lubricant of the bearings.

The position is optically detected, with a laser diode (a) reflecting a laser beam on a mirror placed on the top of the probe axle (b). The movements of the spot are sensed by an analog photocell (c). As the probe moves, the signal from the photocell is measured. The slow drift is decoupled from the fast vibrations with a band split filter.

A feedback (lowpass, $f_b = 1$ Hz) circuit connected to a power source drives the electric motor (m), ensuring that, on average, the spot of the laser beam always falls in the center of the photocell. The average rotation of the photocell and motor assembly (*not* the rotating probe) can be used to compute the average speed of rotation of the probe. This could be useful, for example, to test non-symmetric probes [180]. The detection of the position is done by an optical rotary encoder disc and its corresponding decoder (g, of Gurley Precision Instruments, U.S.A.) The signal from the photocell is passed from the rotating support to the base via a sliding contact (f). All the data, both from the photocell and the rotary decoder, are measured with a digitizing voltmeter (National Instruments NiDAQ 6009) at different sampling frequencies, and they are eventually recorded on a computer for analysis.

For what concerns the granular material, as it was the case for the torsion oscillator, the vibrated medium is studied by the means of a probe immersed by a given length L in a granular medium of depth D. The granular bath is kept in similar containers than those shown for the torsion oscillator setup. Also, the vertical vibrations are imposed by an identical set of vibration motor and driving electronics.
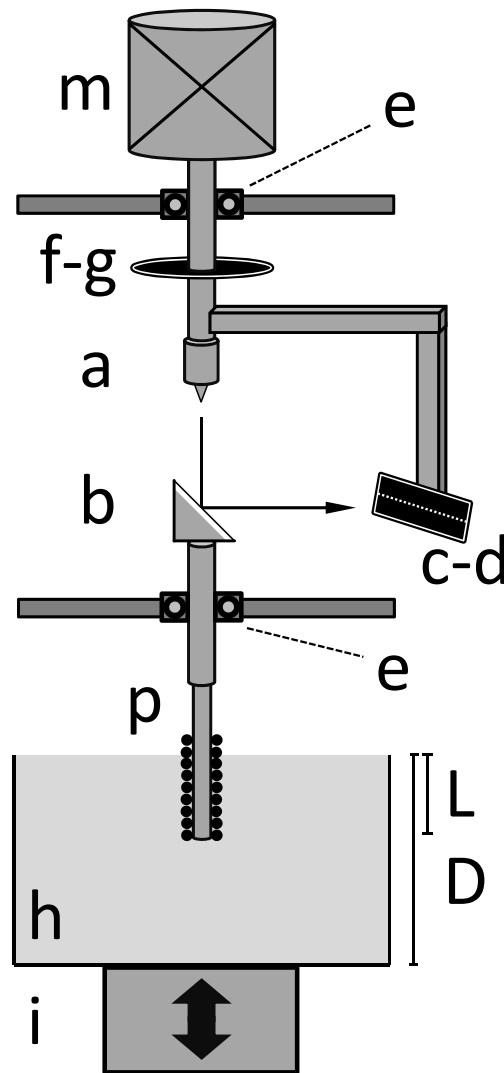
Figure 2.9: Sketch of the Brownian motor installation. The cylindrically shaped probe p is immersed for a length L into a granular bath of depth D. Completely analogous to what happens in the torsion oscillator setup, the granular material is vertically shaken by a vibration motor. An accelerometer (not shown) measures the intensity of vibration, Γ. The scheme of the oscillator includes: a = laser diode; b = mirror; c = photocell; d = anchor point for stick-slip measurements; e = ball bearings; m = electromagnetic motor; f = rotating electric contacts; g = position encoder for the electric motor; p = cylindrical probe; h = granular medium; i = vibrator motor.
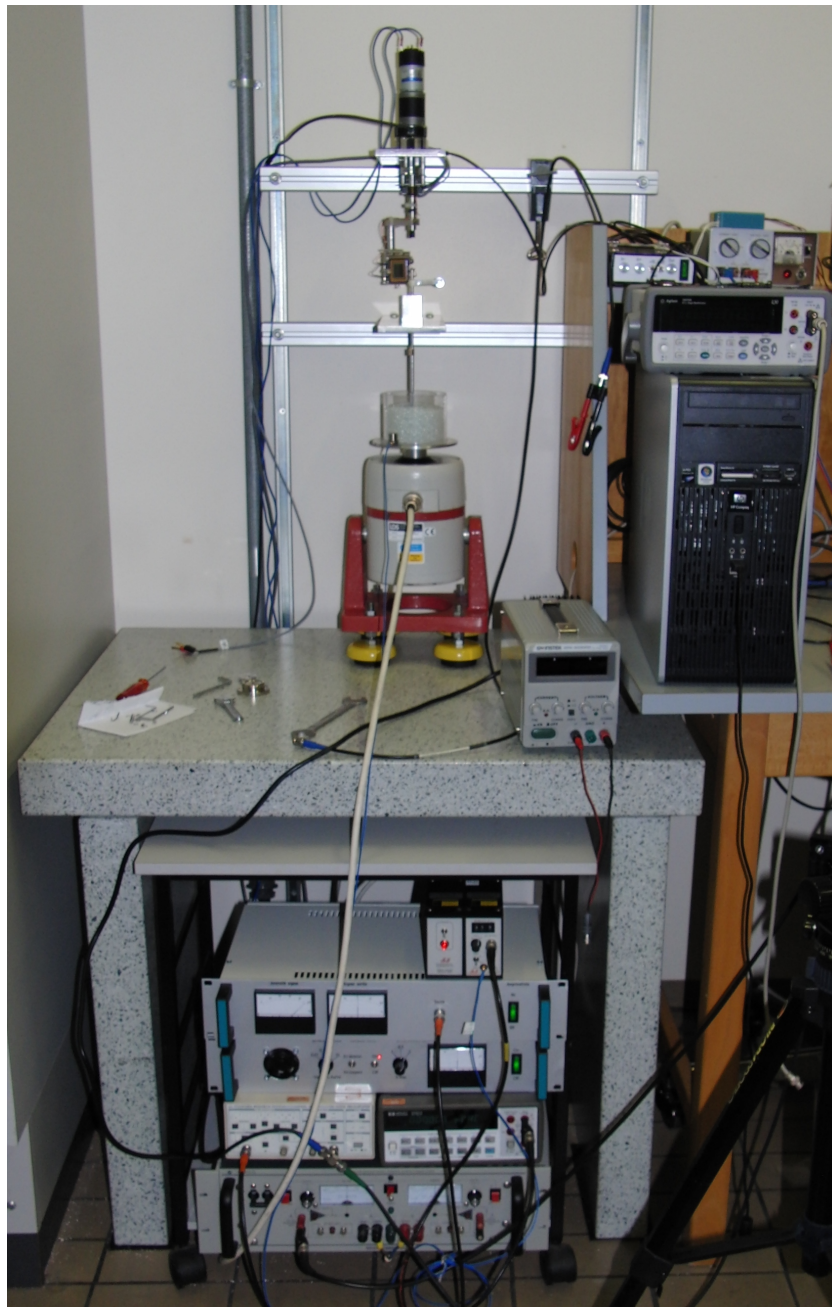
Figure 2.10: Complete view of the Brownian motor experimental setup. The driving motor is fastened coaxially with respect to the upper rotating axis, above the first horizontal support. The position sensing electronics lies between the two plates, while the Brownian motor axis is seen rising from the bottom support, where it is held by two ball bearings. This lower part is shown more in detail in Fig. 2.11. The container for the granular medium and the relative vibration motor compose the bottom part of the installation, and are placed on a heavy marble laboratory table. Below the table, part of the electronic chain of measurement together with the feedback loop can be seen.
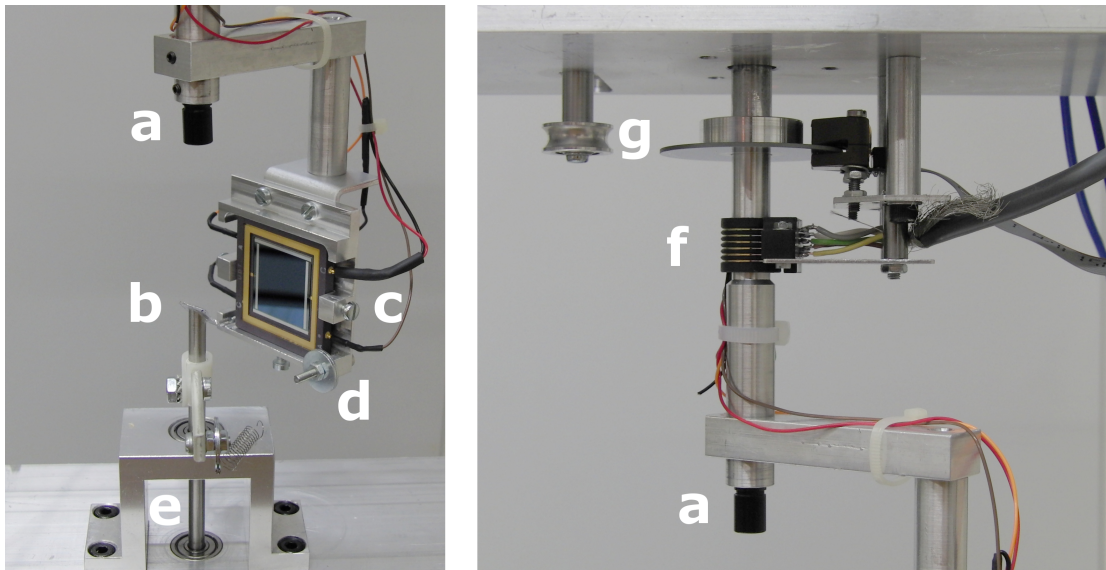
Figure 2.11: Detailed view of the brownian motor experimental setup. The letters indicating the different parts of the installation correspond to the ones shown in the sketch of Fig. 2.10. **Right image**: Bottom part of the setup. We can see the laser diode, mirror and cell. Besides the cell we see the anchor point d; here we can connect the spring that can be seen in the image. The other end of the spring is fastened to a plastic rod which in turn is connected to the rotating axle. When the spring is connected the system can be employed to perform stick-slip experiment using the electric motor to drag the probe. **Left image**: Upper part of the setup. The rotating electric contacts f and the position encoder g that measures the position of the photocell arm can be seen.

2.3.3 Stick and slip detection

A slightly different configuration is possible using the brownian motor installation, and used to study stick and slip phenomena in granular materials. This could allow a direct comparison with identical experiments performed on traditional materials [186].

The experimental configuration is very simple. A lightweight plastic arm, 50 mm long, can be installed on the probe axis just below the mirror b. This arm is then connected to one side of the photocell support on the rotating arm, in a specifically designed anchor point d. The connection is realized via an extremely weak spring ($k = 1$ mN/mm, 10 or 25 mm long. The arm is positioned so that the reflected laser spot falls in the middle of the photocell, while an external power source is used to activate the rotation motor m. The movement of the rotating arm is transmitted to the probe axis via the spring, resulting in a series of depinning and repinning events as the probe is trained in the granular bath. The resulting stick and slip movement is recorded as fluctuation around the center of the photocell. Some preliminary observations performed with this technique will be shown in Ch. 5.

Chapter 3

Jamming and the Glass Transition

In this chapter we present the experimental results obtained when a granular system is submitted to vibrations intensities, for which the average vibration intensity parameter Γ is typically in the range $0 \leq \Gamma < 10$.

Past work has shown that strongly vibrated granular materials can be modeled as thermal liquids [187]. In this driven "liquid phase", energy is continuously provided to the granular systems and dissipated via inelastic collisions between grains; however, the system can be seen at "equilibrium" in the sense that the grains explore randomly all possible configurations. It has also been observed [188] that there is a significant change in behavior in the system as the $\Gamma = 1$ boundary is crossed. This threshold has an implicit physic relevance. As discussed in the previous chapter, we can consider the simplest case of a sinusoidal shaking $z(t) = a_s \sin(\omega_s t)$, where a_s denotes the shaking amplitude and ω_s the angular pulsation. If we write $r = a_s \omega / g$, the value $r = 1$ marks the threshold above which grains may start to move without being in constant contact with one another. Therefore, there exists a certain threshold below which the vibrated grains are not allowed free motion any more, even if they are still free to rearrange and mix. This threshold is approximately defined by an average acceleration equal to gravity, or $\Gamma = 1$.

Below this threshold, the grains are subject to continuous contact interactions, and start to randomly form contact networks. These structures are responsible of a radical change in the dynamics of the system. It is in this meaning that the system undergoes a "jamming" transition. This dynamic region, dominated by the rapid increase of hard-sphere interaction in the granular system, has been extensively studied, and a few general properties were observed. The experiments show that there a strong analogy can be drawn between the behavior of the granular system with respect to the so-called glass-transition that is observed in a large number of "glass forming" materials, such as silicate glasses, polymers and colloids [189, 190, 191, 192, 193, 194, 195].

From an experimental point of view, it is important to stress the fact that the onset of the jamming transition, as Γ becomes smaller than 1, drastically reduces the mobility of the grains, and also it increases the size of contact networks between the grains. For these reasons, experimental approaches must be careful not to introduce external perturbations which might mask the behavior of the system. The measurements require much more refined techniques than those that can be employed in the case of strongly vibrated systems. A few important

physical observation, that are relevant to this point, are discussed in Appendix C.

3.1 Forced mode data

This section will present one mode of operation of the torsion oscillator setup. In this configuration, a probe senses the granular medium and computes the mechanical response function to an externally imposed stress, hence the denomination of "forced mode".

Before starting with that, it is however important to briefly review the current state of the art of the subject, and to highlight a few important observations. Past work [196] has shown that a torsion pendulum can be usefully employed to study the behavior of strongly vibrated granular systems. However, difficulties arise when addressing the behavior of non-fluidized granular media, for to two main reasons.

First, as the vibration intensity decreases, there is simply not enough energy in the system, to allow a continuous energy flow at all frequencies. Data in [197] was interpreted with the existence of a sort of "equipartition", which in turn allowed to describe the system along the lines of a fluctuation-dissipation theorem framework. However, the same data suggest that already in the range $\Gamma \leq 3$, this equipartition is lost, so that there is no longer the possibility of using a fluctuation-dissipation theorem as a framework to interpret the experimental data.

Secondly, as the vibrations approach the fludization threshold ($\Gamma = 1$), the mobility of the granular particles decreases by orders of magnitude. This means that any experimental technique used to study the mechanical response of the medium should do it in such a way that it does not excessively perturbs the grains. This is not possible, using a torsion pendulum, if one approaches the pendulum eigenfrequency. Unfortunately, the technique in [196] requires driving the torsion probe with a frequency sweep through a wide frequency window (*chirping* [198]) that comprises the oscillator eigenfrequency. This disrupts the granular system and does not give useful informations.

To overcome these problems, it is possible to study the mechanical response system in a slightly different way, using only sub-resonant excitations. This technique, well known in the physics of materials, is called *mechanical spectroscopy*. In the following sections we will discuss more in detail the key ideas of this technique, and why it is reasonable to apply it to our system. We will then show an example of its application, using our installation to measure the glass transition of an alcohol. Finally, we will present experimental data obtained on the vibrated granular material.

3.1.1 Method

This subsection is composed of two parts. In the first, we will briefly describe two simple rheological models that can be used to describe the behavior of very simple mechanical system. While these models are very far from capturing the complexity of granular materials, they will be useful to introduce and explain the key concepts of the experimental technique. In the second part, we introduce the theoretical basis of our measurement method, in the light of the considered models.
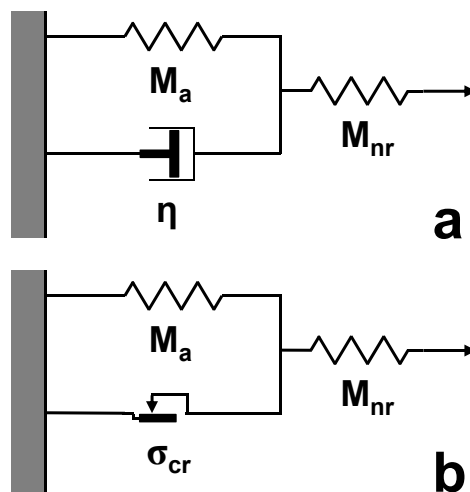
Figure 3.1: Two simple rheologic models of vibrated granular media. (a) the linear anelastic solid model, or *Zener* model. This model describes a system held in place by a potential energy term (the spring element), damped by viscous friction. Such a model can be used to describe the behavior of solids showing both elastic and anelastic response to an externally imposed stress. (b) dry friction solid model. In this case, the model shows a dry friction term. This leads to an threshold phenomenon that is responsible of plastic deformations. A more general overview of similar (and more complex) models, especially in the framework of glass transitions, can be found in [117].

Simple rheologic models

The measurement techniques we used are based on the fact that granular materials can behave as plastic solids or as non-Newtonian fluids. We start with a general overview of two simple rheologic models, as presented in Fig. 3.1.

The model shown in Fig. 3.1a is called standard linear solid model. It combines aspects of the Maxwell and Kelvin-Voigt elements, and describes the overall behavior of a material undergoing recoverable strain under a small applied stress. In this case, if stress jump is applied, the material shows an instantaneous response corresponding to elasticity. But the system also shows a time-dependent response (anelasticity), as the second spring, paired to the dashpot, deforms to the equilibrium value. Instantaneous release of the stress also results in a discontinuous decrease in strain, and subsequent recovery of anelastic deformation. One interesting feature of this model, and the one that is most relevant to this work, is that it can be solved exactly when a sinusoidal stress is applied. This we will be discussed further in the following subsection.

Fig. 3.1b, on the other hand, represents a slightly different situation, in which the dissipation is ruled by a dry friction element. In general, the introduction of dry friction allows to describe different materials and conditions (for example, hysteresis). In fact, this is the situation that we expect to be more relevant for the case of granular materials, the inter-grain interaction being dominated by local, dry friction contact terms. The model cannot be solved analytically, because of the non-linear response of the dry friction element. However, it has been shown

that [123], if the dry friction constraint is thermally activated, we can still recover an intrinsic relaxation time as defined in the following section. Under an externally imposed sinusoidal stress, the response function has the same qualitative behavior as case a, and a maximum in damping appears, similar to that described in Eq. 3.2.

Mechanical spectroscopy

Mechanical spectroscopy is an experimental technique that can measure with high accuracy and precision the mechanical response function of materials. It is traditionally used to measure the mobility of crystal structure defects (lattice point defects, dislocations, presence and properties of grain boundaries). However, it is also quite sensitive to phase transformations, recrystallization, magnetic domain relaxations [199, 117]. It has been applied to a wide range of glass formers as silicate glasses, polymers and colloids. This technique consists in applying periodic stress oscillations to the sample: $\sigma = \sigma_0 e^{i\omega t}$ and in measuring its mechanical strain response characterized by the amplitude ϵ_0 (proportional to the elastic compliance) and by a phase lag δ: $\epsilon = \epsilon_0 e^{i(\omega t - \delta)}$

More specifically, it can be demonstrated [124] that the mechanical loss $\tan(\delta)$ is related to the damping capacity, sometimes called internal friction, of the material:

$$\tan(\delta) = \frac{1}{2\pi} \frac{\delta W_{\text{diss}}}{\delta W_{\text{el. max.}}} \tag{3.1}$$

where W_{diss} represents the energy dissipated during one oscillation cycle and $W_{\text{el. max.}}$ is the maximum stored elastic energy. The internal friction is often indicated with *IF*, or Q^{-1} (referring to the inverse of the quality factor of the resonator).

If one considers a model and is allowed to assume that there is a linear relationship between stress and strain, then it can be shown [124] that:

$$\tan(\delta) = \Delta \frac{\omega\tau}{1 + \omega^2 \tau^2} \tag{3.2}$$

where ω is the oscillation frequency and τ is the relaxation time. Such a function is shaped as a peak (called Debye peak by analogy with the dielectric relaxation), exhibiting a maximum at

$$\omega\tau = 1 \tag{3.3}$$

The presence of a mechanical loss peak is associated with an elastic modulus change:

$$\frac{\Delta E}{E} = -\frac{1}{1 + \omega^2 \tau^2} \tag{3.4}$$

If the relaxation time τ is thermally activated, $\tau = \tau_0 e^{\frac{-Q}{k_B T}}$, an internal friction peak shows up both as a function of temperature and frequency. Given the condition (3.3) and equation (3.4), the activation energy Q and the attempt frequency τ_0 can be measured by fitting the displacement of the peak maximum as a function of frequency and temperature according to

an Arrhenius law:

$$\ln \omega = -\frac{Q}{k_B T} + \ln\left(\tau_0^{-1}\right) \tag{3.5}$$

If the system is studied with frequency sweeps (so that one obtains a graph of the loss tangent as a function of the excitation frequency) the resulting relaxation peaks can be fitted by broadened Debye peaks [200]. In the case that the physical mechanism inducing the relaxation shows a distribution of relaxation times, the relaxation can be described as:

$$\tan(\delta) = \sum_i \frac{\omega \tau_i}{1 + \omega^2 \tau_i^2}$$

This leads to a so called "broadened" Debye peak, that is empirically described by the function:

$$\tan(\delta) = \Delta \frac{(\omega \tau)^\alpha}{1 + (\omega \tau)^{2\alpha}} \tag{3.6}$$

where α is the empirical broadening factor of the distribution. A very simple example of this method is given, for example, by the so-called Snoek relaxation [124]. The Snoek relaxation is the anelastic relaxation of interstitial solute atoms in bcc metals. In this case, solute atoms induce elastic dipoles in the structure. Application of stress leads to a redistribution of the interstitials between three possible axial orientational symmetries. Every jump is connected with a reorientation of the dipole axis, and the induced reorientation gives rise to a mechanical loss peak, that can be treated by a Debye equation.

From an experimental perspective, mechanical spectroscopy requires the simultaneous measurement of the stress $\sigma(t)$ that is imposed on the system, and of the strain $\epsilon(t)$ that is correspondingly induced. In our installation we consider the torque applied to the probe and the resulting angular displacement, as discussed in Ch. 2. The oscillator is submitted to a torque $T(t) = T_0 \exp(i\omega_p t)$, in a frequency range going from 10^{-4} Hz to 10 Hz. The complex frequency response of the system, $G = T/\theta$, is then computed by a Schlumberger Solartronic 1250 frequency response analyzer. The electronic chain of measure is controlled by a computer program, which is also responsible for the archiving of all the experimental results.

Typically we show the argument, $\arg(G_1)$ ("loss angle"), and the absolute modulus, $|G_1|$ ("dynamic modulus"), of the first harmonic, as a function of either T_0, Γ, or f_p. For a linear system, $\tan[\arg(G_1)]$ coincides with the loss factor and, if the damping is low, with the systems internal friction (or damping capacity). The dynamic modulus, on the other hand, is a measure of the relative instantaneous stiffness.

The data are obtained via Fourier analysis and no error estimates is provided directly. Therefore, all the error bars for the response function were obtained by repeating the measurements and subsequently computing the standard deviation from the mean value. Typically this has been done for the experimental conditions which had shown more scattered data. In principle, this choice should provide us with a worst-case estimate. Since the standard deviation tends to increase as the measurement frequency decreases, we indicate the values obtained by repeating 10 times the measurements performed at 0.05 Hz.

Therefore, as it has been shown, mechanical spectroscopy allows access to observables that are directly related to the microscopic structure of the sample under study. In the following section, this technique will be applied to granular system. We also tested both the technique and the installation using a real glass former, the alcohol 1-Hexadecanol. This is discussed in Appendix D.

3.1.2   The jamming peak in granular materials

In the previous subsections we have described how sub-resonant probing represents a useful tool to measure the mechanical response of a system, with a high sensitivity: this allows to study the evolution of the system under the variation of external parameters. For example, in real glass forming systems, such as the 1-Hexadecanol, one important external parameter is the temperature.

Vibrated granular system, on the other hand, are sensitive to different parameters of the driving excitations. Besides the average intensity of vibrations, Γ, one can vary the vibration frequency (or frequency band, in the case of broadband driving signals), and (in some cases) the age of the sample.

In these systems, the measurement of the mechanical response function provides a way to study the jamming transition. The experiments indicate that the transition induces a peak in the dissipated power, which is analogous to what is observed in real glass formers. The peak can clearly be seen in vibration intensity or frequency scans, as it will be shown in the following section. Before that, however, it is necessary to verify that the experimental parameters do not induce artifacts in the measurements.

Finally, we note that, unless otherwise stated, all the measurements discussed in the following, for all Sec. 3.1, were obtained by vibrating the granular medium using the standard filtered wave noise signal, and by probing it with the two-tip probe geometry (probe **f**).

3.1.3   The linear regime

During the measurements, the amplitude of the applied torque T_0 should be large enough for the measurements to have a good signal to noise ratio. On the other hand, it also should be small enough to observe an amplitude-independent response, *i.e.*, that the linear response regime is reached.

The linearity of the measurements can be assessed by observing the high harmonic content of the response function. The electronic frequency response analyzer that calculates the response function can be set so that it consider any given harmonic of the stress signal selected with the function generator. Normally, one studies the response function at the fundamental tone. All the data shown in this work are computed considering the fundamental tone. The linearity of the response was tested by plotting the first three harmonics of the response function for different choices of experimental parameters (vibration intensities, vibration frequencies, imposed stress amplitude and frequency, probe immersion depth). In general, the high harmonic content is only noise, for almost all the tested configurations, provided that the probe has at least a few millimeters of contact with the granular system, and that

the imposed torque does not exceed a value of approximately 10^{-3} N m (and which is an exceedingly high value for our configuration).

This linear response, however, does not mean that the system response function is not sensitive to the intensity of the imposed stress. In fact, the excitation exerted on the probe is transmitted to the granular, and induces local rearrangements. A few experimental curves, obtained with values of stress intensities far below the linear response limit can be seen in Fig. 3.2.

The evolution of these curves as a function of the stress intensities suggest a second, important observation. This experimental technique can be meaningfully applied as long as the rearrangement due to the "natural" evolution of the granular system are significantly more important than the one caused by the local perturbation of the probe. Otherwise, other technique have to be considered, as we will discuss in Sec. 3.3 and following. It is also worth noting that, in general, glassy system do show a nonlinear response with diverging effects as the glass transition is reached [201, 202]. Our experimental limits, however, appear to be dictated by the effects of induced local rearrangements due to the torsion probe.

The previous observation on the role of applied torque intensities indicates that, in typical measuring conditions, the displacement of the probe should not exceed 0.01 radians. This corresponds approximately to displacements of 0.1 mm for probe **g** (cylindrical shaped) and about 1 mm for probe **f** (fork shaped). If one considers the data shown in Fig. 3.2, they indicate that, for vibrated systems, the best compromise between strong signal and low perturbation is obtained with torque levels of approximately 2 to $5 \times 10^{-5} Nm$. We also note that the data corresponding to $\Gamma = 0$ also show the presence of a peak. The presence of the peak is in fact determined by the relaxation induced by the movement of the probe, and is dependent on the aging of the system.

The same situation can be tested by performing scans in the torque intensity, for different values of forcing frequencies and vibration intensities, as shown in Fig. 3.3. In this case, the data on the first row show what happens when the system is not vibrated. In this case we observe three different regimes, for low, average, and high torques. If the applied torque is weak, the probe is blocked in the medium. For this reason, the dynamic modulus, which is in fact an indicator of the stiffness, is very high. On the contrary, the dissipation is low, because the incoming energy tends to be stored in elastic deformation of the granular network. This curve is dependent on the imposed frequency, because this frequency dictates the time scale in which the system must respond to the perturbation. At zero vibrations, the granular system cannot evolve, and is trapped in a specific configuration. Its characteristic time is divergent, or very large (there is always a tiny amount of vibration coming from the exterior, from noise, or vibrations in the buildings and transmitted to the sample). For this reason, the apparent stiffness is much lower at low frequencies: the granular medium can indeed rearrange and dissipate energy. This becomes much more difficult as the torque frequency is increased. The dynamic modulus grows, and the peak in the loss angle moves towards higher torque intensities: to rearrange at this time scale, a larger stress is required.

As the amount of stress is increased, we observe that the apparent stiffness has a sharp decrease. The decrease is more accentuated the higher is the considered frequency. In parallel, the loss angle shows a peak. In this region, the torque is strong enough to cause rearrangement in the granular force chain network. As the probes breaks through these chain of forces, the
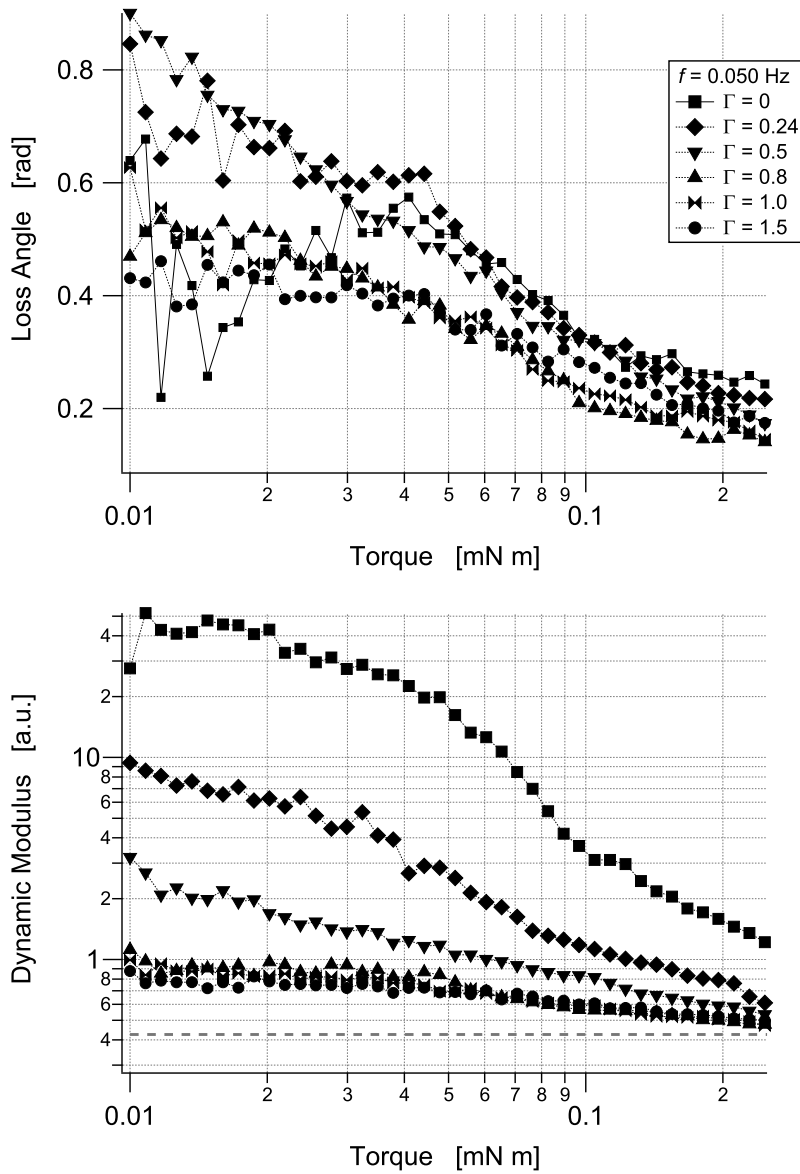
Figure 3.2: Effect of different imposed torque intensities. The graph shows the loss angle and the dynamic modulus of the granular system (respectively, the imaginary and real part of the complex susceptibility), plotted as a function of the intensity of the imposed torque, for different vibration intensities Γ. The oscillation frequency is set at 0.05 Hz. The data show that both quantities continuously decrease for increasing stress and Γ. A relaxation peak is instead observed for Γ = 0, indicating a significant change in behavior.
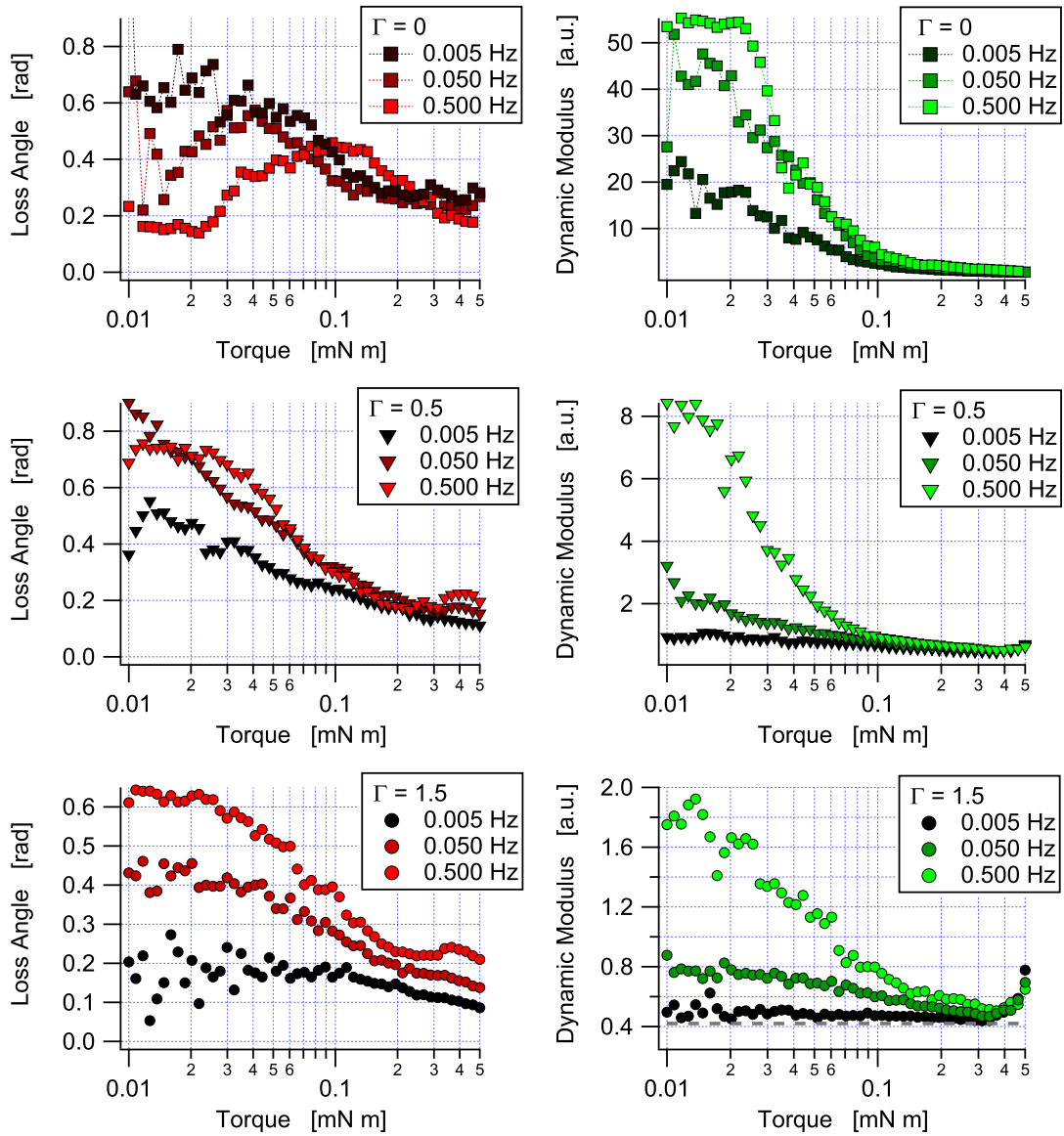
Figure 3.3: Effect of the variation of imposed torque parameters. The graph shows the loss angle and the dynamic modulus of the granular system, plotted as a function of the imposed torque, at different excitation frequencies f_s (indicated in the legend),and for three different vibration intensities Γ (also in the legend). Together with Fig. 3.2, the data indicate that system is sensitive to both the applied torque and frequency.

stiffness decreases, and the dissipation of the energy due to friction between the grains (and between the grains and the surface of the probe) is responsible for the appearance of the peak in the loss angle.

Finally, as the torque intensities become much larger, the probe is actually piercing its way in the granular system. The grains do not have the time to relax into an equilibrium position, and the granular medium as a whole does not oppose anymore a strong resistance to the rotating probe. This is also reflected in the loss angle data, because the granular system is not able to dissipate energy in an efficient way any more.

It should be noted that these measurements were performed with a fully aged granular sample. With this technique, and with a little care in the preparation of the granular sample, is indeed possible to observe hysteresis effects that depend on the way the sample was vibrated before the beginning of the measurements, or on the history of the application of the torque on the probe.

The situation changes when vibrations are imposed on the system. In this case, the grains are submitted to a vibration that causes them to rearrange. The probe is much more free to move, and in these condition the amount of rearrangements that it induces in the granular system becomes smaller than the spontaneous evolution. This is clearly seen in the dynamic moduli data, that drop by more than a factor 10 with respect to the non vibrated conditions.

The measurements indicate that the overall behavior of the system becomes weakly dependent on the imposed torque, regardless if the system is driven above or below the fludization threshold. In these conditions it appears that the stress frequency plays the most important role. At high frequencies, the time scale of the measurements is still small enough, so that the probe can probe the response of the granular medium, and distinguish between the different torque values (this can be seen by looking at the 0.5 Hz data). On the other hand, when the frequency becomes small enough, the time scale of the induced rearrangements grows longer than the characteristic time scale of the granular system. In this case, a much weaker interaction is observed.

3.1.4 Γ **scans**

A different way of observing the system is done by performing sweeps of the vibration intensities. This is represented in Fig. 3.4, Fig. 3.5 and Fig. 3.6.

In Fig. 3.4 the data show the behavior of the system as a function of Γ, for different stresses. A peak is observed below the fludization threshold. In a naive interpretation of the vibration intensity parameter Γ as a measure of the energy available to the system, the peak can be interpreted as a relaxation peak that is activated by the presence of this energy. This is analogous to the phenomenon of "thermal activation" in thermodynamics. From these curves, once again, we can also extract useful information for the experimental driving parameters. In fact, the curves for 80 and 65×10^{-6} N m deviate significantly from the ones at lower stress. This means that the probe can still induce significant breakdowns in the granular contact network, at low Γ. The best compromise seems to be the curve for 35×10^{-6} N m, which is only a little more noisy than the one for 50×10^{-6} N m, but much less noisy than the one obtained with a stress of 20×10^{-6} N m.

Figure 3.4: Γ scans for different stresses. The graph shows the curves for the loss angle and the dynamic moduli as a function of the vibration intensity, for different values of the externally imposed torque. The data correspond to 0.05 Hz frequency excitations, while the system is vibrated with the broadband signal.

Once the optimal torque is selected, the role of the imposed frequency f_p can be studied more in detail. Fig. 3.5 presents the curves obtained with Γ sweeps, for different values of f_p. Very similar results are shown in Fig. 3.6. In this case, the data were obtained by imposing a sinusoidal vibration, with $f_s = 113$ Hz, instead of using the standard broadband vibrations. This difference will prove useful in the following discussion; due to the strong similarities between the data sets, Fig. 3.5 will be the reference for the rest of this section.

The loss angle data (Fig. 3.5, top) show the presence of a peak as a function of Γ. As the value of f_p increases, the peak moves towards higher vibration intensities Γ. This is, again, the effect of the relationship between the characteristic relaxation time of the system (that depends on the vibration) and the time scale of the measurement. It is interesting to note that a considerable part of the peak is found above $\Gamma = 1$, especially for the higher frequencies ($f_p > 0.1$). The dynamic moduli data complement the picture in the following way. For low enough vibration, the system shows a dynamic stiffness which is independent of f_p. As the vibrations become stronger, the stiffness stays constant up to a given point where the probe actually "unfreezes" and start moving. The value of Γ where this happens depends on f_p.

Before concluding, it is interesting to note that the data in Fig. 3.5 suggest a complex behavior once the vibration intensities reach the fluidization threshold. There, the dynamic moduli stop their rapid decrease, and either stabilize, or continue in their decrease, albeit at a much lower pace. This interesting phenomenon however is not related to the jamming transition and it will be discussed later, in section 5.5.

3.1.5   Frequency scans

In the previous sections we have seen that granular materials show a distinct relaxation peak in the vibration intensity region just below $\Gamma = 1$. As we have seen, the mechanical loss data clearly show that the jamming peak moves toward higher vibration levels as the frequency of measurement is increased. Furthermore, the simple models we discussed at the beginning of the section suggest that the observed relaxation, corresponding to the mechanical loss peak as a function of the level of vibration Γ, can be described with a functional form that is equivalent to the one used to express thermally activated phenomena. In this interpretation, the control parameter will then act as an "effective temperature", whose effect is analogous to the role of the actual temperature in real, thermal systems, in the sense of Eq. 3.5.

In order to understand more into detail the link between the Γ parameter and the fluidization of the system, it proves useful to performed frequency scans at fixed values of vibration intensities. In fact, the amplitude and frequency sweeps shown on the previous sections indicate that the relationship existing between the mechanical response function and the amplitude of vibration Γ is quite complex. The essential conclusions that can be drawn are the following: (*i*) a relaxation peak is observed; (*ii*) the relaxation has strong analogies with the relaxation due to the glass transition, as discussed in Appendix D; (*iii*) the measurements indicate that, if the experimental conditions are properly chosen, the frequency f_p influences the properties of the relaxation peak (which, in turn, defines a characteristic relaxation time as in the sense of Eq. 3.3).

This leads to the following observation. There is a big advantage in performing measurements
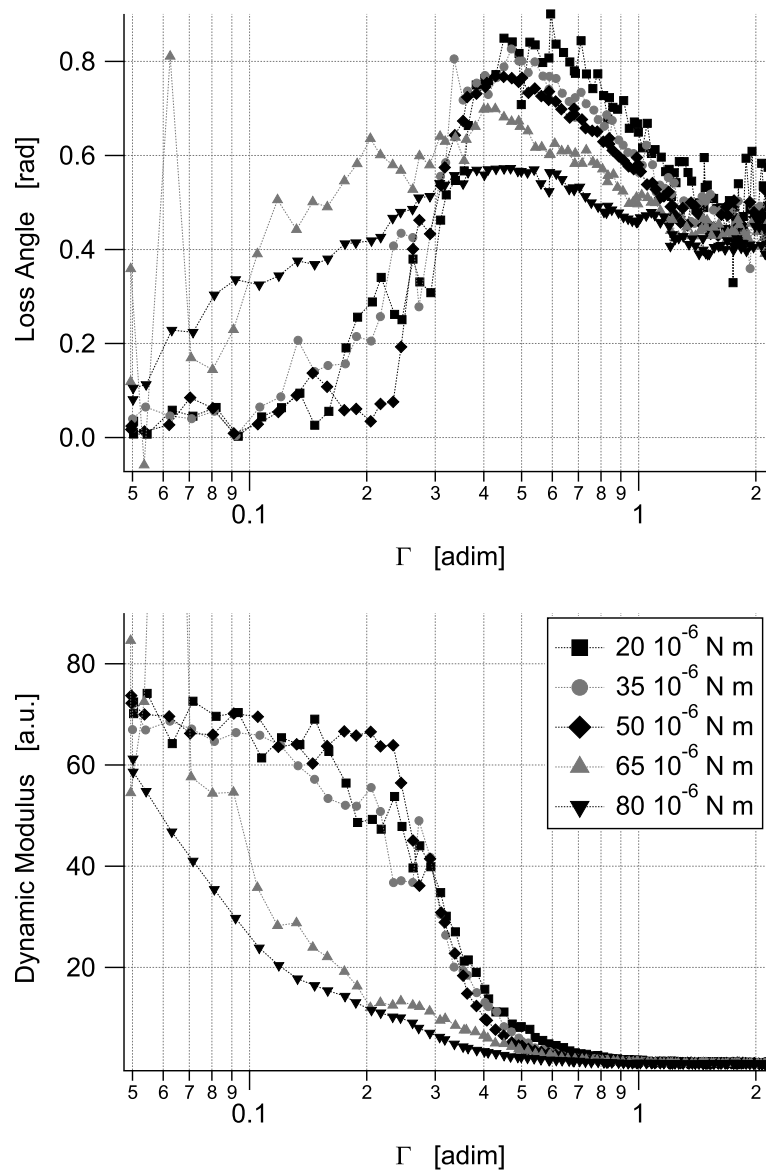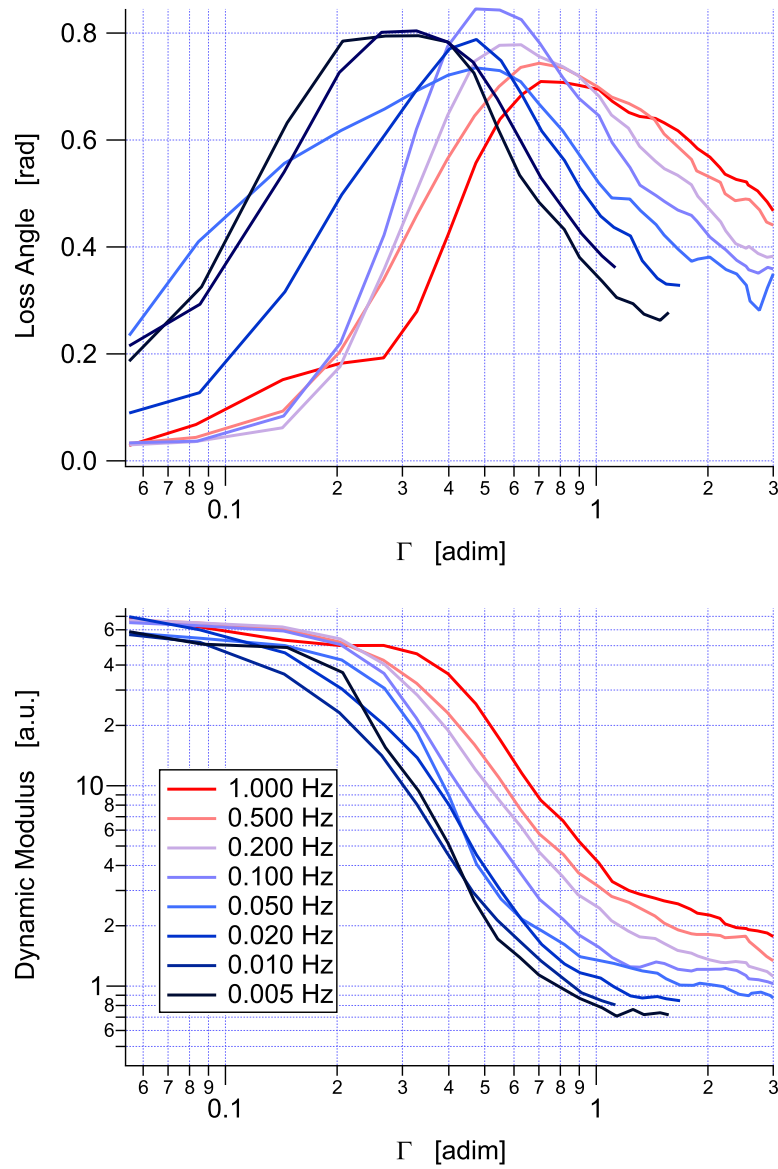
Figure 3.5: Γ scans for different probe frequencies f_p. The graph shows the curves for the loss angle and the dynamic moduli as a function of the vibration intensity, for different values of the imposed frequency f_p. The data correspond to a stress amplitude of 35×10^{-6} N m, and broadband vibrations.
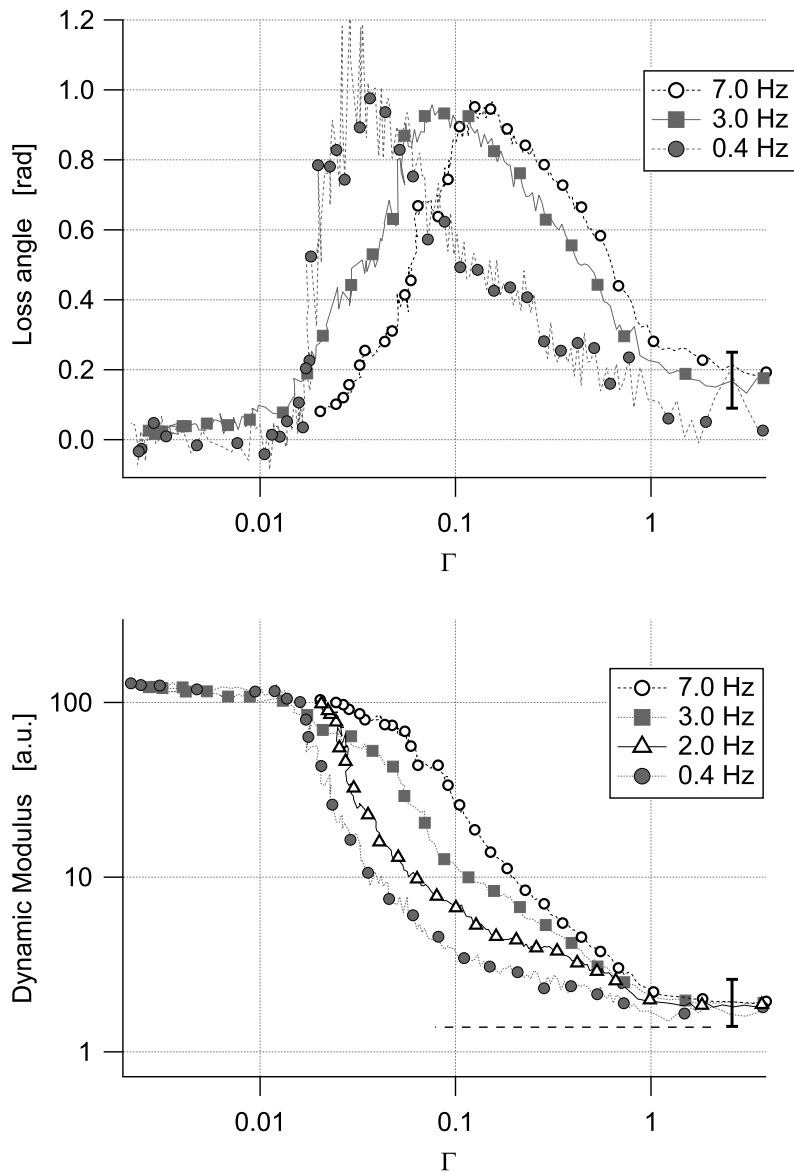
Figure 3.6: Γ scans for different probe frequencies f_p. The data were obtained in the same experimental conditions as those of Fig. 3.5; but in this case the granular medium was excited with sinusoidal excitations, $f_s = 113$ Hz.

with constant Γ (for example a f_p frequency sweep), because the functional dependence of the response function (and therefore, of the characteristic time) on the vibration amplitude does not influence the shape of the relaxation peak during each single measurement.

This is clearly seen in Fig. 3.7, where the data contain exactly the same information as those of Fig. 3.4, Fig. 3.5, or Fig. 3.6, but in a more accessible form. The strong advantage of this approach is that, at a fixed Γ, the functional form which connects Γ to any possible control parameter (supposingly some kind of *effective temperature*, from analogy with real glass formers). does not influence the shape of the measured curve. In real system, this would correspond to an isothermal measurement.

In the graphs, the abscissa is given by the excitation frequency f_p. The accessible frequency range is limited to the window from 0.001 Hz to below 20 Hz, which is not large enough to show the full relaxation peaks marking the transition between the liquid regime (obtained, for fixed Γ, at low frequencies) and the glassy regime (at high frequencies), for all the accessible experimental conditions. At the lower end of the spectrum, the limiting factor is dictated by the duration of the stress cycles, 1 mHz being the practical limit for reasonable experiment durations. The upper end instead is limited by the appearance of the exponential increase of the pendulum eigenfrequency, above 1 Hz.

The data correspond to three different levels of imposed torque, 50, 35 and 20×10^{-6} N m. For each torque intensity, we performed different measurements with average vibration intensities Γ going from 0.01 to approximately 1.5. In analyzing the data, we have to take into account the buildup of noise due to poor statistics at low frequencies. On the other hand, as we approach the high frequency domain ($f > 1$ Hz) we we also have to take into account the perturbations due to the approaching of the resonance ($f_p \approx 14$ Hz).

Besides these problems, the curves appears to be broadened relaxation peaks as of Eq. 3.6. The broadening exponent α, in this case, appears to be such that $\alpha_{\rm b}^{-1} \approx 3$. This fact is very important, because it allows a meaningful definition of a characteristic time (or frequency) associated to each curve. These measurements were repeated for different experimental condition, so that the position of the relaxation peak were obtained for wide range of Γ and stress amplitude values.

3.2 Analogy with thermal activated phenomena

The positions of the peaks (*i.e.* the frequency corresponding to the maximum of the curve) of Fig. 3.7 depend on the vibration intensity. These can be plotted as a function of the inverse of the vibration intensity Γ. The idea is that Γ is proportional to some effective temperature, and that the jamming transition can be described as a thermally activated phenomenon (as in Eq. 3.5) [57, 203, 204].

When the data are plotted on an Arrhenius diagram, as in Fig. 3.8 they align only if the effective temperature is proportional to Γ elevated to the power 1/2. This graph therefore suggests that the jamming phenomenon observed with the torsion oscillator can be described in the same way as a thermally activated mechanism, with an effective temperature parameter proportional to $\Gamma^{1/2}$.
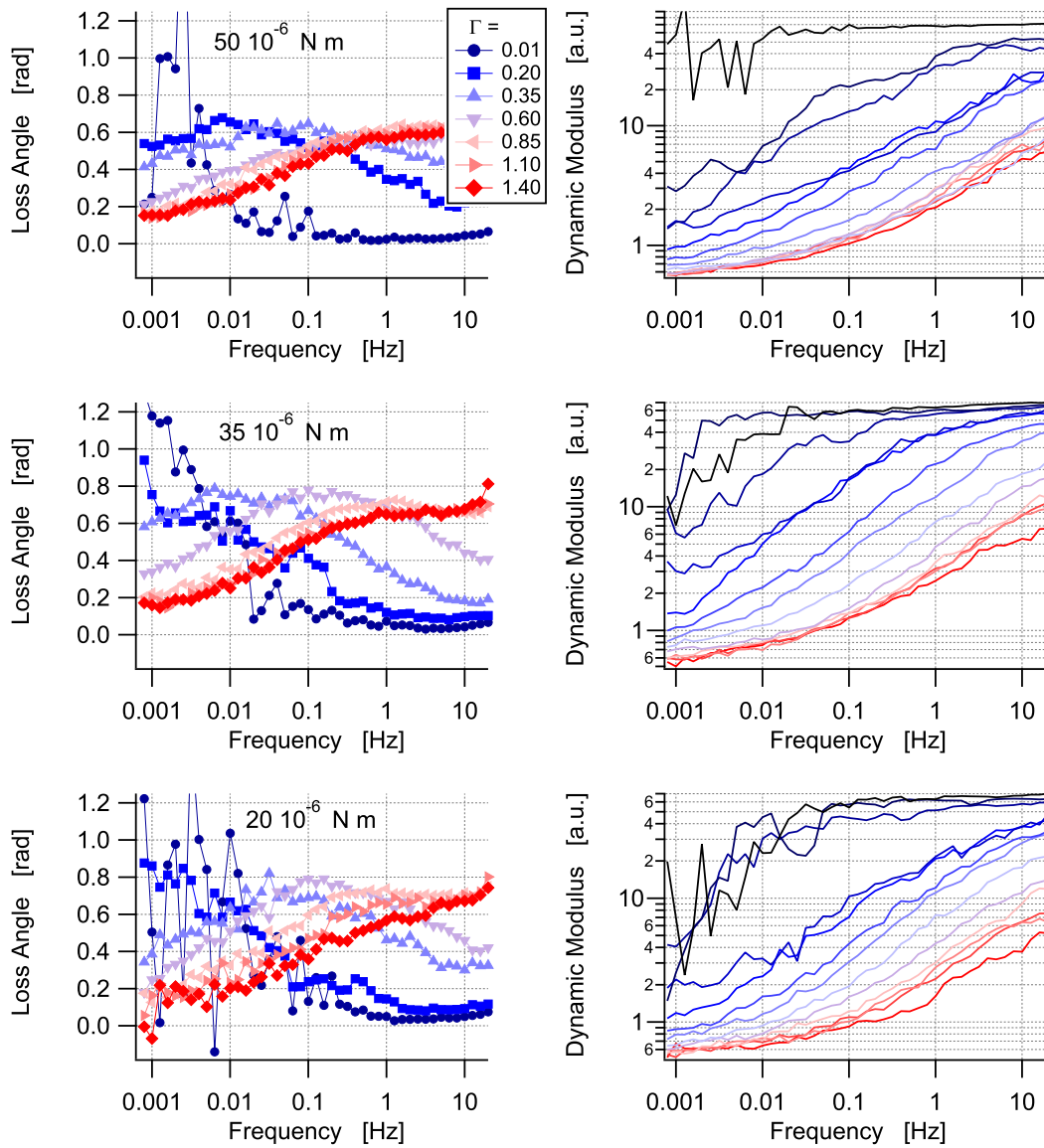
Figure 3.7: Mechanical loss angle (left) and dynamic modulus (right) plotted as a function of the frequency of imposed stress f_p, for three different levels of imposed torque. Each graph shows data for different vibration intensities: stronger vibrations are indicated by the red tones, and progressively weaker vibrations are marked as violet and blue colors. The data were fitted with broadened Debye peaks (fit not shown), used to determine the peak position. Data were obtained with probe **f**, positioned at a depth of approximately 8 mm.
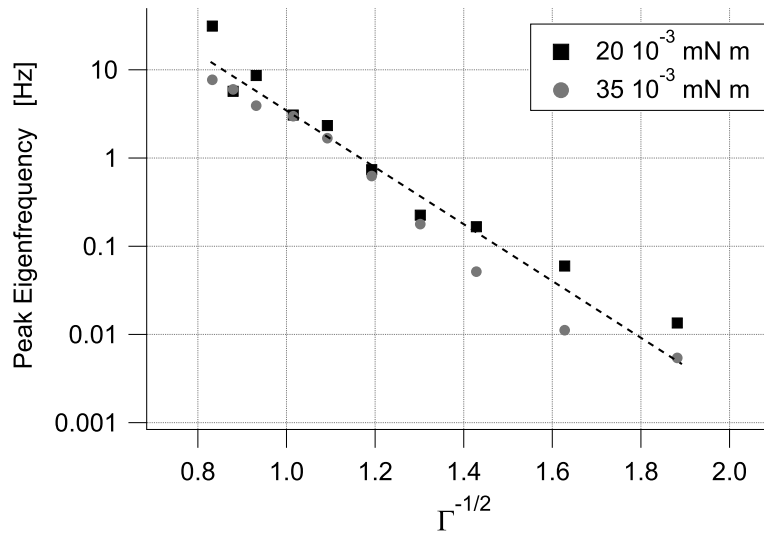
Figure 3.8: Arrhenius plot of relaxation peaks eigenfrequency as a function of $\Gamma^{-1/2}$. The data show the position (frequency) of the peak of fitted Debye peaks, as a function of the inverse of $\Gamma^{1/2}$. The exponent $1/2$ is the only choice that aligns all the point of the data on a line (besides the dispersion due to noise). The dashed line is a power law fit for the points.

From the data in Fig. 3.8 one can also observe that the points (despite the dispersion) do not seem to align completely on the straight line, that would correspond to a pure-Arrhenius behavior. Instead, they seem to have a slight downward curvature. This would correspond to a non-Arrhenius behavior during the jamming, which would better described by a VFT-like equation. Unfortunately, the experimental window on the control parameter is rather narrow, and the dispersion of the points does not allow to verify if the small apparent curvature of the points is a real effect or not.

The experimental technique could be improved further, to enlarge the accessible region of measurement. This will be the goal of the free mode measurements discussed in the following section. The combination of both techniques will provide complementary informations, showing that the system has actually a weak non-Arrhenius behavior.

3.3 Free mode data

In the previous sections the jamming transition was probed by measuring the mechanical response function. In suitable conditions, one can observe a relaxation peak that is due to the onset of jamming. A characteristic time can be therefore naturally associated to this relaxation, as shown in the previous section.

Forced mode measurements, however, are not the only way that can be used to investigate granular materials with a torsion oscillator. A different technique, that does not require the application of an external torque, had already been discussed in the past [204]. The fundamental idea behind this method says that one can observe the power spectral density

of the probe and define from there a characteristic time scale for the system. Furthermore, the shape of the power spectral densities suggests that the system has a brownian nature: the power spectral density spectra, in the low frequency range, assumes a $1/f$ behavior, indicative of the presence of diffusion phenomena. We anticipate that an independent argument, demonstrating that a probe immersed in a granular system actually has a brownian-like behavior will be given in Ch. 4.

Another interesting feature that had already been observed with this approach is a dependence of the power spectra on the frequency f_s of the vibrations imposed on the sample. It had been observed [204] that, if a granular sample is vibrated with a sinusoidal waveform, the amount of spectral power is inversely proportional to the pulsation $\omega_s = 2\pi f_s$.

In the following, we will present a systematic study of granular samples vibrated with both broadband (white noise) and narrowband (sinusoidal) waveforms. The first part of this section will discuss more into detail the experimental method, the meaning of the data and the principal differences with respect to the forced mode approach. Afterwards we discuss the dependence of the power spectral data, on the parameters Γ and ω_s, and present a possible interpretation of the resulting data based on an analogy with thermal system. Then we show how the characteristic time scale of the system can be compared between the two methods. Due to different geometries of the probes, and to the differences between sinusoidal and white noise vibrations, this requires to review the some of the effects described in Sec. C. The collection of data sets suggest a scaling law that defines an unique control parameter responsible for the evolution of the granular material in the jamming region [205]. We use this information to develop a model that combines rheologic effects with a simple extreme event statistic approach. This model justifies the definition of the control parameter. Finally, we test the model by observing its dependence on parameters that depend on the nature of the granular medium under observation, considering for comparison spheres with a much rougher surface.

3.3.1   Method

The key idea of free mode measurements is the following. In a vibrated granular system, the grains move with respect to each other. This can be seen as if the system moves from a specific "configuration" to the next. As the strength of the perturbation is decreased, the motility of the grains decreases, until the system "freezes" and becomes trapped in a static configuration.

The dynamic of the system, as it moves from one configuration to the next, can be studied by observing the time series of angular deflection of an immersed probe [204]. The oscillator can move a step back or forward every time the grains change configuration, and, in proper experimental conditions, the corresponding angular time series can be used to measure the configurational noise of the system, by computing the Fourier transforms of the time series of the position data.

In particular, comparison between continuous vibrations and tapping mode measurements demonstrates that the resulting Fourier spectra can be decomposed into a low-frequency configurational component, and into a high-frequency viscous-like one.

The measurements of the configurational noise can finally be related to an intrinsic con-

figurational (or structural) relaxation time, provided the assumption of the validity of the Wiener-Khintchine theorem (as discussed in [204, 206]). It is this relaxation time that will be compared with the characteristic relaxation time observed in free mode measurements.

The measurements consist in recording the time series of the angular position of the probe. A spectrum analyzer is used to compute the Fourier transformation of the signal, obtaining the corresponding power spectral densities. The spectra are averaged over a large number of time series, to reduce the noise. The typical duration of one series varies between a few seconds to a few hundreds, depending on the low frequency cutoff. The averaged power spectral densities are recorded for different values of Γ, and other experimental parameters.

The dynamics of the oscillator, and the probe-granular interactions are very different from those of forced mode measurements of Sec. 3.1. For this reason, it is important to underline that the appropriate experimental conditions, required to obtain good quality data, are different. In this case, the probe needs to sense the rearrangements of the granular medium without perturbing it. It has been shown [204] that in good experimental conditions, a brownian-like behavior can be observed when the low frequency region of the power spectral density has a $1/f$ behavior.

The main possible source of error in these measurements is represented by the relative importance of the moment of inertia of the oscillator with respect to the total contact surface with the granular medium and its overall capacity to dissipate the motion of the probe. Depending on the exact geometry, and due to the difference in size, the moment of inertia of the probe is much larger than the one (relative to the rotation axis) of a single grain situated in proximity of the probe surface. If, at any time, the torsional kinetic energy acquired by the oscillator becomes large enough to overcome the resisting force due to the chains of forces in the granular medium, the oscillator will continue moving after the rearranging event that originally put into motion. This will lead to successive failure of the resisting grains arrangement, and the oscillator comes eventually to a complete halt only well after the end of the event. In the forced mode section this was interpreted as the oscillator producing a sort of local "inertial heating effect". This unwanted effect was observed in the spectra (not shown here); it produces the appearance of a viscous-like damping peak at about the natural frequency of the oscillator f_p. This situation can be at least partially avoided by increasing the global force opposing the motion of the oscillator. In turn, this can be obtained by an increase of the immersion depth, and by increasing the contact surface between the probe and the granular medium. Furthermore, it is also useful to reduce the amount of movement that the probe has in the granular system, by using probes shaped as thin cylinders. While in principle this reduces the sensitivity of the measurement, it also strongly reduces the relative importance of the peak at the torsion oscillator eigenfrequency, with respect to the rest of the spectrum. For these reasons the experiment in free mode are generally performed using the cylindrical probe g, installed on the same torsion oscillator used for forced mode measurements (see Ch. 2, Fig. 2.4). Probe g has an optimal shape with respect to all the needed requirements, and allows immersion depths L large enough to avoid the inertial effects. Probe f was also used (historically, before probe g), in order to verify that a direct comparison can be made with forced mode data, as will be discussed later.

The minimal required immersion depth L_{min} is found by driving the system to the desired

vibration intensity, and by measuring the spectral power density of the probe position around its resonant frequency f_p. For low immersion, the system is still sensitive to inertial effects, and the resonance can be clearly distinguished. As the immersion depth is increased, the peak becomes smaller and smaller with respect to the background. The limit immersion is found empirically when the peak is low enough not to perturb the overall $1/f$ behavior of the power spectral density at low frequencies. For the experimental setup considered in this work, the minimum immersion depth is found to be approximately 40 mm. In general, the data presented here are obtained with an immersion depth $L = 65$ mm.

Once the experimental conditions are properly set, the power spectral density curves can be measured. The configurational noise is defined as the spectral power density at a chosen fixed frequency $f = 1$ Hz[1], and has the units of a time (rad^2/Hz). In the following we will often refer to the configurational noise as noise level, characteristic time, or generally "power spectral density", depending on the context. Noise level stresses the role of this parameter as an indicator of brownian motion; the characteristic time is more useful (and more dimensionally correct) when comparing with forced mode data, or when interpreting models; finally, the power spectral densities (at 1 Hz) are the values that are measured with the instruments, and shown on most of the graphs. It should be also noted that elsewhere [204, 197] this observable has been sometimes indicated by $|\theta(1)|$).

Note that the absolute value of the configurational noise (and the characteristic time) is determined up to an arbitrary multiplicative factor. This is because the choice of the frequency, at which the characteristic time is calculated, is chosen arbitrarily (1 Hz). This means that comparison of these time scales with those obtained with forced mode measurements, are offset by a multiplicative scale factor. For this reason, and since we are not interested in the absolute value, the configurational noise data will be shown in arbitrary units ([a.u.]).

Finally, there are a few differences in the techniques, which influence the reliability of the data, that should be mentioned. Forced mode measurements measure the response function of the system to an external perturbation. The imposed external constraint can be tuned with respect to the experimental conditions, and if the system is maintained in the linear response regime, the results are always meaningful. This is not a problem at high values of vibrations, when the probe is subject to strong accelerations. If the noise level grows larger, the applied torque can be increased. On the other hand, the free mode approach is much more sensitive to the regime change around $\Gamma = 1$, because above that level inertial effect start to play an important role. This fact will be thoroughly discussed in Ch. 4.

As the intensity of vibrations is decreases, the mobility of the grains decreases proportionally. In this situation, rearrangement still occur in the bulk, but the evolution slows down, and the system behaves more and more like an amorphous solid. At this point, the presence of an external probe that induces a forced constraint on the system can become problematic. In fact, the forced torsion probe induces a local rearrangement of the granular structure, as it breaks its way in the granular sample. The strength of the imposed torque can be tuned down, but when the characteristic time of the granular medium becomes very short, the local rearrangements that last longer than the duration of a forced oscillation cycle could influence

---

[1]To reduce the noise, the precise value of the noise is obtained by computing the average of the power spectral density in the frequency window 0.95–1.05 Hz.

the perceived dynamic of the sample under investigation. On the other hand, the amount of torque cannot be reduced below a certain value, because the resulting motion (that takes place in a medium growing stiffer as Γ is reduced) must be large enough to be measured. This is limited by the sensitivity of the installation.

In the case of free mode measurements the situation is similar, but for different reasons. In the jamming regime, the probe becomes jammed enough so that inertial effects are not important any more, but there is a significant number of rearranging events. When the vibration levels become very small, on the other hand, the number of rearrangements drops. Furthermore, the duration of the time series is limited, due to technical reasons in the spectrum analyzer, by an upper maximum of a few minutes. This fact imposes a cutoff on all the rearrangements that happen in time scales slower than this limit. Experimental data indicate that the overall behavior of the spectra is $1/f$ over a rather wide range of frequencies (approximately 0.05 to 10 Hz, in fact larger than what was shown in [204]) and vibration intensities Γ.

For these reasons, both approaches should be considered adequate in the regions $0.1 < \Gamma < 1$. In these conditions, a good agreement is found. It also appears that, with our installation, forced mode data are slightly more accurate at extremely weak vibrations.

3.3.2 Results

We consider free mode measurements, obtained with vibration amplitude (Γ) sweeps. Other parameters considered in this work are the type of signal used to drive the vertical acceleration (narrow band sinusoid, or broadband white noise), and the geometry of the probe.

Historically, the first measurements were performed with probe f, to complement the data obtained with the forced mode method. However, it is simpler to present first the data obtained with sinusoidal vibration and using the cylindrical probe g. The measurements are performed in optimal experimental conditions: the sensing probe is immersed of a length $L = 65$ mm in a granular medium of average height $h = 90$ mm. Fig. 3.9 shows a few spectra obtained with a vibration frequency $f_s = 200$ Hz, for a few values of vibration intensities. The curve for $\Gamma = 1.29$ (light gray), shows no sign of the oscillator resonance peak around 10 Hz, indicating that in these conditions there are no influences from inertial effects. As the intensity of shaking is decreased, so is the relative position of the spectra. The curves maintain an approximate $1/f$ behavior until the sensitivity limit is reached, at least in the low frequencies region of the spectrum. Eventually, the change in slope, and the appearance of resonance peaks in the low Γ curves (dark gray and black dots) indicate that the limit of sensitivity of the measurement has been reached.

The characteristic times corresponding to these data are shown in Fig. 3.10. The different curves correspond to a granular medium vibrated at a different fixed frequencies from 70 to 650 Hz, indicated with a color progression red, blue, green, brown.

Each data set suggest that the dynamic state of the system can be divided into three distinct domains. For weak vibrations, there is an intermediate region where the configurational noise decreases rapidly as Γ is decreased (ideally vanishing before Γ goes to zero). This is the region of interest. On the rightmost part of the graph, as the vibration intensities are increased and the limit $\Gamma = 1$ is reached, a discontinuity can be seen in the curves, as the system changes
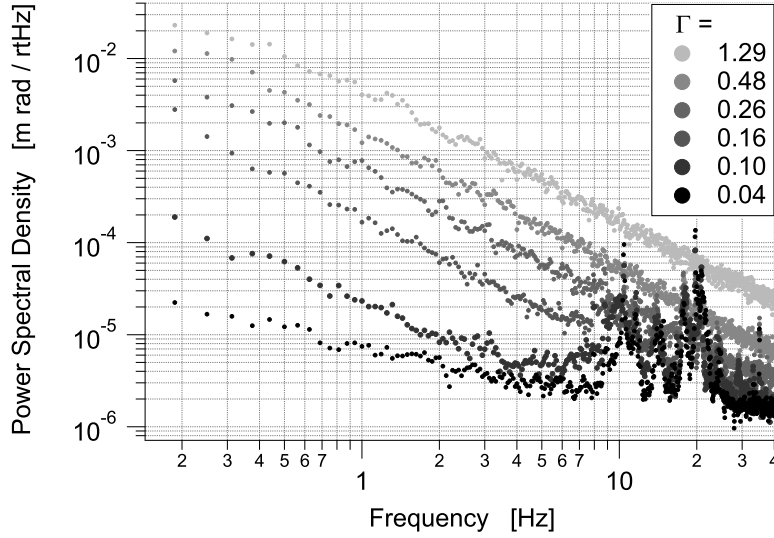
Figure 3.9: Power spectral densities, as a function of frequency, for different vibration intensities. The data were obtained with the cylindrical probe **g**, positioned at an approximate depth of 65 mm in a granular medium composed of smooth glass spheres. The system is vibrated with a sinusoidal signal with $f_s = 200$ Hz.

regime. This region will be discussed more in detail in the last sections. Finally, for very weak vibrations, and depending on the excitation frequency, the sensitivity limit of the apparatus is reached and the curve reaches the constant value of approximately 7×10^{-6} [a.u.].

From the experimental data corresponding to the region of interest, it is clear that: (*i*) the relaxation times are not related to Γ by an Arrhenius-like behavior, and (*ii*) the vibration pulsation ω_s is strongly influencing the power spectral density at each fixed average intensity Γ.

The data were fitted with the VFT expression $Y = A \exp\left(\frac{B}{\Gamma^p - \Gamma_0^p}\right)$. This expression allows adequate fitting for a large number of experimental conditions. In this case, the parameters $A = 0.1$, $\Gamma_0 = 0.001$ and $p = 0.5$ are kept constant. The curve fits indicate that the dependence on ω_s is contained in the factor B. For the four fits, we obtain $B = 0.70$; 2.00; 3.85; 4.85. The ratio of these values for two curves, for example with the first one, that fits the curve for $f_s = 100$ Hz, are: 1.00; 2.85; 5.50; 6.50. These correspond to a good extent to the ratios of the relative vibration frequencies, indicating that $B \propto \omega_s$.

As had already been observed, these data suggest that in the jamming region, a given granular system can be characterized by a relaxation time which is function of both Γ and ω_s. The fitting suggest a scaling as a function of a unified control parameter $a_s = \sqrt{\Gamma}/\omega_s$. As a function of this new control parameter, the relaxation time curve collapse on a single master curve. This is clearly shown in the Arrhenius plot ($\log \text{PSD}$ vs $\omega_s/\sqrt{\Gamma}$) of Fig. 3.11. Despite some little discrepancies, especially for the curves obtained with very high frequencies of vibration, the overall behavior is consistent.

These results can now be compared to the relaxation times obtained with forced mode mea-
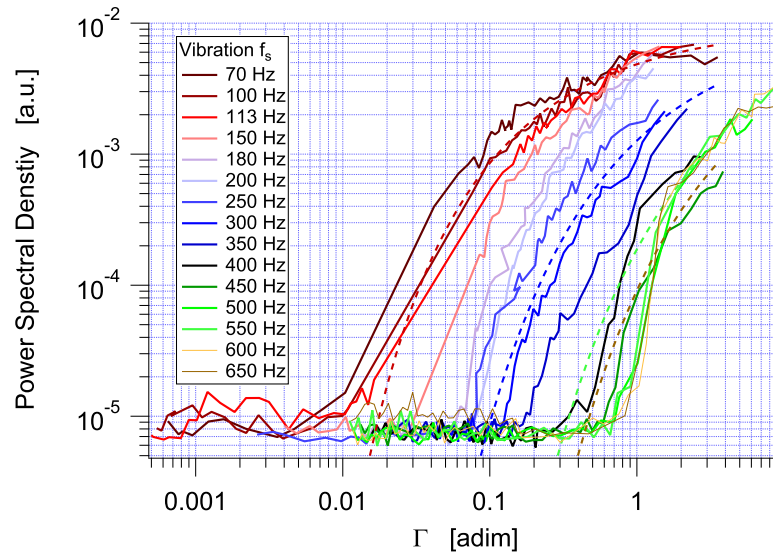
Figure 3.10: Configurational noise values for different vibration intensities Γ. The different solid curves indicate the different vibration frequencies f_s, from 70 to 650 Hz. Increasing frequencies are indicated with the color progression red, blue, green, brown. Dashed lines correspond to curve fitting of the VFT function $Y = A\exp\left(\frac{B}{\Gamma^p - \Gamma_0^p}\right)$.
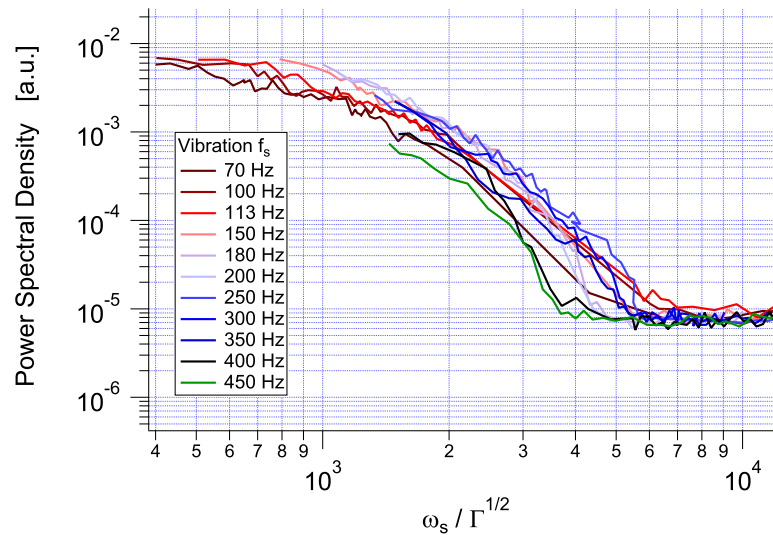
Figure 3.11: Arrhenius plot of the master curve obtained by plotting the data of Fig. 3.10 as a function of the inverse of the control parameter $a_s = \sqrt{\Gamma}/\omega_s$.
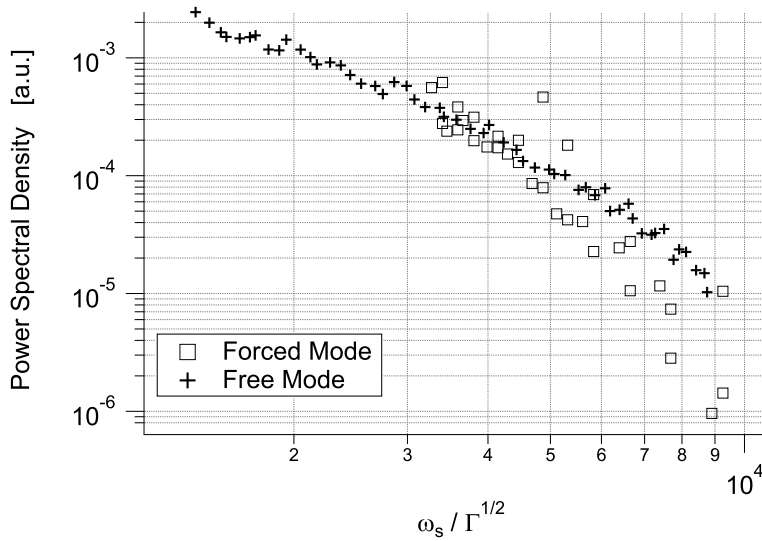
Figure 3.12: Arrhenius plot showing the comparison of characteristic times obtained with forced and free mode measurements. The relaxation times from forced mode measurements correspond to those of Fig 3.7. The free mode data were obtained with the same experimental conditions of forced mode measurements.

surements, but this reveals some complications. As it is discussed in detail in Appendix C, the internal dynamics of vibrated granular material strongly influence the vibrations that propagate through it. For this reason, the geometry of the probe interacts in complex way with the nature of the vibration that is fed to the vibration motor. Since the forced mode measurements required the use of white noise and probe **f**, the simplest way to perform a comparison is to perform a free mode measurement with the same probe and vibration used for forced mode data.

This is done in Fig. 3.12. In this case, all experimental conditions are the same as during forced mode measurements, and therefore they result in suboptimal condition for free mode data acquisition. For these data, the pulsation ω_s was calculated as the weighed average of the power spectrum measured with the accelerometer. After applying a proper scaling to the relaxation times of forced mode measurements, the agreement between the two curves is remarkable. This is a clear indication that both techniques can be used to measure the same intrinsic relaxation time that characterizes the granular sample.

One could also consider the effect of white noise vibrations on a probe of a cylindrical geometry. In this case, it appears that the correct pulsation needed to correct the data is not the weighted average frequency of the vibration spectrum, but the frequency that correspond to its maximum value. This correspond to a frequency of approximately 120–140 Hz, as indicated in the Appendix. A comparison between the curves resulting from broad and narrow band vibrations is shown in Fig. 3.13.

The superposition of the collection of all the data series, once the correct effective ω_s has been considered, allows to extend the range where the characteristic time can be measured reliably. The complete collection of the data curves, cleaned of the unnecessary noise, is shown in
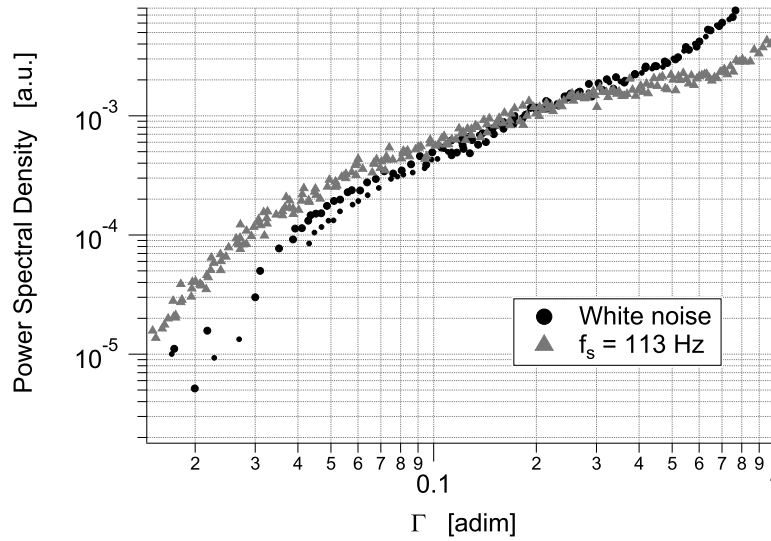
Figure 3.13: Comparison between configurational noise data obtained using a cylindrical probe and two different vibrations: the broad band white noise and the narrow band sinusoidal vibration.

Fig. 3.14.

The superposition of the curves provides further evidence that the control parameter $a_s = \sqrt{\Gamma}/\omega_s$ can superpose all the data sets. Furthermore, thanks to the larger accessible experimental window, it is now evident that the measured relaxation time does not follow an Arrhenius behavior and is instead well described by a VFT behavior, in a very broad spectrum of possible conditions. A model suggesting why the relevant control parameter is a_s and why the relaxation time of the system is given by a VFT of it will be the subject of the following section.

3.4 Modeling

The comparison of the data coming from forced mode and free mode experiments indicates that: (**a**) a weakly vibrated granular system is described by a characteristic time that is only function of a control parameter of the form $\sqrt{\Gamma}/\omega_s$; (**b**) the functional form relating the characteristic time to the control parameter is identical to a thermally activated VFT expression.

In general, the experiments at low Γ (those discussed here and in the literature [204, 197, 205]), essentially sense modifications in the configuration of the grain assembly, while they are much less sensitive to temporary oscillations around equilibrium position.

This reordering corresponds to a change in the fabric of force distribution in the bulk. In fact, in presence of an external force, the grains arrange in such a way that a fraction of them support most of the load by forming a ramified network of force chains [54, 207]. The average orientation opposes the direction of the applied force. For example, when the granular system is only subject to gravity, the network is mainly ramified vertically.

Under weak external perturbation, the grains move relative to each other by small elastic
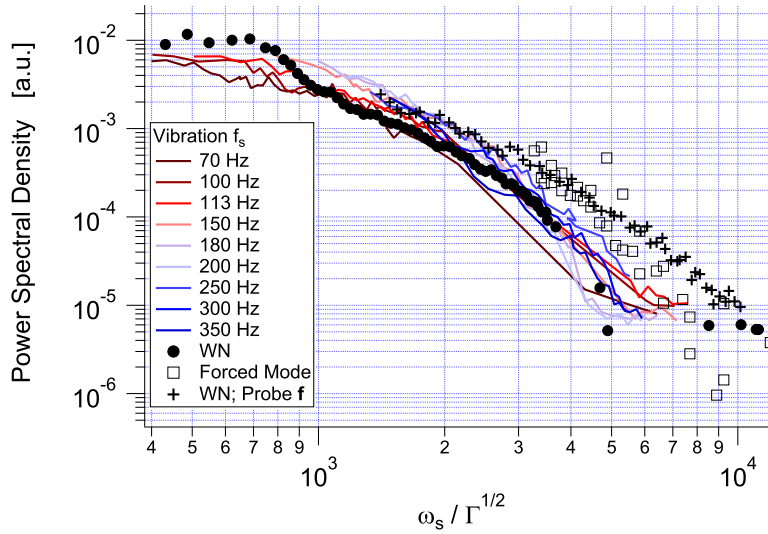
Figure 3.14: Arrhenius plot showing the configurational noise as a function of the control parameter a_s. As discussed in the text, a master curve is obtained. All the data coming from the data sets discussed in this section, together with data obtained from forced mode measurements, align on the same curve.

oscillations and small scale sliding events. The idea is that a macroscopically observable effect happens only when a *critical occurrence* (to be discussed below) causes a redistribution of the applied load over the supporting chains of force.

In order to gain a statistical description of this process at the scale of the whole granular sample, we proceed in the following way. First, the grain-grain interaction is discussed, and a few general assumptions are made; afterwards, the analysis is extended to a larger scale: the key ingredient is to relate the macroscopic energy dissipation in the granular system to the local interaction between the grains. Finally, the evolution of the global granular structure is modeled with extremal-event-driven behavior, that will emerge as the real effect driving the dynamics of the "jammed" regimes.

3.4.1 The grain-grain interactions

At the grain size scale there are two "microscopic" processes that have to be taken into account: (**i**) the elastic oscillations of the grains in contact; (**ii**) the elementary sliding events, occurring when the friction force between two grains is overcome.

Elastic oscillations

Consider two grains, assumed spherical, interacting elastically at their contact point. Under the effect of a force along the common axis, they deform until the elastic force balances the load. This so-called Hertzian contact elasticity is non-linear, and the relationship between the deformation h and the force F is given by $F = \kappa h^{3/2}$, where κ is an effective "elastic" constant [97]. Fig. 3.15 **a** shows a sketch of the deformations of the (For two spheres of radius
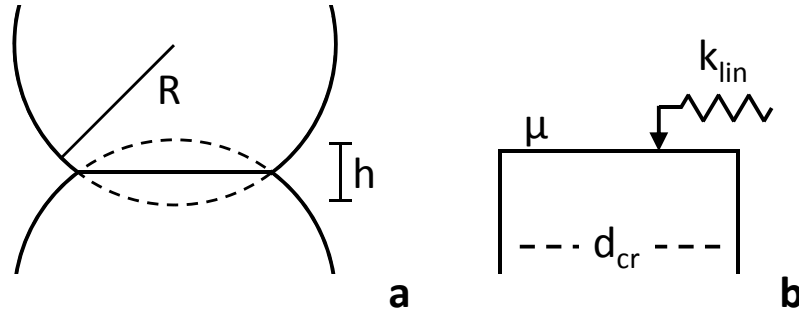
Figure 3.15: Sketch representing two features of the model. (**a**) Two spheres (representing the granular particles) deform when pressed against each other. The amount of deformation h depends on the sphere radius R, on the force acting on them and on the mechanical properties of the material, as discussed in the text. (**b**) Simplified model of the resulting interaction. The flat surface represents the relative displacement below which one spheres can be considered in a stable position, kept in place by dry friction and pushed around by elastic effects and external forces. If the displacement becomes greater than this critical distance d_{cr}, the structure has to rearrange.

R, $\kappa = \frac{2}{3} E (1 - \nu)^{-1} \sqrt{R/2}$, with E the Young's modulus and ν the Poisson's ratio. Also the radius, r, of the circular contact area is given by $F = (\kappa r)^3 (2/R)^{3/2}$.)

In a large container, granular pressure can be approximately treated as hydrostatic, and at a fixed depth z, the load is given by $F_g = img$, where $i = z/2R$ represents the number of layers located above. Let the equilibrium position under this load be $h_0 = (F_g/\kappa)^{2/3}$. The small free oscillations of the two spheres in elastic contact are described by the equation of motion $m\ddot{x} = -\kappa \left(h_0 + x \right)^{3/2} + F_g$, with $x \ll h_0$. By series expansion, and considering only the first order terms, the linearized version is obtained: $m\ddot{x} \approx -\kappa \frac{3}{2} \sqrt{h_0} x$. Note that the absolute orientation of the two spheres is not necessarily vertical, due to the redistribution of the forces in the bulk. This equation suggests that the granular medium is characterized by an intrinsic frequency, given by the natural pulsation of the harmonic oscillator:

$$\omega_0^2 = \frac{k_{\text{lin}}}{m} = \frac{3}{2} \frac{\kappa}{m} \sqrt{h_o} \tag{3.7}$$

where $k_{\text{lin}} = \frac{3}{2} \kappa \sqrt{h_o}$ is the linearized spring constant.

It should be noted that, in general, the interaction of the two spheres is not completely elastic. Energy is continuously absorbed via microscopic processes arising close to the interface between grains. In this work, however, these effects can be neglected. As discussed below, the dissipation arising from sliding friction is much larger, and completely dominates energy dissipation in the interior of the particles.

At this point, it is also useful to check some numerical value of the parameters discussed so far. In the case of the glass beads used in this work, the following properties are observed. The particle radius is $R = 0.55$ mm, and the mass is $m = 1.86 \cdot 10^{-3}$ kg. Assuming a number of layers i approximately varying from 10 (top) to 60 (bottom), and $\kappa = 6.9 \cdot 10^8$ N m$^{-3/2}$, the

equilibrium values for the deformation and the intrinsic frequency are $h_0 \approx 0.4 - 1.4\,\mu$m and $f_0 = \omega_o/2\pi \approx 3 - 4$kHz respectively. In the real case, due to anisotropy, h_0 and ω_0 should depend on the depth, and these estimations are valid in a suitably limited volume of the medium.

Elementary sliding event

In general, the force acting between a pair of grains is not directed along the common axis that joins the center of the two grains. In this case, the two grain will start sliding relatively to each other if and when static friction is overcome. The important features that characterize such sliding events can be obtained considering that, at low Γ, displacements are small, and the grains are linked by multiple linear elastic springs. A sketch of this behavior is given in Fig. 3.15 **b**.

The duration of each elementary sliding event can be estimated, and approximately lasts a fixed time interval $\tau_0 \approx \pi\omega_0^{-1}$. This is a reasonable hypothesis for the following reason. Let us consider two grains, subject to a shear stress, and that do not slide because they are kept in place by a static friction threshold F_s. The threshold is given by $F_s = \mu_s F_g = \mu_s img$, where μ_s is a coefficient of static dry friction (grain-grain friction coefficient), and acts on the plane of contact. In this case, all the small oscillations of the two particles that arise along the perpendicular will facilitate the onset of sliding, because they reduce the load F_g. On the other hand, the reversal in direction of the same force in the subsequent semi-period of the oscillation will determine the end of the sliding event (because it adds up to F_g). In other words, the position of a grain during the sliding event can be described with a semi-period of the harmonic oscillation, of the form $x(t) \sim x_a \cos(\omega_0 t)$, $0 < t < \pi/\omega_0$, where x_a represents the displacement amplitude.

We now consider the dissipation due to friction. All sliding events arise randomly in the granular medium, and dissipate the incoming energy flux differently at each event. However, if $x(t)$ indicates the displacement of one grain, the elastic energy involved in the process should be given by $x_a^2 k_{\text{lin}}$. This energy is approximately the energy that is dissipated during the sliding event. Therefore, the average absorption power due to the sliding, defined as the elastic energy over the semi-period, can be written as $P_a = \omega_0 x_a^2 k_{\text{lin}} \pi/2$.

The definition of P_a is very useful, because it provides the link between the "microscopic" sliding process and the external driving. In fact, the system is stationary, and all the energy inserted into it is dissipated by the interaction of the grains.

The container of the granular medium is modeled as a sliding block subject to an apparent friction force. The position of the container, $z(t) = a_s \sin(\omega_s t)$, is dictated by the driving motor. The apparent (and dynamic) sliding friction force is due to the granular interactions, and is indicated by F_{tot}. The corresponding dissipated power (Φ_{tot}) is therefore given by $\Phi_{\text{tot}} = \pi F_{\text{tot}} a_s \omega_s$, where $a_s \omega_s$ is the maximum velocity of the block during the sinusoidal cycle. On the average we assume that the total power can be evenly distributed to the granular interactions: $P_a = \Phi_{\text{tot}}/N$, and we ascribe the power dissipation to the effect of the friction force at the contact interfaces. In other words, on average each contact dissipates a power P_a via a friction force F_d such that $P_a = \pi F_d a_s \omega_s$. These assumptions can be substituted in the

definition of P_a to obtain:

$$x_a = \left(\frac{2 F_d a_s \omega_s}{k_{\text{lin}} \omega_0} \right)^{1/2} \tag{3.8}$$

Eq. 3.8 links the average amplitude of an elementary sliding event to the experimental driving parameters.

3.4.2   Statistics of sliding events

Dissipative random walk

Still remaining at a "microscopic" (grain-scale) level, it is now necessary to consider the dynamics of the *sliding unit* (Fig. 3.15 **b**) of each contact point submitted to a random power source with average value P_a. As a consequence, the unit undergoes a (1D) random walk, at a regular time interval τ_0; each step is an elementary sliding event of average length x_a, to the right or to the left. For example, one could consider a probability density distribution $w(x_a)$ for the step length. This distribution is determined by the way the external power reaches the sliding unit, and a simple assumption is that it is composed of two symmetric peaks centered about $+x_a$ and $-x_a$; σ_{x_a} indicates the standard deviation of $w(x_a)$.

During subsequent cycles of the sinusoidal vibration, i.e., for a number of steps $n_s = \omega_o / \omega_s$, the sliding unit undergoes a random walk. For large n_s, according to the central limit theorem, the probability density distribution for the displacement d (the distance from the initial position) of the sliding unit is Gaussian, with zero mean and standard deviation $\sigma_d = \sigma_{x_a} \sqrt{n_s}$. This means that $w(d) = (\sigma_d \sqrt{2\pi})^{-1} \exp\left[-d^2 / 2\sigma_d^2 \right]$. For example, if we consider a fixed value for the step length (all steps of the random walk are exactly either $-x_a$ or $+x_a$), then the distribution $w(x_a)$ can be seen as composed of two "Dirac" peaks. In this case $\sigma_{x_a} = x_a$, and $\sigma_d = x_a \sqrt{n_s}$. However, we assume that there must be a minimum value P^* for which the input energy flux is completely dissipated by anelastic and plastic effects inside the grains. In other words, when this happens, no rearrangement takes place. This defines a minimum step length $x^* < x_a$, and the distribution $w(x_a)$ becomes truncated between $+x^*$ and $-x^*$. In this case, $\sigma_{x_a} \approx x_a - x^*$, and in turn $\sigma_d \approx (x_a - x^*) \sqrt{n_s}$.

Occurrence of a critical event

Each of the N sliding units of the granular system is driven in this dissipative random walk with the same Gaussian distribution, but unless a "critical event" occurs, we expect that there is no discernible macroscopic effect. A *critical sliding event* is defined as one in which the displacement d of a sliding unit reaches a critical distance d_{cr} and "falls off", as evocatively shown in Fig. 3.15. The contact between the two grains is lost, and the underlying network of force-chains reorganizes.

Each critical event happens with a certain probability, that is the probability that the displacement d of *one* of the N sliding units reaches the critical distance d_{cr}. This "first passage probability" can be estimated considering our large ensemble of N sliding units, driven by the same external power source, and the displacements $D_1, D_2, \ldots, D_N$ of each unit, considered

as independent random variables. We define the normalized quantities $Y_i = D_i/\sigma_d$, and indicate with $Z_N = \max\{Y_1, Y_2, ..., Y_N\}$, the largest normalized displacement. The problem is now to calculate the probability that the there is at least one random displacement (the maximum) larger than d_{cr}. This probability is called $S_N(y_{cr})$, where $S_N(y_{cr}) \equiv \Pr\{Z_N > y_{cr}\}$, with $y_{cr} = d_{cr}/\sigma_d$. This is a classical problem of statistics of extremes (for example, see [208]). To solve it, one has to calculate the cumulative probability distribution for all the walkers to *not* trespass the maximum (that is, $\Pr\{Z_N \leq y_{cr}\} = 1 - S_N(y_{cr})$). Formally, this is solved by taking the power of the corresponding cumulative distribution F:

$$\Pr(Z_N \leq y_{cr}) = \Pr(Y_1 \leq z) \times \cdots \times \Pr(Y_N \leq z) = \left(F(z)\right)^n \tag{3.9}$$

For example, in the case of simple Gaussian distribution, the corresponding cumulative distribution is given by the error function and the problem is solved exactly. Even if the distribution F is unknown, the Fisher-Tippett-Gnedenko theorem [209] provides an asymptotic result for an arbitrary starting distribution. If there exist sequences of constants $a_n > 0$ and b_n, H is a non-degenerate distribution, and $\Pr\{Z_N - b_n)/a_n \leq y_{cr}\} \rightarrow H(z)$ as $n \rightarrow \infty$, then H belongs to one of 3 possible distributions: the Gumbel distribution, the Fréchet distribution, or the Weibull distribution.

In this case, for a Gaussian parent probability density distribution, convergence can be demonstrated [208, 210] to a Gumbel distribution, that has the form:

$$H(x) = \exp\left\{-\exp\left[-\frac{x-b}{a}\right]\right\} \tag{3.10}$$

The limit distribution is calculated using the two normalizing sequences a_n and b_n, that depend on the number of walkers n. The sequences required for this case have the form: $b_n = 1/\sqrt{2\ln n}$ and $a_n = 1/b_n - \frac{1}{2}b_n(\ln\ln n + \ln 4\pi)$. Since the number of walkers in the system is given by the (extremely large) number of contacts N in the granular material, the large n limit can be computed by letting $n \rightarrow N$. In the limit: $\lim_{n \rightarrow N} H_n(a_n + b_n x) = \exp[-\exp(-x)]$. Therefore, the probability is given by $S(y_{cr}) = 1 - H = 1 - \exp[-\exp[-(y_{cr} - a_N)/b_N]]$. In the current case one can assume that $(y_{cr} - a_N)/b_N \gg 1$, leading to the approximation $1 - H(x) \approx \exp(-x)$. Therefore the expression for the probability can be simplified to obtain $S(x) \approx \exp(-x)$. As a consequence, the probability for a critical event is given by

$$S(d_{cr}/\sigma_d) = c_N \exp\left[-\frac{d_{cr}\sqrt{2\ln N}}{(x_a - x^*)\sqrt{n_s}}\right] \tag{3.11}$$

where $c_N = N^2/\sqrt{4\pi\ln N}$.

This formula describes the collective effect of all the microscopic random walks for one cycle of the external sinusoidal vibration. The result can be interpreted as a characteristic relaxation time, $\tau_x \equiv (f_s C_N)^{-1} S(d_{cr}/\sigma_d)$. This time is the average time separating critical (configuration reorganizing) events in the force chain fabric. The random occurrence of a "fall off" therefore plays the role of the activation process that will ultimately govern the overall macroscopic

dynamics, and Eq. 3.11 is the final result.

3.4.3 Consequences: control parameter and VFT behavior

From Eq. 3.11 it is straightforward to derive an expression that is more directly comparable to the experiments. The probability can be rewritten as a characteristic time; then, both the numerator and the denominator of the argument of the exponential are multiplied by $\sqrt{k_{\text{lin}}}/g\sqrt{2\mu_d i m}$. The result is:

$$\tau_x = (f_s C_N)^{-1} \exp\left[\frac{d_{cr}\sqrt{e}\omega_o/g\sqrt{2\mu_d i}}{\frac{\Gamma^{1/2}}{\omega_s} - \frac{x^*\omega_o\sqrt{n_s}}{g\sqrt{2\mu_d i}}}\right] = (f_s C_N)^{-1} \exp\left[\frac{\tau_{cr}}{\bar{t} - \tau^*}\right] \tag{3.12}$$

where, in this expression, all the coefficients can be calculated from the model with the only exception of $d_c r$ and x^{*2}.

The expression 3.12 can immediately reduced to another even expression, allowing a simpler comparison with experimental data, by rewriting the terms in the exponential:

$$\tau_x = (f_s C_N)^{-1} \exp\left[\frac{\tau_{cr}}{\frac{\Gamma^{1/2}}{\omega_s} - \frac{\Gamma^{*1/2}}{\omega_s}}\right] = (f_s C_N)^{-1} \exp\left[\frac{\tau_{cr}\omega_s}{\Gamma^{1/2} - \Gamma^{*1/2}}\right] \tag{3.13}$$

Eq 3.13 is very important because it covers all the observed phenomenological relations [205, 197]. This approach can therefore demonstrate that the behavior of vibrated granular materials has to be described as an activated-like phenomenon, in which its intrinsic time scale shows a simple Vögel-Fulcher-Tammann behavior as a function of a control parameter $\sqrt{\Gamma}/\omega_s$.

More specifically, we observe that this behavior (or the corresponding Arrhenius expression, if the divergence due to Γ^* is neglected) results from the fact that only extreme events emerge macroscopically, even-tough a very large number of under-critical sliding and elastic events arise at the "microscopic" level. It is this extremal nature of the relevant events that makes driven granular matter and thermal systems so remarkably similar.

This finding is conceptually different from what is observed for strongly fluidized systems. In these conditions, the system shows a fluctuation-dissipation behavior [187], from which an effective temperature parameter can be defined. It had been shown that this effective temperature is proportional to Γ^2. From the data in [187, 197], it appears that this fluctuation-dissipation relation breaks down below $\Gamma = 3$. On the other hand, for weakly vibrated system, the control parameter $a_s = \sqrt{\Gamma}/\omega_s$ represents a characteristic time scale required to observe a macroscopic rearrangement. Furthermore, the athermal nature of this parameter can be understood if we consider the following observation. In [204], free mode measurements were performed both using continuous vibrations, and with discontinuous vertical shocks, or "taps". Each of these taps consisted in a single sinusoidal cycle of the continuous vibration (with identical frequency and amplitude). The corresponding power spectral density data were

---

[2]It is actually possible to estimate the value of x^*. This value represents, at least to a first approximation, the elastic deformation boundary given by $x^* k_{\text{lin}} = F_s$.
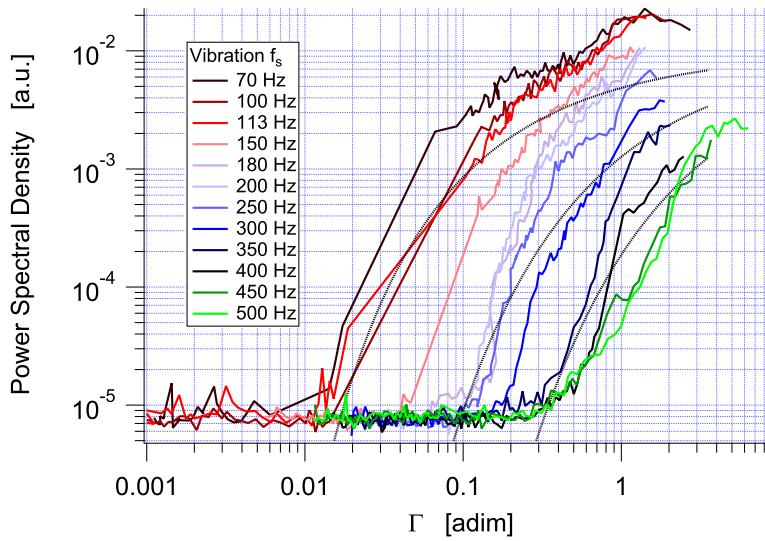
Figure 3.16: Configurational noise levels for a granular system composed of acid etched glass beads, driven with sinusoidal vibrations at different frequencies f_s and for different values of Γ.

identical, the only exception being that tapped mode data required longer time to achieve the same statistics. This fact shows that weak vibrations do not sustain an ergodic system, but instead allow for a step-wise chance of rearranging the bulk structure of the granular system.

3.4.4 Surface state

The model discussed in the previous section allows a comparison with experimental data. In particular, the surface state of the granular particles should influence the coefficients of frictions that appear in the model.

This is indeed the case, and a qualitative yet remarkable dependence can be observed by comparing a standard granular medium with one composed of spheres that have been strongly acid etched. To this end, identical 1 mm glass beads were etched in a 8 % HF solution for approximately 10 minutes, as it was done in [197]. A complete set of measurement was performed with the same experimental conditions of the data sets shown in Fig. 3.10. This is shown in Fig. 3.16. The data indicate that the altered state of the surface leads to different characteristic times. The curves appear to decrease more sharply than the ones relative to smooth spheres, shown in Fig . 3.10. This can be seen by observing the black dashed lines, which correspond to the VFT data corresponding to smooth spheres.

It is possible to compare two data sets, corresponding to the same experimental conditions, for both smooth and rough spheres. This allows a quantitative comparison of the coefficients of friction that appear in the model, as of Eq. 3.12. This is done in Fig. 3.17. The graph shows two configurational noise series for both smooth (circular markers) and rough (square markers) glass spheres. The vibration frequency is chosen here to be $f_s = 200$ Hz, so that most of the data points falls in the region of optimal experimental condition.
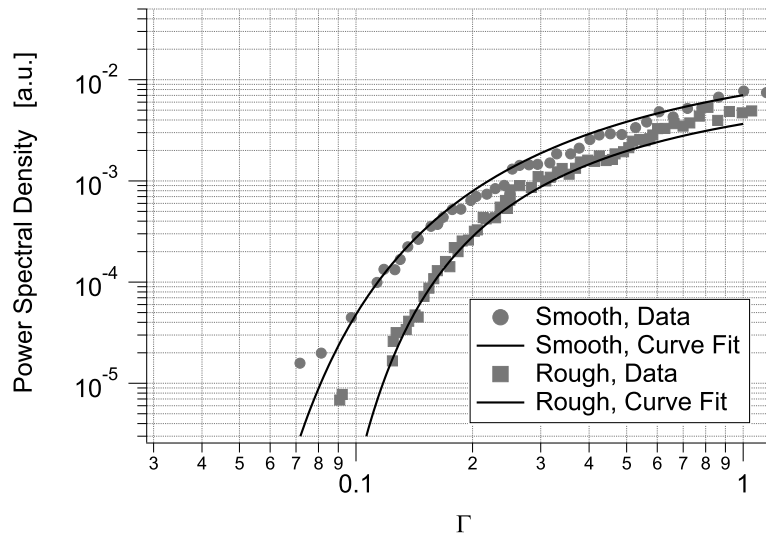
Figure 3.17: Configurational noise level plotted as a function of Γ, for two different surface states of the beads. The circular markers correspond to smooth spheres, while the square markers correspond to beads that have been acid etched, and therefore have a much rougher surface. The superposed lines correspond to a curve fit of Eq. 3.12.

The two data set can be fitted using Eq. 3.12. A good agreement is found for the smooth particles if $\mu_d \approx \mu_s \approx 0.4$, while the acid etched spheres show, as expected, larger friction coefficients $\mu_d \approx 0.6$, $\mu_s \approx 0.7$. All the other parameters of the model are left untouched, as indicated in the main text. The other parameters corresponding to the model curve do not vary between the two fits and have the following values: A = 0.01 (preexponential factor), $\epsilon = 4$, $d_c r = 9.5 10^{-7}$, $\omega_0 = 22000$, $\omega_s = 2\pi f_s = 1250$, and $i = 40$.

These measurements suggest that the proposed model describes quite well the grain-grain interactions in weakly vibrated granular materials. As one would imagine, the state of the surface influences the dynamics of the system, leading to an earlier complete jamming, even if the observed critical distance d_{cr} is not varied.

3.5 Conclusion

The main result of this chapter can be summarized as follows. By performing forced mode experiments, the data give indication of a relaxation mechanism in granular materials, that depends on two physical observables, Γ and ω_s. This mechanical relaxation can be linked, on theoretical and experimental grounds, to a characteristic relaxation time. This is the time that the system needs to "recover" from induced rearrangements. If these data are plotted on an Arrhenius diagram, a non Arrhenius behavior can be hinted, but the data are too scattered to give a definitive answer.

Free mode experiments were then performed to extend the range of the measurable experimental conditions. The comparison between the two results allows to identify a non-Arrhenius,

VFT-like behavior of the relaxation time with respect to the average vibration of the system. Furthermore, the free mode technique is found to be more adapt to perform measurements with single frequency vibrations. This allows to clearly observe the scaling law also as a function of ω_s.

From experimental evidence it becomes clear that the relaxation time is only function of a single control parameter, $a_s = \sqrt{\Gamma}/\omega_s$, and that it has a VFT-like dependence on it.

Finally, these two features can be modeled if both macroscopic rheologic ideas and statistics of extreme events are considered. The resulting model depends on microscopic properties of the granular medium, and can be therefore directly tested with measurements. A comparison between granular media composed of beads of different surface roughness highlights the dependence on friction coefficient terms.

Chapter 4

Fractional Brownian Motion

4.1 Brownian motion in granular materials

In the previous chapters we have discussed some experimental evidence of the jamming transition in weakly vibrated granular media. In this work, we mainly exploit the interaction of a macroscopic probe with the granular system. As we discussed, one of the key problem in such measurements is how to extract useful information, without concurrently introducing perturbations.

For example, we discussed how the mechanical loss measurements were more useful for the case of strongly vibrated media. In this case, the external torque applied on the probe does not substantially perturb the system. On the other hand, at low vibration intensities, even weak torques can induce rearrangement and aging in the granular medium, which can make data interpretation more difficult. In the case of free mode spectral measurements, the situation is reversed. The absence of an external torque proves ideal for weakly vibrated conditions, but the inertial effects due to the pendulum suspension become more and more relevant as the vibration intensities increase.

These two approaches, however, do not yet suggest any interpretation on what happens in the system as we switch from the high vibration, fluid regime, to the low vibration, jamming, regime. In order to be able to study the behavior of the granular medium all the way from the fludization limit down to the jammed phase, we developed a new approach. In short, this technique does not require the application of an external torque, and is conceptually valid for all vibration intensities.

However, before moving on to the discussion of the technique, there is also a second, deeper reason that motivated us to further investigate the matter. In fact, it has been widely observed that granular materials interact with macroscopic objects in a way that reminds a brownian particle. This remains true, independently on the dynamic region in which the system is driven by the vibrations. For example, the fluid-like phase was studied using a Langevin approach [196, 187]; in this work, on the other hand, we discussed the subcooled liquid conditions (around the jamming transition; see also [205]). The configurational noise spectrum was studied [204, 205] in both situations, and it shows a $1/f$ behavior, suggesting a brownian-like behavior. This fact can also be used as a starting point for modeling [211].

On the other hand, there is little direct and consistent evidence showing that three dimensional granular media interact with "macroscopic objects" in a true "brownian" way.

To overcome the experimental limits of the approaches discussed above, and to study directly the problem of the characterization of the movement of probes in granular media, we present an analytical approach based on *fractal analysis* of experimental and simulated time series. This technique demonstrates that macroscopic objects immersed in vibrated granular matter can indeed act as probes that behave as brownian particles. The technique allows us to measure the presence of constraints acting on the probe, constraints that can be due to granular interactions or to external forces acting on the probe.

4.2   Experimental setup and simulation

In this section we present the experimental setup (already discussed in Ch. 2), how we treated the data, and how the experiments can be compared to simulation. For clarity, we first recall the more relevant features of the granular medium and of its interaction with the probe. Taking this as a starting point, we discuss a simple model that we can simulate. Simulation allow us to discuss the details of signal processing techniques under controlled conditions and to evaluate the limits and the reliability of this approach. Afterwards, we can finally discuss the experimental data.

4.2.1   Simulation

As we will discuss briefly here and in the experimental section that follows, our measurements suggest that the granular system interacts with the probe in a very complex way: we observe normal and fractional brownian motion, together with the presence of a constraining force. We performed simulations on a very simplified model of the system, representing a constrained random walk. The simulations allow us to address two specific subject-matters.

First, it is known that the fractal analysis of time series presents numerical difficulties. In this work, we use simulated data to assess the solidity of our data analysis, since they are applied to sets of data over which we have full control.

Second, part of our experimental results take place in a dynamic region where brownian objects are submitted to an external constraint. With the aid of simulations, we can study, in controlled conditions, the behavior of such a system, that we can relate to experimental data.

Two simple models

In the experiments discussed in the previous chapter, a cylindrical probe is suspended in the granular system by the means of a relatively weak torsion spring. In this context, weak means that the stiffness of the torsion spring is lower than the average stiffness of the non-vibrated granular. The assembly, described in Ch. 2, is sketched in Fig. 4.1 (left).

When the granular is vibrated, the probe behaves in a way similar to a (rotational) brownian particle. This cam be ascribed to the global effect of the large number of interactions between the probe and the smaller grains. However, it is clear that the probe cannot move in a completely brownian way. In fact, the torque that is transmitted to the probe at each collision (in

the high vibration regime) or which can be transmitted by a local rearrangement of the chains of forces in the granular medium (in the low vibration regime) is finite. Therefore, there will be a limit angle (from the origin) at which the restoring torque due to the elastic constraints (due to the suspension wire or to the full ensemble of force chains in the granular) cannot be overcome. This will eventually limit all movement in a confined range of configurations. Another possible source of non-brownian effects is the large relative moment of inertia of the probe. If the rotational velocity of the probe increases, it can in principle overcome the collisional strength of a large number of "impacts" with the granular system, therefore leading to inertial effects causing anomalous diffusion (superdiffusion).

In a simplified model we can separate the effect of fractional brownian motion, on one side, from the case of dynamics constrained by the presence of and external potential, on the other side. For a complete review of the subject one can refer to Metzler [212].

Constrained random walk

Let us consider a particle moving on a lattice. For a simple random walk, at each step the probability to move to the right ($\Delta = +1$) is $P(\Delta = +1) = 0.5$ and vice versa for ($\Delta = -1$). We modify the random walk simulation to take into account this phenomenon, in two very simple ways.

In the first case, we modify the probability to move in either direction, so that, at each lattice point n, the probability to move to point $n + 1$ is given by $P(n \rightarrow n + 1) = 0.5 - A \times n$ where A is the constraint parameter that we can choose. This contribution proportional to the distance from the origin can be interpreted as the presence of a quadratic potential. From this definition, it is clear that the simulated "constrained" random walk does not differ from the standard one at the origin (and in the immediate neighborhoods). On the other hand, for the lattice point m such that for the chosen A we have that $Am = 0.5$, we see that it can only span the region $(-m; +m)$. With this rule, we performed simulations for different values of the parameter A between 10^{-6} and 10^{-2}.

To ensure that the constraint does not introduce unwanted effects due to the "hard wall", we repeated the simulation using a transition probability of sigmoidal shape: $P(n \rightarrow n + 1) = 1 - \frac{1}{1+e^{-\sigma n}}$ In this case, we can tune the sharpness of the sigmoid, changing the parameter σ, while ensuring that there is no hard wall effect. We ran different simulations with $10 \leq \sigma \leq 10^6$. Simulations were run for 10^6 steps, and statistical analysis was performed on 10^5 samples to get good statistics. At each fixed amount of time steps (typically 2000 or 10000) the actual position of the random walker with respect to the origin was recorded. From these data, we constructed histograms showing the relative frequencies of finding a walker at a given distance from the origin. For each simulated configuration, we also recorded a small number of simulated time series, so that they could be studied directly with fractal analysis.

Fractional Brownian motion

As we will see in the following sections, the effect of introducing the constraint described in the previous paragraph is to reduce the size of the region accessible to the particle, at least

for large times. Therefore we cannot employ this technique to study the case of the inertially driven (or superdiffusing) random walk.

This is, however, a well studied problem, and we could employ a computational toolbox for the MatLab platform, called "Fraclab" [213]. We could use it to simulate time series of fractional brownian motion, as discussed in Appendix B (Pag. 139). We note that in this case, for technical reasons, the random walk is constructed all at once, and not stepwise. This fact prevents us to impose a bias on the step transition probability as we did in for the normally diffusing random walk.

We simulated time series of different lengths (1024, 2048, 4096 and 8196 steps) for different values of the diffusion or "Hurst" exponent.

4.2.2 Experimental setup

For the experimental part of this work, we consider the same granular and vibration motor assembly discussed in the previous chapters. The experimental setup responsible for the measurements is, on the other hand, composed of two different equipments: the torsion oscillator and the brownian motor. In particular, the brownian motor setup was specifically designed and built so that we could measure the rotational movements of a probe that was not torsionally constrained (as is the case of the torsion oscillator). We recall the sketches of both setups, shown respectively in the left and right part of Fig. 4.1.

As before, an accelerometer measures the average vibration intensity Γ. Through the experiments, we feed the vibration motor with the same broadband signal as for the other experiments, that is a filtered white noise cut off below 70 Hz and above approximately 1 kHz. The granular medium is sensed via a probe connected to a low-frequency torsion oscillator, or to a freely-turning rod, suspended on ball bearings. In this case, the probe consists of a cylinder covered by a layer of glued beads, with effective radius $R_e \approx 2.5$ mm, and immersed at a depth $L \approx 45$ mm.

In the case of the torsion oscillator setup, the probe is left free to move, with constraints arising from the interaction with the granular material and the suspension wires. The global effect of these interactions on the probe can be summarized as follows:

a a local restoring coefficient. This arises partly from the actual spring constant of the suspension (in the torsion oscillator setup) and partly from the interactions between the granular medium and the probe. In the high Γ, fluid condition, the apparent elastic modulus ascribed to the granular interaction is approximately three to four times higher than the one coming from the suspension. As the vibration strength is reduced, the granular becomes much stiffer and the ratio between the two contributions can rise up to 100:1 and above.

b a damping effect due to viscous friction. This comes from both mechanical loss in the suspension and from the dissipation of energy within the granular sample. Since the damping due to the suspension is always lower of at least a factor 100 with respect to the damping due to grain interaction, we will only consider the latter.
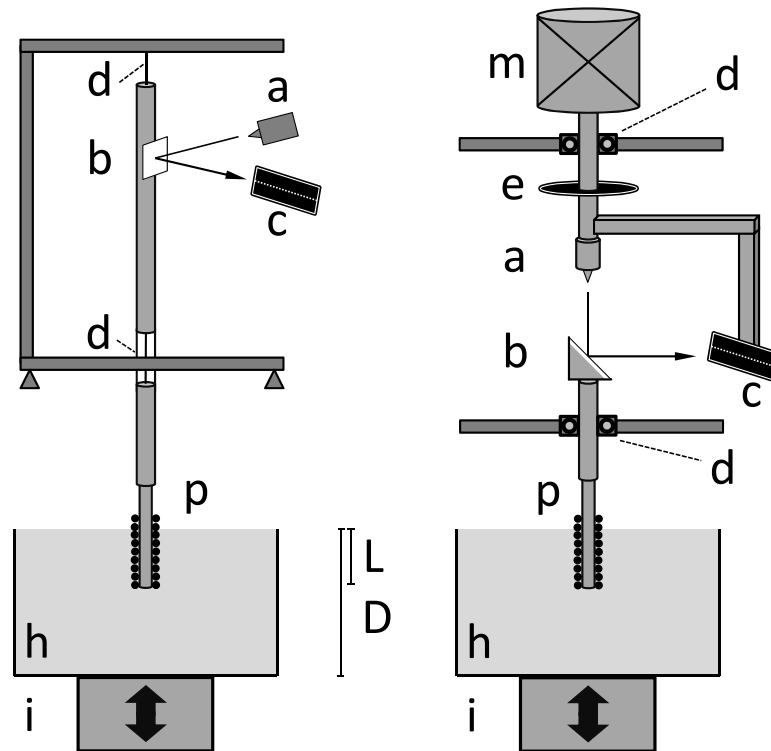
Figure 4.1: Sketches of the two experimental setups. On the left, the forced torsion oscillator configuration. On the right, the brownian motor configuration. In both cases, a cylindrical probe is used. Glass beads, identical to those in the granular medium, are glued on the probe walls, making it sensitive to the local movements of the grains. The probe is immersed at a depth L into a granular medium of glass beads of depth D. The container, filled with the granular material, is shaken vertically by a vibration motor. An accelerometer measures the intensity of vibration, Γ. The sketch of the oscillator (left) includes: a = laser diode; b = mirror; c = position sensing photocell; d = suspension wires; p = cylindrical probe; h = granular medium; i = vibrator motor. The sketch of the browninan motor (right) includes: a = laser diode; b = mirror; c = position sensing photocell; d = suspension ball bearings; e = motor speed sensor; m = alignment motor; p = cylindrical probe; h = granular medium; i = vibrator motor.

c a white noise term (in the Langevin sense), responsible for the Brownian behavior of the probe.

In the case of the brownian motor, the same conditions apply, with the exception of the absence of the torsional restoring coefficient. In principle, we should take into account the minimum torque needed to release the probe from the possible sticking of the spheres in the ball bearings. However, the friction coefficient of our bearings is very low, and the axial alignment is very precise. These two facts keep the starting torque to extremely low values, less than 10^{-7} N m, and we can ignore this effect.

As in the previous, free mode, measurements, typical angular displacements during the experiments do not exceed 0.01 radians. This corresponds approximately to a maximum linear displacement of 0.1 mm of any point at the surface of the probe.

Again,in order to control compaction effects [57], all measurements are taken in the same conditions, e.g., starting from a granular material shaken at $\Gamma \approx 6$ with a large band signal (f_s between 70 and 1000 Hz) for 10-20 minutes.

In both setups, the angular position of the oscillator, $\theta(t)$, is optically detected with a linear analog photocell. The optical arm (the distance between the rotation axis and the photocell) is approximately 70 cm for the torsion setup, and approximately 8 cm for the brownian motor setup.

In the case of the brownian motor, the signal measured from the cell is electronically decomposed into an average drift (slow movement) and fluctuations (fast movement). Via a feedback circuit, the average drift is fed to the electric motor placed on top of the structure. The average drift of the probe is therefore compensated by the rotation of the upper section, so that on the average, the reflected laser beam always falls on the center of the photocell (the zero position). The fluctuations are sampled at high frequency in the same way it was done in the torsion oscillator setup.

In both setups, the resulting position data are recorded at sampling rates of 10 or 20 kHz with a National Instrument NIDaQ 6009 digital voltmeter, and are stored on a computer. The electrical noise level do not exceed the value of 1% in the most delicate measurement conditions.

We performed the experiments with vibration levels in the range $0.01 < \Gamma < 5$. For each Γ, we recorded a 600 or 1200 seconds long time series.

4.3 Fractal analysis of time series

Our experimental time series were studied by the means of fractal analysis. This approach was originally proposed by Mandelbrot [214], and consist in calculating the fractal dimension of a given signal, as discussed in Section A.4.2. One of the inherent advantages of this method is that it can be used to extract stable observables from data that cannot be easily treated otherwise (for example, with Fourier analysis). More specifically, our experimental data are time series of the angular position of the probe. These represent, therefore, one dimensional trails as a function of time.

In Section B it has been shown that, if h indicates the diffusion (or Hurst) exponent, and D the dimension of the time series of the position of the diffusing particle, it can be demonstrated that in Brownian motion the dynamics of diffusion obey the equation $\langle x \rangle \propto t^h$, with $h = 0.5$, so that $D + h = 2$.

However, the mathematical conditions that define a Brownian motion can be relaxed, and the transition probability can be modified to introduce a term that locally either opposes the movement Brownian object, or that propels it. The effect of such modifications is visualized on the graphs shown in Fig. 4.2. A propulsive effect (for example due to inertial phenomena) tends to smoothen out the graph, while constraining effects make the trails look "noisier".

This observation allows us to interpret our experimental and simulated data as examples of anomalous diffusion [215, 167, 216]. In short, one system is said to show (normal) diffusion when the variance of some position observable scales linearly as a function of time (for large enough times). When this is no longer true, we speak of anomalous diffusion. In this case the
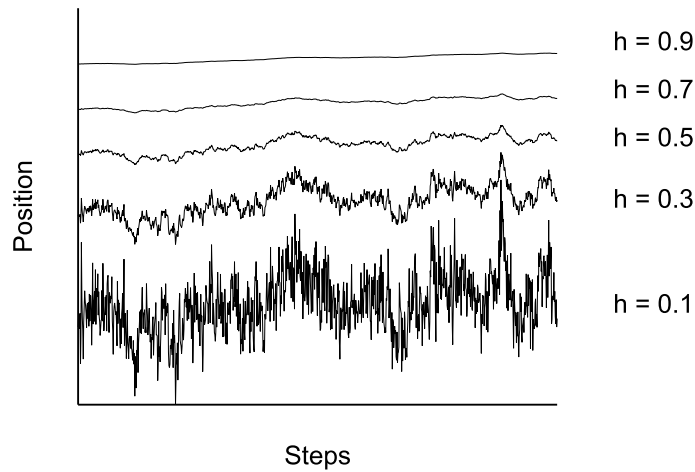
Figure 4.2: Representation of different simulated FBM obtained with five values of Hurst exponent. In this case, the fractal dimension d is related to the Hurst exponent h by the equation $d = 2 - h$ (as discussed in the main text). A small Hurst exponent has a higher fractal dimension and a rougher surface, while a larger Hurst exponent has a smaller fractional dimension and a smoother surface. The data were obtained by simulating fractional brownian motions with different h exponents, but keeping the random seed fixed [220].

square root of the variance of the observable position no longer increases as $\sigma_x \propto \sqrt{t}$, but instead behaves as a power law with exponent $h \neq 1/2$. In this context, the Brownian motion is said to be "fractional" (abbreviated to FBM), and the exponent h is often called "'Hurst exponent". This fact, and general properties of anomalous diffusion, have been widely studied in other works, such as the review by Bouchaud and Georges [167], and also to the studies of Balakrishnan [215], Schneider [217], Saichev [218], and Barkai [219].

4.3.1 Simulation

As discussed before, our simple model consists of a random walk with a transition probability, which is modified as a function of the position. Simulations consist in generating a large number of instances of random walks with identical parameters (constraint, number of steps, etc). For a given set of parameters, the large number of instances is used to construct the position frequency histograms. This is repeated for a large number of intermediate time steps between start and end steps. Furthermore, for every set of parameters, a few simulated instances (or "realizations") are recorded, for further analysis. A few remarks should be highlighted.

First, the frequency histograms constructed from the simulated time series are Gaussians, even for the strongest constraints. This is shown in Fig. 4.3. We used this fact to impose a stronger constraint on data analysis: the variance parameter is computed, at each step, by fitting a gaussian curve to the histogram. The same procedure will then be applied to the experimental time series, where a gaussian distribution is not expected a priori. This will be discussed in the following section, but we can anticipate that also the experimental data
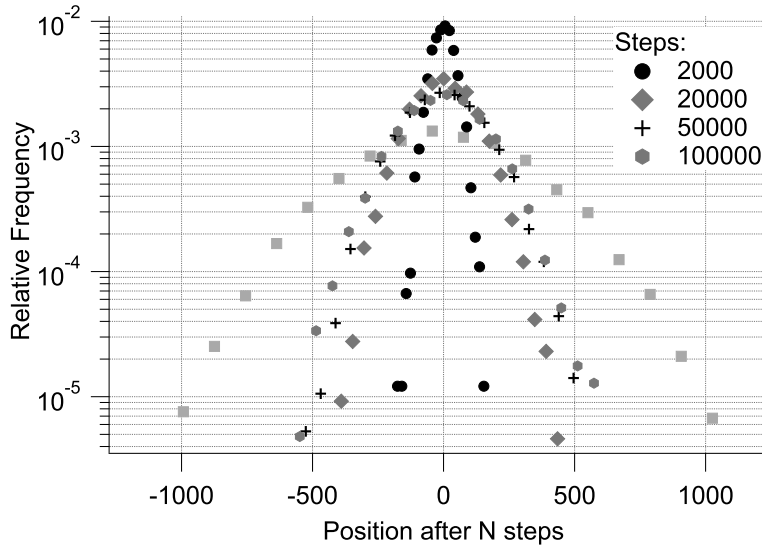
Figure 4.3: Evolution of the width of the distributions for a constrained random walk. In this case we consider a linear constraint of parameter $A = 10^{-5}$. At first, below 20000 steps, the frequency histograms broadens as in the free case (circles and diamonds). As the walkers move far from the origin the effect of the constraint starts to be relevant, and between 50000 (crosses) and 100000 (hexagons) steps, the evolution stops. This is evident if we compare the results with a free random walk after the same number of steps (gray squares).

behave in a similar way.

Second, the addition of this constraint breaks the usual diffusion rule $\langle \Delta \rangle = \sqrt{t}$ for large times, as the random walker starts exploring the regions far from the origin where the constraint becomes larger. The limit width of the distributions can be computed and (as expected) it is proportional to the square root of the constraining parameter. A comparison with non constrained data is shown in Fig. 4.4, which shows the final width of the distributions as a function of the constraint parameter. We also noticed that the choice of the constraining method (linear spring or sigmoidal correction) does not influence the results.

A comparison between non constrained and constrained data is also shown in a different way in Fig. 4.5. In this case, we show the evolution of the width of the gaussian peaks fitting the histograms of the end position of a large number of simulated paths, for constrained and unconstrained random walkers. It is very clear from these data that the unconstrained random walk evolves as expected ($\sigma \propto t^{1/2}$), while the constrained motion appears to saturate, and stop evolving after a certain amount of steps.

The graph in Fig. 4.5 is of particular interest, since it allows a direct comparison with its experimental counterpart shown in Fig. 4.8, which will be discussed in the next section.

From all these simulations, we can therefore conclude that the presence of a constraining force applied on a brownian particle lowers the diffusion exponent h.
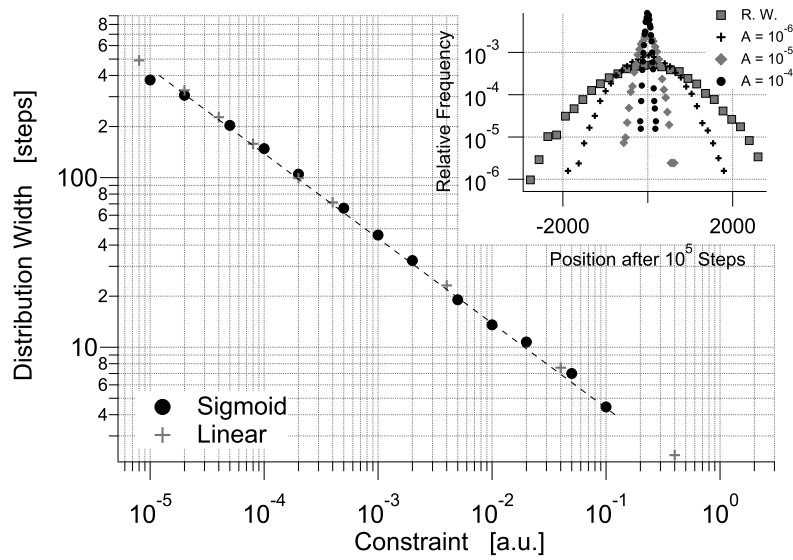
Figure 4.4: Effect of varying constraints. Data shows the width of histograms calculated after 10^5 steps, for different values of constraints and using the two functional forms for the probability. Sigmoidal and linear constraints are represented respectively by circles and crosses. The width of the histograms appear proportional to the square root of the constraining parameter. The inset shows three actual examples of the simulated histograms, for the case of linear constraint and constraint parameter $A^{-1} = 10^6$, 10^5 and 10^4. The free random walk is also shown for comparison.
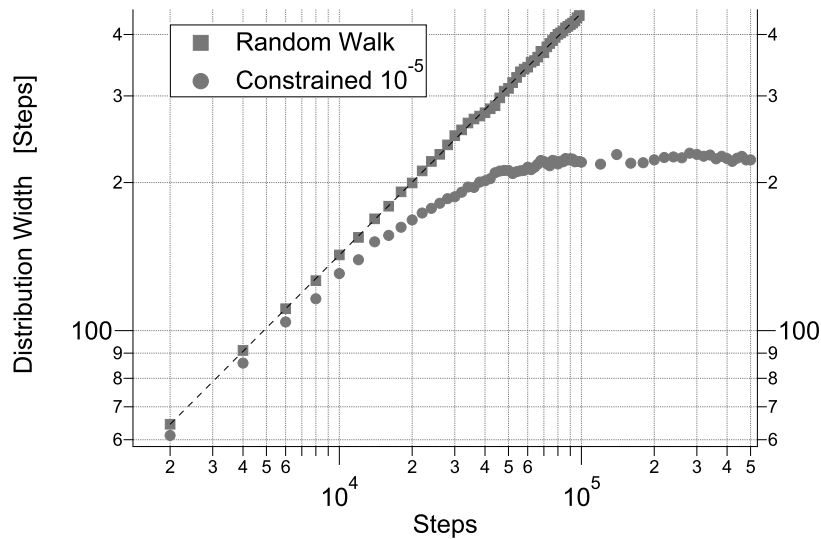
Figure 4.5: Evolution of the width of the simulated distributions for the standard random walk and for a constraint parameter $A = 10^{-5}$. The unconstrained random walk (crosses) shows the classic diffusion rate $\propto \sqrt{x}$, indicated by the dashed black line. The constrained data (circles) instead saturates to a fixed width. This was computed up to step 10^6.
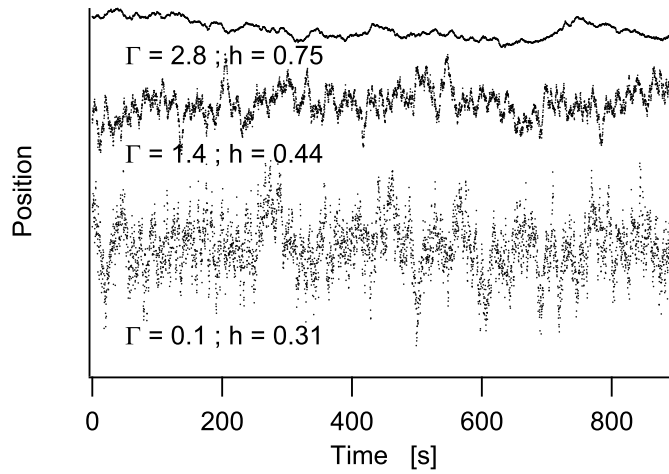
Figure 4.6: Three experimental time series obtained with different levels of vibration Γ (as indicated). For each curve, the corresponding Γ value and Hurst exponent (as defined in the discussion section) are reported.

4.3.2 Experiment

It is not trivial to directly repeat the analysis performed on simulated data when we consider experimental time series. This, for two main practical reasons. First, it will take too long (centuries) to record the same number of time series needed to perform the time averages as we just did for the simulation. Second, it is true that we can perform the ensemble averages: in this case it means computing the histogram of the "number of visits at location x" as a function of time. However, the system has a non-ergodic behavior at the time scales which are experimentally accessible. In fact, as the granular approaches complete jamming ($\Gamma \to 0$), the probe spends exponentially growing times in each consecutive position (following granular rearrangement).

Since the characteristic times diverge, there is simply no way to access the quantity of data necessary to get good statistics, in order to apply conventional analytical approaches. This is evident in the experimental data shown in Fig. 4.6. Here we show three typical time series, obtained with the cylindrical probe, for different values of the vibration level Γ.

The trails of the probe change as a function of Γ. The overall behavior reminds closely the fractional brownian trails of Fig. 4.2: in the low Γ region, the probe is strongly confined, and it oscillates frequently around the same equilibrium positions; as the vibration intensity increases, the constraining effect of the granular medium becomes less important and the evolution becomes smoother. We anticipate that this property can be described with the Hurst exponent (also shown besides each curve). This observable will be discussed in detail in the following section.

The experimental data is further analyzed as follows. For each level of vibration intensity Γ, we record a time series. At any given time T, after the beginning of the measurement, a given angular region will then have been swept. We divide this region into small slices and we compute the occupancy histogram considering the amount of time spent in a given slice, from
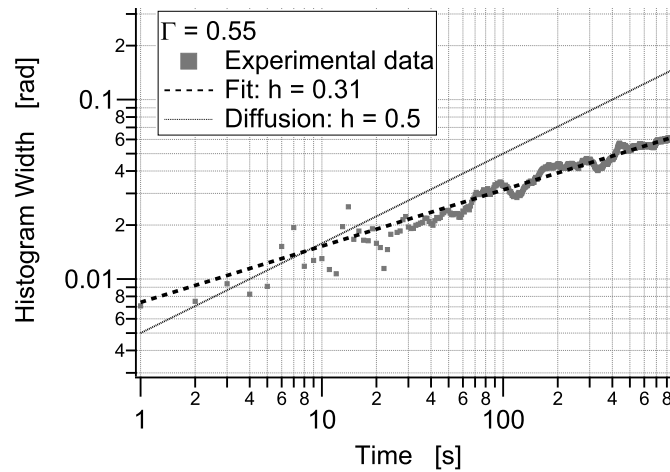
Figure 4.7: Example of the broadening of the region spanned in the experimental time series. The data, though noisy, indicate that the probe sweeps an increasing area, with an anomalous diffusion exponent.

$t = 0$ to $t = T$. Therefore, for each time T, we can construct an histogram. We split the time series in 1 s interval. The histograms are then fitted with a gaussian curve. We note that the computation of the variance of the data is performed via the gaussian fit to keep consistency with the simulated time series (where the gaussian shape of the distribution is guaranteed by the CLT). As an example, we show the fitted gaussian width for $\Gamma = 0.55$ in Fig. 4.7.

Finally, Fig. 4.8 shows the final width of the time-series occupancy histograms as a function of the vibration intensity Γ. In the strong vibration regime, the swept area appears to be constant. It starts to decrease as the intensity of shaking is reduced, but in this case the noise level becomes much more important.

4.4 Discussion

4.4.1 Defining the fractal dimension: Hurst exponent

Once the time series are measured, the fractal dimension and the Hurst exponent can be inferred. The fractal analysis performed in this work was performed with the software toolbox *FracLab* for the MatLab platform. It is available as Open Source software and is developed by the Regularity team of INRIA – CNR Saclay (see [213, 221]).

With the help of this package, it is possible to compute two different approximations of the Haussdorf dimension of a time series. The simplest, and less computationally intensive is the well known Box Counting (or simply "Box") method [222]. Unfortunately, this method has the disadvantage of converging very slowly to the fractal dimension, as the length of the considered time series is increased. This means that, if the considered time series are not long enough, they only could give a rough estimate of the correct Box dimension. We performed some simulations and we observed worst-case deviations by up to 15%, by comparison with expected theoretical values. This fact has been already discussed in the past [223].
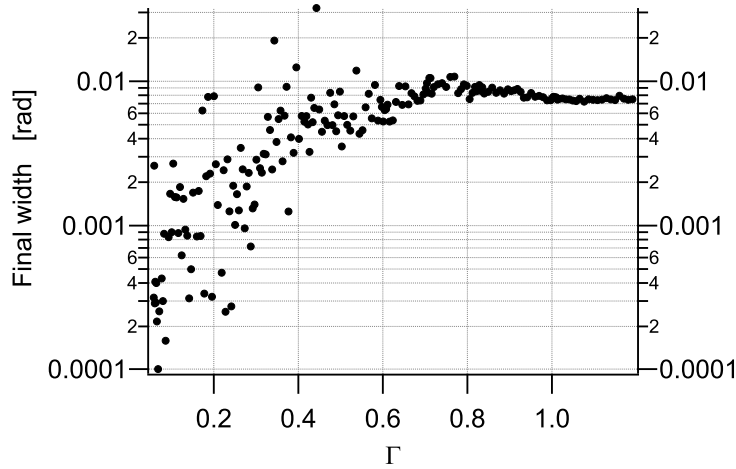
Figure 4.8: Final width of the histograms of the experimental time series. The data correspond to the final width of all histograms computed as in the example of Fig. 4.7. For the lower vibrations, the swept area increases with the vibration intensity. However, as the vibrations increase, the width of the histograms stabilizes.

In principle one could use other, more powerful methods, such as the "regularization" method provided in the same software package. Unfortunately, the regularization technique is quite computationally intensive and, in the current implementation is not suitable to systematic analysis of experimental data.

4.4.2   Simulations

First, some analysis on the simulated data was performed. The computed Hurst exponents are shown in Fig. 4.9 for the data obtained with a linear constraint. Simulated random walks for different values of the constraint parameter A are considered and the Hurst exponent is plotted as a function of the inverse of the constraint parameter A. The ordinate show the estimates for the Hurst exponent h obtained with the Box method for 10^4 and 10^6 steps random walks (respectively indicated by the gray and black markers).

For the case $A \to 0$ (pure Brownian motion), we know that the Hurst exponent must be exactly $h = 0.5$. If we consider the 10^6 steps data set (black dots), the agreement with the theory is good, although not perfect: the data indicate that the exponent is slightly overestimated. For $A = 0$ we obtain $h = 0.56 \pm 2.0\%$, which is indicated on the graph by the dashed horizontal line on the right part. The estimations of h become worse as we shorten the considered length to 10^4 steps (grey data set).

As discussed above, a further increase in the number of steps has a progressively smaller effect on the computation of h. From these observation, we conclude therefore that the data set composed of 10^6 steps already allow a reasonable estimate of the Hurst exponent.

The evolution of h as a function of A is remarkable. As already noted, the limit $A = 0$ corresponds to a normal brownian motion. When the constraint increases, on the other hand, we observe that the Hurst exponent decreases as A increases. In the region defined by
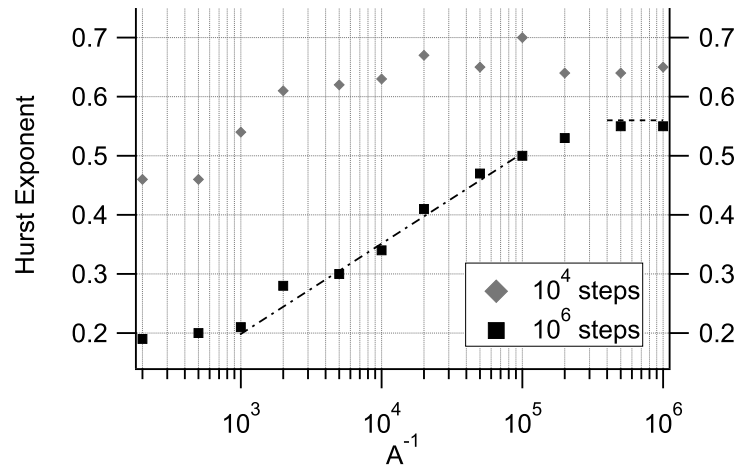
Figure 4.9: Computed values for the Hurst exponent, h, plotted as a function of the inverse of the constraint parameter A. We considered one instance of a simulated random walk for each value of A. The exponent h is estimated by the Box method over a RW of 10^4 (gray markers) and 10^6 steps (black markers). Short time series lead to overestimation of h; this improves, albeit very slowly, with the size of the data sets. The horizontal dashed line indicates h obtained in the limit case $A = 0$ for a 10^6 steps time series.

$10^{-5} \leq A \leq 10^{-3}$, the data suggests an approximate decrease of 0.15 per decade. This is highlighted by the dot-dashed diagonal guideline. Finally, below this region, for $A > 10^{-2}$, the effects of the constraint become very large, so that the region of space available for the random walk is extremely reduced. In this limit, the Hurst exponent progressively loses importance, since the system becomes only sensitive to the random term.

It is also important to note that our simulation technique does not allow to generate propelled brownian trails with an exponent h larger than 0.5. This occurs because our simple model constructs the 1-D random walks step by step, and the constraint is directly introduced as a bias in the transition probability $P(x)$. However, unfortunately, for technical reasons there is no simple way to simulate a FMB in which the stepwise transition probability can be modified of a given amount (as we did with the simple random walker). For this reason our simulated data can only span the region $0 < h \leq 0.5$.

Despite these limitations, we can conclude this section with the following three key observations. First, the simulations show the reliability of the estimation of the Hurst exponent via the Box dimension. The computed data do not substantially depart from the expected theoretical value, provided that the time series are long enough for the computation algorithms to converge to a reasonable estimation. Second, the generation of simulated time series allows the computation of the variance of the position distribution in a well defined framework, and allows a direct comparison with experimental data. This can be seen by comparing Fig. 4.5 and Fig. 4.8. Third, the simulated data clearly show that the addition of a constraining effect makes the time series look more "irregular", thereby increasing their dimensionality; this fact can be meaningfully described with the Hurst exponent.
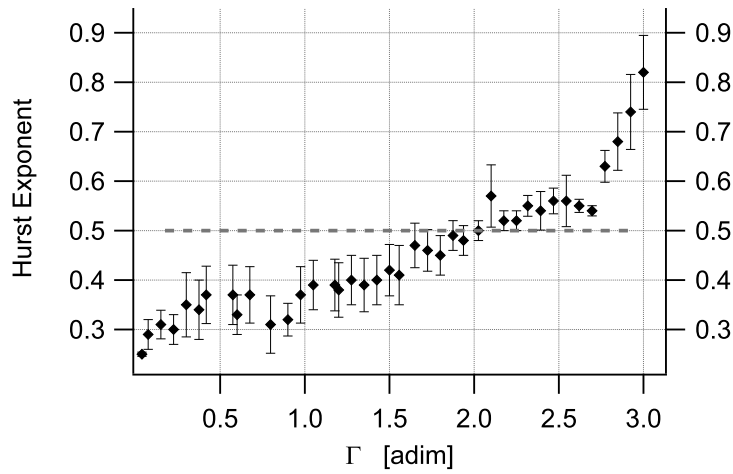
Figure 4.10: Hurst exponent for experimental time series obtained with the torsion oscillator setup. The data are plotted as a function of the average acceleration intensity Γ, and were computed with the Box dimension method. The graph shows that for strongly vibrated system the exponent is compatible with a superdiffusive behavior. As the strength of the excitations is reduced, the system "slows down" to a jamming regime where diffusion is inhibited.

4.4.3 Experimental data

In Fig. 4.10 the computed Hurst exponent is plotted as a function of Γ. It is clear that, as the vibration intensity is decreased, the average rate of diffusion is reduced. As discussed in the previous section, the use of the Box method can introduce inaccuracies in the results. However, a slight systematic deviation does not significantly change the interpretation of the data.

At higher vibration intensities, the granular medium is fluidized. In this phase, dynamic effects due to convection influence the motion of the probe and superimpose to a simple random walk. In this region, have a "superdiffusive" behavior: the Hurst exponent is greater than 0.5. As the vibration intensity is lowered, we approach the jamming transition. When motion slows down, the Hurst exponent lowers, since convection effects become less and less important. Finally, as the vibration is further reduced, we reach the jamming phase, and the Hurst exponent becomes lower than 0.5. This fact suggests the following interpretation. In the jamming region, the probe is subject to the correlated movement of a large number of granular particles. However, with decreasing vibrations, the network of chains of forces in the granular medium becomes more and more complex. In this situation, the overall position of the probe can change only if a large scale re-arrangement event takes place. If such a rearrangement does not happen, the probe has a greater probability to jump back to the previous position. Therefore, we obtain a behavior similar to a constrained random walk. In other words, the dynamics of the system is dominated by Lévy flights and/or extreme event statistics [224, 140]. One interesting observation is the fact that, as the Hurst exponent decreases, apparently no plateau is reached. We attribute this fact to the presence of the weak restoring coefficient due to the torsion suspension, which is always constraining the movement of the probe independently of the condition of the granular system.
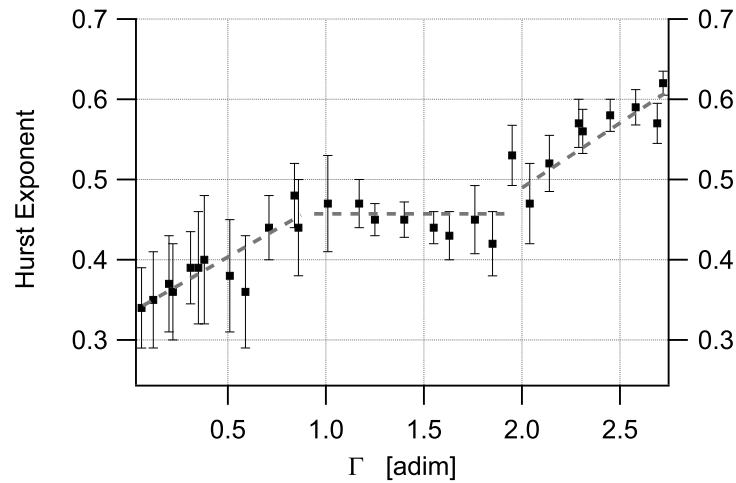
Figure 4.11: Hurst exponent for experimental time series, obtained with the torsionally uncon-strained apparatus ("Brownian motor"). Apart from this, the data were obtained otherwise using the same method of those shown in Fig. 4.10. In this case, despite the larger dispersion of the data, a plateau can be seen for $h \approx 0.5$, in the region $1 < \Gamma < 2$.

As discussed in the experimental setup, the torsion constraint due to the suspension wires is much smaller that the effect of jammed granular media, but it accounts for around 1/3 of the "apparent" restoring force of a fluidized medium. In order to fully asses the effect of this external constraint, we consider the data obtained with the free rotating, "Brownian motion", setup (Fig 4.1). In this case, the probe is suspended with two ball bearings that allow the rotational motion with very little friction. In this configuration, a symmetric probe can rearrange freely in any direction, not being subject to a preferential spatial direction (due to the torsion spring). All the other experimental conditions (granular medium, probe, spectrum of the vibration noise, etc.) are otherwise identical to those employed in the torsion oscillator measurements.

The resulting data are shown in Fig 4.11. First, it should be noted that, for sensitivity reasons, there is a larger scatter of the data points. In fact, the optical arm of the brownian motor setup is, currently, approximately 9 times shorter than that of the torsion pendulum. For this reason, the Signal-to-Noise ratio of the brownian motor installation is smaller. Considering similar displacements in the granular medium, and similar amount of electronic noise in both photocell electronic chains, this fact explains the larger scatter of Fig. 4.11 with respect to Fig. 4.10.

The graph in Fig. 4.11 shows three distinct regions. For strong vibrations, $\Gamma > 2$, h is larger than 0.5 and increases as the system becomes more and more prone to convection effects. The corresponding rightmost, dashed, gray line corresponds to a least square fit (in this case, the slope is approximately $m = 0.16$). If the vibration intensity is reduced, for vibrations of intermediate strength $1 < \Gamma < 2$, the Hurst exponent stabilizes and reaches a plateau (indicated by the central gray dashed line, $h \approx 0.46$. In this region, it seems that the system evolves as a normally diffusing brownian particle, if the deviation from the expected value of 1/2 can

be attributed to numerical approximations. This region is not present in Fig. 4.10, as the constraining effect of the torsion suspension is relatively important. Finally, as Γ becomes smaller than 1, the system starts to jam and the Hurst exponent decreases (leftmost gray dashed line is again obtained by least square fit of a straight line of slope $m = 0.13$). We note that a similar phenomenon, showing a crossover between simple diffusion and a caging behavior has been observed in an analogous (albeit two dimensional) system [225].

We can now compare the Hurst exponent obtained with the simulations, with the one obtained with the experiments (Fig. 4.11). Our simulations only allow us to study the dynamical region where $h < 0.5$. In the experimental data, this corresponds approximately to the vibration intensities window $0 \leq \Gamma \leq 1$, where we observe an increase of h as Γ increases. If we focus in this region, the simulations (Fig. 4.9) indicate that for values of constraint in the range $10^{-5} \leq A \leq 10^{-3}$, the Hurst exponent h decreases by approximately 0.15 for each tenfold increase (decade) of the constraint parameter A. The experimental analogue in Fig. 4.11 gives $h_{\Gamma=0} \approx 0.35$, and $h_{\Gamma=1} \approx 0.55$: therefore, we observe a variation $\Delta h = 0.2$. If this change of the experimental Hurst exponent can be attributed to an increase of a constraining force acting on the probe (and ultimately depending on the granular medium), this would correspond to a change of $10^{\frac{0.2}{0.15}} \approx 20$ times in the constraint value. While this approach only provides rough estimates is nonetheless very interesting. With the techniques discussed in Ch. 3, the evolution of the stiffening of a granular system as a function of Γ has been observed (see also [205]). Comparison with the data in Fig. 3.4 indicates that the change in the measured stiffness (the dynamic modulus, representing the real part of the complex susceptibility) has approximately the same magnitude.

As a final remark, we remind that the effect of electronic noise is negligible, since in typical measurements it accounts for less than 1% of the mechanic signal. We have also estimated the Hurst exponent of the signal of this electronic noise, obtaining 0.50. As expected, the electrical noise in our cell has a random walk like behavior.

Further development of this work will involve a more detailed characterization of the freely rotating system. One field of interest will be the study of the dynamics of asymmetric probes. Asymmetric geometries can be put into rotation by rectification of granular collision noise [180]. In this latter case the interaction is between "macroscopic" constant speed movement, and "microscopic" Brownian fluctuations.

4.5 Conclusion

In this chapter we have studied the behavior of a macroscopic probe immersed in a vibrated granular systems. We have questioned the validity of the interpretation of the movement of such probes as brownian-like objects, and we have studied the system in a dynamic window that comprises the fluidization limit and the jamming transition.

In order to do so, we implemented fractal analysis techniques to the time series of (*i*) a torsion pendulum immersed in vibrated granular materials and, (*ii*) a free rotating brownian motor. In this latter case, the probe is not constrained by a torsion suspension, and this allows us to observe the torsional constraint arising purely from the interaction between the probe and the vibrated granular material.

We have, for the first time, provided a direct evidence that the dynamics of such a system is well described by the Brownian motion model. Further analysis and comparison with a very simple constrained random walk allows us to interpret the dynamics of the probe as a fractional Brownian motion, with a well defined Hurst exponent.

In effect, a torsion probe immersed in a vibrated granular system behaves as an anomalously diffusing brownian-like particle. The Hurst exponent depends on the intensity of the vibrations imposed on the granular medium, and, if present, on an externally imposed constraint. In general, we observe that at high vibration intensities the system is superdiffusive and is eventually dominated by convection, while at low vibration intensities it describes a constrained random walk. If there is no significant externally applied torque, as is the case for the brownian motor setup, an intermediate region appears where the probe exhibits regular (non anomalous) diffusion.

This normally diffusing region is not present in the data obtained with the torsion pendulum, where the Hurst exponent is always smaller than 0.5 in the $1 < \Gamma < 2$ range. This means that the system becomes sensitive to the constraining effect of the suspension wires.

Finally, in both cases, these data systematically show an Hurst exponent smaller than 0.5, when Γ is sufficiently small, which is related to a constrained random walk. It is interesting to notice that, in these conditions, inertial effects are negligible (which would be signaled by an Hurst exponent greater than 0.5).

5

Perspectives

5.1 Introduction

In the previous chapters we have shown different dynamic approaches to the study of weakly vibrated granular media. In order to complete the description of the jamming transition, starting from the fluidization limit and down to the completely still, frozen conditions, it is necessary to study accurately an unperturbed granular sample. Unfortunately, this goal proves to be very complicated, if only using the techniques developed for the weakly vibrated conditions. To address this problem, two different approaches were tested, and will be discussed in this Chapter, which is composed of five parts.

In the first part, the main properties of an unperturbed granular system are briefly reviewed, especially in the light of the problem it presents to the measurement of its mechanical properties.

The second part of the *Perspectives* is devoted to a detailed description of an imaging technique that allows the reconstruction of a three dimensional granular medium. The method is thoroughly reviewed; also, a few preliminary but very promising results are shown. The possible further developments of this technique are vast and intriguing, and a brief panoramic is presented.

The chapter continues with another possible approach to the study of aging granular media, using the torsion oscillator. In the ideal case, being able to perform both measurements should be possible, and we propose the possible advantages of a paired measurement.

The fourth part focuses on the vibrated states around the fluidization threshold. The higher sensitivity of the installation used in this work allows to investigate this region. This allows to compare our technique with other approaches [197] and to complete the compilation of a phase diagram that shows the possible behavior of vibrated granular system, from the strongly vibrated regimes to the complete dynamical halt.

Finally, the fifth part presents a few other interesting ideas and observations that arose during the development of this work, and that we felt were interesting enough to be mentioned here.

5.2   Jammed granular media

The experimental evidence discussed in Ch. 3 and 4 indicates that a unique control parameter $a_s = \sqrt{\Gamma}/\omega_s$ dictates the main characteristics state of weakly vibrated granular media. In particular, in the jamming regime, the characteristic time scale of the system can be calculated, and is a function of this parameter. The functional form of this relationship is identical to the one describing thermally activated phenomena, in VFT terms. As the perturbation parameter decreases, the system evolves towards a frozen state, because the characteristic time diverges. Because of this divergence, the experimental approaches used in this work, due to their dynamic nature, do not allow access the region $\sqrt{\Gamma}/\omega_s \leq 10^{-4}$. This approximate value marks the point below which the system is too jammed to allow dynamic measurements, at reasonably short time scales.

The behavior of an unperturbed granular system is, on the other hand, a very interesting subject on itself. In fact, with respect to our results, a deeper knowledge of the overall characteristic of the intergranular chain of forces would allow the development of more detailed microscopic models, and clarify the relative importance of the different parameters that appear in the calculations. More in general, the main goal of these measurements is to fill the knowledge gap that currently exists between the two extremal description of granular media: on one side, the picture given by the grain-grain interactions; on the other hand, the granular system as a bulk material with its large scale rheologic properties [226].

Even more importantly, unperturbed granular media are excellent model systems that have been explored to study open problems of rheology and non-equilibrium statistical mechanics [227, 228, 229, 108]. The interest in studying unperturbed granular materials as models for non equilibrium thermodynamic system started with Edwards [230]. He proposed a thermodynamic analogy where the mechanically stable configurations of a granular material play the role of *inherent structures*, as those proposed by Goldstein [107]. In standard glassformers close to undergoing freezing, the viscosity diverges and the diffusivity approaches zero. This phenomenon can be explained by considering a progressive build up of geometrical constraints [110, 104] that reduce the available phase space. The mechanically stable configurations represent then the analogy to the potential local minima of the phase space of "real" systems. The general idea [231] is that if one could understand in detail which configurations are accessible from other configurations, and how rapidly the transition from the two configuration can occur, then this could provide with strong insights on how to relate to thermodynamical concepts.

5.3   MRI imaging of granular systems

Most of the information regarding a static granular pile depends on the geometric placement of the constituting elements. For this reason, it would be ideal to be able to observe this geometry for a large number of granular samples, in a systematic way. If this were possible, the knowledge of their geometry could be used to extract informations related to the different history of each sample.

In itself, the study of granular media using image reconstruction techniques is not completely

new. Kawaguchi [232] has recently and throughly discussed the state of the art of experimental setups and results. In recent times, the most successful experimental results were obtained by Aste et al. [233] using X-ray tomographic imagery.

All the experimental approaches used before, however, are limited by some key factor: precision, time required to perform the reconstruction, costs. To this end, we developed a precise, reliable and fast method to measure the exact position of the constituting element of a model granular medium. A standard Magnetic Resonance Imaging (MRI) technique was employed, and applied to granular samples composed of approximately 10^5 spheres.

In the past, MRI was also already considered. However, mainly due to resolution constraints that could not be overcome, the MRI approach was only used to study average dynamics of flows in granular media. The main objective of this Chapter, however, is to show that using existing technology and non dedicated hardware it is possible to extract and reconstruct the complete 3D structure of a millimeter sized granular sample, with unprecedented precision. This approach also offers many practical advantages that would allow, in principle, a systematic application to a large number of samples. In fact, the MRI is performed using a clinical MRI scanner: its specifications allow a quick analysis (complete reconstruction is obtained in the time scales of hours).

Finally, once the structure of the granular medium has been reconstructed, it becomes necessary to extract all the important informations that are hidden in it. In this Chapter, we will only show a few key results obtained from rather small samples; however, these already illustrate the scientific possibilities opened by this approach. We anticipate that our first results, obtained with smaller, unprepared samples already indicate that this method allows to reach accuracy values at the level of current state of the art measurements indicated in the References.

5.3.1 Sample details

During Nuclear Magnetic Measurements (NMR), the standard borosilicate glass spheres used in the previous experiments need to be replaced with a different material. The most important reason being that most glassware materials are not compatible with MRI measurements. In fact, the impurities contained in glass, when exposed to the electromagnetic fields of a NMR experiment, interact with it and induce local perturbations that make the reconstruction impossible.

To solve this problem, the glass spheres were therefore replaced with a polymer based equivalent medium. The main requirements for the plastic matrix were: high density, to reduce the hydrostatic Archimedean lift due to the contrast medium, and good surface hardness, to prevent a rapid degradation of the surface (which in turn strongly influences the behavior of the granular medium). The best compromise between these mechanical properties, MRI compatibility and a narrow dispersion in size was found in the samples made of Polyoxymethylene. In the following we will consider a granular sample composed of 3 mm Polyoximethylene spheres. The spheres are used as components for ball bearings, and were provided by *R.P.G. International*, Italy. In this case, the plastics is sold under the commercial name of "Delrin".

The reconstruction of the three dimensional structures, and subsequent data analysis are
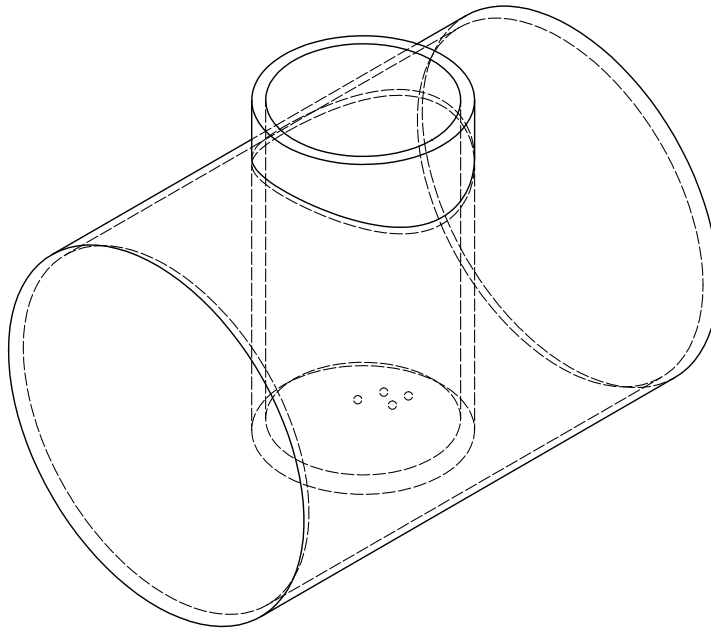
Figure 5.1: Sketch of the experimental sample and container (often called "phantom" in MRI). The vertical cylinder holds the sample composed of plastics spheres (the sample), immersed in a $CuSO_4$ solution that acts as contrast medium. Due to the small quantity of water present in the sample, with respect to the scanner design specifications, it is necessary to increase the load of the scanner coil. The coil is conveniently loaded by approximately two liters of deuterium dioxide (D_2O), placed in the exterior horizontal cylinder. The cylindrical shape of the external container allows easier shimming of the magnetic field inside the scanner.

extremely sensitive to the size dispersion of the medium. For this reason, the narrow dispersion of the sphere diameters is required. The average beads volume has been measured directly, to verify the size distribution and to check the nominal value. Differential volume measurements allows to obtain a value of $V_b = 14.348$ mm^3 and thus a diameter $d = 3.0148$ mm. The measured volume differs by about 1.5% of the nominal volume, and this must be taken into account in the following calculations.

The granular sample is placed in a special container that was designed to adapt to the specification of the MRI scanner, while allowing easy manipulation of the granular sample. The plastic spheres show a very small NMR echo. The measurements are performed in the negative, and the sample is immersed in a water solution of $CuSO_4$. The salt is used to control the NMR relaxivity of water protons (T_1). A sketch of the container and the granular material is shown in Fig. 5.1.

The sample is scanned with a Varian $7T$ clinical scanner; its specifications dictate the requirements in the design of the "phantom"[1]. The measurements are performed using a standard, single channel NMR coil. The 3D images are obtained using a MRI technique called Gradient Echo Imaging (GRE). Further details on the MRI technique can be found in a number of good

textbooks; for example, consider [234].

The final output of the measurement with the MRI scanner consists in a 3D matrix, each element of which represents a voxel. The matrix contains the water density map of the sample: an high value at a point means a high water content in the corresponding voxel, while a low value mens a low water content. This matrix is often represented as an image: in this case, bright pixels correspond to high water density and indicate the space outside the spheres.

5.3.2 Reconstruction technique

The analysis of the raw data matrix $\mathbb{I}_r(x, y, z)$ is performed directly in a three dimensional space. This ensures the highest possible accuracy in the reconstruction. To this end, specific software routines were written to perform all the necessary computations, as it will be discussed in the following.

First, a binary local thresholding is applied to the raw data matrix. This thresholding is used to remove the eventual noise in the measurement and to prepare the sample for the subsequent steps of the analysis. Every voxel is compared to the maximum and minimum value of other voxels at a distance lower than a certain radius.

$$T(x, y, z) = \left(\max\left(\mathbb{I}_r(x', y', z') \right) - \min\left(\mathbb{I}_r(x', y', z') \right) \right) \cdot t + \min\left(\mathbb{I}_r(x', y', z') \right) \tag{5.1}$$

where: T is the threshold value for the examined voxel (x, y, z); $0 < t < 1$ defines the relative strength of the thresholding; and R_T is the threshold radius used: $\left| (x - x', y - y', z - z') \right| < R_T$. A thresholded matrix $\mathbb{I}_t$ is therefore constructed. Each voxel of $\mathbb{I}_t$ is set to 1 only if its value is below the threshold, 0 otherwise. This can be written as

$$\mathbb{I}_t(x, y, z) = \theta\left(T(x, y, z) - \mathbb{I}_r(x, y, z) \right) \tag{5.2}$$

where: $\mathbb{I}_t$ is the thresholded matrix and $\theta(\cdot)$ indicates the Heaviside function.

As already noted, all these calculations are performed in the 3D space. However, slices of the matrices can be shown to demonstrate the method, and to assess the quality of the measurements. An example slice is shown in Fig. 5.2. More in detail, Fig. 5.2 (**left**) shows a comparison between a slice of the raw data matrix, and the corresponding thresholded data. As it can be seen, the observed mismatch is very low.

Afterwards, a thresholded spherical Hough transform [235] in real space is applied to $\mathbb{I}_t$ (Eq. 5.2). The Hough transform is used to detect and isolate the agglomerate of voxels of spherical shape in the data set. The transform is implemented as follows. First, the sum of the values of $\mathbb{I}_t$, within a certain distance from the voxel (x, y, z), is calculated. Then the corresponding voxel of $\mathbb{I}_H$ is set to 1 only if the number of active voxels is bigger than a certain fraction of the total volume h; otherwise it is set to 0. This corresponds to the following definition:

$$H(x, y, z) = \sum \mathbb{I}_t(x', y', z') \theta\left(\left| (x - x', y - y', z - z') \right| - R_H \right) \tag{5.3}$$

---

[1]Often, in MRI measurement, the term "phantom" indicates a generic inanimate sample or equipment for instrument testing purposes.
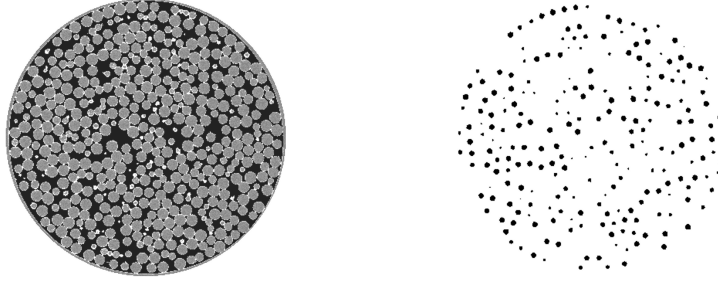
Figure 5.2: MRI of the granular sample, examples. **Left**: false colors image showing the recognition of a slice of data. The tones of gray indicate the differences from raw data and the corresponding thresholded image (used to binary discriminate between water and spheres). Grey areas indicate a match between the as-measured slice and the thresholded slice in a region of low water signal. Vice versa, black areas indicate a match in a region of high water signal (the space between the spheres). White pixel indicate a low match. The raw data obtained present a very high Contrast to Noise (CtN) ratio. **Right**: the image shows the corresponding slice in the Hough-transformed 3D data matrix. The black circles indicate sections of the Hough-transformed spheres.

where H is the value of the spherical Hough transform with a radius of R_H. The Hough transformed matrix is then computed as:

$$\mathbb{I}_H\left(x, y, z\right) = \theta\left(\frac{H\left(x, y, z\right)}{n_H} - h\right) \tag{5.4}$$

where: $\mathbb{I}_H$ is the image after the thresholded hough transform; n_H is the total number of voxels that are found within the sphere of radius R_H; and h is the threshold value. An example slice of the Hough-transformed matrix is shown in Fig. 5.2 **Right**.

The experimental data show a very high Contrast-to-Noise ratio: $CtN \approx 10$. No further data refinement procedure is needed in this case, while more complex workflows (oversampling and rescaling) have been tested to operate on smaller samples. The parameters used in the reconstruction for the sample shown here, with d the measured diameter, are $R_T = 1.5d$, $t = 0.5$, $R_H = \frac{d}{3}$ and $h = 0.975$.

After this treatment $\mathbb{I}_H$ (Eq. 5.4) shows almost spherically-shaped agglomerates of voxels, separated by more than $\frac{d}{4}$. These agglomerates are then associated to a sphere the center of which is defined to be center of mass of the agglomerate. The resulting three dimensional structure of the sample under consideration can be seen in a Computer Generated Image (CGI), in Fig. 5.3.

In order to ensure perfect reconstruction of the sample, different quality checks have been implemented. During the reconstruction, assignment of isolated voxels as spheres is avoided, together with possible errors coming from misshaped or connected agglomerates. After the
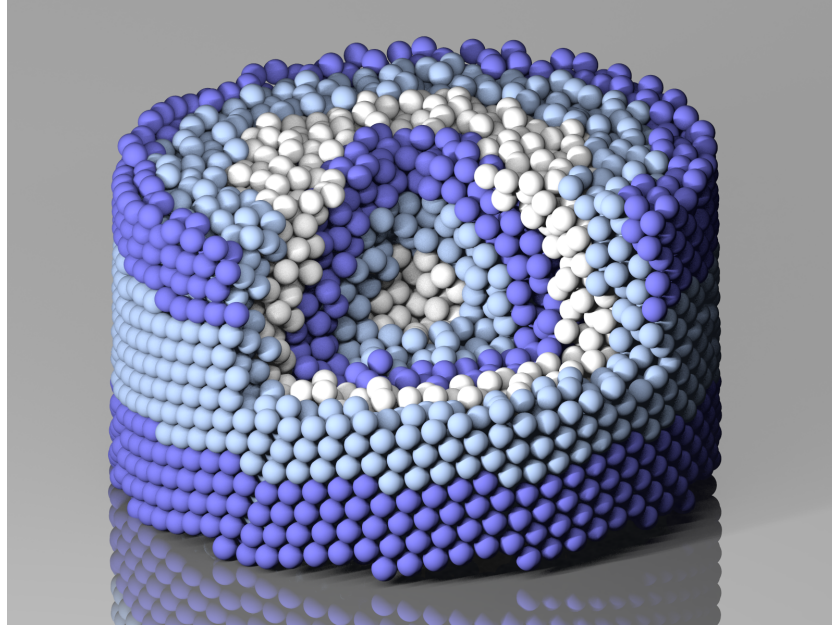
Figure 5.3: CGI representation of a granular sample. The image shows the reconstructed three dimensional structure of the sample. One eighth of the sample is not rendered to show the geometry of the central part. The color code (white, light blue, dark blue) is used to highlight the distance of each particle from the barycenter of the sample.

reconstruction, the data matrix is checked *a posteriori* to exclude the presence of agglomerates that were not assigned to a sphere.

The precision of the reconstruction is tested in two ways:

- within a single dataset, the nearest neighbor distance r_{nn} of every bead has been calculated. The distribution of r_{nn} shows a gaussian peak centered in d with a standard deviation $\sigma_{r_{nn}} = 14 \mu$m. This translates to an absolute error in the single bead positioning of $\sigma^1_{\vec{x}} = 10 \mu$m.

- two dataset of the same sample were acquired sequentially, reconstructed and then compared. A bead-per-bead displacement was computed. Also in this case the displacements between corresponding sphere pairs were found to be gaussian distributed. The corresponding standard deviation is found to be $\sigma_{\vec{x_1}-\vec{x_2}} = 12 \mu$m and again this corresponds to an error in the single bead position of $\sigma^2_{\vec{x}} = 8 \mu$m.

In these expression σ^1 contains both the dispersion of the beads d (less than 10μm) and the pure experimental error σ^2. Although this error is about 5 times higher than the one reported in previous experiments [236], the calculation shown here is derived from a direct measurement, rather than an ad-hoc estimate. For this reason, we consider this estimation to be more reliable.

5.3.3 Data analysis

The analysis of the previous sections allow the calculation of the positions of the spheres in the sample with a high degree of accuracy. Starting from this information, many interesting properties can be computed. In the following, we will discuss the two-body correlation function, the so-called Steinhardt order parameters, and the number of nearest neighbors.

Correlation function

The first quantity discussed here is the the two-body correlation function of the sample. To extract the maximum possible amount of information from the experimental data set, we followed the method proposed by Scott [237]. There the correlation function is computed up to a large amount of diameter lengths; this is made possible by the computation of an asymptotic long range correction. This idea can be extended using computers, and by calculating the exact correction for each particle, instead of a general asymptotic one.

The computation of the exact correction to the correlation function allows to measure it over a range of over $12d$. In turn this is very interesting, because it allows to precisely measure the exact bulk beads density independently on the boundary conditions. Furthermore, due to its rather rapid convergence (rapid with respect to the number of considered particles) this method allows to extract the bulk density of small agglomerate, and could in principle be used to study "mesoscopic" local fluctuation of densities.

The two-body correlation function is calculated, following [237], with the following steps.

1. The dataset is cropped, removing the outer regions that are under the influence of the boundary conditions imposed by the container walls and base. This defines a region in space, or Volume of Interest (*VoI*).

2. For each bead in the VoI, spherical shells are generated. They are are centered in the bead center and of increasing size. Each progressive spherical shell is intersected with the VoI.

3. The number of beads centers contained in each intersection in step (2) is counted and divided by the volume of the intersection.

4. The previous steps are repeated all the beads and for all the spherical shells. The thickness of the shell is chosen small enough to conserve detailed information, but large enough so that there is a reasonable amount of centers in each intersection.

The resulting function is then averaged over the sample and normalized to obtain the distribution function $\rho(r)$. This procedure is expressed in mathematical form in Eq 5.5. The expression at the numerator represents the number of all the beads centers found in the spherical shell. The denominator indicates the volume of the intersection between the spherical shell ("Ssh") centered in $\vec{r}_i$ and the VoI. The value of the shell thickness is indicated by δ, and as mentioned above it is chosen in order to have a good compromise between resolution and noise.

$$\rho(\frac{r}{d}) = \frac{V_b}{N_b} \sum_{i=1}^{N_b} \frac{\sum_{j \neq i} \theta(|\vec{r}_j - \vec{r}_i| - (r - \delta)) - \theta(|\vec{r}_j - \vec{r}_i| - (r + \delta))}{V(Ssh(\vec{r}_i, r - \delta, r + \delta) \cap VoI)} \tag{5.5}$$
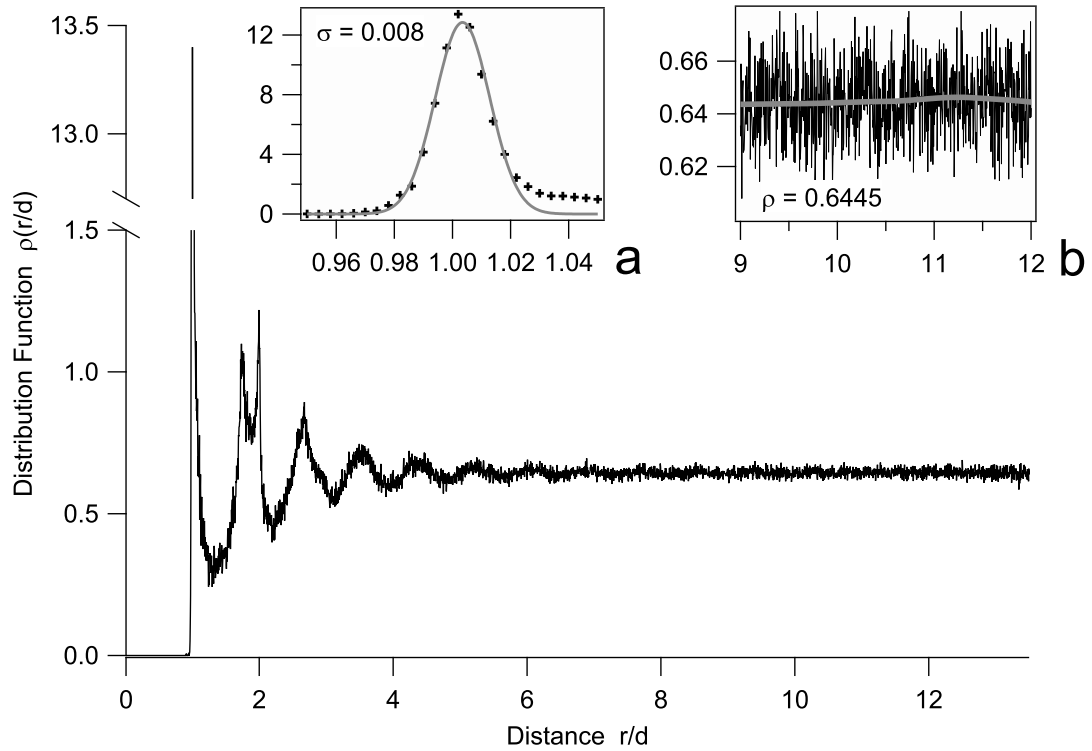
Figure 5.4: Correlation function $\rho(\frac{r}{d})$ for the granular sample of Fig. 5.3. The actual VoI is shown in Fig 5.8 **Left**; it corresponds to a cylinder of radius $5d$ and height $10d$ (d is the sphere diameter); it is composed of approximately 4000 spheres. Inset **a** shows a detailed view of the peak at $r/d = 1$, and a gaussian fit (grey curve). Inset **b** shows the high $\frac{r}{d}$ region: here the oscillation of $\rho(\frac{r}{d})$ are smaller than the noise and the density can be measured. The horizontal gray line represents a smoothing of data.

The innovative part in this work is represented by the method used to compute the ρ function. In the past, the computation of the distribution function had to be stopped at a value r_{Max}, corresponding to the maximum distance from the particle at which the corresponding spherical shell starts to be partially outside the VoI. This has the disadvantage of neglecting all the information coming from all the particles found at a distance $r > r_{\text{Max}}$.

This problem is resolved by exactly determining the volume of the fraction of the shell that is still contained in the VoI. This choice allows to stop the calculation once the spherical shell has completely outgrown the VoI. The resulting correlation function for the sample under consideration is shown in Fig. 5.4

The main graph shows the complete correlation function: it is stable up to almost $14d$. The exponential decrease of the oscillations can be used to compute the spatial correlation length. For this sample, the characteristic length is $L_c \sim 1.4d$.

Looking at larger distances, as shown in inset **b**, allows to compute $\rho(\frac{r}{d})$ very precisely. More specifically, the sample under consideration (a cylinder of radius $5d$ and height $10d$, containing about 4000 beads centers) allows to define the granular density ρ_0 with an unprecedented

precision.

It is important to underline that this definition, provided that the long range isotropy hypothesis holds, is free of effects due to the actual shape of the VoI used. For this reason it can be applied to different parts of the sample, for example to study the density fluctuations as a function of height. As noted in previous section, this method requires a very accurate measurement of the average particle volume V_b. The precise measurement of V_b is extremely important because the dependence of the computed density ρ_0 on it is much stronger than the effects of experimental error.

Finally, inset **a** shows a detailed view of the peak at $r/d = 1$. The exact shape and width of the peak depends on the experimental error in the reconstruction of the structure, on the width of the distribution of the radii of the spheres and on the true distribution of distance at $r/d > 1$. This part of the correlation function therefore can be used to estimate the average number of *mechanical* contacts in the granular system. In general, the distribution of the nearest neighbors (not necessarily in contact) is also a problem of extreme event statistics. In short, once the experimental distribution of sphere pair distances is given, it means to calculate the probability to find the nearest particle (between the nearest possible $n \leq 12$ neighbors) at a distance $b \geq 0$. Since all the other factors can be estimated, and using the knowledge of the distribution of the nearest neighbors, it is possible to directly fit the peak at $\rho(\frac{r}{d} = 1)$, and to determine the average amount of spheres found exactly at distance equal to d without using any other hypothesis. Although this method cannot be applied to a specific particle, it provides a good estimation of the number of the average mechanical contacts for large enough regions.

Voronoi volumes and Steinhardt order parameters

In the previous sections we have discussed the parameters that can be extracted from the measurement of the correlation function ρ. The main strength of this method lies in the fact that the large amount of averages keeps the noise level low. Unfortunately, this averaging nature also represent its main limit, because it does preclude access to the single particle details of the sample.

This problem can be overcome in a straightforward way using Voronoi volume decomposition. The Voronoi analysis relies on the local geometric properties of the sample, rather than on quantities extrapolated by large scale observations. This is the main reason that makes Voronoi analysis a very robust technique, and why it its useful to define local order parameters. As an example, two observables that depend on the local structure, and that can be computed from the reconstructed data, are the Steinhardt order parameters [238], also indicated by Q_6 and Q_4. The Voronoi decomposition and the Steinhardt order parameters are discussed more in detail in Appendix E.

The exact determination of Q_6 and Q_4 is performed in the following way. For each sphere the following parameters are calculated:

- the Voronoi volume of the particle;
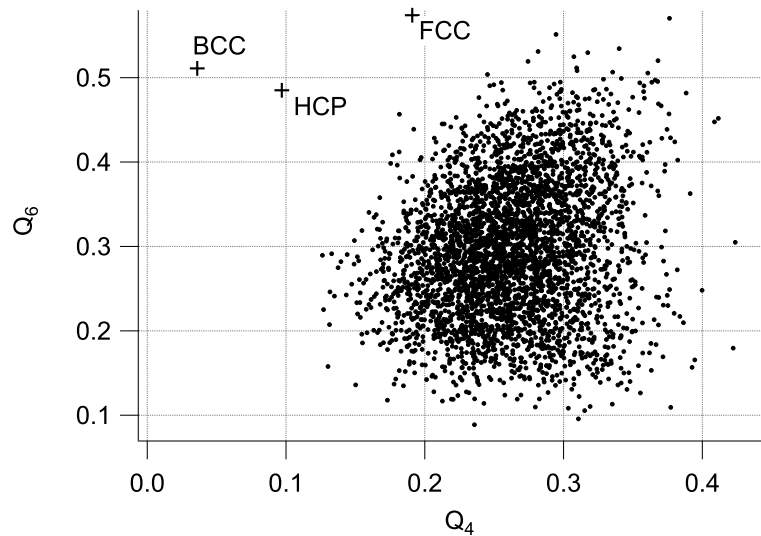
Figure 5.5: Scatter plot of the Steinhardt order parameters representing the sample under consideration. Each black dot represents the position of each particle in the Q_4, Q_6 space. The values corresponding to regular lattices (HCP, FCC and BCC) are indicated by the gray markers.

- the number of geometrical nearest neighbors defined by the Voronoi space decomposition;

- the values of Q_6 and Q_4, again using the geometrical neighbors determined by the Voronoi decomposition.

This technique allows to assess the presence of ordered structures in the bulk of the sample. The strictly local nature of this approach has the advantage that it allows a direct interpretation of the meaning of the order parameters associated to each sphere. For example, if one considers a bead enclosed in a full crystalline shell (for example, HCP or FCC), the values computed for Q_6 and Q_4 will coincide to the ones expected for a crystal (except for the effect of the noise). Also, the computation of Voronoi volumes allows the definition of a "single particle density", that is in fact the ratio between the volume of the sphere V_b (considered constant), and the volume of the Voronoi cell corresponding to the sphere.

Once the sample is decomposed in Voronoi cells and the Q_6 and Q_4 parameters have been computed, the simplest way to present them is to show a scatter plot for all the particles. This is done in Fig. 5.5, where the X and Y axis represent respectively Q_4 and Q_6. Each black dot represents a sphere in the sample If the data are compared to the expected values for regular lattices (indicated by the gray markers), it is clear that no particle is part of localized regular structure. Instead, it appears that the whole sample is located quite far away (in Q_4, Q_6 space) from the ordered structures.

Another interesting way to study the data shown in Fig. 5.5 is to plot a frequency count (computing the histogram of the relative frequencies) of the Q_4, Q_6 data. This is shown in Fig. 5.6, where the color codes blue, green, yellow, red and white represent an increasingly high amount of particles with similar values of Q_4 and Q_6.

Figure 5.6: Image plot of the frequency count of Steinhard order parameters. The image allows to characterize the relative frequencies of given intervals of values for Q_4 and Q_6. Fig. 5.6 (**a**) shows the data corres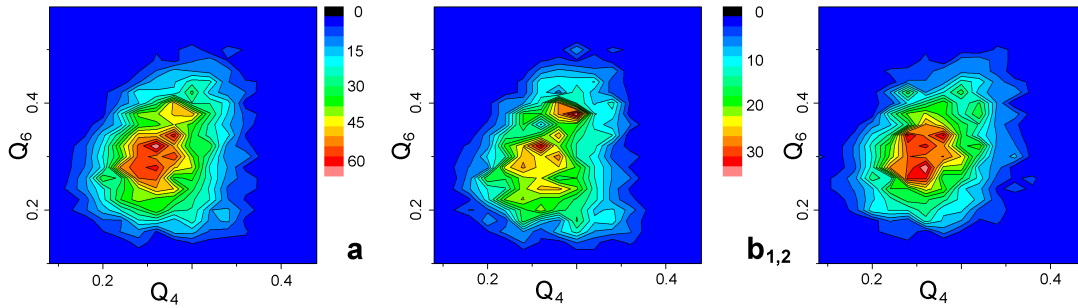ponding to the spheres in the complete VoI. Fig. 5.6 (**b** 1) and (2), on the other hand, show the data corresponding to the particles found in the upper and lower half (respectively) of the VoI. Data are obtained considering a binning of 0.02 for both parameters.

The upper an lower part of the VoI, as shown in Fig. 5.6 (**b** 1 and 2), clearly indicate the presence of points where the beads described by a given pair (Q_4, Q_6) accumulate. The peaks appear to be different for the two halves. This behavior suggest that the beads that share similar values may be localized in space. When considering the total VoI, shown in Fig. 5.6 (**a**), it appears that the peaks are averaged out and a smoother, more complex shape is observed.

The changes in the distribution of the Steinhardt parameters indicate that the two halves of the VoI possess different geometrical properties. The distribution of the volumes of the Voronoi cells also shows a very interesting behavior. Fig. 5.7 shows the relative fraction of particles as a function of the Voronoi volumes. The three curves show respectively the data for the complete VoI (black dots), the upper half (dashed line) and the lower half (continuous line). Most of the spheres have a single particle density very close to the average density of the sample (ρ_0. However, there is a non negligible part, consisting of slightly less than the 10% of the sample (approximately 350 spheres) that have either a density higher than the random close packing (RCP) or lower than the random loose packing (RLP) [239].

It is interesting to note that the curve relative to the upper part indicates a slightly higher compaction that the lower part of the sample. This can be explained by the following consideration. The sample was not specifically prepared in a configuration of low or high specific density. During the test, it has been manipulated and gently shaken to ensure the absence of air bubbles. These weak vibrations cannot perturb the lower part of the sample, which is kept in place by the pressure of the grains above. As it is common in granular materials, avalanche-like behavior only influence the upper layers, that were the only ones having a chance to densify to higher compaction values.

Considerations on RCP

In Ch. 1, it was hinted that there is a growing concern on the fact that "random close packing" could be an ill-defined concept [34]. We consider the results shown in the previous section as evidence supporting this idea, together with the following considerations.
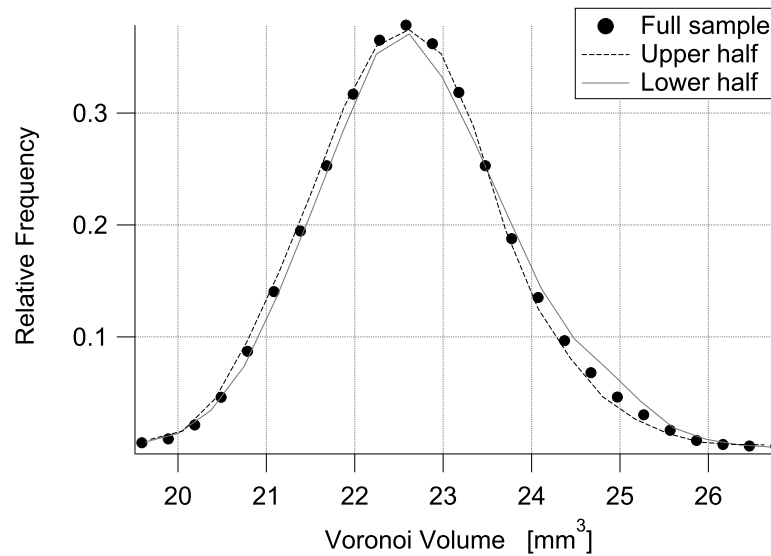
Figure 5.7: Distribution of Voronoi volumes for the spheres in the VoI. The three curves show respectively the data for the complete VoI (black dots), the upper half (dashed line) and the lower half (continuous line). The bin size is to 0.25 mm^2.

In the literature, there can be found a large variety of strategies to obtain "extremal" densities. Also, it appears that finding the "closest" possible packing is the objective of a large number of studies. Most of them are, in our opinion, fatally flawed for the following two reasons.

The first one is that most experimental results do not consider the possible presence of local crystallization. In most cases, this is because, due to the experimental technique, the structure cannot be reconstructed with complete certainty. The impossibility to check for the presence of local order, however, is a fundamental problem, because the presence of even a small fraction of microcrystals can dominate the measurement of the packing fraction. This comes from the fact that stable crystalline structures have densities much larger than the average "disordered" packing (as shown in Table 1.1), so that even small crystalline region can influence the estimated packing fraction. This problem becomes even more evident for those experimental techniques that do not safely extract all and only the particles actually present in the sample. In this case, it is easily calculated that even a missing particle over 1000 leads to an overestimation of the density of a relative error of more than 2%.

The second, largely underestimated source of error in both experimental measurements and even some simulations of packing density is the error propagation from the particle size diameters. Calculations show that a dispersion of 0.3% on particle diameters (or an equivalent error in the measurement) can fatally influence the third significant digit of the packing fraction.

These experimental observations are associated with some theoretical considerations. Mean field models seem to indicate that stable random packing can be found for a finite range of densities [240], suggesting that there is a whole "region" of compact configurations available to the system, and not just one RCP.
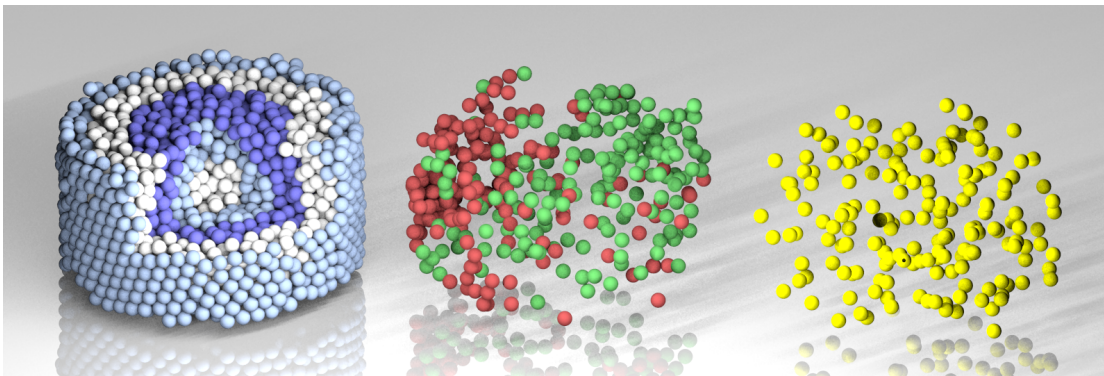
Figure 5.8: CGI generated image of the granular sample. **Left**. The image shows the spheres contained in the VoI of the sample discussed in the text, corresponding to the central part of the complete sample of Fig. 5.3. **Center**. The image represents a color code indicating the Voronoi volume of the spheres. In green, the 5% spheres that have the largest Voronoi volumes. In red, the 5% spheres that have the smallest Voronoi volumes. These colored particles correspond, respectively, to the spheres that have a single particle density smaller than RLP, and larger than RCP. **Right**. The image shows the 5% of spheres that possess the smallest values of Q_4 and Q_6.

Clustering

This section is concluded with a pair of example images that show the concept of "clustering". As discussed before, the definition of local observables allow to extract sets of particles that share similar properties. These cluster can then be isolated for further analysis, and shown with CGI images to allow a direct visual observation of the sets. As discussed before, Fig. 5.8 (**Left**) shows the spheres in the considered VoI. Fig. 5.8 (**Center**) shows a selection of spheres with correspondingly large (green) and small (red) Voronoi volumes. More specifically, the CGI image shows the 5% extremes of the distribution of Voronoi volumes; this range loosely corresponds to those particles that have a single particle density respectively smaller than RLP, and bigger than RCP. Finally, Fig. 5.8 (**Right**) shows (in yellow) the 5% of spheres with the lowest values of (Q_4, Q_6).

5.3.4 Conclusions

The preliminary results shown in this section indicate that this MRI technique can be used to study bulk characteristics of granular media. The reconstructed structure gives access to properties relevant on both large scale structures and small localized regions.

Even more interestingly, this technique gives access to characteristic properties (e.g. ρ_0, L_c, nearest neighbor and mechanical neighbors distributions, etc.) that are very important, and have been studied in details from both a theoretical and computational perspective. This technique allows a systematic and detailed comparison with both theory [241, 242, 243] and simulations [244].

Finally, the MRI approach could in principle be extended to allow a different kind of direct dynamic measurements. A few preliminary test were performed to assess the possibility

of performing particle tracking of selected particles. In this case, the sample is composed of a standard granular system, without contrast medium. In one single particle, a cavity was drilled, filled with water and resealed with glue. The water core allows to measure the position of the particle with a frequency of up to 10 Hz. These measurements are much faster than the complete reconstruction of the sample, because only one peak has to be detected. This technique, also, has very large margins of improvements if dedicate equipment were employed.

5.4 Induced aging in granular systems

In all the experiments discussed in Ch. 3 and 4, efforts were made so that the measurements did not directly influence the system under study. In other words, independently on the vibration state of the system, the experimental techniques were adapted so that all possible "transient" effect did not influence the results, as discussed in Sec. 3.3. In particular, *aging* phenomena appear to be negligible in the case of strongly vibrated systems ($\Gamma > 1$, and still does not seem to be playing a relevant role even for weaker perturbations ($\Gamma > 0.2$), as it could be observed in the experiments discussed in these Chapters.

Aging effects however become important in the case of non vibrated (better, extremely weakly vibrated) samples. In fact, all granular sample evolve as a consequence of any vibration induced through them. While purposefully induced vibrations were employed in Ch. 3 and 4, any sample undergoes aging, albeit slowly, as a consequence of being exposed to the weak vibrations of the floor (for example, by being placed nearby an active motor that vibrates another sample), or to strong ambient sounds (as during MRI scans). For example, a different aging, dependent on the depth of the layers[2], is probably the origin of the different microstructures observed in the sample of Fig. 5.6. The mostly uncontrolled preparation of the sample has allowed aging phenomena to occur.

In the standard experimental conditions of the methods discussed in this work, it is generally difficult to directly observe aging effects. During the optimization of the technique we have observed that such phenomena can, however, be highlighted using a specific preparation of the sample, and using a slightly modified experimental setup. As a perspective work, we observed the effect of aging on a freshly prepared granular sample, using the forced torsion oscillator.

5.4.1 Method

The samples under consideration are composed of glass beads of different surface state: one sample is made of smooth glass spheres, while the second one is composed of the acid etched spheres already studied in Sec. 3.4.4. The main idea was that the different roughness of the surface of the spheres in the two samples should influence the aging of the system, as very rough spheres should interlock and jam more easily than smooth, polished ones.

---

[2]As it is clear in avalanches, the upper layers of a granular medium are more mobile than the lower ones, that are more strongly locked in place by the higher pressure.

The sample was prepared in the following way. The spheres were slowly poured in the cylindric metallic container, through a small metallic funnel. As the container was filled, the lower end of the tip of the funnel was raised slowly, so that the falling beads would hit the surface of the already deposited layers with minimal kinetic energy. This recipe, discussed for example in [28, 33], is commonly used to prepare granular sample in (random) loose packing (RLP) conditions. These conditions tend to evolve towards more packed states, and are ideal to study fast aging effects.

In order to avoid aging effects due to external vibrations, the container was directly placed (without the vibration motor) on the same suspension system on which the torsion oscillator resides. This configuration protects the sample from unwanted vibrations coming through the vibration motor from the building itself. The sample is then probed using the torsion oscillator. The contact between the sample and the oscillator is done using another cylindrical probe, the surface of which is covered by (respectively) smooth or rough spheres. To enhance the sensitivity to local effects, the probe used in these experiments is smaller than the one of Ch. 3: the effective diameter is approximately 2.5 mm and the probe is immersed to a depth of approximately 20 mm. Once the sample is in position, on the suspensions, the torsion oscillator is slowly lowered, so that the probe penetrates vertically in the granular material.

Once the probe is set, the sample is ready for the measurements, that consist of forced mode measurements of increasing imposed torque. When the measurements are completed, the probe is raised again, and the granular sample is removed and prepared again with the same technique. This allows to verify that the measurements are meaningful and are not influenced by a single special configuration.

5.4.2   Results

The two granular samples are subject to forced mode measurements, and undergo measurements cycles that consist of increasing and decreasing imposed torque. The starting level of torque imposed on the probe is chosen so that it is too low to induce a significant displacement of the probe. The torque is then increased up to a given level, and then the progression is reversed. The cycle completes once the starting torque is reached. During the cycle, the increasing strain induced in the sample allows subsequent rearrangements in the granular structure. In turn, this induces energy losses in the system, and this can be observed in the response function.

Afterwards, each subsequent cycle is programmed so that the torque is increased up to a higher maximum. The loss angle (imaginary) part of the response function eventually evolves into a relaxation peak, and when the imposed torque becomes high enough the probe starts to break loose (strong decrease in the real part, or dynamic modulus, of the response function). Finally, when the breakaway conditions are found, and a maximum torque is determined, the last cycle is repeated, until no further evolution of the response function is observed.

The data corresponding to the loss angle of both smooth and rough samples, are shown in Fig. 5.9. The curves show the averaged last four cycles (corresponding to an high final torque), measured in the same experimental conditions. The data clearly indicate an aging effect in the granular system.

The top graph (smooth spheres) shows that the moving probe induces a rearrangemement in the structure of the medium. The first full peak (light gray, stopping at 2 N m) is taller than the following ones, indicating that a larger amount of energy is dissipated during this first run. Subsequent runs (darker gray tones, stopping at 4 N m) have the main relaxation peak displaced and of reduced height. The second run appears to be placed at the same, or a little higher torque, while the following ones are found at lower torque values. These effects can be interpreted in this way. After the first big rearrangement of the structure, the local density increases, because the spheres can slide easily over one another from their original loose packed conditions. This leads to a rapid increase of the density around the probe, which increases the strength required to displace again the probe. This can be seen in the corresponding dynamic modulus data, as shown in Fig. 5.10, top graph. During the first run the apparent dynamic restoring coefficient is smaller, and increases with the following cycles. The fifth cycle (not shown) does not indicate any further evolution. This can be interpreted as if subsequent rearrangements eventually end up "digging a hole", where the local microstructure finds an optimal structure that allows the probe to move with a minimal amount of successive reordering events.

The effect of aging on the mechanical response of the system appears to be significantly different in the case of rough bead surfaces. The loss angle curves are shown in the lower graph of Fig. 5.9, that corresponds to otherwise identical experimental conditions. In this case, after each run, the peaks evolve towards larger torque amplitudes, and decrease in height. By comparison with smooth beads, it is also evident that the peak are slightly higher, indicating a larger amount of dissipation, but they decrease during the cycles. The corresponding dynamic modulus data of Fig. 5.10, bottom graph, indicate a parallel increase of stiffness during the subsequent cycles of measurements. Due to the rougher surface of the spheres, this behavior can be interpreted as follows. When the system is prepared in a sufficiently loose packing conditions, it is relatively easy for the beads to slide around, even if their surfaces are not perfectly smooth. However, as the system undergoes a series of measurement cycles, the particles start to compact. As the density increases, it becomes more and more likely that the asperities of the grains induce a buildup of "locked in" structures, that interact more like gears. Therefore, successive movements need to displace an increasing amount of particles, thereby increasing the apparent stiffness of the system. The increased roughness of the surface explains the overall larger dissipation (larger loss angles), while the lowering of the peaks during the measurements indicates a progressive reduction of sliding events as the system becomes more and more interlocked.

5.4.3 Conclusion

The comparison of the two system indicate that aging effect can be studied with this technique. The high sensitivity of the installation allows to discriminate effects due to the surface state of the system, and to possibly interpret the evolution of the local structure.

It would be interesting to be able to complement the two techniques discussed here (induced aging and MRI reconstruction), to be able to link features of the mechanical response function (or of the free mode time series), with the geometric properties of the bulk structure
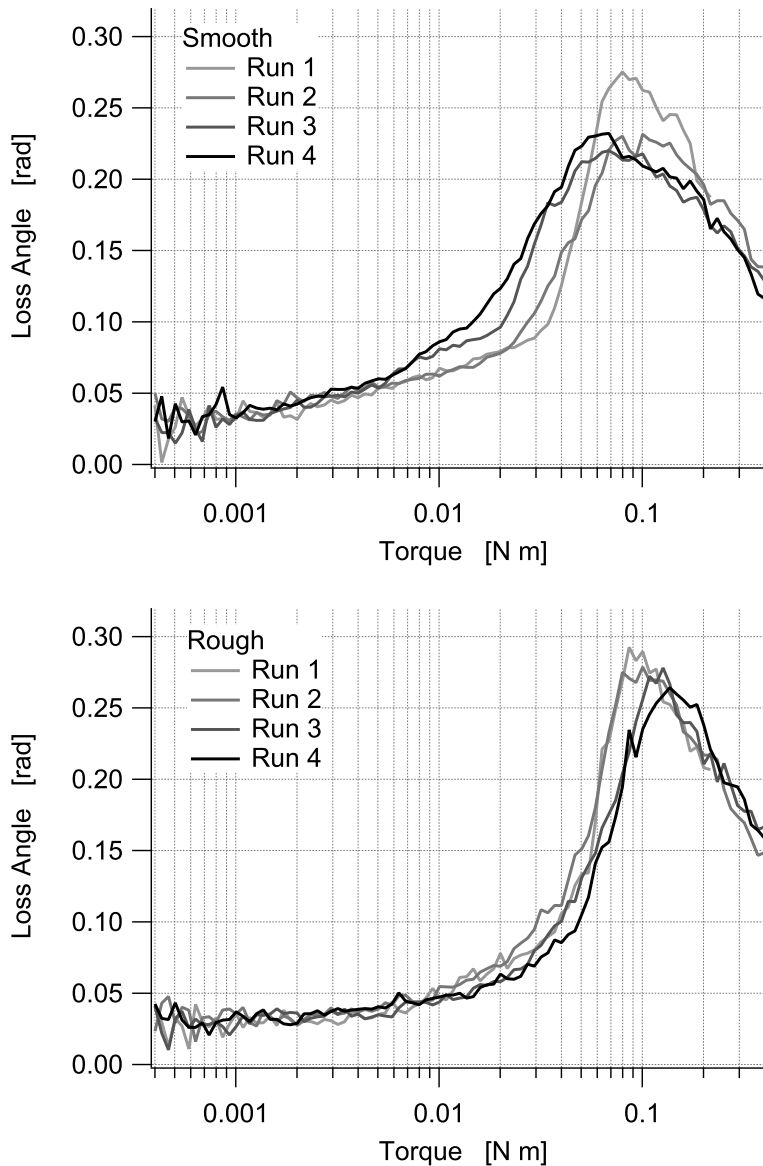
Figure 5.9: Loss angle measurements in aging granular mediums. The data correspond to granular samples composed of smooth (top) and rough (bottom) glass spheres, prepared in a loose packing initial configuration. The curves show the evolution of the loss angle as a function of the torque applied on the probe. The first cycle is indicated by the light gray tone, while subsequent ones are darker gray and black. Both samples indicate that during the experiments the system ages, and this reflects on the measured mechanical response function. The two samples indicate that the surface state of the beads has a strong influence on what happens when the sample starts to compact under the effect of the oscillating probe, as discussed in the text.

118
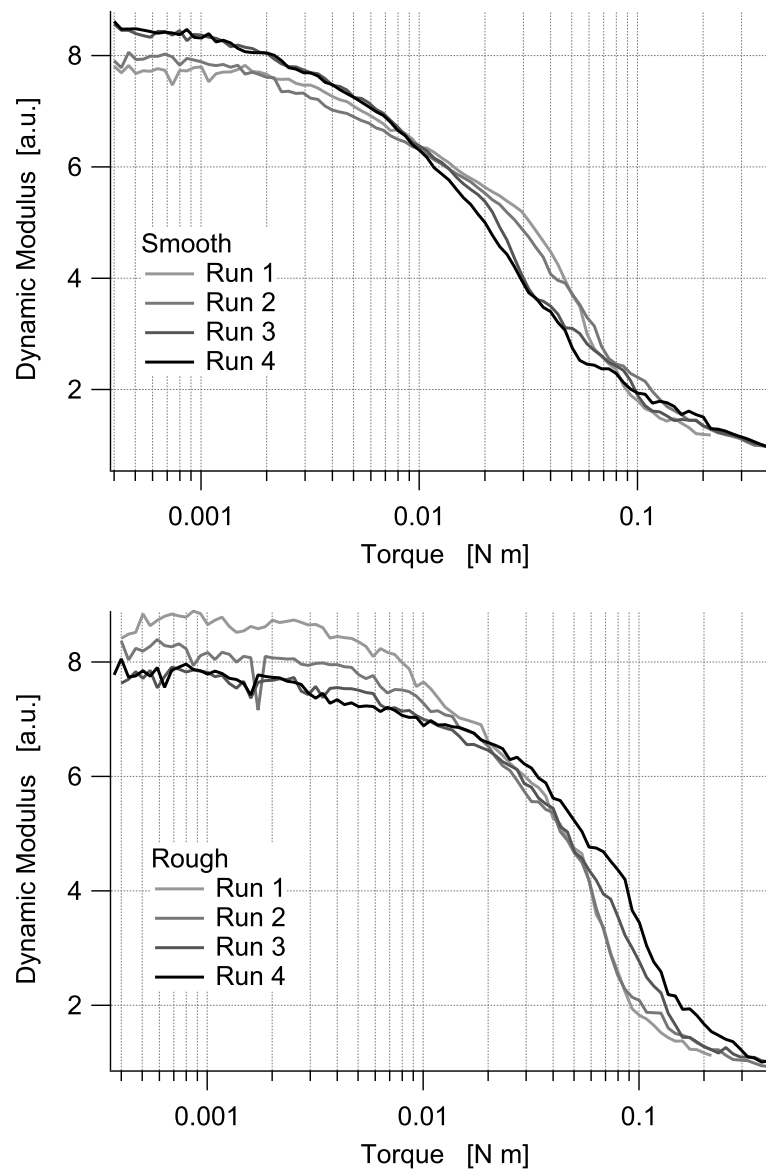
Figure 5.10: Dynamic modulus data corresponding to the loss angle curves of Fig. 5.9. Again the two granular samples show a different evolution during the measurements. In the case of smooth particles (top graph), the apparent stiffness of the system decreases with aging, while the opposite is true for rough particles (bottom graph).

119

reconstructed with MRI techniques. This would conceptually correspond to what is done for traditional materials (glasses, polymers, alloys and ceramics) that are studied today, by both a mechanical response technique and by microscopy and structure diffraction analysis.

5.5   Above the jamming transition

In Ch. 3 and 4, most of the experiments that have been discussed were focused on studying the behavior of granular system in the dynamic regions below $\Gamma = 1$, where the jamming transition is observed. This Perspective departs slightly from this approach, and shows that the same experimental techniques can be used to characterize the behavior of the vibrated granular medium just above the fluidization threshold. This is interesting for two reasons. First, the accord observed with respect to different experimental approaches [197, 245, 196] suggest that our results are really meaningful. Second, as will be discussed in the Conclusions, a wide range of different experimental conditions is now accessible, and this can be used to compose a possible phase diagram for vibrated granular media.

The key idea is the following. The data sets shown in Fig. 3.5 or Fig. 3.6 contain detailed information on what happens to the granular system as it crosses the jamming transition. The region corresponding to higher Γ values were smoothed numerically, using a box averaging algorithm, to improve readability, and the results are shown in Fig. 5.11. It is worth noting now that in this section, the data corresponding to the phase measurements are presented as "loss tangents" ($\tan(\delta)$), instead of loss angle δ. This makes it simpler to relate to the rheologic models that are used to interpret the data.

The behavior of the system above the jamming clearly shows two distinct regimes. In the case of the lower excitation frequencies, after the large decrease due to the glass transition, the dynamic moduli tend to reach an asymptotic value. This value corresponds to the elastic coefficient of the torsion suspension: in this situation, the stiffness of the granular system becomes negligible.

On the other hand, if the frequency of the pendulum is higher, the measured moduli do not tend towards a constant value. In this case, the probe is still sensing the effects of the grains. The corresponding internal friction curves, though noisier, show a similar behavior: for small frequencies the loss angle becomes almost constant, while it is higher, and decreases with increasing Γ, for high frequencies.

5.5.1   Two, different, high Γ regions

If one considers the loss tangent and dynamic moduli data of Fig. 5.11, the experimental curves suggests that the response of the granular media has a non trivial dependence on both the vibration intensity parameter Γ and the frequency of the imposed torsion oscillations f_p. In the following we will consider the pulsation $\omega_p = 2\pi f_p$ (not to be mistaken with the vertical vibration frequency and pulsation $\omega_s = 2\pi f_s$ described in Ch. 3).

As the vibration intensity is increased, it is clear that the granular system becomes more and more fluid-like, and its characteristic relaxation time decreases. On the other hand, the faster
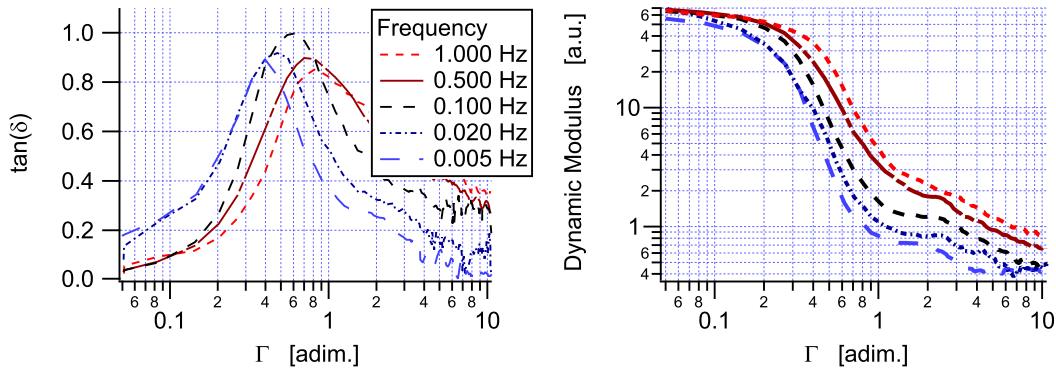
Figure 5.11: Loss tangent ($\tan(\delta)$) and dynamic moduli of the vibrated granular system, plotted as a function of the vibration intensity Γ, for different values of the frequency of the forced oscillations f_p. In the fluid region, for high values of Γ, two different trends are observed. At low frequencies, the mechanical loss becomes very small, and the corresponding dynamic modulus approaches the spring coefficient of the torsion suspension. On the contrary, for high frequencies, even at the highest vibration intensities the amount of internal friction stays high, and the dynamic modulus curves show that the granular shows a residual stiffness.

the probe moves, the more the pendulum becomes sensitive to the apparent stiffness of the granular medium.

The opposite effect of the two parameters can be seen more clearly in Fig. 5.12, where $\tan(\delta)$ is plotted as a function of the control parameter ω_p/Γ^2. This parameter is interesting for two reasons. The Γ^2 term was chosen because it has been shown [196] that in the fluid case, an effective temperature could be defined with a functional form $T_{\mathrm{eff}} \propto \Gamma^2$. In this interpretation, therefore, the control parameter (abscissa) is inversely proportional to this effective temperature.

Secondly, the presence of ω_p at the numerator makes all the curves collapse on a single one (master curve). In the graphs of Fig. 5.12 two rather different regions are found, and are indicated by (**a**) and (**b**).

5.5.2 Regime (a): high fluidization

For high Γ and low ω_p, $\tan(\delta)$ increases with decreasing Γ. Despite a rather large dispersion in the data set, fitting these curves suggests that $\tan(\delta) \propto \omega_p/\Gamma$. This is shown in Fig. 5.12, for two different data sets ($f_p = 0.005$ and 0.01 Hz).

Since the loss tangent is proportional to the pulsation, a linear model can be used to model the system. In this case, the system behaves like a Newtonian fluid, and the simplest choice for a model is shown in Fig. 5.14**a**.

The stiffness K_p of the torsion suspension is known, therefore the defining equations of the model can be solved to compute the internal friction, Q^{-1}. The solution is given by $Q^{-1} = \eta\omega_p/K_p$, where η indicates the *apparent* viscous coefficient. Then, solving for η one
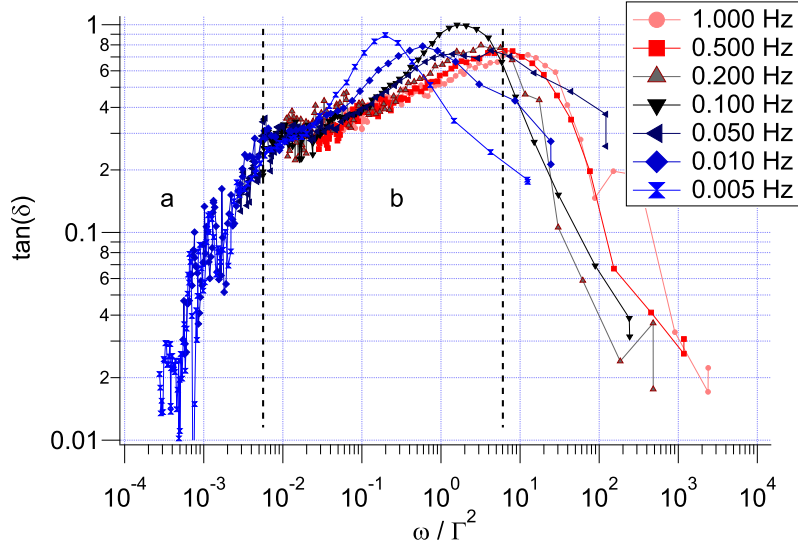
Figure 5.12: Fluid phase; $\tan(\delta)$ plotted as a function of ω_p/Γ^2. The data show that in the fluid phase there are two different regimes, delimited by the dashed lines and indicated with (**a**) and (**b**).

finally obtains:

$$\eta = Q^{-1}K_p/\omega_p \tag{5.6}$$

Now, the value of the internal friction is known from the experiment, and $\tan(\delta) \propto \omega/\Gamma$ can be substituted for the analytical expression of the internal friction in Eq. 5.6. This gives the following result: the apparent coefficient of viscosity is inversely proportional to Γ: $\eta \propto 1/\Gamma$ (Fig. 5.15).

This fact is very interesting, because it is in good agreement with a previous empirical observations obtained with a completely different exploitation of a similar oscillator [245]. Considering the analogy $T_{\text{eff}} \propto \Gamma^2$ described by [196] one can infer that the apparent viscosity varies as $\eta \propto 1/\sqrt{T_{\text{eff}}}$, which could be used as a starting point for modeling.

5.5.3 Regime (b): low fluidization

For high Γ and high ω_p, the data show that the behavior of the system changes considerably. In this situation, the Newtonian fluid picture is no longer correct. Fig. 5.12 (**b**) shows that in this region all the curves collapse on a straight line. This unified behavior remains valid (as the ratio ω_p/Γ^2 increases) until each of the curves reaches the glass transition at $\Gamma = 1$. From data fitting, we obtain the empiric power law $\tan(\delta) \propto (\omega_p/\Gamma^2)^\alpha$ with $\alpha = 1/6$. It is reasonable to imagine that the system, approaching the glass transition, becomes sensitive to the effect of the chain of forces that starts to form between the grains. In this case, it is more useful to consider the apparent stiffness due to grain-grain interaction. For this reason the best choice was to use a simple but nonlinear model of a dry friction element, shown in Fig. 5.14 (**b**). The
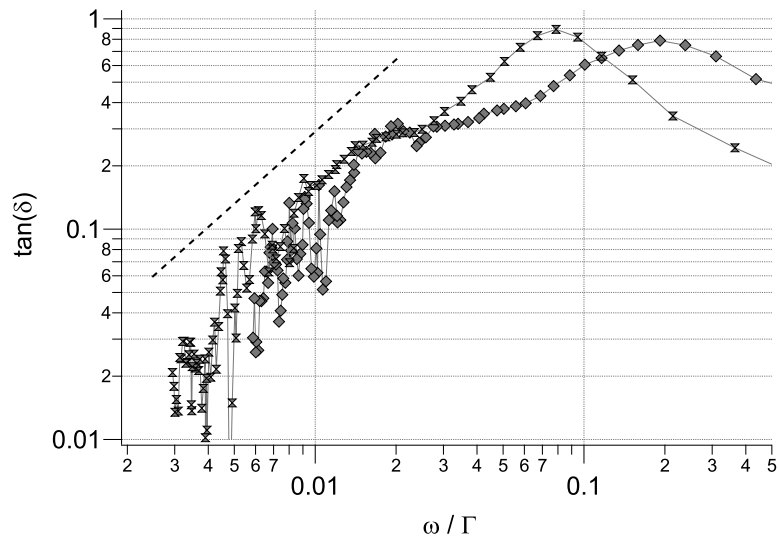
Figure 5.13: High fluidization regime; $\tan(\delta)$ plotted as a function of ω_p/Γ, for $f_p = 0.005$ and 0.01 Hz. The data show that in this regime the loss tangent $\tan(\delta) \propto \omega_p/\Gamma$. The dashed black line, with slope 1, is a guide for the eye.
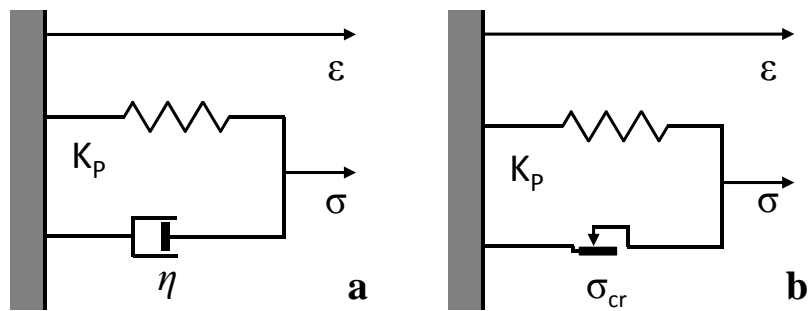
Figure 5.14: Two rheologic models used to interpret the data of Fig. 5.12 and 5.13. Model (**a**) represent a simple Newtonian fluid, and corresponds to the highly fludized region of Fig. 5.13. In this case, K_p indicates the stiffness of the pendulum suspension, while η represent an *apparent* viscous friction coefficient, due to the granular material. Conversely, model (**b**) corresponds the regimes that are dominated by the growth of chains of forces between the grains, as in Fig. 5.12 (**b**).
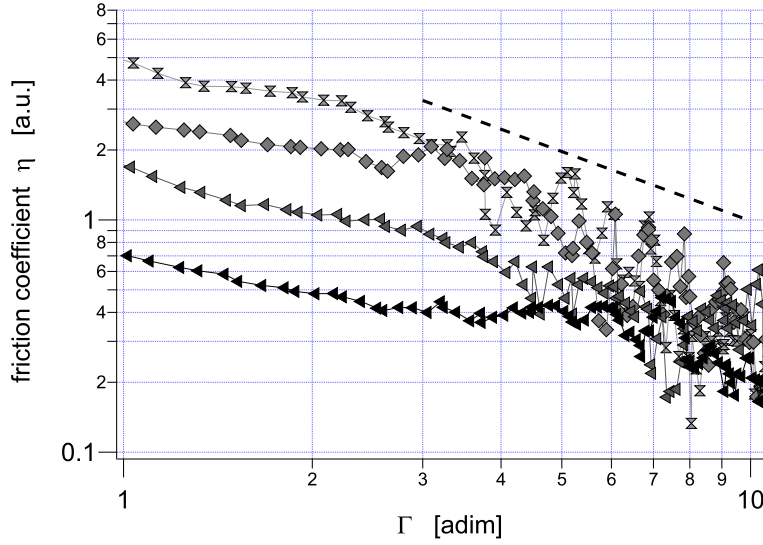
Figure 5.15: Plot of the apparent viscous coefficient in region (**a**), plotted as a function of Γ. Despite the large dispersion, the overall trend for large Γ indicates that $\eta \propto 1/\Gamma$, as had already been observed [245]. The black dashed line representing $1/\Gamma$ is a guide for the eye.

corresponding motion equation can be solved to obtain:

$$\sigma_{cr} = \text{IF } \pi K_p \tag{5.7}$$

In this model, the critical stress σ_{cr} needed to depin the sliding element represents the minimum stress which is needed to break the chain of forces in the granular sample. Now, if we consider the $\tan\delta$ data of Fig. 5.14 (**b**), and we substitute this into Eq. 5.7, we obtain that $\sigma_{cr} = (\omega_p/\Gamma^2)^\alpha$. This means that, in terms of the effective temperature T_{eff}, the critical stress appears to be described by $\sigma_{cr} = (\omega_p/T_{\text{eff}})^\alpha$.

5.6 Possible developments and other ideas

With this project, we were able to study the behavior of vibrated granular media as they evolve from strongly fluidized states to completely frozen ones. The knowledge gathered during the development of this work, together with the new experimental techniques that have been developed, open up many possible scenarios of interesting research fields.

5.6.1 Brownian motor

The installation of the brownian motor could be employed to continue fractal analysis of time series for different experimental conditions. In principle, the jamming and diffusion data could be also compared with similar measurements performed on the torsion pendulum setup. Finally, the installation could be used to perform measurement of energy conversion efficiency, an interesting observable that should be related to other noise rectifier observed in

different fields of physics and biology.

5.6.2 Stick and slip measurements

As discussed in Ch. 2, the brownian motor installation can be modified to allow stick and slip measurements. These experiments allow a different approach to the study of granular system [246], and also show features that can be directly compared to identical experiments performed on other materials, such as metals [186].

Stick and slip measurements also have a strong importance in using granular materials as models system for rock mechanics [247]. The nature of the grain-grain interaction, and the possible presence of other effects (such an external vibration), make granular media an excellent tool to study geologically inspired models, such as the Burridge-Knopoff model [248]. To perform stick and slip experiments, a probe is immersed in a granular system, and a solid arm is mounted perpendicular to the axis of rotation. By the means of a very weak spring (ideally, much weaker than the average apparent restoring coefficient due to the granular medium), the probe is put into rotation, and care is taken so that the spot of the laser falls, approximately, in the center of the photocell. The electrical motor mounted on the top axis is then put into motion, so that it slowly trains the probe in the granular bath. In this configuration the photocell only senses the positional deviations from the constant speed circular motion.

An example of the recorded data is given in the top graph of Fig. 5.16. After the probe gets stuck, the angular distance between the axis and the center of the probe rises linearly. When finally the probe is released, it slips forward, trained by the spring, until it becomes trapped again in another position, leading to the jagged behavior shown in the graph. The bottom graph correspond to the autocorrelation of the signal. This graph indicates that the average duration of each stable configuration is of the order of one second.

5.6.3 Colloids

The transition from a liquid to an amorphous solid has been widely investigated by using colloidal suspensions of spheres as model material. A number of results show a transition from a liquid-like behavior to that of a glass as a function of packing density. Such systems were also used as model for atomic hard sphere systems. The MRI technique opens new perspectives to study the structure of colloidal systems. Even if the size of particles that have been used in traditional colloids must be increased, the precision in particle position obtained in our present research is encouraging. The total structure of the system could be analyzed in order to study sedimentation, crystallization and flow of colloids. As in the present study, the structure data collected with MRI, could by compared with the dynamical analysis provided by the pendulum, in both free and forced mode measurements, with or without applied vibrations.
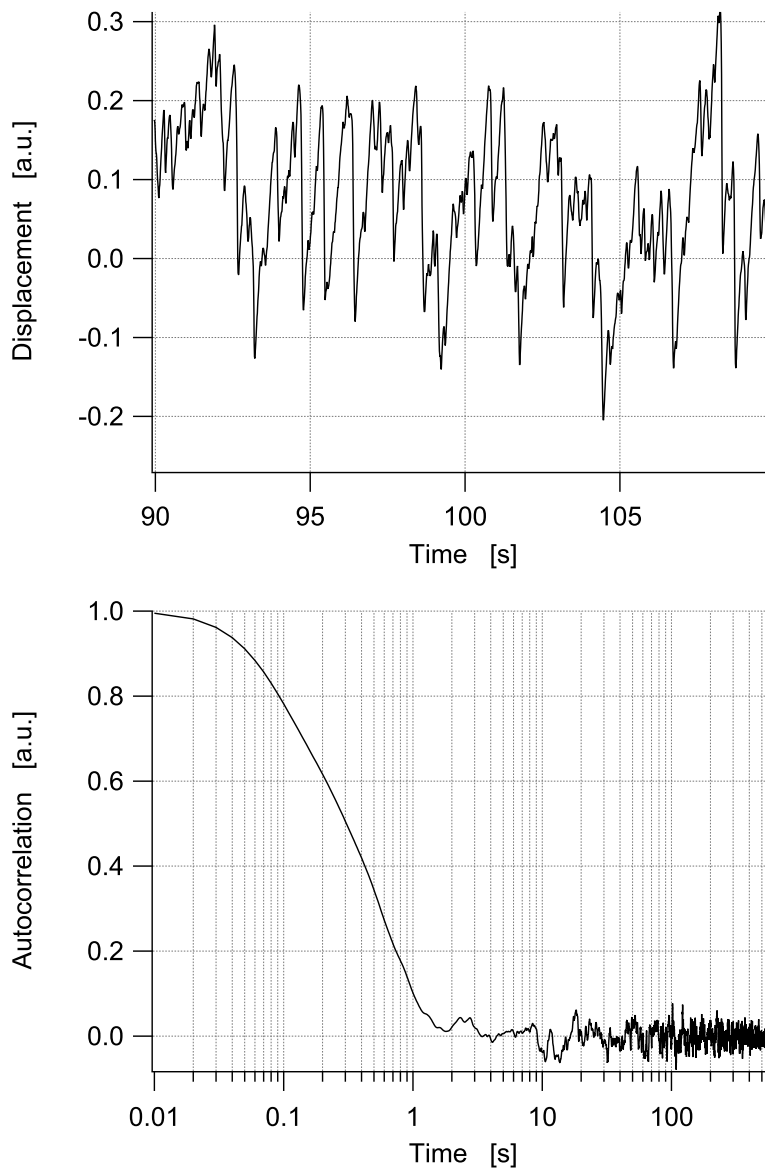
Figure 5.16: Stick and slip measurements. The top graph shows a short fraction of a time series of a measurement performed with a cylindrical probe trained in a non vibrated granular bath, and showing the characteristic behavior of a stick and slip dynamics. The bottom graph shows the autocorrelation of the signal, that can be used to estimate the duration of a stable configuration.

Conclusion

The study of dynamics of vibrated granular media allowed the observation of different phases and the transition that separate four dynamic regimes.

For low, but non negligible vibration intensities the granular medium evolves over finite time scales. This is called the jamming region. The measurements performed in these conditions allowed the measurement of the evolution of the relaxation time of the granular system as a function of different experimental parameters. The resulting data indicate that granular media in the jamming regime are characterized by an unique control parameter $a_s = \sqrt{\Gamma}/\omega_s$, that depend on both the average vibration intensity Γ and on a characteristic frequency ω_s that can depend on the specific waveform used to vibrate the sample and on the geometry of the probe. Moreover, the relaxation time of the system appears to be well described by a thermally activated, non-Arrhenius function of the form $\tau \propto A \exp\left(\frac{B}{a_s^p - a_0^p}\right)$ (VFT behavior).

The experiments could then be interpreted by a model that combines a large scale rheological description (justifying the energy dissipation) and a microscopic approach (that, in turn, allows a statistical description). The model could be directly compared to experiments, testing the effects of the different parameters that are found in the formula. A specific highlight is given to the role of friction coefficients, studied with granular particles having smooth and rough surfaces. The model suggests the origin of the observed thermally activated dynamics. It derives from the extremal event statistics that dominates the evolution of the networks of force chains formed in the granular system. This interpretation differs substantially from what had been found for highly fluidized system, where the control parameter was directly defined as an effective temperature via a fluctuation-dissipation theorem.

Different experimental setups were used to investigate the transition that separates the jamming region from highly fluidized states. Forced mode measurements provided evidence of two distinct regions when the vibration intensities Γ are greater than 1. In the case of a very fluidized system (consisting of conditions where the average vibrations are stronger than $\Gamma = 3$), the forced mode approach confirmed the viscous-like behavior that had already been observed [197]. However, the high sensitivity of the technique allowed to discriminate an intermediate state ($1 < \Gamma < 3$), that is observed between the two (highly fluidized and jamming) regions. It appears that this dynamic region is dominated by the growth of networks of chains of forces. A more detailed study should be carried on, to reach deeper understanding of these effects.

Free mode measurements also proved to be an extremely useful tool to characterize the
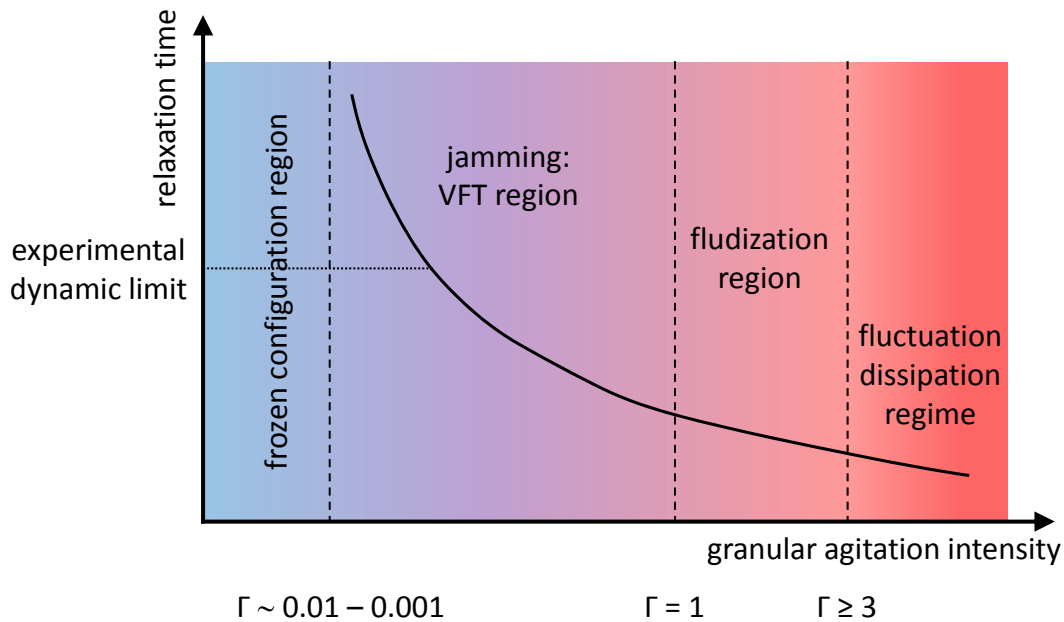
Figure 5.17: A possible phase diagram for vibrated granular material, showing the observed dynamic regions.

physics of the interaction between the probe and the granular medium. A fractal analysis was implemented, and the Hurst exponent of experimental time series of the angular position of the probe were computed. This was used to demonstrate that the movement of a probe immersed in a granular bath is compatible with a rotational brownian motion model. This is a very useful result, because such an assumption is fundamental for many theoretical descriptions and experimental approaches (both in this work and, more generally, in the literature). Despite some technical difficulties the evaluation of the Hurst exponent allowed, again, to distinguish between different regimes. In the case of very weak vibrations, the diffusion exponent becomes smaller than 0.5, due to the appearance of an apparent restoring force. This can be interpreted to the effect of the growth network of chain of forces. On the opposite, strongly vibrated system show a superdiffusive behavior that corresponds to the onset of convection phenomena.

The overall situation can be sketched in a phase diagram as shown in Fig. 5.17. The colors, from red to violet to blue indicate the progressive reduction in the strength of the vibration imposed on the granular system (which can, in principle, a function of Γ only, or both Γ and ω_s.

Approximately above $\Gamma = 3$ lies the fluctuation-dissipation regime. The intermediate conditions, roughly between $\Gamma = 1$ and $\Gamma = 3$ are characterized by the growth of the chain of forces.

As the vibrations are further decreased in intensity, the jamming region is reached. The relaxation time of the system increases, leading to a divergence for a *finite* value of the strength of the vibrations. This point marks the conditions in which dynamic measurements start to

become sensitive to aging phenomena.

If this "frozen" regime is to be studied, different approaches must be used. Two promising techniques are discussed. Static granular assemblies can be studied with a MRI reconstruction technique. This approach permits to study many observables that are not directly accessible with dynamic methods. In short, the MRI approach represent the granular material equivalent of the high resolution microscopy studies for conventional materials, and for this reasons it is a very promising field. Another possibility is to employ forced mode measurements to induce aging in a specially prepared sample. It would be interesting to apply both techniques in parallel, and observe the effects of aging in both the mechanical response function and on the reconstructed bulk structure.

Appendix A

Fractals and Brownian motion

A.1 Brownian motion and granular materials

The direct application of brownian motion principles to granular system is quite interesting, but requires a special attention. In general, grains are not subject to traditional Brownian motion. It appears that this phenomenon is inconsequential when it comes to granular materials and is only exhibited when the particles are in a uniform vertical air flow [249], or otherwise very strongly shaken.

This observation could explain why granular materials do not really respond to being mixed; when shook, instead, they tend to segregate according to size. This is often the exact opposite of what is expected or sought. On the other hand, the recent observations that have been discussed in Ch. 3 and 4 ([204, 205]) seem to suggest that Brownian motion is indeed a useful framework to interpret some features of granular systems and their interaction with external probes.

More specifically, in Ch. 4, experimental data was shown, indicating that normal and anomalous diffusion in vibrated can be observed in granular media. The conceptual flow of ideas used to derive that interpretation is the following: the Brownian motion can be derived (as some kind of limit) from random walks. The specific characteristic of the random walks influence the nature of the limit brownian motion. However, these random walks can be directly recorded (they are the experimental time series of the angular position) or simulated. The properties of the corresponding brownian motion trails finally allowed to interpret the data via Einstein relations and diffusion exponents.

The goal of this Appendix is therefore to present a review of a few properties of time series, which in turn will require knowledge about fractals. Therefore, we start from the definitions of fractals and we progressively demonstrate all the properties needed to our goal. Note that, in the following Appendix A, and also in Appendix B, we will closely follow the book by Falconer [250], to which we will be often referring.

A.2 Fractals and time series

The position of a particle can be recorded at a given frequency, and for a given length of time. The resulting experimental dataset contains information of the times and the positions of the object, and is called a time series. As we have seen, the mere observation of a time series of a Brownian particle does not allow to compute directly the speed of the particle. Early theories of Brownian motion were inconsistent, because they (incorrectly) assumed that the space traveled by the particle was proportional to the elapsed time. This is what happens for "normal", macroscopic objects, for which we expect a kinematic equation of the form $D = vt$. Instead, the successful theories we have discussed above, proved that the problem requires that we consider law of evolution where the characteristic length scale evolves as the square root of time. What is the difference between a time series of a Brownian particle and that of a macroscopic one? If we inspect the shape of the time series, we can see that it is very irregular, broken, or "noisy". This is a typical example of fractal.

In nature there are many examples of these phenomena. For example, the path of a lightning is extremely irregular, as it can clearly be seen in the *Lichtenberg figure* [251] of Fig. A.1. Upon close inspection, many objects show the same behavior: broccoli of the "romanesco" variety, the shape of mountains, the structure of the basin of rivers with their affluents, frost crystals (an example of dendritic structures), graphs of networks, blood vessels and capillary structures. The term *fractal* itself was coined by Mandelbrot [214], from the Latin *fractus*, meaning broken, to describe the geometrical properties of objects that were too irregular to fit into traditional geometric categories. The traditional example, discussed by Mandelbrot himself, is the problem of determining the length of a coastline. Therefore, in order to be able to discuss the properties of the time series of Brownian objects, we will now introduce a few key concepts about fractals.

A.3 Self similarity

In mathematics, a self-similar object is exactly or approximately similar to a part of itself. In other words, an object is said to be self-similar if the whole has the same shape (or more in general, some crucial property) as one or more of the parts. Many objects in the real world are statistically self-similar. This means that parts of them show the same statistical properties at many scales.

A stronger form of this property is called scale invariance. In this case, an object is exactly self-similar at any magnification scale: there is always a smaller piece of the object that is similar to the whole.

In this regard, fractals are a class of self-similar (often scale invariant) objects. Some examples of fractals are shown in Fig. A.2.

A.4 The concept of dimension

Each geometrical object occupies a region of the space in which it is defined. The defining properties of each object indicate how much "space" it occupies, as we measure it at all
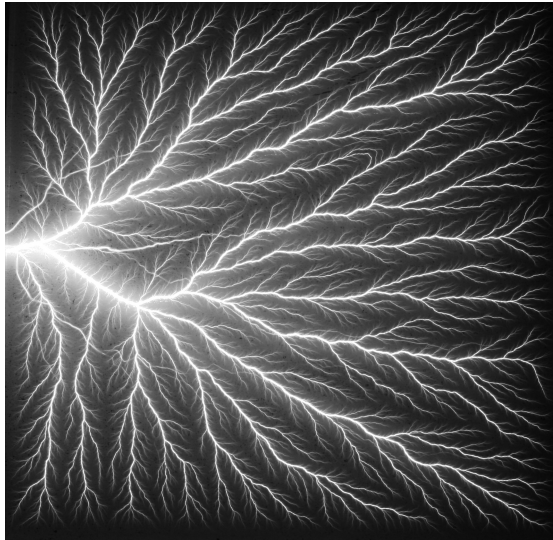
Figure A.1: A 30 × 30 cm. specimen of a Lichenberg figure as it's being discharged. Lichtenberg figures are branching, tree-like or fern-like patterns that are created by high voltage discharges along the surface or within dielectrics. The first figures were observed by the German physicist Georg Christoph Lichtenberg (1742-1799) from whom they were named after [251].
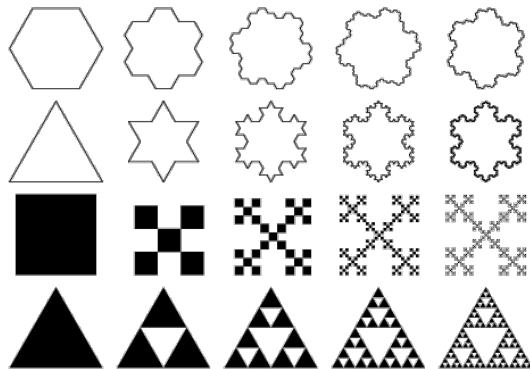
Figure A.2: Examples of fractals objects. These geometric shapes are exactly defined via recursion formulas and are embedded in a 2 dimensional space (for example a plane). From top to bottom we have: Gosper island, $d = 2\ln 3/\ln 7 \approx 1.12915$; Koch snowflake, $d = 2\ln 2/\ln 3 \approx 1.26186$; box fractal, $d = \ln 5/\ln 3 \approx 1.46497$; Sierpiński sieve, $d = \ln 3/\ln 2 \approx 1.58496$. Image and data from [252].

the possible scale sizes. This heuristic idea is at the basis of the parameter which is called *dimension.* Traditionally we say that the space we live in is 3-D (or 4-D if you take into account General Relativity), and that surfaces are 2-D, lines are 1-D and points are 0-dimensional objects [253].

In modern geometry, the dimension of a geometric object (such as a curve or shape) is a generalized version of the geometrical dimensions that are postulated in the work of Euclid. If we recur to analysis, this corresponds to computing the size of a set using the Riemann-Lebesgue theory of measure (see for example [254]). There are however countless examples of sets that are composed of an infinite number of elements, but that have zero size, (for example "Cantor's Dust"). For a few of these objects, however, the traditional geometric concepts of length or area are meaningless, or their calculation results in deceiving results. A few example of such mathematical structures are shown in Fig. A.2.

We could say that the fractal dimension, D is a statistical quantity that gives an indication of how completely a geometric object appears to fill space, as one measures at all possible scales. It should be noted that there are many specific definitions of dimension. This comes from the fact that, in general, the dimensionality is computing via some limit procedure that is arbitrarily defined, with the only constraint that the generalized dimension of "regular" geometric objects should correspond to the usual euclidean one.

The most important theoretical fractal dimensions are the *Rényi* dimension, the *Hausdorff* dimension and the *packing* dimension. Practically, when estimating the dimension of some object that cannot be treated analytically, other dimension algorithms can be used. Among them are, for example, the box-counting dimension and the correlation dimension. In the following we will try to briefly review the basic concepts and key ideas to what means defining a generalized dimension, and what practical limit procedures can be exploited to compute them from finite data sets.

To show a precise example, we define the *capacity* dimension (sometimes also called *fractal,* *Hausdorff* or *Hausdorff-Besicovitch* dimension) in the following way. The dimension of a compact metric space X is a Real number d such that if $n(\epsilon)$ denotes the minimum number of open sets of diameter less than or equal to epsilon, then $n(\epsilon)$ is proportional to ϵ^{-d} as $\epsilon \leftarrow 0$. Explicitly,

$$d = - \lim_{\epsilon \to 0^+} \frac{\ln N}{\ln \epsilon} \tag{A.1}$$

(if the limit exists), where N is the number of elements forming a finite cover of the relevant metric space and ϵ is a bound on the diameter of the sets involved (informally, and this will be useful in the following, ϵ is the size of each element used to cover the set, which is then taken to approach 0).

Mathematical shapes that are defined in X, and that have a Haussdorf dimension that is different from their Lebesgue covering dimension [254] are what we call fractals. More in general, we can consider objects described with two parameters N and s, so that a power law relationship stands: $N = s^d$ where again $d = \ln N / \ln s$ is the dimension of the scaling law.

A.4.1 Example: Koch's curve

For many objects that are defined recursively or analytically, we can compute the exact dimension. We discuss, as an example, the famous fractal called "Koch Snowflake" [214]. This is the second object shown in Fig. A.2.

This shape is constructed via a recursion rule, by which we divide each segment in three equal parts, and we replace the middle one with two other segments forming an angle with the two remaining external one. Let us consider the n-th iteration of the construction of the fractal: N_n is the number of sides, L_n is the length of each single side, l_n is the length of the perimeter, and A_n the snowflake's area. Further, let us denote the area of the initial ($n = 0$) triangle Δ, and let the length of an initial side be 1. Then:

$$N_n = \frac{3}{4^n} \tag{A.2}$$

$$L_n = \left(\frac{1}{3}\right)^n \tag{A.3}$$

$$l_n = N_n L_n = 3\left(\frac{4}{3}\right)^n \tag{A.4}$$

$$A_n = A_{n-1} + \frac{1}{4}N_n L_n^2\Delta = A_{n-1} + \frac{1}{3}\left(\frac{4}{9}\right)^{n-1}\Delta \tag{A.5}$$

Solving the recurrence equation, with $A_0 = \Delta$ gives

$$A_n = \frac{1}{5}\left[8 - 3\left(\frac{4}{9}\right)^n\right]\Delta \tag{A.6}$$

so that as $n \to \infty$, $A_\infty = 8/5\Delta$. The capacity dimension is then:

$$d = -\lim_{n\to\infty}\frac{\ln N_n}{\ln L_n} = \log_3(4) = \frac{2\ln 2}{\ln 3} \approx 1.26186 \tag{A.7}$$

A.4.2 Calculating the dimension

In experimental data, curves and shapes are not defined by recursion rules or via analytic properties, and in general there is not a simple way to describe them as such. However, it is possible to define algorithms that allow to approximate the exact definitions of the generalized dimensions discussed above. In the following we will try to focus on the estimators of the Haussdorf dimension. This is the useful definition of dimension for time series that we will discuss in the following subsections.
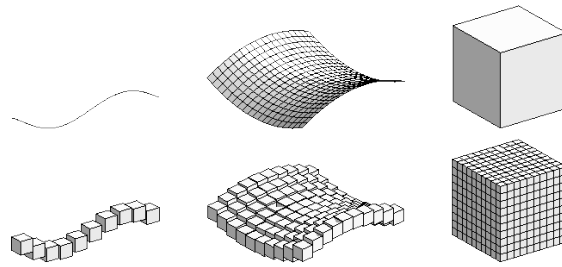
Figure A.3: Representation of the Box Counting method of Eq. A.8. for Euclidean objects (a line, a surface and a volume) embedded in a 3-dimensional space. If we try to cover the unit square with little squares of side length ϵ, we will need a number $N_s = 1/\epsilon^2$ of them. To cover a segment of length 1, we only need $N_l = 1/\epsilon$ little squares. If we think of the square and segment as sitting in space and try to cover them with little cubes of side length ϵ, we get the same answer. Finally, if we use the little cubes to cover a cube of volume 1, $N_c = 1/\epsilon^3$. As expected, the computed exponent is the same as the Euclidean dimension of the thing we are trying to cover. (Fig. from [222]).

Box, or box counting dimension

The box-counting dimension (also called Minkowski-Bouligand dimension) is the simplest approximant to the capacity dimension of a set $\mathbb{S}$ defined generally in a metric space (X, d).

To calculate this dimension, consider a graph $\mathbb{S}$, and imagine this object as lying on an evenly-spaced grid. The algorithm proceeds by counting how many boxes are required to cover the set. Then, the size of the cover boxes is changed, and the counting is repeated. The box-counting dimension is the scale law between the number of cover boxes and the grid size.

A more detailed mathematical demonstration follows these lines [222]. Let us suppose that we can embed our object in an metric space such as $\mathbb{R}^n$ (for our case $n = 1$). For any $\epsilon > 0$, let $N_\epsilon(\mathbb{S})$ be the minimum number of n-dimensional cubes of side-length ϵ needed to cover $\mathbb{S}$. If there is a number d so that:

$$N_\epsilon(\mathbb{S}) \sim 1/\epsilon^d \qquad \text{as} \qquad \epsilon \to 0 \tag{A.8}$$

we say that the box-counting dimension of $\mathbb{S}$ is d. An example for Euclidean objects is shown in Fig. A.3.

The implementation of the box method is therefore quite simple and straightforward. Many data treatment and image analysis software packages now include a box dimension estimator. However, it must be noted that there is a practical problem in the implementation of the box dimension algorithm. It has been shown [255, 250] that in some cases the speed of convergence can scale slower than $1/\epsilon^2$. This means that to obtain a good estimate of the dimension one has to consider samples of (potentially infinitely) large size. The box dimension represents, therefore, a good estimator for fractal dimension provided one knows the possible drawbacks.

Regularization dimension

A more robust estimator of the Haussdorf dimension can be loosely defined in the following way. First, one computes smoothed approximations of the original object. In our case, this means taking a signal and convoluting it with a smoothing kernel. Now, if the original shape is really self-similar, its graph has infinite length, while all regularized versions have finite length. When the smoothing parameter tends to 0, the smoothed version tends to the original signal, and its length will tend to infinity. The regularization dimension measures the speed at which this convergence to infinity takes place. This definition is more broadly discussed in [221, 213], while an application example can be found in [223].

In (non pathologic) general cases this definition allows to obtain the same results of the box dimension algorithm, with a faster convergence. More specifically, the regularization dimension is a better approximant to the Hausdorff dimension [221].

A brief, more mathematical, overview follows these lines [213]. Let f be a real-valued function defined on a finite interval K, and $X(t) \in S$ (S is a Schwartz class) be a kernel function such that:

$$\int X = 1 \tag{A.9}$$

Let $X_a(t) = \frac{1}{a} X\left(\frac{t}{a}\right)$ be the dilated version of X at scale a. Let f_a be the convolution of f with X_a: $f_a = f \otimes X_a$.

Condition A.9 insures that X_a tends to the Dirac distribution and f_a to f, in the sense of distributions, as a goes to 0. Since $f_a \in S$, the length of its graph Γ_a on K is finite and given by

$$L_a = \int_K \sqrt{1 + f'(a)^2}\, dt \tag{A.10}$$

So that the regularization dimension of Γ is

$$\mathrm{Dim}_r(\Gamma) = 1 + \overline{\lim_{a \to 0}} \frac{\log L_a}{-\log a} \tag{A.11}$$

Numerically, the regularization dimension lends to more robust estimation procedures for various reasons: for example, the regularization kernel can be adapted to the features of the original objects. Also, the smoothing parameter can be varied in very small steps, while box sizes have to undergo sudden changes. This is especially useful in the presence of noise.

A.4.3 Errors in the estimates

There are two main problems that may introduce errors during the calculations of the dimension of a graph, apart from the known weakness of the chosen algorithms.

First, in general, if a shape consists of distinct pieces, the overall dimension that is estimated numerically is the largest of the dimensions of the pieces. However, while performing the calculation, the convergence to the correct value can be very slow, and is also influenced by the lowest considered box/renormalization characteristic size.

Second, the presence of noise perturbs the convergence of the estimators. An example relevant for our work is the case of the graph of a Brownian motion with an added gaussian white noise. While the expected dimension of a Brownian path is 1.5, the computation of the dimension estimator will not show a significant spectral region in which a fixed dimension can be seen. The reason for this is the following. For the points correspond to a large amount of smoothing (low frequencies), the signal will dominate over the noise. On the other hand, for the points corresponding to the least smoothing values, the noise tends to dominate. In case one suspects a big amount of random noise in the signal (greater than 10-20%), this should be taken into account.

Wiener processes, anomalous diffusion and Hurst exponent

In the previous sections we introduced the fundamental ideas of self-similar structures, fractals and fractal dimensions. These facts were not know in Wiener's time, so the approach we discuss here is much more modern than his original paper, and allows for a much easier extension of the results of the first part (regarding normal diffusion) to the situation of anomalous diffusion. This will allow to define the Hurst exponent in a simple way, and to show what is the link between some key properties of brownian motion and the way they diffuse. As Appendix A, the following brief review will closely follow Ref. [250].

B.1 Standard brownian motion

The starting idea is to consider a Brownian particle of which we are recording (sampling) the movements. Any trail in space may be described by a function $f : \mathbb{R} \to \mathbb{R}^n$ where $f(t)$ is the position of the particle at time t. We can study f from two different viewpoints. Either we can think of the *trail* or the *image* $f([t_1, t_2]) = \{f(t) : t_1 < t < t_2\}$ as a subset of $\mathbb{R}^n$ (t is a parameter); or we van consider the *graph* of f, $\mathrm{graph} f = \{(t, f(t)) : t_1 \le t \le t_2\} \subset \mathbb{R}^n$, as a record of the variation of $f(t)$ with time. Brownian trails and their graphs are, in general, fractals.

Let us consider a particle performing "random movements", in 1 dimension for clarity. During each interval τ it can move of a small distance δ randomly in either direction. Let $X_\tau(t)$ denote the position of the particle at time t.

For $t > 0$ (assuming that we consider an integer number of time steps, but this can be relaxed), the position of the particle is given by

$$X_\tau(t) = \delta(Y_1 + \ldots + Y_{t/\tau}) \tag{B.1}$$

where the Y_i are independent random variables, each having probability $1/2$ of being $+1$ and $1/2$ of being -1. The step length can also be renormalized by setting $\delta = \sqrt{\tau}$.

Using the central limit theorem, for fixed t and small enough τ, the distribution of the random variable $X_\tau(t)$ is approximately normal with mean 0 and variance $\approx t$ (since the Y_i have mean 0 and variance 1). Now we take the limit for $\tau \to 0$.

Let (Ω, F, P) be a probability space. We call X a *random process* or *random function* from $[0, \infty)$ to $\mathbb{R}$ if $X(t)$ is a random variable for each t with $0 \le t < \infty$. We think of X as defining a *sample function* $t \mapsto X(\omega, t)$ for each point ω of the sample space Ω. The points of Ω thus parametrize the functions $X \in F$; $X : [0, \infty) \to \mathbb{R}$, and we consider P as a probability measure on this class of functions.

A Brownian motion is then a random process X which obeys the following rules:

BM1 with probability 1, $X(0) = 0$ (the process starts at the origin); $X(t)$ is a continuous function of t.

BM2 for all $t \ge 0$ and $h > 0$ the increment $X(t + h) - X(t)$ is normally distributed with mean 0 and variance σ; thus

$$P(X(t + h) - X(t) \le x) = (2\pi\sigma)^{-1/2} \int_{-\infty}^{x} \exp\left(\frac{-u^2}{2\sigma}\right) \mathrm{d}u$$

BM3 if $0 \le t_1 \le t_2 \le \ldots \le t_{2m}$, the increments $X(t_2) - X(t_1)$, $X(t_4) - X(t_2)$, $\ldots$, $X(t_2 m) - X(t_m)$ are independent.

From this definition of Brownian motion many interesting properties can be computed, but for shortness we will only report here the statement of the following theorem.

Theorem 1 With probability 1, the graph of a Brownian sample function $X : [0, 1] \to \mathbb{R}$ has Haussdorf and box dimension 1.5.

B.2 Fractional brownian motion

In general, a Brownian motion as described above, is a *Gaussian process*. In short, this means that its increments are independent, and that they are stationary and of finite variance. If we relax the first condition we have the *Fractional Brownian motion*. On the other hand, if we dispense with the normal distribution of the increments, we get the *Lévi processes* [224], (also called "Lévi's flights").

We define the Fractional Brownian motion of index h ($0 < h < 1$) as a Gaussian process $X : [0, \infty) \to \mathbb{R}$ on a probability space such that:

FBM1 with probability 1, $X(t)$ is continuous and $X(0) = 0$

FBM2 for every $t \ge 0$ and $\sigma > 0$ the increment $X(t + h) - X(t)$ is normally distributed with mean zero and variance σ^{2h}, so that

$$P(X(t + h) - X(t) \le x) = (2\pi)^{-1/2} \sigma^{-h} \int_{-\infty}^{x} \exp\left(\frac{-u^2}{2\sigma^{2h}}\right) \mathrm{d}u$$

We can note that the increments $X(t + h) - X(t)$ are stationary: in other words, their probability distribution does not depend on t. However, the distribution of functions specified by the

FBM cannot have *independent* increments except in the pure Brownian case of $h = 1/2$. In fact, in virtue of the two conditions above, $E(X(t)^2) = t^{2h}$ and

$$E\left((X(t+\sigma) - X(t))^2\right) = \sigma^{2h}$$

It can be shown that the expectation value

$$E\left((X(t) - X(0)) \times (X(t+\sigma) - X(t))\right)$$

is positive or negative according to whether $h > 1/2$ or $h < 1/2$ respectively. Therefore the increments are not independent. If $h > 1/2$ they tend to be of the same sign, so that past increments lead to more increments and vice versa. Otherwise, if $h < 1/2$, the increments tend to be of opposite sign.

The observation above directly translates into a graphical feature of FBM. When $h > 1/2$ the realization tends to look "smoother", while for $h < 1/2$ the graph looks "noisier". This is shown in Fig. 4.2, and it is related to the following theorem.

Theorem 2. With probability 1 the graph of an index h Brownian sample function $X : [0,1] \to \mathbb{R}$ has Haussdorf and box dimensions $2 - h$.

This theorem, therefore, represents the bridge between the fractal properties of the experimental time series and the properties of normal and anomalous diffusion for a model Brownian object. Thanks to it, we can relate the variance of the observable position to a power law function of time, with exponent $h \neq 1/2$. In this context, the exponent h is often called "'Hurst exponent". For more details we refer to the review by Bouchaud and Georges [167], the one by de Gennes [216] and also to the works of Balakrishnan [215], Schneider [217], Saichev [218]. and Barkai [219].

Appendix C

Experimental evidence of transition

This Appendix contains a few experimental observations, performed with different techniques, that complement the experiments made with the torsion oscillator. These observations clarify relevant points relative to the experiments discussed in Ch. 3 and 4, and play an important role in the interpretation of the data discussed in Sec. 3.1 and 3.3.

When one observes a granular system submitted to a vertical vibration, it is very easy to see that, depending on the intensity of vibrations, the system behaves in very different ways. Namely, if the vibration intensities system are "strong", the particles can acquire enough energy to bounce off the surface, colliding with each other. In these conditions, the granular system presents some similarities with the well known hard-sphere model of the kinetic theory of gas [53, 256].

As the intensity of the vibrations is decreased, the particles stop flying around, and eventually they start to amass on top of each other. At some point, the shaking is reduced to a point where they do not possess the energy to significantly move around (while still interacting, as measurements indicate). One can imagine that the system ends up in a disordered state, where the interaction between the particles becomes dominated by surface forces described by a contact network.

C.1   Accelerometer integral response

As discussed in Ch. 2, the intensity of vibration imposed on the system is measured by the means of an accelerometer, fastened to the bottom vibrating plate. The placement of the accelerometer on the bottom plate makes it sensitive to the combined effect of the forces acting on it: the one due to the vibration motor, and the one coming from the granular bath. This configuration is not sensitive enough to directly study the details of the dynamic behavior of vibrated granular materials, because the accelerometer can only feel the "average" effect of all these phenomena. But, at least, it can provide some insight on large scale changes in the behavior of the medium.

In the following experiments, the base assembly, composed of the vibration motor, the granular container and a sample granular material, is considered. The vibration motor is set into motion by a sinusoidal waveform, and the excitation intensities are swept by driving the
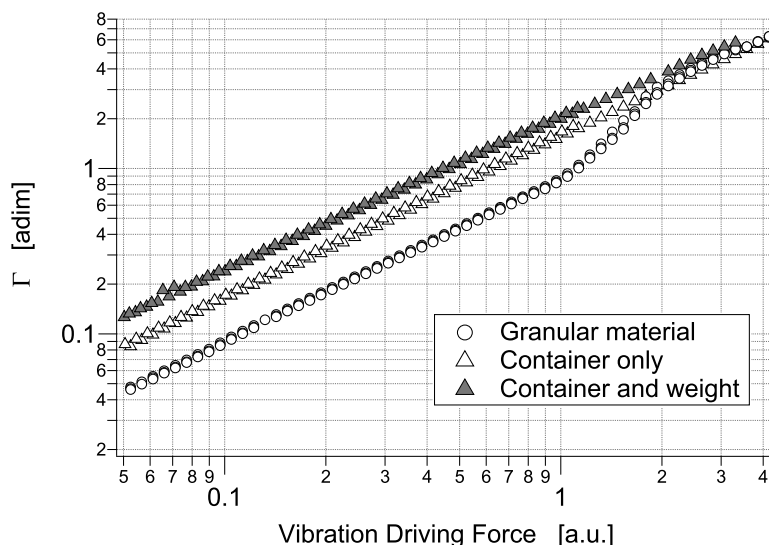
143

Figure C.1: Acceleration response of vibrated granular systems. The graph shows the average vibration parameter Γ measured as a function of the driving strength imposed on the vibration motor (ultimately proportional to the current intensity flowing in the vibration motor). The white circles represent three different granular media, each composed of approximately 560 g of glass beads of different surface roughness, as indicated in the main text. The three curves cannot be resolved. The white triangles instead indicate the measured average acceleration obtained for the system without the granular medium. Finally, the gray triangles show the data obtained by substituting the granular system with an equivalent weight (560 g) fastened to the vibrating element.

vibration motor with electric currents of varying amplitudes. The experiment was repeated (all other conditions unchanged) with the standard broadband (white noise) vibrations, and no significant differences were observed. For this reason, in the following discussion, we restrict to the sinusoidal case only.

The average acceleration of the moving element is then measured. Three different cases are considered: (**a**) the container only (empty); (**b**) the container, filled with grains; (**c**) the container and a weight fastened to it. The fastened weight of case **c** corresponds to the weight of the granular medium. In all of the three cases, the accelerometer output is fed to a broadband voltmeter, while the vibration motor is driven by increasing programming tension (resulting in increasing driving currents). The accelerometer signal, for each vibration intensity, is averaged for 120 s. The resulting average accelerations are shown in Fig. C.1.

The empty container data (white triangles) show that the measured acceleration varies linearly as a function of the imposed tension. This is expected, as long as the linear response window of the vibrator motor is respected. In fact, the behavior of the vibration motor and assembly has been studied in detail, as it was partially discussed in Ch. 2. For what concerns all the experiments discussed in this work, the intensity of shaking never induces nonlinear behavior in the vibration motor. On the other hand, in standard working conditions the eigenfrequency of the oscillating element is approximately 1 kHz; this, considering an average granular sample

weight of approximately 0.5 kg. It is important not to directly excite this frequency band. In case of broadband excitations, the high frequency cutoff of the broadband signal is chosen to be around 800 Hz to avoid this resonance.

The second data set (gray triangles) shows the behavior of the system, with an increase in the mass of the oscillating element. The linear response of the motor/accelerometer setup can be described as a function of the mass of the oscillating element. When an additional weight is added, provided it is correctly fastened to the moving plate, the increase in the mass translates into a larger measured acceleration. This can be interpreted as follows. The addition of mass reduces the eigenfrequency of the system. If the motor is loaded with reasonable weights ("reasonable", in this context, means lower than 2 or 3 kg), the resonance frequeny is still higher than the driving frequency, but the difference in frequencies between the two decreases. Then, the oscillator is driven with a frequency nearer to its resonance conditions, and its response show larger amplitudes, which in turn induce larger accelerations.

Finally, the third data set (white circles) indicates the behavior of the system, loaded with the granular sample. The addition of the granular medium give rise to an interesting behavior.

At low vibration intensities, for a fixed level of driving force, the observed acceleration is lower than both previous cases. This fact can be interpreted as follows. Even if the granular material is below the fludization limit $\Gamma < 1$, the grains can still rearrange themselves. In doing so, they interact by sliding one above the other. The presence of a coefficient of dry friction induces then a large amount of energy dissipation (due to the very large amount of contact points between the grains). This is measured by the system as if it was a macroscopic "friction" force that increases the damping of the oscillator.

This behavior can be interpreted in the following way. The increase in this "effective" damping modifies the amplitude frequency response of the oscillator, which is described by Eq. C.1:

$$A\left(\Omega\right) = \frac{\omega_0^2 A_0}{\sqrt{\left(\omega_0^2 - \Omega^2\right) + 4\eta^2\Omega^2}} \tag{C.1}$$

Therefore, the absolute amplitude observed at a fixed frequency Ω decreases for an increase of η. This happens even if the actual resonance frequency $\Omega_r = \omega_0\sqrt{1 - \eta^2/C}$ is reduced by an increase in η. theoretically approaching the resonance frequency to the measurement frequency.

On the other hand, when the strength of the vibrations is increased to just below $\Gamma = 1$ a sharp increase in the acceleration is observed. In this region, the grains start to fly, and the energy dissipation due to contact reduces in strength. Eventually, as the fludization threshold is traversed, the apparent damping effect of the granular medium disappears, and the measured vibration intensities become similar to those observed in the weight-loaded system.

This experiment therefore shows that there is a substantial change in regime as the $\Gamma = 1$ boundary is crossed. Furthermore, for low vibrations, even if the dynamics appears to slow down, the granular medium is still dissipating a large amount of energy.

As a final remark, it should be noted that a similar measurement, could be interesting in the light of the theory of extremal event statistic. If the sensitivity of the measurements is high
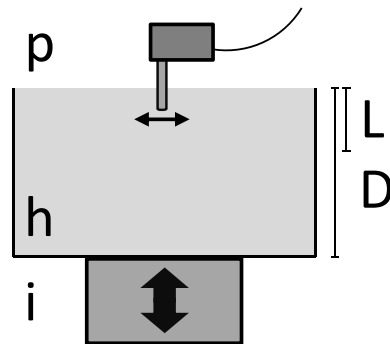
Figure C.2: Sketch of the piezoelectric probe setup. The piezoelectric sensor replaces the torsion oscillator setup. The piezoelectric element is connected to a thin and short metallic rod that is in contact with the topmost granular layer. The piezoelectric sensor is sensitive to horizontal movements, and is therefore decoupled from the vertical vibrations imposed by the vibration motor.

enough, the observations could be compared with the total amount of dissipated energy in the granular system as described by the model of Ch. 3.

C.2   Piezoelectric probe

Another observation indicating a strong change in the dynamics can be made by studying the behavior of the surface of the granular medium. This region is a special one in granular system, because the topmost layer is the only one that is not submitted to the pressure of other grains standing above. This fact makes it easier to interpret the mobility of the grains in this region, as no motion is hindered by the presence of constraints.

In order to characterize the behavior of the granular surface, the topmost layers were probed with a piezoelectric sensor, as shown in Fig. C.2. This probe is composed of a short and thin metallic rod that acts as sensor for a piezoelectric element. The piezoelectric system is placed above the granular system, so that the tip of the rod barely touches the granular surface. The piezoelectric element is sensitive to horizontal displacements, so that it is practically decoupled from the vertical movement of the vibration motor. The piezoelectric probe has a large bandwidth covering more than the acoustic spectrum, up to 40 kHz, and the generated electric signal is analyzed by a digital spectrum analyzer (HP DVA mod. 87400).

The Fourier representation of the output signal can be integrated to obtain an estimation of the total power that is available in a given frequency window. The corresponding data are shown in Fig. C.3. At high vibration intensities, the power output is dependent on the strength of the shaking intensities. When Γ reaches 1, even the beads found on the top layer do not have any more enough kinetic energy to jump above the surface. The system changes regime, and the average output of the probe stabilizes to a constant level independent of the vibration intensities.

The drastic change in behavior can be interpreted as follows. The piezoelectric probe is
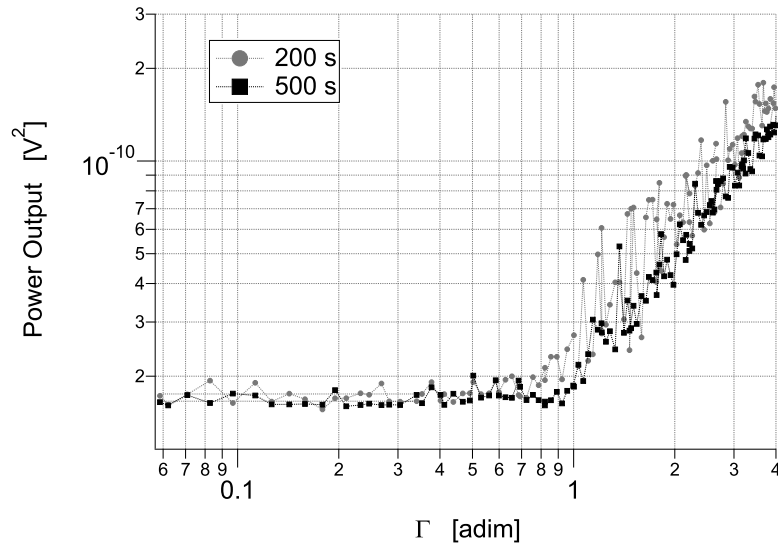
Figure C.3: The $\Gamma = 1$ transition on the surface of the granular system. Data show the power output of a piezoelectric probe immersed at a depth of 1 mm, integrated over its complete nominal bandwidth (5 Hz to 40 kHz). This configuration senses the average amount of vibration on the top layer.

sensitive to the rearrangement of the few particles it is in contact with. As the energy available to the system decreases, so decreases the energy transfer to the rod. However, as we reach the threshold $\Gamma = 1$, the beads cannot rearrange independently, so that much less frequent collective phenomena becomes important. In these conditions, the extremely small contact surface of the probe (which is a cylindrical metallic tip with polished sides) is not sensitive enough to pick up these kind of rearrangements.

This experiment should be compared with the average acceleration discussed in the previous section. If fact, these data show that the fludization limit is in fact a "hard" limit for the granular system. Since the topmost layer is the one allowing less constraints on the grains, these measurements clearly show that this threshold does indeed separate two really different regimes. In other words, there is no "smooth" change at the transition: the vibration intensities rise above $\Gamma = 1$, the sample is completely outside the jamming region, and enters in a new phase. There is no evidence of a dependence on ω_s.

C.3   Acoustic measurements

When a granular system is vibrated, the energy imparted in the system is quickly dissipated via inelastic collisions and frictional forces. Part of the energy dissipated in the collisions is emitted as acoustic noise.

The noise emitted by the granular system was recorded using a high sensitivity microphone. The corresponding electric signal was preamplified, and then analyzed with the HP DVA frequency analyzer. The frequency window from 10 Hz to 40 kHz represents the linear response
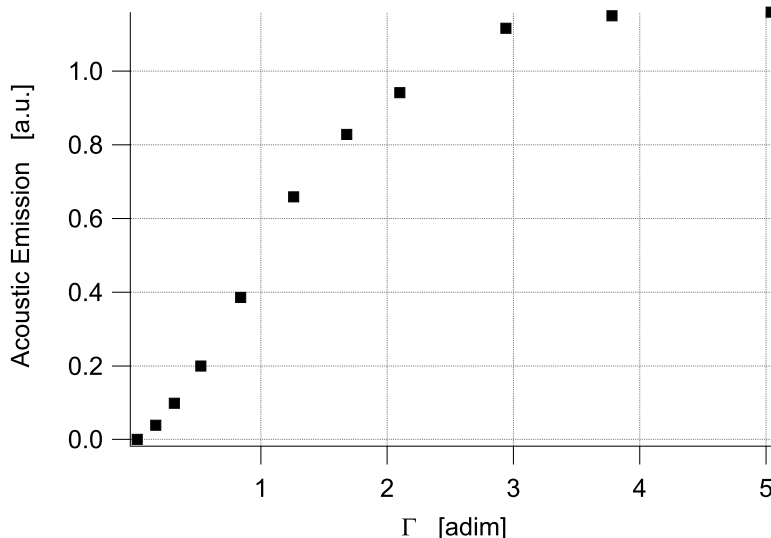
Figure C.4: Acoustic measurements. The graph shows the integrated noise output over the measurement bandwidth. The data indicate that, if the vibration intensities are not too strong, the amount of noise emitted is linearly proportional to the vibration intensities.

band of the equipment; all frequencies outside this band were discarded.

From the recorded time series data, the power spectra were computed; the data was averaged 30 times using 120 s long time series. The data was then integrated over the bandwidth to assess the total amount of noise emitted, as shown in Fig. C.4 The graph shows a linear increase of the emitted noise, up to a certain saturation threshold.

A large fraction of the emitted noise, in fact, is produced by the collisions between the grains and between grains and the container. It is interesting to study the distribution of power at different frequencies, when the vibrator motor is driven by a broadband signal (white noise) that injects a sufficient amount of power in a large enough frequency window. Since the vibrating element itself produces noise, the acoustic spectra of the vibrated granular medium has to be compared to the noise emitted by the installation when the granular system is removed, but in otherwise identical experimental conditions.

The data are shown in Fig. C.5. It appears that, due to the interactions between the grains, part of the energy that is fed with the vibration motor is distributed to higher frequencies. The leaking spectral power appears to peak in the region 1-2 kHz.

This observation will become very useful in both the interpretation of the experimental data of the following section, and the discussion of a possible model. In fact, we will show that the dynamics of vibrated granular media, around the jamming transition, depends on just one control parameter. However, to correctly compute it, one must know the average frequency of vibration of the system, and these data show that the correct frequency is not just the average frequency with which the system is fed, especially in the case of broadband ("white noise") driving signals.

Furthermore, as it can be seen in Fig. C.5, the peak of leaking spectral power is around 1
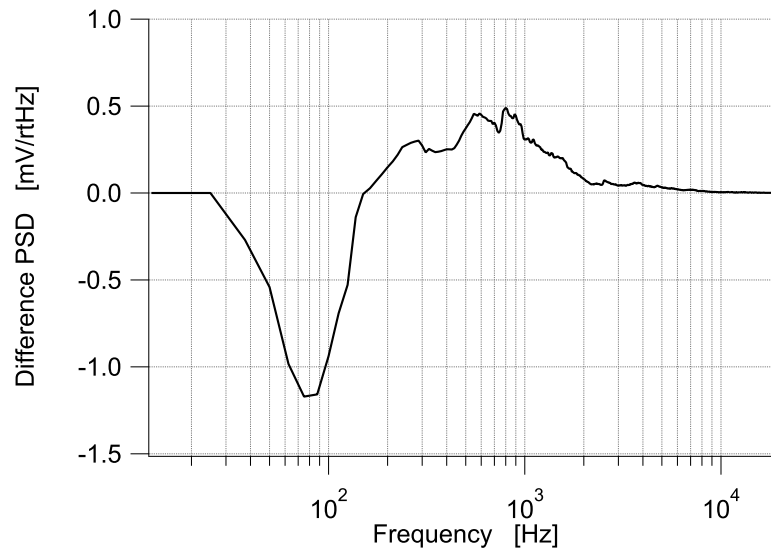
Figure C.5: Acoustic measurements, high frequency leakage. The graph shows the difference in power spectral density obtained by measuring the acoustic emission of the system with and without the granular system. The negative values at low frequencies and the positive values at high frequencies indicate that, due to the interactions between the grains, part of the energy that is fed with the vibration motor is distributed to higher frequencies. The leaking spectral power appears to peak in the region 1-2 kHz.

or 2 kHz. This band of frequency is easily driven into resonance since it corresponds (for the specific granular system under consideration) to the intrinsic frequency of a pair of glass spheres in mechanical contact, as discussed in the model of Ch 3.

C.4   Accelerometer frequency response

The acoustic frequency response spectra indicate that the granular material is responsible for frequency shifts in the spectral power available in the granular bath. This fact suggest that it could be wrong to assume that, when the system is excited with a broadband signal, all the frequencies in the excited bandwidth have comparable energies.
In order to clarify this fact the power spectra of the accelerometer where studied more in detail In this case the system is again vibrated with a filtered white noise between 70 and 800 Hz. The region of interest is the jamming region, the study is focused on vibration intensities $0.1 < \Gamma < 1$. The measured spectra, for four different value of Γ are shown in Fig. C.6.
As already noted in Ch. 2, the spike found around 1000 Hz represents the eigenfrequency of the oscillating element of the vibration motor, lowered from the factory value from the added weight of the container and the granular medium. This peak is clearly visible even if it is not directly excited (the upper cutoff is set at 800 Hz).
Now, if one considers the main driving frequency window (70 to 800 Hz), it is clear that the granular response is not completely flat, and that there is a small but visible peak around 110 Hz. While the appearance of this peak is still unexplained, we believe it is due to some

149
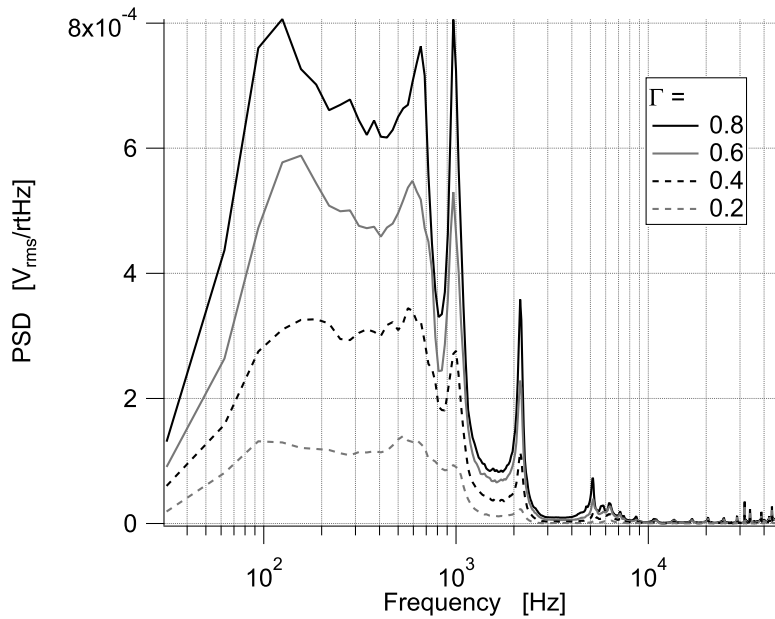
Figure C.6: Power spectral densities measured on the accelerometer. The data correspond to four different values of the vibration intensity Γ, chosen in the jamming region and indicated in the legend. This value is obtained by integrating the curve over the frequency window shown in the graph, knowing that the accelerometer has an integral response of 10 mV/g. The driving signal is a filtered white noise in the band 70-800 Hz.

mechanical resonance in the vibration motor assembly. This peak plays an important role in the response of the system, as it will be discussed in detail in Section 3.3.

From the same spectral densities curves one can also compute a "average" frequency f_s. The systems linear response region was considered (for both frequency and intensity), and a background correction, described by S_0, was applied. The average frequency f_s is then given by: $f_s = \int \left[S_\Gamma(f) - S_0(f) \right] f \, df \, / \int S_\Gamma(f) \, df$, with integration extended to a 5 kHz bandwidth. This gives an approximate value of 650 Hz for $0.1 < \Gamma < 1$, as it is shown in Fig. C.7. This average frequency is another important quantity needed to interpret the behavior of the system in forced mode, as will be discussed in the following section.

Figure C.7: Average frequency measured with the accelerometer and computed from the power spectra as discussed in the main text. We see that in the region of interest, $0.1 < \Gamma < 1$, this value does vary but is approximately 650 Hz.

Appendix D

The glass transition in polymers

In order to better understand the nature of the transition in vibrated granular media, the installation was tested with a glass forming polymer (alcohol). This test also allowed to assess 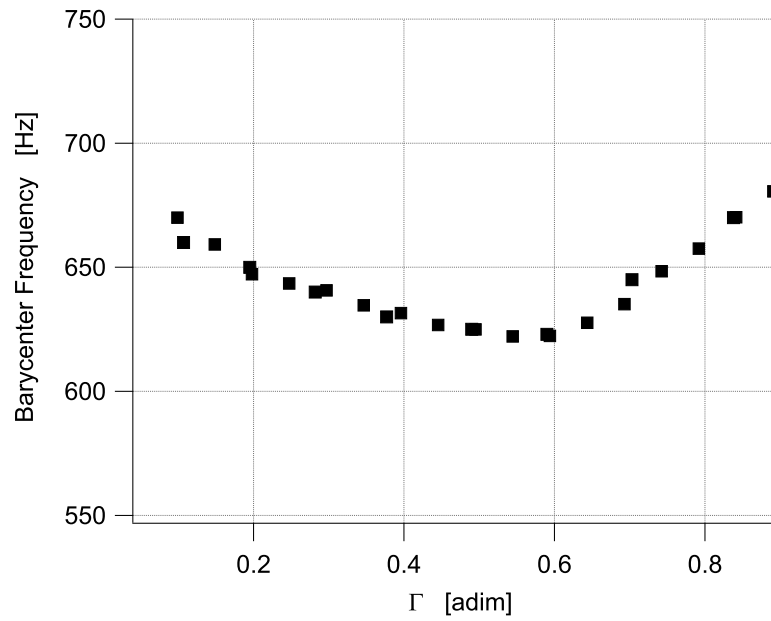the quality of the data that can be measured with the experimental setup of Ch. 2, in the slightly modified form of Fig. D.1. The reason to use an organic compound is straightforward. Alcohols have a rather broad range of transition temperatures; the specific 1-Hexadecanol alcohol was selected because its transition temperature (melting point 49° C) is readily accessible with simple laboratory equipment. The transition, as the melting point is crossed, could then be studied without the need to rework our installation. Also, with respect to generic paraffins, sufficiently pure material show very sharp transitions ranges, and this is ideal for testing purposes.

The experimental setup of the torsion oscillator was modified as shown in the sketch of Fig. D.1. The granular material and the vibration motor are removed. Below the torsion probe we placed an heating plate and a heath bath. This is used to regulate the temperature of the alcohol sample, and to allow slow enough heating and cooling ratios. The sample itself is held in a slightly smaller glass container, placed in the heat bath and tightly fastened in position with metallic clamps. The measurements are performed with a special two-tip finger probe, geometrically identical to the one used in granular materials; the tips are made of ceramics (instead of aluminum) to reduce local cooling effects, due to heat conductivity, at the probe-paraffin interface.

The alcohol can be heated up and melted with the heating plaque, and then again left to cool down to perform measurements during heating and cooling. The other experimental conditions (torque, excitation frequency, sampling frequency, etc.) are the same as those considered for granular systems (their role will be discussed more in detail in the following sections).

At high temperature, the alcohol is a liquid: in these conditions the apparent restoring coefficient is proportional to the elastic dynamic modulus, and it is very small (in fact the data show the intrinsic restoring coefficient due to the torsion suspensions). The loss angle, proportional to the energy dissipation, is also negligible. As the system is cooled down, it approaches the glass transition. This is marked by a sharp increase in the stiffness of the system, that starts to actively oppose the movement of the probe. At the transition temperature an increase in the energy dissipation is observed; this is marked by the appearance of a relaxation peak in the
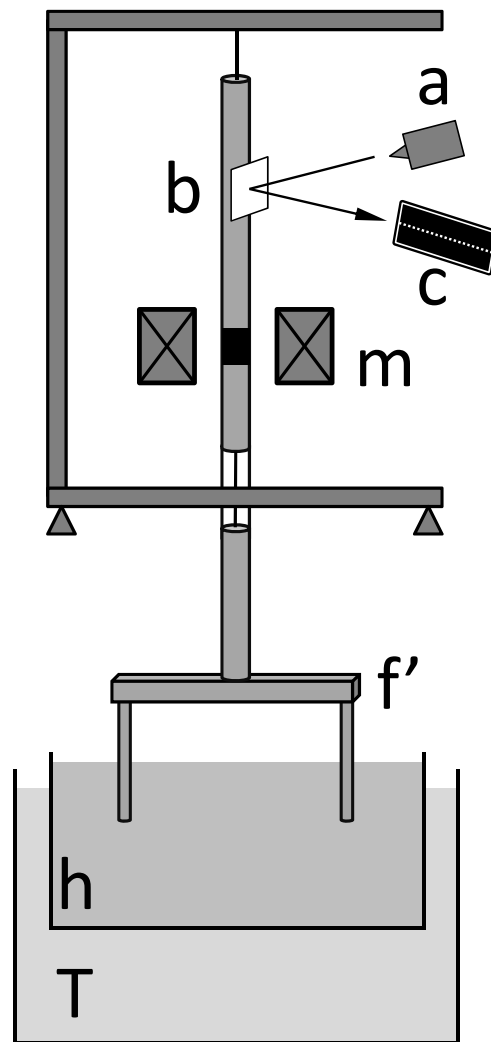
Figure D.1: Sketch of the configuration used to measure the glass transition in amorphous solids. The torsion oscillator is the same described in Ch. 2. The vibration motor and the granular system are replaced by a heating plate connected to an heath bath used to allow slow variation of the temperature of the alcohol. A thermocouple is used to monitor the temperature, and is visible on the right, besides one of the two tips of the probe. The two-tip finger probe shown here is similar to the one used in granular systems. In this case, the tips are made of ceramics instead of aluminum, to reduce heat conduction.
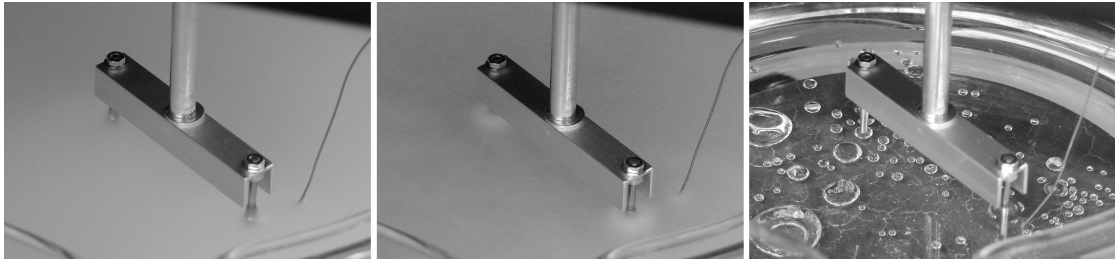
Figure D.2: The glass transition observed in 1-Hexadecanol. The probe and the alcohol sample are shown, as described in the sketch of Fig D.1. The temperature is controlled by an heat bath, which in turn is heated by the means of a hot plate (not visible here). The first photograph (left) shows the 1-Hexadecanol at low temperature, as a solid white colour. Around the transition temperature, the alcohol becomes translucent (middle). Around the colder tips of the probe, two whiter spots can be still observed. Finally, as the transition temperature is crossed, the alcohol becomes liquid and transparent (the bubbles of air that can be seen are trapped between the heath bath and the bottom of the glass contained, and not within the alcohol sample itself).

loss angle data. This peaks indicates that in these experimental conditions the interactions of the freezing polymers maximize the dissipation of energy in the system. Finally, as the transition is complete, the 1-Hexadecanol becomes an amorphous solid. Its stiffness is now much higher than the one due to the suspension wires, and reaches a limit value. Below the melting temperature, the polymers have little possibility to rearrange themselves, and therefore the system can only respond to external stresses with elastic deformations. For this reason the rate of energy dissipation drops considerably and, correspondingly, the measured loss angle goes down again to zero.

These observation allow to draw two interesting conclusion. The first is that the system is appropriately designed to detect and measure a glass transition in a real glass former, even if, *per se*, this is nothing new. In fact, using purposefully built instruments, glass transitions have been throughly studied in amorphous solids, such as true glasses, ceramics and plastics [117, 105]. Recent measurements were accurately performed on different polymers [194, 190]. The second is that, as it has been shown in the data of Ch. 3, many characteristic properties of the glass transition of the polymer are found in the transition of granular media: for example the height of the peak (stable around 0.8 rad), or the broadening factor. This is another indication that it is indeed meaningful to draw a direct parallel between real glasses and vibrated granular media in the jamming regime.
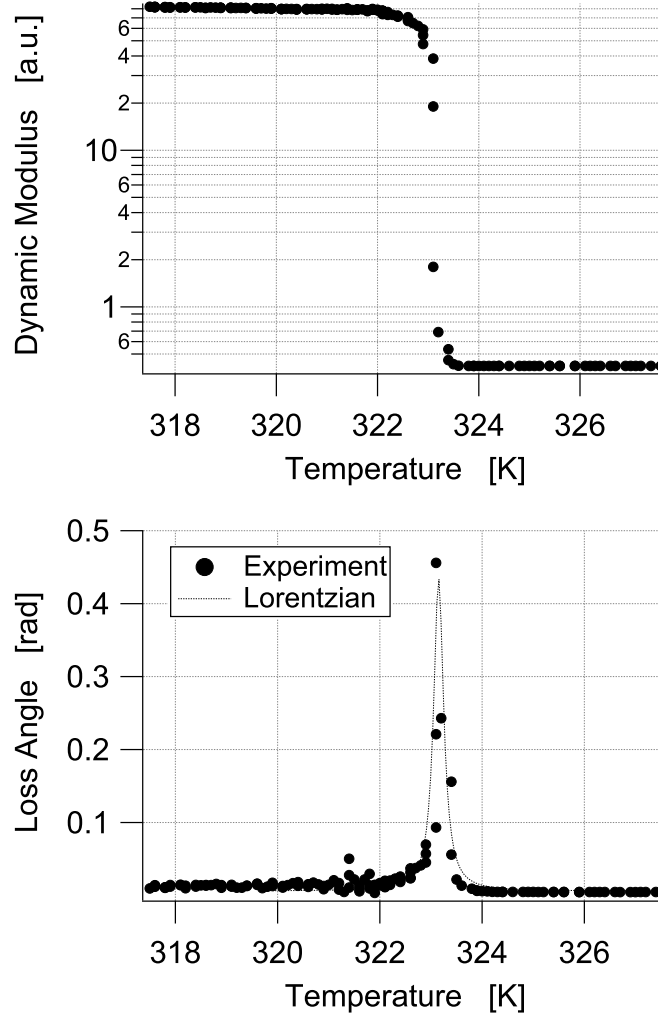
Figure D.3: Loss Tangent and Dynamic Modulus data from 1-Hexadecanol sample. The graph shows the two linearly independent components of the response function of the alcohol. The data span over a temperature window that covers the glass transition. At high temperature, the alcohol behaves as a liquid (low restoring force, low dissipation). In cooling, as the transition temperature is reached, the stiffness increases and we observe a relaxation peak. Finally, the peak vanishes as we complete the transition to the low temperature, amorphous phase. The system shows no hysteresis, but careful heating and cooling ratios have to be chosen to allow good measurements.

Appendix E

Voronoi volumes and Steinhardt order parameters

In Ch. 5, part of the data analysis applied to the MRI reconstruction of the granular sample required the introduction of the concepts of the Voronoi space decomposition and of the Steinhardt order parameters. This Appendix presents a brief introduction to these parameters.

E.1   Voronoi decomposition

The Voronoi decomposition is a way to subdivide a metric space into "area of pertinence", with respect to a collection of points, depending on the distance. For example, let us consider the standard 2D plane on which we have a collection of n poins. The Voronoi decomposition is the partitioning of the plane into convex polygons such that each polygon contains exactly one generating point; furthemore every other point of the plane in a given polygon is closer to its generating point than to any other generating point.

Voronoi diagrams as a way to extract information from geometrical properties of a series of points were considered as early as 1644 by Descartes. They were used by Dirichlet (1850) in the investigation of positive quadratic forms. They are named after the mathematician Georgy Voronoi (1907), who was the first to study them in detail, extending the definition of Voronoi diagrams to arbitrary dimensions. Due to the diffusion in many fields of science, a Voronoi diagram is sometimes also known as a Voronoi tessellation, a Voronoi decomposition, or a Dirichlet tessellation. The elements, or cells, are called Dirichlet regions, Thiessen polytopes, or Voronoi polygons.

The simplest and most familiar case is shown in Fig. E.1. In this case we have a finite set of points $(p_1, \ldots, p_n)$ in the Euclidean plane. In this case each site p_k is simply a point, and its corresponding Voronoi cell, R_k, consists of all points whose distance to p_k is not greater than their distance to any other site $p_j \neq p_k$. Each such cell is obtained from the intersection of half-spaces, and hence it is a convex polygon. The segments of the Voronoi diagram are all the points in the plane that are equidistant to the two nearest sites. The Voronoi vertices (nodes) are the points equidistant to three (or more) sites.

Numerically, all the geometric objects discussed in this section are easily computed. For each
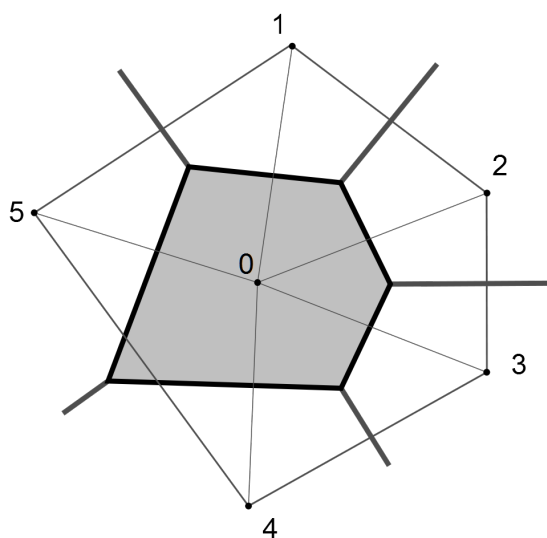
Figure E.1: Voronoi space decomposition of an Euclidean plane. The central point p_0 has five nearest neighbors. The gray colored area corresponds to the Voronoi cell relative to p_0. This area is delimited by the Voronoi segments, points equidistant from p_0 and one of its neighbors. The thin lines connecting the points are orthogonal to the Voronoi segments and define the Delaunay space decomposition, which is the dual transformation of the Voronoi decomposition.
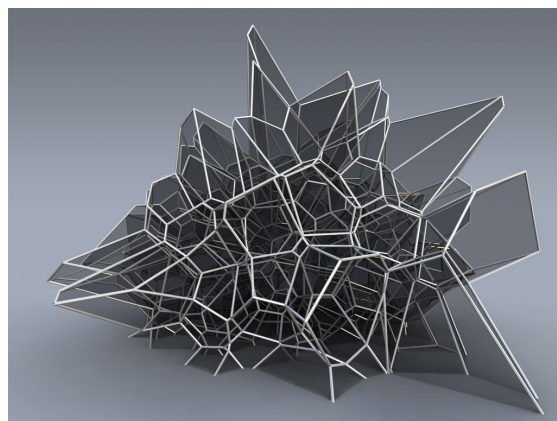
Figure E.2: Graphical representation of the spatial decomposition of a 3D region in Voronoi volumes. The image is an example of the Voronoi decomposition performed by the *qHull* software toolbox; it is generated by a seed consisting of a random arrangement of points in space.

site, a list of nearest neighbors is required. Afterwards, all the calculations involve simple affine geometry. A much more comprehensive review can be found in [257].

E.2 Steinhardt order parameters

When studying phase transitions, such as crystallization or a polymorph transformation, it is often useful to define a set of mathematical functions, or order parameters, that can be used to differentiate one of the states from the other and from the intermediate states. One would want, for example, to define parameters that have a value of zero for one phase and a nonzero value for another.

Steinhardt et al. [238] were among the first to define a a set of geometrically based order parameters that are now widely used for many systems, such as monoatomic fluids, highly symmetric molecules or colloids [258]. They were mainly interested in highlighting the symmetry breaking that happen in a crystalline structure upon melting: translational invariance and rotational symmetry.

The definition of the order parameters follows basically these lines. First, each particle has a certain number of "bonds" with the neighboring objects. This "bond" is a generic relationship, and is indicated by a vector $\vec{r}$ designating the mid point between the two particles, and calculated with respect to a coordinate system. To this bond is associated a set of number corresponding to the spherical harmonics averaged over the nearest neighbors (NN):

$$Q_{lm}(\vec{r}) = \left\langle Y_{lm}\left[\theta(\vec{r}), \phi(\vec{r})\right]\right\rangle_{NN}$$

These quantities depend on the orientation in space. For this reason one introduces the rotationally invariant combinations Q_l and W_l:

$$Q_l = \left[\frac{4\pi}{2l+1}\sum_{m=-l}^{+l}|Q_{lm}|^2\right]^{1/2} \tag{E.1}$$

and

$$W_l = \sum_{\substack{m_1,m_2,m_3 \\ m_1+m_2+m_3=0}}\begin{pmatrix} l & l & l \\ m_1 & m_2 & m_3 \end{pmatrix} \times Q_{lm_1}Q_{lm_2}Q_{lm_3} \tag{E.2}$$

where in this case the elements in the parenthesis are the Wigner $3j$ symbols [259].

As discussed in Ch. 5, these observables are useful because they are highly sensitive to the local order structure surrounding the particle for which they are calculated. A much more detailed discussion can be found in the original article [238].

Bibliography

[1] H J. Herrmann, J.-P. Hovi, and S. Luding, editors. *Physics of dry granular media.* Kluwer Academic Publishers, Dordrecht, The Nederlands, 1988.

[2] M. Modell and R.C. Reid. *Thermodynamics and its applications.* Prentice-Hall international series in the physical and chemical engineering sciences. Prentice-Hall, 1974.

[3] H. Hinrichsen and D.E. Wolf. *The physics of granular media.* Wiley-VCH, 2004.

[4] H. M. Jaeger, S. R. Nagel, and R. P. Behringer. The physics of granular materials. *Physics Today*, 32:220–222, April 1996.

[5] S.P. Pudasaini and K. Hutter. *Avalanche dynamics: dynamics of rapid flows of dense granular avalanches.* Springer, 2007.

[6] G. R. Darbre and J. P. Wolf. Nonlinear elastic constitutive law for granular materials applicable to pebble-bed core. *Nuclear Engineering and Design*, 88(2):161 – 168, 1985.

[7] K. Terzaghi, R.B. Peck, and G. Mesri. *Soil mechanics in engineering practice.* Wiley, 1996.

[8] R. P. Behringer. The scientist in the sandbox: Time-dependence, fractals and waves. *International Journal of Bifurcation and Chaos*, 7(5):963–978, 1997.

[9] F. Spahn and J. Schmidt. Hydrodynamic description of planetary rings. *GAMM-Mitt.*, 29(1):115–140, 2006.

[10] B. Armstrong-Hélouvry. *Control of machines with friction.* Kluwer international series in engineering and computer science: Robotics. Kluwer Academic Publishers, 1991.

[11] O. Reynolds. On the dilatancy of media composed of rigid particles in contact, with experimental illustrations. *Phil. Mag., Series 5*, 20(20):469–481, 1885.

[12] O. Reynolds. Experiments showing dilatancy, a property of granular material, possibly connected with gravitation. *Proc. Royal Institution of Great Britain*, 15-2:217–227, Feb 1886.

[13] J. Leech. The problem of the thirteen spheres. *The Mathematical Gazette*, 40(331):pp. 22–23, 1956.

Bibliography

[14] K. Schütte and B. L. van der Waerden. Das problem der dreizehn kugeln. *Mathematische Annalen*, 125:325–334, 1952.

[15] J.H. Conway, N.J.A. Sloane, and E. Bannai. *Sphere packings, lattices, and groups*. Grundlehren der mathematischen Wissenschaften. Springer, 1999.

[16] T. C. Hales. Historical overview of the kepler conjecture. *Discrete and Computational Geometry*, 36:5–20, 2006.

[17] T. C. Hales. The kepler conjecture. Retrieved online, July 2011., Nov 1998.

[18] M. Gardner. *Martin Gardner's new mathematical diversions from Scientific American*. University of Chicago Press, 1966.

[19] H. S. M. Coxeter. Close-packing and froth. *Illinois J. Math.*, 2(4B):746–758, 1958.

[20] H. S. M. Coxeter. An upper bound for the number of equal nonoverlapping spheres that can touch another of the same size. In V. Klee, editor, *Convexity: Proceedings of the Seventh Symposium in Pure Mathematics of the American Mathematical Society*, Proceedings of symposia in pure mathematics. University of Washington, American Mathematical Society, 1974.

[21] D. Hilbert and S. Cohn-Vossen. *Geometry and the imagination*. AMS Chelsea Publishing Series. AMS Chelsea Pub., 1999.

[22] H. Steinhaus. *Mathematical Snapshots*. Dover science book. Dover Publications, 1999.

[23] B. Cipra. Packing challenge mastered at last. *Science*, 281(5381):1267, 1998.

[24] D. A. Kottwitz. The densest packing of equal circles on a sphere. *Acta Crystallographica Section A*, 47(3):158–165, May 1991.

[25] S. Torquato and Y. Jiao. Dense packings of the platonic and archimedean solids. *Nature*, 460:876–879, August 2009.

[26] G. D. Scott. Packing of equal spheres. *Nature*, 188(4754):908–909, Dec 1960.

[27] T. Aste and D.L. Weaire. *The pursuit of perfect packing*. Taylor and Francis, New York, 2008.

[28] G. D. Scott and D. M. Kilgour. The density of random close packing of spheres. *Journal of Physics D: Applied Physics*, 2(6):863, 1969.

[29] J. D. Bernal. A geometrical approach to the structure of liquids. *Nature*, 183(4655):141–147, January 1959.

[30] J. L. Finney. Random packings and the structure of simple liquids. i. the geometry of random close packing. *Proceedings of the Royal Society of London. A. Mathematical and Physical Sciences*, 319(1539):479–493, 1970.

[31] D. J. Cumberland and R. J. Crawford. *The packing of particles.* Handbook of powder technology. Elsevier, 1987.

[32] C. Radin. Random close packing of granular matter. *Journal of Statistical Physics*, 131:567–573, 2008. 10.1007/s10955-008-9523-1.

[33] G. Y. Onoda and E. G. Liniger. Random loose packings of uniform spheres and the dilatancy onset. *Phys. Rev. Lett.*, 64(22):2727–2730, May 1990.

[34] S. Torquato, T. M. Truskett, and P. G. Debenedetti. Is random close packing of spheres well defined? *Phys. Rev. Lett.*, 84(10):2064–2067, Mar 2000.

[35] H. A. Janssen. Versuche über getreidedruck in silozellen. *Zeitschr. d. Vereines deutscher Ingenieure*, 39(35):1045–1049, 1895.

[36] Ja.B. Lvin. Analytical evaluation of pressures of granular materials on silo walls. *Powder Technology*, 4(5):280 – 285, 1971.

[37] J.-P. Bouchaud, M. E. Cates, and P. Claudin. Stress distribution in granular media and nonlinear wave equation. *J. Phys. I France*, 5(6):639–656, 1995.

[38] U. Marini Bettolo Marconi, A. Petri, and A. Vulpiani. Janssen's law and stress fluctuations in confined dry granular materials. *Physica A: Statistical Mechanics and its Applications*, 280(3-4):279 – 288, 2000.

[39] R. L. Michalowski. Arching prediction in granular materials with a nonlinear yield condition. *ASCE Conf. Proc.*, 188(40830):89–89, 2006.

[40] K. Terzaghi. *Theoretical soil mechanics.* J. Wiley, New York, 1943.

[41] M. Ammi, D. Bideau, and J. P. Troadec. Geometrical structure of disordered packings of regular polygons; comparison with disc packings structures. *Journal of Physics D: Applied Physics*, 20(4):424, 1987.

[42] M. Renouf, F. Dubois, and P. Alart. A parallel version of the non smooth contact dynamics algorithm applied to the simulation of granular media. *Journal of Computational and Applied Mathematics*, 168(1-2):375 – 382, 2004. Selected Papers from the Second International Conference on Advanced Computational Methods in Engineering (ACOMEN 2002).

[43] J. Zhang, T. Majmudar, and R. Behringer. Force chains in a two-dimensional granular pure shear experiment. *Chaos*, 18(4):041107, 2008.

[44] D. Howell, R. P. Behringer, and C. Veje. Stress fluctuations in a 2d granular couette experiment: A continuous transition. *Phys. Rev. Lett.*, 82(26):5241–5244, Jun 1999.

[45] F. Radjai, M. Jean, J.-J. Moreau, and S. Roux. Force distributions in dense two-dimensional granular systems. *Phys. Rev. Lett.*, 77(2):274–277, Jul 1996.

Bibliography

[46] C. Liu, S. R. Nagel, D. A. Schecter, S. N. Coppersmith, S. Majumdar, O. Narayan, and T. A. Witten. Force fluctuations in bead packs. *Science*, 269(5223):513–515, 1995.

[47] D. M. Mueth, H. M. Jaeger, and S. R. Nagel. Force distribution in a granular medium. *Phys. Rev. E: Stat., Nonlinear, Soft Matter Phys.*, 57(3):3164–3169, Mar 1998.

[48] C. Thornton. Force transmission in granular media. *KONA Powder and Particle*, 15:81–90, 1997.

[49] C. S. O'Hern, S. A. Langer, A. J. Liu, and S. R. Nagel. Force distributions near jamming and glass transitions. *Phys. Rev. Lett.*, 86(1):111–114, Jan 2001.

[50] J. H. Snoeijer, T. J. H. Vlugt, M. van Hecke, and W. van Saarloos. Force network ensemble: A new approach to static granular matter. *Phys. Rev. Lett.*, 92(5):054302, Feb 2004.

[51] A. J. Liu and S. R. Nagel. Nonlinear dynamics: Jamming is not just cool any more. *Nature*, 396(6706):21–22, November 1998.

[52] M. E. Cates, J. P. Wittmer, J.-P. Bouchaud, and P. Claudin. Jamming and static stress transmission in granular materials. *Chaos*, 9(3):511–522, 1999.

[53] K. Huang. *Statistical mechanics*. Wiley, 1987.

[54] P. Richard, M. Nicodemi, R. Delannay, P. Ribiere, and D. Bideau. Slow relaxation and compaction of granular systems. *Nat. Mater.*, 4(2):121–128, February 2005.

[55] H. A. Makse, J. Brujić, and S. F. Edwards. *Statistical Mechanics of Jammed Matter*, pages 45–85. Wiley-VCH Verlag GmbH & Co. KGaA, 2005.

[56] M. Jerkins, M. Schröter, H. L. Swinney, T. J. Senden, M. Saadatfar, and T. Aste. Onset of mechanical stability in random packings of frictional spheres. *Phys. Rev. Lett.*, 101(1):018301, Jul 2008.

[57] J. B. Knight, C. G. Fandrich, C. N. Lau, H. M. Jaeger, and S. R. Nagel. Density relaxation in a vibrated granular material. *Phys. Rev. E: Stat., Nonlinear, Soft Matter Phys.*, 51(5):3957–3963, May 1995.

[58] D. Arsenović, S. B. Vrhovac, Z. M. Jakšć, Lj. Budinski-Petković, and A. Belić. Simulation study of granular compaction dynamics under vertical tapping. *Phys. Rev. E: Stat., Nonlinear, Soft Matter Phys.*, 74(6):061302, Dec 2006.

[59] E. Caglioti, V. Loreto, H. J. Herrmann, and M. Nicodemi. A "tetris-like" model for the compaction of dry granular media. *Phys. Rev. Lett.*, 79(8):1575–1578, Aug 1997.

[60] J. T. Jenkins and S. B. Savage. A theory for the rapid flow of identical, smooth, nearly elastic, spherical particles. *Journal of Fluid Mechanics*, 130:187–202, 1983.

[61] E. R. Nowak, J. B. Knight, E. Ben-Naim, H. M. Jaeger, and S. R. Nagel. Density fluctuations in vibrated granular materials. *Phys. Rev. E: Stat., Nonlinear, Soft Matter Phys.*, 57(2):1971–1982, Feb 1998.

[62] J. Brujić, P. Wang, C. Song, D. L. Johnson, O. Sindt, and H. Makse. Granular dynamics in compaction and stress relaxation. *Phys. Rev. Lett.*, 95(12):128001, Sep 2005.

[63] P. Philippe and D. Bideau. Compaction dynamics of a granular medium under vertical tapping. *EPL (Europhysics Letters)*, 60(5):677, 2002.

[64] S. F. Edwards, D. V. Grinev, and J. Brujic. Fundamental problems in statistical physics of jammed packings. *Physica A: Statistical Mechanics and its Applications*, 330(1-2):61 – 76, 2003. RANDOMNESS AND COMPLEXITY: Proceedings of the International Workshop in honor of Shlomo Havlin's 60th birthday.

[65] A. Chakravarty, S.F. Edwards, D.V. Grinev, M. Mann, T.E. Phillipson, and A.J. Walton, editors. *Proceedings of the Workshop on Quasi-static Deformations of Particulate Materials.* Budapest University of Technology and Economics Press, Budapest., 2003.

[66] P. Philippe and D. Bideau. Granular medium under vertical tapping: Change of compaction and convection dynamics around the liftoff threshold. *Phys. Rev. Lett.*, 91(10):104302, Sep 2003.

[67] F. X. Villarruel, B. E. Lauderdale, D. M. Mueth, and H. M. Jaeger. Compaction of rods: Relaxation and ordering in vibrated, anisotropic granular material. *Phys. Rev. E: Stat., Nonlinear, Soft Matter Phys.*, 61(6):6914–6921, Jun 2000.

[68] J. B. Knight, E. E. Ehrichs, V. Yu. Kuperman, J. K. Flint, H. M. Jaeger, and S. R. Nagel. Experimental study of granular convection. *Phys. Rev. E: Stat., Nonlinear, Soft Matter Phys.*, 54(5):5726–5738, Nov 1996.

[69] E. L. Grossman. Effects of container geometry on granular convection. *Phys. Rev. E: Stat., Nonlinear, Soft Matter Phys.*, 56(3):3290–3300, Sep 1997.

[70] F. Melo, P. B. Umbanhowar, and H. L. Swinney. Hexagons, kinks, and disorder in oscillated granular layers. *Phys. Rev. Lett.*, 75(21):3838–3841, Nov 1995.

[71] T. H. Metcalf, J. B. Knight, and H. M. Jaeger. Standing wave patterns in shallow beds of vibrated granular material. *Physica A: Statistical and Theoretical Physics*, 236(3-4):202 – 210, 1997.

[72] P. Eshuis, K. van der Weele, D. van der Meer, R. Bos, and D. Lohse. Phase diagram of vertically shaken granular matter. *Phys. Fluids*, 19(12):123301, 2007.

[73] C. Bizon, M. D. Shattuck, J. B. Swift, W. D. McCormick, and Harry L. Swinney. Patterns in 3d vertically oscillated granular layers: Simulation and experiment. *Phys. Rev. Lett.*, 80(1):57–60, Jan 1998.

[74] P. B. Umbanhowar, F. Melo, and H. L. Swinney. Localized excitations in a vertically vibrated granular layer. *Nature*, 382(6594):793–796, August 1996.

[75] L. S. Tsimring and I. S. Aranson. Localized and cellular patterns in a vibrated granular layer. *Phys. Rev. Lett.*, 79(2):213–216, Jul 1997.

Bibliography

[76] T. Shinbrot. Competition between randomizing impacts and inelastic collisions in granular pattern formation. *Nature*, 389(6651):574–576, October 1997.

[77] L. Stenflo and M. Y. Yu. Origin of oscillons. *Nature*, 384(6606):224–224, November 1996.

[78] D. Blair, I. S. Aranson, G. W. Crabtree, V. Vinokur, L. S. Tsimring, and C. Josserand. Patterns in thin vibrated granular layers: Interfaces, hexagons, and superoscillons. *Phys. Rev. E: Stat., Nonlinear, Soft Matter Phys.*, 61(5):5600–5610, May 2000.

[79] C. Mankoc, A. Janda, R. Arévalo, J. Pastor, I. Zuriguel, A. Garcimartín, and D. Maza. The flow rate of granular materials through an orifice. *Granular Matter*, 9:407–414, 2007. 10.1007/s10035-007-0062-2.

[80] P. G. Rognon, J.-N. Roux, M. Naaim, and F. Chevoir. Dense flows of cohesive granular materials. *Journal of Fluid Mechanics*, 596:21–47, 2008.

[81] Y. Ben-Zion, K. Dahmen, and J. Uhl. A unifying phase diagram for the dynamics of sheared solids and granular materials. *Pure and Applied Geophysics*, 1:1–17, 2011. 10.1007/s00024-011-0273-7.

[82] J. Lee and H. J. Herrmann. Angle of repose and angle of marginal stability: molecular dynamics of granular particles. *Journal of Physics A: Mathematical and General*, 26(2):373, 1993.

[83] A. Daerr and S. Douady. Two types of avalanche behaviour in granular media. *Nature*, 399(6733):241–243, May 1999.

[84] J. M. Luck and A. Mehta. Dynamics at the angle of repose: jamming, bistability, and collapse. *Journal of Statistical Mechanics: Theory and Experiment*, 2004(10):P10015, 2004.

[85] H. M. Jaeger and S. R. Nagel. Physics of the granular state. *Science*, 255(5051):1523–1531, 1992.

[86] H. M. Jaeger, Chu-heng Liu, and Sidney R. Nagel. Relaxation at the angle of repose. *Phys. Rev. Lett.*, 62(1):40–43, Jan 1989.

[87] J.-P. Bouchaud, M. E. Cates, J. Ravi Prakash, and S. F. Edwards. A model for the dynamics of sandpile surfaces. *J. Phys. I France*, 4(10):1383–1410, 1994.

[88] L. Mahadevan and Y. Pomeau. Propagating fronts on sandpile surfaces. *Europhys. Lett.*, 46(5):595–601, 1999.

[89] A. Aradian, E. Raphaël, and P.-G. deăGennes. Surface flows of granular materials: a short introduction to some recent models. *Comptes Rendus Physique*, 3(2):187 – 196, 2002.

[90] J. Gollub. Discrete and continuum descriptions of matter. *Physics Today*, 56(1):10–11, 2003.

[91] F. Froiio, G. Tomassetti, and I. Vardoulakis. Mechanics of granular materials: The discrete and the continuum descriptions juxtaposed. *International Journal of Solids and Structures*, 43(25-26):7684 – 7720, 2006.

[92] E. B. Pitman, C. C. Nichita, A. Patra, A. Bauer, M. Sheridan, and M. Bursik. Computing granular avalanches and landslides. *Phys. Fluids*, 15(12):3638–3646, 2003.

[93] T. Börzsönyi, T. C. Halsey, and R. E. Ecke. Two scenarios for avalanche dynamics in inclined granular layers. *Phys. Rev. Lett.*, 94(20):208001, May 2005.

[94] A. Garcimartín, C. Mankoc, A. Janda, R. Arévalo, J. M. Pastor, I. Zuriguel, and D. Maza. Flow and jamming of granular matter through an orifice. In Cécile Appert-Rolland, François Chevoir, Philippe Gondret, Sylvain Lassarre, Jean-Patrick Lebacque, and Michael Schreckenberg, editors, *Traffic and Granular Flow Š07*, pages 471–486. Springer Berlin Heidelberg, 2009.

[95] R. Kubo, M. Toda, and N. Hashitsume. *Statistical Physics*, volume II. Springer-Verlag, Berlin, 1991.

[96] H.E. Stanley. *Introduction to phase transitions and critical phenomena*. International series of monographs on physics. Oxford University Press, 1987.

[97] L. D. Landau and E. M. Lifshits. *Statistical physics*, volume 5 and 9 of *Course of Theoretical Physics*. Butterworth-Heinemann, 1980.

[98] J.R. Partington. *A short history of chemistry*. Dover Publications, 1989.

[99] S. Carnot, R.H. Thurston, H. Carnot, and W.T. Kelvin. *Reflections on the motive power of heat and on machines fitted to develop this power*. J. Wiley, 1890.

[100] J.R. Welty. *Fundamentals of momentum, heat, and mass transfer*. Wiley, 2008.

[101] M. C. Wendl. General solution for the couette flow profile. *Phys. Rev. E*, 60(5):6192–6194, Nov 1999.

[102] C. A. Angell. Relaxation in liquids, polymers and plastic crystals – strong/fragile patterns and problems. *Journal of Non-Crystalline Solids*, 131-133(Part 1):13 – 31, 1991.

[103] G. Tarjus, D. Kivelson, and P. Viot. The viscous slowing down of supercooled liquids as a temperature-controlled super-arrhenius activated process: a description in terms of frustration-limited domains. *Journal of Physics: Condensed Matter*, 12(29):6497, 2000.

[104] P. G. Debenedetti and F. H. Stillinger. Supercooled liquids and the glass transition. *Nature*, 410(6825):259–267, March 2001.

[105] A. K. Varshneya. *Fundamentals of inorganic glasses*. Gulf Professional Publishing, 1994. ISBN 0127149708, 9780127149707.

[106] E.L. Bourhis. *Glass: mechanics and technology*. Wiley-VCH, 2008.

Bibliography

[107] M. Goldstein. Viscous liquids and the glass transition: A potential energy barrier picture. *The Journal of Chemical Physics*, 51(9):3728–3739, 1969. cited By (since 1996) 608.

[108] F. H. Stillinger and T. A. Weber. Packing structures and transitions in liquids and solids. *Science*, 225(4666):pp. 983–989, 1984.

[109] C. Angell, P. Poole, and J. Shao. Glass-forming liquids, anomalous liquids, and polyamorphism in liquids and biopolymers. *Il Nuovo Cimento D*, 16:993–1025, 1994. 10.1007/BF02458784.

[110] C. A. Angell, K. L. Ngai, G. B. McKenna, P. F. McMillan, and S. W. Martin. Relaxation in glassforming liquids and amorphous solids. *J. Appl. Phys.*, 88(6):3113–3157, 2000.

[111] K.J. Rao. *Structural chemistry of glasses*. Elsevier, 2002.

[112] H. Vogel. Temperaturabhangigkeitsgesetz der viskositat von flussigkeiten. *Phys. Z.*, 22:645–646, 1921.

[113] G. S. Fulcher. Analysis of recent measurements of the viscosity of glasses. *Journal of the American Ceramic Society*, 8(6):339–355, 1925.

[114] G. Tammann and W. Hesse. Die abhängigkeit der viscosität von der temperatur bie unterkühlten flüssigkeiten. *Zeitschrift für anorganische und allgemeine Chemie*, 156(1):245–257, 1926.

[115] G. W. Scherer. Editorial comments on a paper by gordon s. fulcher. *Journal of the American Ceramic Society*, 75(5):1060–1062, 1992.

[116] C. A. Angell. Liquid fragility and the glass transition in water and aqueous solutions. *Chemical Reviews*, 102(8):2627–2650, 2002.

[117] J. Pérez. *Matériaux non cristallins et science du désordre*. Presses Polytechniques et Universitaires Romandes, Lyon, 2001.

[118] L. F. Cugliandolo. Dynamics of glassy systems, 2002.

[119] M. Mézard, G. Parisi, and M. Á. Virasoro. *Spin glass theory and beyond*. World Scientific lecture notes in physics. World Scientific, 1987.

[120] K.H. Fischer and J. Hertz. *Spin glasses*. Cambridge studies in magnetism. Cambridge University Press, 1993.

[121] Dapeng Bi, Jie Zhang, Bulbul Chakraborty, and R. P. Behringer. Jamming by shear. *Nature*, 480(7377):355–358, December 2011.

[122] Sebastian Bustingorry, Leticia F. Cugliandolo, and Daniel Domínguez. Out-of-equilibrium dynamics of the vortex glass in superconductors. *Phys. Rev. Lett.*, 96(2):027001, Jan 2006.

[123] R. Schaller, G. Fantozzi, and G. Gremaud. Mechanical spectroscopy q^{-1} 2001. *Mat. Sci. Forum - TTP*, 366-368(178-247):200–246, 2001.

[124] A. S. Nowick and B. S. Berry. *Anelastic Relaxation in Crystalline Solids.* Academic Press, Inc., New York and London, 1972.

[125] A. J. Liu and S. R. Nagel. *Jamming and Rheology: Constrained Dynamics on Microscopic and Macroscopic Scales.* Taylor and Francis, New York, 2001.

[126] G. Biroli. Jamming: A new kind of phase transition? *Nat Phys*, 3(4):222–223, April 2007.

[127] P. W. Anderson. Through the glass lightly. *Science*, 267(5204):1615–1616, 1995.

[128] L. Berthier and T. A. Witten. Glass transition of dense fluids of hard and compressible spheres. *Phys. Rev. E*, 80:021502, Aug 2009.

[129] A. Einstein and J. J. Stachel. *Einstein's miraculous year: five papers that changed the face of physics.* Princeton paperbacks. Princeton University Press, 2005.

[130] S.G. Brush. *The kind of motion we call heat.* Number Vol. 2 in North-Holland personal library. North-Holland, 1986.

[131] E. Nelson. *Dynamical theories of Brownian motion.* Mathematical notes. Princeton University Press, 1967.

[132] A. Pais. *Subtle Is the Lord: The Science and the Life of Albert Einstein.* Oxford University Press, 2005.

[133] N. Wax. *Selected Papers on Noise and Stochastic Processes.* Dover phoenix editions. Dover Publications, 2003.

[134] B. Duplantier. Brownian motion, "diverse and undulating", 2005.

[135] E. Frey and K. Kroy. Brownian motion: a paradigm of soft matter and biological physics. *Annalen der Physik*, 14:20, 2005.

[136] H. S. Van Klooster. Jan ingenhousz. *Journal of Chemical Education*, 29(7):353, 1952.

[137] J. J. Bennett, editor. *The miscellaneous botanical works of Robert Brown*, volume 1. R. Hardwicke, London, 1866.

[138] R. Brown. A brief account of microscopical observations made in the months of june, july, and august, 1827, on the particles contained in the pollen of plants; and on the general existence of active molecules in organic and inorganic bodies. *Ann. Sci. Naturelles*, 14:341–362, 1828.

[139] R. Brown. A brief account of microscopical observations made in the months of june, july, and august, 1827, on the particles contained in the pollen of plants; and on the general existence of active molecules in organic and inorganic bodies. *Phil. Mag.*, 4:161–173, 1828.

Bibliography

[140] P. Lévy. *Processus stochastiques et mouvement brownien.* Éditions Jacques Gabay, Sceaux, 1992. Followed by a note by M. Loève, Reprint of the second (1965) edition.

[141] J. Perrin. L'agitation moléculaire et le mouvement brownien. *C. R. Acad. Sci. Paris,* 146:967–70, 1908.

[142] L.-G. Gouy. Note sur le mouvement brownien. *J. de Physique,* 7:561, 1888.

[143] M. D. Haw. Colloidal suspensions, brownian motion, molecular reality: a short history. *Journal of Physics: Condensed Matter,* 14(33):7769, 2002.

[144] G. Parisi. Brownian motion. *Nature,* 433(7023):221–221, January 2005.

[145] A. Einstein. Über die von der molekularkinetischen theorie der wärme geforderte bewegung von in ruhenden flüssigkeiten suspendierten teilchen. *Ann. Phys.,* 322(8):549–560, 1905.

[146] A. Einstein. Zur theorie der brownschen bewegung. *Annalen der Physik,* 324(2):371–381, 1906.

[147] A. Einstein. Eine neue bestimmung der moleküldimensionen. *Annalen der Physik,* 324(2):289–306, 1906.

[148] A. Einstein. Theoretische bemerkungen über die brownsche bewegung. *Zeit. f. Elektrochemie,* 13:41–42, 1907.

[149] A. Einstein. Elementare theorie der brownschen bewegung. *Zeit. f. Elektrochemie,* 14:245–239, 1908.

[150] P. Langevin. Sur la theorie du mouvement brownien. *C. R. Acad. Sci. Paris,* 146:530–533, 1908.

[151] M. Smoluchowski. Zur kinetischen theorie der brownschen molekularbewegung und der suspensionen. *Ann. Phys.,* 21:756–780, 1906.

[152] A. Fick. Über diffusion. *Annalen der Physik,* 170(1):59–86, 1855.

[153] J. Zinn-Justin. *Quantum field theory and critical phenomena.* International series of monographs on physics. Clarendon Press, 2002.

[154] G. E. Uhlenbeckm and L. S. Ornstein. On the theory of the brownian motion. *Phys. Rev.,* 36:823–841, 1930.

[155] M. C. Wang and G. E. Uhlenbeck. On the theory of brownian motion ii. *Rev. Mod. Phys.,* 36:323–342, 1945.

[156] M. J. Nye. *Molecular Reality: a perspective on the scientific work of Jean Perrin.* Macdonald, London, 1972.

[157] P. Hänggi and P. Jung. *Colored Noise in Dynamical Systems*, pages 239–326. John Wiley & Sons, Inc., 2007.

[158] M.J. Buckingham. *Noise in electronic devices and systems*. Ellis Horwood series in electrical and electronic engineering. E. Horwood, 1983.

[159] A.W. Drake. *Fundamentals of applied probability theory*. McGraw-Hill series in probability and statistics. McGraw-Hill, 1967.

[160] W. Rudin. *Functional analysis*. International series in pure and applied mathematics. McGraw-Hill, 1991.

[161] H. Goldstein, C. Poole, and J. Safko. *Classical Mechanics*. Addison Wesley, San Francisco, 2002.

[162] V.I. Arnol'd. *Mathematical methods of classical mechanics*. Graduate texts in mathematics. Springer-Verlag, 1989.

[163] J.D. Jackson. *Classical electrodynamics*. John Wiley & Sons, 1999.

[164] W. Gerlach and E. Lehrer. Über die messung der rotatorischen brownschen bewegung mit hilfe einer drehwage. *Naturwissenschaften*, 15:15–15, 1927. 10.1007/BF01504873.

[165] G. E. Uhlenbeck and S. Goudsmit. A problem in brownian motion. *Phys. Rev.*, 34(1):145–151, Jul 1929.

[166] D. Ben-Avraham and S. Havlin. *Diffusion and reactions in fractals and disordered systems*. Cambridge University Press, 2000.

[167] J.-P. Bouchaud and A. Georges. Anomalous diffusion in disordered media: Statistical mechanisms, models and physical applications. *Physics Reports*, 195(4-5):127 – 293, 1990.

[168] N. Wiener. The average of an analytic functional and the brownian movement. *Proc. Natl. Acad. Sci. U. S. A.*, 7(10):pp. 294–298, 1921.

[169] M. Kac. On distributions of certain wiener functionals. *Transactions of the American Mathematical Society*, 65(1):pp. 1–13, 1949.

[170] A. H. Guth. Eternal inflation and its implications. *J. Phys. A*, 40:6811–6826, 2007.

[171] B. Fischer and M. Scholes. The pricing of options and corporate liabilities. *Journal of Political Economy*, 81(3):pp. 637–654, 1973.

[172] Wikipedia. Wiener process — Wikipedia, the free encyclopedia, 2010. [Online; accessed 19-October-2010].

[173] L. Bocquet, E. Charlaix, S. Ciliberto, and J. Crassous. Moisture-induced ageing in granular media and the kinetics of capillary condensation. *Nature*, 396(6713):735–737, December 1998.

Bibliography

[174] G. D'Anna. Mechanical properties of granular media, including snow, investigated by a low-frequency forced torsion pendulum. *Phys. Rev. E: Stat., Nonlinear, Soft Matter Phys.*, 62(1 Pt B):982–92, 2000.

[175] H. K. Pak, E. Van Doorn, and R. P. Behringer. Effects of ambient gases on granular materials under vertical vibration. *Phys. Rev. Lett.*, 74(23):4643–4646, Jun 1995.

[176] W. Kaplan. *Advanced calculus.* Addison-Wesley, 2002.

[177] Z. Farkas, P. Tegzes, A. Vukics, and T. Vicsek. Transitions in the horizontal transport of vertically vibrated granular layers. *Phys. Rev. E: Stat., Nonlinear, Soft Matter Phys.*, 60(6 Pt B):7022–31, 1999.

[178] Z. Farkas, F. Szalai, D. E. Wolf, and T. Vicsek. Segregation of granular binary mixtures by a ratchet mechanism. *Phys. Rev. E: Stat., Nonlinear, Soft Matter Phys.*, 65:022301, 2002.

[179] D. C. Rapaport. Mechanism for granular segregation. *Phys. Rev. E: Stat., Nonlinear, Soft Matter Phys.*, 64(6):061304, Nov 2001.

[180] R. Balzan, F. Dalton, V. Loreto, A. Petri, and G. Pontuale. Brownian motor in a granular medium. *Phys. Rev. E: Stat., Nonlinear, Soft Matter Phys.*, 83(3):031310, Mar 2011.

[181] M. Smoluchowski. Experimentell nachweisbare, der üblichen thermodynamik widersprechende molekularphänomene. *Phy. Z.*, 13:1069, 1912.

[182] R.P. Feynman, R.B. Leighton, and M. Sands. *Feynman lectures on physics. Vol. 1: Mainly mechanics, radiation and heat.* Addison-Wesley, 1979.

[183] P. Hänggi, F. Marchesoni, and F. Nori. Brownian motors. *Annalen der Physik*, 14(1-3):51–70, 2005.

[184] P. Hänggi and F. Marchesoni. Artificial brownian motors: Controlling transport on the nanoscale. *Rev. Mod. Phys.*, 81(1):387–442, Mar 2009.

[185] P. Reimann and P. Hänggi. Introduction to the physics of brownian motors. *Applied Physics A: Materials Science & Processing*, 75:169–178, 2002. 10.1007/s003390201331.

[186] M. Duarte, J.M. Molina, R. Prieto, E. Louis, and J. Narciso. Self-similar fluctuations and 1/f noise in dry friction dynamics. *Metallurgical and Materials Transactions A*, 38:298–305, 2007.

[187] G. D'Anna, P. Mayor, A. Barrat, V. Loreto, and F. Nori. Observing brownian motion in vibration-fluidized granular matter. *Nature*, 424(6951):909–12, 2003.

[188] G. D'Anna and G. Gremaud. The jamming route to the glass state in weakly perturbed granular media. *Nature*, 413(6854):407–409, Sep 2001.

[189] E. I. Corwin, H. M. Jaeger, and S. R. Nagel. Structural signature of jamming in granular media. *Nature*, 435(7045):1075–1078, June 2005.

172

[190] S. Cerveny, A. Ghilarducci, H. Salva, and A. J. Marzocca. Glass-transition and secondary relaxation in sbr-1502 from dynamic mechanical data. *Polymer*, 41(6):2227–2230, March 2000.

[191] S. Cerveny, R. Bergman, G. A. Schwartz, and P. Jacobsson. Dielectric α- and β-relaxations in uncured styrene butadiene rubber. *Macromolecules*, 35(11):4337–4342, May 2002.

[192] J. Y. Cavaille, J. Perez, and G. P. Johari. Molecular theory for the rheology of glasses and polymers. *Phys. Rev. B: Condens. Matter Mater. Phys.*, 39(4):2411–2422, Feb 1989.

[193] Q. Wang, J.M. Pelletier, J. Lu, and Y.D. Dong. Study of internal friction behavior in a zr base bulk amorphous alloy around the glass transition. *Mater. Sci. Eng., A*, 403(1-2):328 – 333, 2005.

[194] D. Mari and R. Schaller. Mechanical spectroscopy in carbon nanotube reinforced abs. *Mater. Sci. Eng., A*, 521-522:255–258, September 2009.

[195] Xuebang Wu and Zhengang Zhu. Dynamic crossover of α' relaxation in poly(vinyl acetate) above glass transition via mechanical spectroscopy. *J. Phys. Chem. B*, 113(32):11147–11152, August 2009.

[196] P. Mayor, G. D'Anna, A. Barrat, and V. Loreto. Observing brownian motion and measuring temperatures in vibration-fluidized granular matter. *New Journal of Physics*, 7:28, 2005.

[197] P. Mayor. *Fluid and glassy phases of vibrated granular matter studied with a torsion oscillator*. PhD thesis, EPFL, 2005.

[198] S. Mann and S. Haykin. The chirplet transform: A generalization of gabor's logon transform., 1991.

[199] G. Gremaud. Dislocation-point defects interaction. *Mat. Sci. Forum*, 366-368:178–247, 2001.

[200] R. M. Fuoss. Electrical properties of solids. vii. the system polyvinyl chloride-diphenyl. *Journal of the American Chemical Society*, 63(2):378–385, February 1941.

[201] M. Tarzia, G. Biroli, A. Lefèvre, and J.-Ph. Bouchaud. Anomalous nonlinear response of glassy liquids: General arguments and a mode-coupling approach. *The Journal of Chemical Physics*, 132(5):054501, 2010.

[202] C. Crauste-Thibierge, C. Brun, F. Ladieu, D. L'Hôte, G. Biroli, and J-P. Bouchaud. Evidence of growing spatial correlations at the glass transition from nonlinear response experiments. *Phys. Rev. Lett.*, 104:165703, Apr 2010.

[203] L. Berthier, L. F. Cugliandolo, and J. L. Iguain. Glassy systems under time-dependent driving forces: Application to slow granular rheology. *Phys. Rev. E*, 63:051302, Apr 2001.

[204] G. D'Anna and G. Gremaud. Vogel-Fulcher-Tammann-type diffusive slowdown in weakly perturbed granular media. *Phys. Rev. Lett.*, 87(25):254302, 2001.

Bibliography

[205] A. L. Sellerio, D. Mari, G. Gremaud, and G. D'Anna. Glass transition associated with the jamming of vibrated granular matter. *Phys. Rev. E: Stat., Nonlinear, Soft Matter Phys.*, 83(2):021301, Feb 2011.

[206] H. Risken. *The Fokker-Planck equation: methods of solution and applications.* Springer series in synergetics. Springer, 1996.

[207] T. S. Majmudar and R. P. Behringer. Contact force measurements and stress-induced anisotropy in granular materials. *Nature*, 435(1079):1079–1082, June 2005.

[208] J. Galambos, J. Lechner, and E. Simiu. *Extreme value theory and applications.* Extreme Value Theory and Applications: Proceedings of the Conference on Extreme Value Theory and Applications, Gaithersburg Maryland 1993. Kluwer Academic Publishers, 1994.

[209] B. Gnedenko. Sur la distribution limite du terme maximum d'une serie aleatoire. *The Annals of Mathematics*, 44(3):423–453, 1943.

[210] E.J. Gumbel. *Statistics of extremes.* Dover books on mathematics. Dover Publications, 2004.

[211] F. Radjai and S. Roux. Turbulentlike fluctuations in quasistatic flow of granular media. *Phys. Rev. Lett.*, 89(6):064302, Jul 2002.

[212] R. Metzler and J. Klafter. The restaurant at the end of the random walk: recent developments in the description of anomalous transport by fractional dynamics. *Journal of Physics A: Mathematical and General*, 37(31):R161, 2004.

[213] F. Roueff and J. Levy Vehel. A regularization approach to fractional dimension estimation. In *Fractals 98*, 1998.

[214] B. B. Mandelbrot. *The Fractal Geometry of Nature.* W. H. Freedman and Co., New York, 1983.

[215] V. Balakrishnan. Anomalous diffusion in one dimension. *Physica A: Statistical Mechanics and its Applications*, 132(2-3):569 – 580, 1985.

[216] P. G. de Gennes. Granular matter: a tentative view. *Rev. Mod. Phys.*, 71(2):S374–S382, Mar 1999.

[217] W. R. Schneider and W. Wyss. Fractional diffusion and wave equations. *Journal of Mathematical Physics*, 30(1):134–144, 1989.

[218] A. I. Saichev and G. M. Zaslavsky. Fractional kinetic equations: solutions and applications. *Chaos: An Interdisciplinary Journal of Nonlinear Science*, 7(4):753–764, 1997.

[219] E. Barkai and V. N. Fleurov. Generalized einstein relation: A stochastic modeling approach. *Phys. Rev. E: Stat., Nonlinear, Soft Matter Phys.*, 58(2):1296–1310, Aug 1998.

174

[220] H. Peitgen and D. Saupe, editors. *The Science of fractal images.* Springer-Verlag, New York, 1988.

[221] J. Lévi Véhel and P. Legrand. *Thinking In Patterns. Fractals and Related Phenomena in Nature.*, pages 321–323. World Scientific, Vancouver, Canada, April 2004. Ed. M. M. Novak.

[222] S. R. Simanca and S. Sutherland. Mathematical problem solving with computers, 2002.

[223] Z. Feng, M. J. Zuo, and F. Chu. Application of regularization dimension to gear damage assessment. *Mechanical Systems and Signal Processing*, 24(4):1081 – 1098, 2010.

[224] P. Lévy. Wiener's random function, and other Laplacian random functions. In *Proceedings of the Second Berkeley Symposium on Mathematical Statistics and Probability, 1950*, pages 171–187, Berkeley and Los Angeles, 1951. University of California Press.

[225] P. M. Reis, R. A. Ingale, and M. D. Shattuck. Caging dynamics in a granular fluid. *Phys. Rev. Lett.*, 98:188301, Apr 2007.

[226] T. Aste, M. Saadatfar, and T. J. Senden. Local and global relations between the number of contacts and density in monodisperse sphere packs. *Journal of Statistical Mechanics: Theory and Experiment*, 2006(07):P07010, 2006.

[227] L. P. Kadanoff. Built upon sand: Theoretical ideas inspired by granular flows. *Rev. Mod. Phys.*, 71(1):435–444, Jan 1999.

[228] H. M. Jaeger, S. R. Nagel, and R. P. Behringer. Granular solids, liquids, and gases. *Rev. Mod. Phys.*, 68(4):1259–1273, Oct 1996.

[229] O. Dauchot. Glassy behaviours in a-thermal systems, the case of granular media: A tentative review. In Malte Henkel, Michel Pleimling, and Roland Sanctuary, editors, *Ageing and the Glass Transition*, volume 716 of *Lecture Notes in Physics*, pages 161–206. Springer Berlin / Heidelberg, 2007.

[230] S. F. Edwards and R. B. S. Oakeshott. Theory of powders. *Physica A: Statistical and Theoretical Physics*, 157(3):1080 – 1090, 1989.

[231] J. Langer. The mysterious glass transition. *Physics Today*, 60(2):8–9, 2007.

[232] T. Kawaguchi. Mri measurement of granular flows and fluid-particle flows. *Advanced Powder Technology*, 21(3):235 – 241, 2010.

[233] T. Aste, M. Saadatfar, A. Sakellariou, and T. J. Senden. Investigating the geometrical structure of disordered sphere packings. *Physica A: Statistical Mechanics and its Applications*, 339(1-2):16 – 23, 2004. Proceedings of the International Conference New Materials and Complexity.

Bibliography

[234] Z.P. Liang, P.C. Lauterbur, and IEEE Engineering in Medicine and Biology Society. *Principles of magnetic resonance imaging: a signal processing perspective.* IEEE Press series in biomedical engineering. SPIE Optical Engineering Press, 2000.

[235] L.G. Shapiro and G.C. Stockman. *Computer visión.* Prentice Hall, 2001.

[236] T. Aste, M. Saadatfar, and T. J. Senden. Geometrical structure of disordered sphere packing. *Phys. Rev. E: Stat., Nonlinear, Soft Matter Phys.*, 71:061302, 2005.

[237] G. D. Scott. Radial distribution functions from small packings of spheres. *Nature*, 217:733–735, February, 24 1968.

[238] P. J. Steinhardt, D. R. Nelson, and M. Ronchetti. Bond-orientational order in liquids and glasses. *Phys. Rev. B*, 28:784–805, Jul 1983.

[239] D. Bernal. Packing of spheres. *Nature*, 188:908–909, December, 10 1960.

[240] G. Parisi and F. Zamponi. Mean-field theory of hard sphere glasses and jamming. *Rev. Mod. Phys.*, 82:789–845, Mar 2010.

[241] C. Song, P. Wang, and H. A. Makse. A phase diagram for jammed matter. *Nature*, 453(7195):629–632, May 2008.

[242] G. Parisi and F. Zamponi. A replica approach to glassy hard spheres. *Journal of Statistical Mechanics: Theory and Experiment*, 2009(03):P03026, 2009.

[243] G. Parisi and F. Zamponi. The ideal glass transition of hard spheres. *Jour. Chem. Phys.*, 123:144501, October, 7 2005.

[244] T. Kawasaki and H. Tanaka. Formation of a crystal nucleus from liquid. *PNAS*, 107(32):14036–14041, August, 10 2010.

[245] P. Mayor, G. D'Anna, G. Gremaud, A. Barrat, and V. Loreto. Mechanical spectroscopy of vibrated granular matter. *Materials Science and Engineering: A*, 442(1-2):256 – 262, 2006. Proceedings of the 14th International Conference on Internal Friction and Mechanical Spectroscopy.

[246] I. Albert, P. Tegzes, B. Kahng, R. Albert, J. G. Sample, M. Pfeifer, A.-L. Barabási, T. Vicsek, and P. Schiffer. Jamming and fluctuations in granular drag. *Phys. Rev. Lett.*, 84:5122–5125, May 2000.

[247] K. E. Daniels and N. W. Hayman. Force chains in seismogenic faults visualized with photoelastic granular shear experiments. *J. Geophys. Res.*, 113(B11):B11411, November 2008.

[248] R. Burridge and L. Knopoff. Model and theoretical seismicity. *Bulletin of the Seismological Society of America*, 57(3):341–371, 1967.

[249] J. Duran. *Sands, powders, and grains: an introduction to the physics of granular materials.* Partially ordered systems. Springer-Verlag, New York, 2000.

[250] K. Falconer. *Fractal Geometry: Mathematical Foundations and Applications.* Wiley, 1990.

[251] G. C. Lichtenberg. Super nova methodo naturam ac motum fluidi electrici investigandi. Göttinger Novi Commentarii, 1777.

[252] E. W. Weisstein. Fractals. haussdorf dimension. self-similarity. From MathWorld – A Wolfram Web Resource.

[253] T.L. Heath. *The thirteen books of Euclid's Elements.* Number bks. 1-2 in Dover classics of science and mathematics. Dover, 1956.

[254] W. Rudin. *Real and complex analysis.* Mathematics series. McGraw-Hill, 1987.

[255] M. Schroeder. *Fractals, Chaos, Power Laws: Minutes from an Infinite Paradise.* Dover Publications, 2009.

[256] R. Clausius. Ueber die art der bewegung, welche wir wärme nennen. *Annalen der Physik,* 176(3):353–380, 1857.

[257] A. Okabe. *Spatial tessellations: concepts and applications of Voronoi diagrams.* Wiley series in probability and statistics: Applied probability and statistics. Wiley, 2000.

[258] E. E. Santiso and B. L. Trout. A general set of order parameters for molecular crystals. *The Journal of Chemical Physics,* 134(6):064109, 2011.

[259] L. D. Landau and E. M. Lifshits. *Quantum mechanics,* volume 4 of *Course of Theoretical Physics.* Butterworth-Heinemann, 1980.

Acknowledgements

I would like to thank my thesis advisor and co-advisor, Prof. Gérard Gremaud and Dr. Daniele Mari, who were always by my side during these years. Their reliable support has allowed me to advance steadily in my work, while I always felt I was entrusted with a lot of freedom to pursue my ideas. They were always available for discussions, ready to answer questions and, in general, to lend a hand. I would also like to acknowledge their never ending enthusiasm, sense of humor and overall kind nature, that made my stay within GSM such an agreeable experience.

Another special acknowledgment goes to Prof. Robert Schaller. He always showed interest for my work, even if he was not personally involved in the project, and I could profit from his experience many times. I would also like to thank Dr. Rosendo Sanjinez, who supervised my work as assistant for the Advanced Laboratory Course. Through this, I learnt the physics and the technical details of many experiments and phenomena, and had enriching and stimulating experiences from the interactions with the students.

My work could not have been possible, at least as it stands now, without all the help I had from my colleagues. A particular acknowledgment goes to Iva Tkalčec. She is the most supportive colleague I could meet, always ready to give advice and help. Special thoughts go to Ronan Martin, with whom I shared my office for most of my stay, and who really helped improve my French; to Claudia Ionaşcu, who took the time to get me started at the EPFL. I would also like to thank my other colleagues Mehdi Mazaheri, Ann-Kathrin Meier, Evelyn Ludi, Riccardo Balzan, Paolo Annibale, John Hennig and Fahim Chowdhury. Spending these years with you, my friends, was fun, challenging and, overall, an amazing chance of personal growth.

I owe a lot to the technical staff with whom I worked to design, build and improve the equipment I used in my experiments. Antonio Gentile, Nicolas Turin, Jean-Louis Marmillon, Alessandro Ichino (and many others) not only had to deal with my requests and ideas, but also took the time and effort to teach me many interesting things about mechanics and electronics.

I shall conclude by saying that my family was, and always is, in my thoughts. I could not have been here if it was not for your love and support through the years. Thank you very much for always believing in me.

Lausanne, le 23 mars 2012   A. L. S.

Alessandro L. Sellerio – Curriculum Vitæ

Born in Saronno, Italy, on July 28th, 1978

Current Work Address: EPFL – IPMC GSM,
                        Station 3, Boîte A, Bâtiment PH D3 495
                        CH-1015 Ecublens (VD), Switzerland.

Mobile phone (CH):   +41 078 2083864
Mobile phone (IT):   +39 347 5163670
Email: alessandro.sellerio@epfl.ch
Email: alessandro.sellerio@gmail.com
`http://mechanical-spectroscopy.epfl.ch/Stafffolder/SAlessandro.html`

Education

PhD in Physics, at EPFL (Lausanne, Switzerland),
in the field of granular materials - since December 2007

Master Degree in Physics, at the Università Statale di Milano (Milan, Italy),
with grade 110/110 *cum laude* - April 2007

High School Diploma, at the Liceo Scientifico (specializing in scientific studies)
"G. B. Grassi" of Saronno (VA, Italy), with grade 60/60 - July 1997

PhD Subject:

Towards the glass transition in vibrated granular matter.
  Supervisors: G. Gremaud (EPFL, Lausanne, Switzerland)
                   D. Mari (EPFL, Lausanne, Switzerland)

My PhD research consisted in the study of transitions in vibrated granular materials. The experimental part of the work consisted in designing and performing experiments, and analyzing the resulting data. The modeling part was focused on the improvement of the general understanding of the relationship between granular jamming and the glass transition. More recently, the work has progressed towards a novel approach of static granular media via NMR analysis.

MSc Subject:

Evolutionary Coarse Grained Models for Genomes and Transcription Networks.
  Supervisors: B. Bassetti (Università di Milano, Milano, Italia)
                   M. Cosentino Lagomarsino (Curie Institute, Paris, France)

In my MSc thesis I studied large-scale evolutionary properties of genomes, using both theoretical and computational approach on models and data. I analyzed in a quantitative framework features related to the structure and interaction of genes. Gene similarities were studied through analysis of the expressed protein structural "domains", while the interaction was studied by modeling the evolution of transcriptional interaction networks.

Subjects characterizing my studies

Physics of materials: during my PhD I have widened my knowledge on different subjects. Apart from the themes directly related to my work, I had the possibility to improve my preparation on materials science, solid state physics, and specifically the properties of metals and ceramics. I have also acquired strong laboratory competences (instrument handling, control, electronics, etc.), and on computer programming.

Theoretical physics: my Master Degree academic curriculum was mainly focused on theoretical physics. As such, a large part of my specialization was focused on statistical mechanics, quantum field theory and computational methods. However, the course book of University of Milan is rather broad and I had the chance to work on different subjects.

Languages

Italian (mother tongue), English, French. A bit of German and Russian.

Past Publications

"Identity and divergence of protein domain architectures after the Yeast Whole Genome Duplication event". *BMC Genomics*, 2010, by D. Fusco, L. Grassi, A. L. Sellerio, D. Corà, B. Bassetti, M. Caselle and M. Cosentino Lagomarsino.

"A comparative evolutionary study of transcription networks. The global role of feedback and hierachical structures". *Mol Biosyst.*, 2009, by A. L. Sellerio, H. Isambert, B. Bassetti and M. Cosentino Lagomarsino.

"Universal features in the genome-level evolution of protein domains". *Genome Biol.*, 2009, by M. Cosentino Lagomarsino, A. L. Sellerio, P. D. Heijning and B. Bassetti.

"Evolution of Hierarchy and Feedback in Transcriptional Control". Poster. *StatPhys 23*, 9-13 July 2007 Genova, Italy.

Other Working Experience

Assistant for 3$^{\text{rd}}$ year Bachelor course of Advanced Physics Laboratory (since 2007).

General atelier machine tools competences (sporadically).

Rescuer on board Italian Red Cross ambulances,
during military service (November 2004 – July 2005).

System administrator and MySQL database maintainer (sporadically).

Professor of mathematics and physics at the Liceo Classico "Legnani" of Saronno (Winter 2001).

Private teacher of physics and mathematics (since 2001).

Publications

"The glass transition associated to the jamming of vibrated granular matter", *Phys. Rev. E* 83, 021301 (2011), by A. L. Sellerio, D. Mari, G. Gremaud and G. D'Anna.

"Fluidized states of vibrated granular media studied by mechanical spectroscopy", *Mat. Sci. Forum* Vol. 184, (2011), by A. L. Sellerio, D. Mari, G. Gremaud.

"Fractional Brownian motion and anomalous diffusion in vibrated granular matter", *JStat* (2011), P01002, by A. L. Sellerio, D. Mari, G. Gremaud.

"On the control parameter for the glassy behavior of granular materials", *in preparation*, by G. D'Anna, A. L. Sellerio, D. Mari, G. Gremaud.

"MRI Imaging and reconstruction of 3D granular media structure" *in preparation*, by R. Balzan*, A. L. Sellerio*, A. Magill, D. Mari, A. Comment and G. Gremaud.

"Cluster localization in 3D reconstructed granular systems" *in preparation*, by R. Balzan*, A. L. Sellerio*, D. Mari, A. Comment and G. Gremaud.